NATIONAL TECHNICAL UNIVERSITY OF ATHENS
SCHOOL OF ELECTRICAL AND COMPUTER ENGINEERING

PHYSICS DEPARTMENT OF SCHOOL OF APPLIED MATHEMATICAL AND PHYSICAL SCIENCES

Analysis of the Boosted Higgs Boson in the $b\bar{b}$ Decay Channel Using the ATLAS Detector at CERN

DIPLOMA THESIS

by

Evripidis G. Koutsioumpas

Supervisors: Evangelos Gazis
Professor Emeritus NTUA

Marco Battaglia
Professor UCSC

Athens, June 2025

NATIONAL TECHNICAL UNIVERSITY OF ATHENS
SCHOOL OF ELECTRICAL AND COMPUTER ENGINEERING

PHYSICS DEPARTMENT OF SCHOOL OF APPLIED MATHEMATICAL AND PHYSICAL SCIENCES

Analysis of the Boosted Higgs Boson in the $b\bar{b}$ Decay Channel Using the ATLAS Detector at CERN

DIPLOMA THESIS

by

Evripidis G. Koutsioumpas

Supervisors: Evangelos Gazis
Professor Emeritus NTUA

Marco Battaglia
Professor UCSC

Approved by the three-member examination committee on 20 June 2025.

....	....	....
Evangelos Gazis	Marco Battaglia	Evangelos Hristoforou
Professor Emeritus NTUA	Professor UCSC	Professor NTUA

Athens, June 2025.

....

Evripidis G. Koutsioumpas
Diploma in Electrical and Computer Engineering, NTUA

Abstract

The study of the Higgs boson at high transverse momentum (p_T) offers a powerful probe for the exploration of potential new physics beyond the Standard Model. This thesis contributes to an inclusive, boosted $H \to b\bar{b}$ analysis conducted by the ATLAS Collaboration at CERN, using data from Run 2 and part of Run 3, corresponding to an integrated luminosity of 300 fb^{-1}. The objective is to measure the signal strength in inclusive, fiducial, and differential p_T regions, aiming to identify possible deviations from the predicted Standard Model values. Improving the uncertainties of the results in comparison to the previous published analysis using only Run 2 data, is of great importance. The work presented in this thesis, mainly focuses on four tasks. First, the b-tagging efficiency is investigated using Monte Carlo samples. The optimal tagging algorithm, which is based on transformer neural networks, is selected. Then, a method using the relative transverse momentum of muons to the jet axis, as a potential discriminant quantity in order to evaluate the $b\bar{b}$ content of the QCD background before and after flavour tagging, is developed. The results prove that indeed this quantity (muon p_T^{rel}), is appropriate for our goal. Furthermore, crucial for the signal extraction strengths, is the resolution of the mass distribution plots on Monte Carlo samples. Hence a detailed study of the resolution across different Working Points of b tagging and across two different methods of object reconstruction (PFlow and mass after regression -bJR), is performed. One important factor that deteriorates the resolution is the energy lost by muons produced in semileptonic b decays. To mitigate this effect, the Muon-In-Jet correction is developed and applied. Two methods were considered and the optimum using Variable Radius (VR) jets is selected. An optimization, regarding the muon p_T cut was conducted and the correction rates between data and Monte Carlo were tested. Based on the results, the correction is applied only in the subleading signal region. Finally, statistical fits were performed on 10 fb^{-1} of 2022 data, before and after the correction. The μ_Z signal strength was extracted, and a 15% reduction in its statistical uncertainty was observed. Similar fits are performed to different p_T bins and to additional datasets from other years.

Keywords: Boosted Higgs boson, Flavour tagging, b tagging efficiency, Muon relative transverse momentum (p_T^{rel}), $b\bar{b}$ content of QCD background, Mass resolution, Muon-In-Jet correction, Semileptonic decays, Correction rate, Statistical fitting.

Περίληψη (Abstract in Greek)

Η μελέτη του μποζονίου Higgs σε υψηλή εγκάρσια ορμή (p_T) αποτελεί ένα ισχυρό εργαλείο για τη διερεύνηση ενδεχόμενης νέας φυσικής πέρα από το Καθιερωμένο Πρότυπο. Η παρούσα διπλωματική εργασία συμβάλλει σε ανάλυση του καναλιού διάσπασης $H \to b\bar{b}$, με υψηλή εγκάρσια ορμή (p_T), όπου όλοι οι τρόποι παραγωγής του μποζονίου Higgs λαμβάνονται υπόψιν. Η ανάλυση αυτή, διεξάγεται από το πείραμα ATLAS στο CERN, χρησιμοποιώντας δεδομένα από το Run 2 και μέρος του Run 3, που αντιστοιχούν σε ολοκληρωμένη φωτεινότητα 300 fb^{-1}. Στόχος είναι ο προσδιορισμός της ισχύος σήματος στις ολικές, fiducial (αναφέρεται σε συγκεκριμένη περιοχή του ανιχνευτή) και διαφορικές περιοχές p_T, με σκοπό την ανίχνευση πιθανών αποκλίσεων από τις προβλέψεις του Καθιερωμένου Προτύπου. Ιδιαίτερης σημασίας είναι η μείωση των αβεβαιοτήτων σε σύγκριση με την προηγούμενη δημοσιευμένη ανάλυση που βασίστηκε αποκλειστικά σε δεδομένα του Run 2. Η παρούσα διπλωματική επικεντρώνεται κυρίως σε τέσσερις άξονες. Πρώτον, μελετάται η απόδοση της ανίχνευσης b quark (b-tagging) μέσω δειγμάτων Monte Carlo και επιλέγεται ο βέλτιστος αλγόριθμος, ο οποίος είναι υλοποιημένος σε νευρωνικά δίκτυα τύπου transformer. Επειτα, μελετάται η σχετική εγκάρσια ορμή των μιονίων ως προς τον άξονα της δέσμης (jet), ως πιθανό μέγεθος για την εκτίμηση του περιεχομένου $b\bar{b}$ στο υπόβαθρο QCD, πριν και μετά την ανίχνευση των b quark (flavour tagging). Τα αποτελέσματα δείχνουν πως η ποσότητα αυτή (p_T^{rel} του μιονίου) είναι κατάλληλη για τον σκοπό αυτό. Επιπλέον, καθοριστική για την εξαγωγή του σήματος είναι η διακριτική ικανότητα (resolution) των κατανομών αναλλοίωτης μάζας στα δείγματα Monte Carlo. Συνεπώς, πραγματοποιείται λεπτομερής μελέτη της διακριτικής ικανότητας για διαφορετικά σημεία εργασίας (Working Points) της ανίχνευσης b quark και για δύο μεθόδους ανακατασκευής (PFlow και μάζα μετά από μοντέλο παλινδρόμησης – bJR). Ενας πολύ σημαντικός παράγοντας που συμβάλλει στην υποβάθμιση της διακριτικής ικανότητας, είναι η χαμένης ενέργεια από μιόνια που προέρχονται από ημιλεπτονικές διασπάσεις b κουάρκ. Αναπτύσσεται και εφαρμόζεται, επομένως, η διόρθωση Muon-In-Jet. Εξετάζονται δύο μέθοδοι και επιλέγεται η βέλτιστη, βασισμένη σε μεταβλητής ακτίνας (Variable Radius – VR) jet. Πραγματοποιείται επίσης βελτιστοποίηση του κατωφλίου p_T των μιονίων, πάνω από το οποίο τα λαμβάνουμε υπόψιν για την διόρθωση και εξετάζονται οι λόγοι διόρθωσης μεταξύ δεδομένων και Monte Carlo. Σύμφωνα με τα αποτελέσματα, η διόρθωση εφαρμόζεται μόνο στην δευτερεύουσα (subleading) περιοχή σήματος. Τέλος, πραγματοποιούνται στατιστικές προσαρμογές σε δεδομένα 10 fb^{-1} από το έτος 2022, πριν και μετά τη διόρθωση. Εξάγεται η ισχύς σήματος μ_Z και παρατηρείται μείωση της στατιστικής της αβεβαιότητας κατά 15%. Παρόμοιες προσαρμογές πραγματοποιούνται και για διαφορικές περιοχές p_T και για επιπλέον σύνολα δεδομένων από άλλα έτη.

Λέξεις-κλειδιά: Ενισχυμένο μποζόνιο Higgs, Αναγνώριση γεύσης (Flavour tagging), Αποδοτικότητα b tagging, Σχετική εγκάρσια ορμή μιονίου (p_T^{rel}), Περιεχόμενο $b\bar{b}$ υποβάθρου QCD, Διακριτική ικανότητα μάζας, Διόρθωση Muon-In-Jet, Ημιλεπτονικές διασπάσεις, Λόγος διόρθωσης, Στατιστική προσαρμογή.

Acknowledgments

I would like to express my sincere gratitude to my two supervisors, Professor Evangelos Gazis and Professor Marco Battaglia. Two years ago, I enrolled in a course on Nuclear and Particle Physics, where I had the opportunity to meet Prof. Gazis. Soon after, our collaboration began. I am truly thankful to him for offering me the opportunity to participate in a high-level physics analysis and to conduct my thesis in collaboration with one of the world's largest experiments; ATLAS at CERN. A few months later, during my visit to CERN, I also had the privilege of meeting Prof. Battaglia in person. Since then, he included me in the analysis presented in this thesis. He has greatly supported me in completing this work by providing valuable material, answering my questions, and guiding me throughout the year in the best possible way. To both of you, thank you for your continuous guidance, support and your trust to my abilities. I sincerely hope this is not the end, but rather the beginning of future collaboration.

Additionally, I would like to thank Professors Theodoros Alexopoulos and Ioannis Kopsalis, members of the NTUA ATLAS group, for reviewing my work and consistently providing valuable feedback. I am also grateful to all my professors at the School of Electrical and Computer Engineering for equipping me with the knowledge and skills necessary to meet the challenges I encountered throughout this thesis.

As Aristotle said, "Without friends no one would choose to live, though he had all other goods". Hence, I would like to also thank all my family and friends. Your trust in me, your unwavering support, and your patience —especially when I eagerly shared every day all the details of my work!— have been truly invaluable. This thesis would not have been the same without each and every one of you by my side. Thank you sincerely, for everything!

I dedicate this work to all of you, but especially to my best friend, Christopher, whom I had the honor of having by my side for twenty years. The discussions we shared, the memories we created, and your support are an inseparable part of who I am.

“Seeking what is true is not seeking what is desirable”
ALBERT CAMUS, *The Myth of Sisyphus*

Contents

List of Figures

List of Tables

Chapter 1

Introduction

The observation of the Higgs boson in 2012, was a landmark achievement, yet the studies are far from finished. More precise measurements of Higgs properties an the use of Higgs as a tool for new discoveries are the reasons searches on the Higgs boson are still very popular in the field of particle physics. This analysis is an inclusive (i.e all production modes are considered) search of the boosted (i.e high transverse momentum) Higgs boson in the $b\bar{b}$ decay channel, using data from the ATLAS detector at CERN, during the periods: Run 2 (2015-2018) and partial Run 3 (2022-2024). The goal is to study observables connected to the Higgs model (like the signal strength (μ_H)) and search for possible deviations from the existing theory; the Standard Model. Such deviations, could possibly indicate the existence of New Physics (NP). A previous analysis conducted using only Run 2 data, reported good agreement with the Standard Model [1]. With more data (a factor of 2.2) to the present analysis, the improvement of the uncertainties accompanying the result, compared to the previous analysis, is of great importance.

My work for the present thesis focuses on four tasks. The first one is the evaluation of b tagging efficiency using various b tagging algorithms, in order to select the optimum. Then, the relative transverse momentum of muons to the jet axis (muon p_T^{rel}) is studied as a potential discriminant for the $b\bar{b}$ content of the QCD background, before and after the flavour tagging. Furthermore, the Jet Mass Resolution of various distributions of Monte Carlo samples is thoroughly examined. Achieving a smaller resolution, holds a key role on having smaller uncertainties accompanying our results. The final task was the optimization and implementation of the Muon-In-Jet correction in the analysis cut flow. With this correction, resolution of the subleading signal region improves and statistical uncertainties decrease. The complete analysis contains several additional subjects which fall outside the scope of this thesis. They will be briefly mentioned when needed, for the sake of coherence. The structure of the thesis is outlined as follows.

Chapter 2, provides the theoretical background most relevant to the present analysis. It begins with an overview of the Standard Model (SM) and the fundamental forces. Essential physical quantities such as the invariant mass, the cross section, the branching ratio and decay widths, are defined. Furthermore, the Lagrangian formalism and Noether's theorem along with some quantum numbers being conserved, are presented. Basic mathematical conventions are introduced, followed by several important equations, one of which is the Standard Model Lagrangian. Then, the ElectroWeak Symmetry Breaking mechanism, which led to the perception of the Higgs boson, is explained. Finally, the experimental profile of the Higgs boson at the Large Hadron Collider, along with mentions to Beyond the Standard Model physics are provided.

Chapter 3, presents an overview of CERN, the LHC, and the ATLAS detector, starting with a concise account of CERN's history to date. The accelerator complex along with the layout and components of the LHC are presented. Furthermore, the ATLAS detector and the various sub detectors are outlined, with particular attention to their individual purposes. Special emphasis is given to the systems on which the data used in this work are primarily based, while trying to keep the technical characteristics to the minimum possible. The chapter ends with a mention to CERN's future program.

Chapter 4, contains an introduction to the analysis. The motivation behind a boosted Higgs search is presented and the data sets/MC samples used are introduced. Subsequently, the event selection strategy and the modeling of signal and background processes are described. Furthermore event reconstruction is presented. The chapter concludes with my studies on the b tagging efficiencies and the method on muon p_T^{rel}.

Chapter 5, presents my study on the mass resolution. Initially basic quantities related to mass distributions and on which the assessment of histograms is based, are introduced. The study is then conducted in two stages, first as a function of different Working Points corresponding to different b tagging efficiencies and secondly through different MC campaigns corresponding to the different data taking years of the analysis.

Chapter 6, is exclusively devoted on the Muon-In-Jet Correction (MIJ). The parameters (correction and mistag rate) evaluating the quality of the correction are thoroughly studied, through two different applications of the Muon-In-Jet correction; one based on large-R jets and the second on Variable Radius jets. After the optimization of the correction is complete, histograms for each regions and p_T bins are evaluated. Finally, MIJ is implemented in the analysis, correction rates are compared through different MC samples and a 2022 data set and a statistical fit is performed extracting the Z boson signal strength in order to determine the statistical error change.

Chapter 7 serves as the conclusion. It begins by summarizing the results presented in Chapters 4, 5, and 6. Additionally, it outlines some anticipated outcomes of the full analysis upon its completion.

Readers already familiar with the theoretical framework, the LHC, and the ATLAS detector configuration may proceed directly to Chapter 4, without any loss of coherence.

Before we begin with the theoretical background, two general remarks regarding the material presented in this thesis are important to highlight. Most of my plots are labeled as "ATLAS Internal" because they have not yet been published by the ATLAS Collaboration. However, they have been reviewed and are approved for inclusion in this thesis. In plots where studies are extended on Monte Carlo samples, simulating the data taking years of the analysis (chapters 5, 6), the year 2022 appears twice as two different Monte Carlo samples were considered. For any questions or comments, feel free to contact me at ekoutsio@cern.ch or ekoutsioumpas@gmail.com.

Chapter 2

Standard Model, Higgs Boson and Beyond

It is impossible to dive deeper into an experiment, without being familiar with the underlying theory. Therefore, this chapter presents the foundational theory of modern high-energy physics. We begin with a brief history, highlighting some major discoveries in the field. A detailed presentation of the Standard Model and the fundamental forces is followed. Subsequently, important quantities (such as the cross section) are defined and some land mark equations are presented. Following this, the Standard Model Lagrangian is provided with particular emphasis on the Higgs term. A thorough mathematical analysis of the Electroweak Symmetry Breaking and the Englert-Brout-Higgs mechanism is conducted. Finally, the chapter concludes with the experimental profile of Higgs boson at the Large Hadron Collider and mentions to Beyond the Standard Model theories.

2.1 History

About 400 BC Greek philosophers Democritus and Leucippus assumed that matter was made up of some elementary particles, which they called atoms. Atom comes for the greek word ”atomos” (written in greek "ἄτομο") which means indivisible. At the end of the 19th century, with the discovery of the electron in 1897 by J.J Thomson, it was determined that atoms could be further divided and the nucleus of hydrogen was characterized as a proton. Moving on, in 1911, Rutherford measured the size of many nucleus and in 1932 James Chadwick discovered the neutron [2]. The same year the positron (the antiparticle of the electron) was discovered by Carl Anderson [3], which was consistent with Dirac's prediction for antimatter made in 1928 (for the famous Dirac equation see section 2.7.4) [4]. Anderson he was awarded the Nobel Prize in 1933, for his discovery. Back in 1932 the known fundamental particles, forming matter, where the proton, the neutron and the electron. As of 1932, more elementary particles were discovered with the latest being the Higgs boson in 2012. Additionally, hundreds of complex particles are also discovered and a summarizing table can be found in [5]. Arriving to 2025, we know that protons and neutrons are not fundamental; in fact they are made up of quarks. Quarks, in combination with other particles form the model of fundamental particles, known as the Standard Model for particle physics, which constitutes the subject of this chapter.

2.2 Standard Model

The Standard Model [6, 7, 8, 9, 10, 11, 12, 13, 14] represents the most comprehensive theory in particle physics, incorporating all known elementary particles and describing their interactions through three of the four fundamental forces (strong, weak and electromagnetic). Apart from being simply a table of particles, it is based on heavy mathematical formalization and constitutes a renormalizable **Q**uantum **F**ield **T**heory (QFT). It presents a $SU(3)_C \times SU(2)_L \times U(1)_Y$ local gauge symmetry, where C stands for color, L for left and Y for the hypercharge (see section 2.6).

Let us now explore the particles and the groups which form. Based on their spin particles can be divided into the following two major categories:

Fermions have half-integer spin and follow Fermi-Dirac theory. They make up all of the known matter and follow Pauli's exclusion principle. Consequently, their final state wavefunction is antisymmetric under the exchange of two fermions.

Bosons have integer spin and follow Bose-Einstein theory. Vector bosons are the carriers of the fundamental forces (see section 2.3) and are desrcibed by symmetric wavefunctions. As a result, many bosons can be found in the same quantum state.

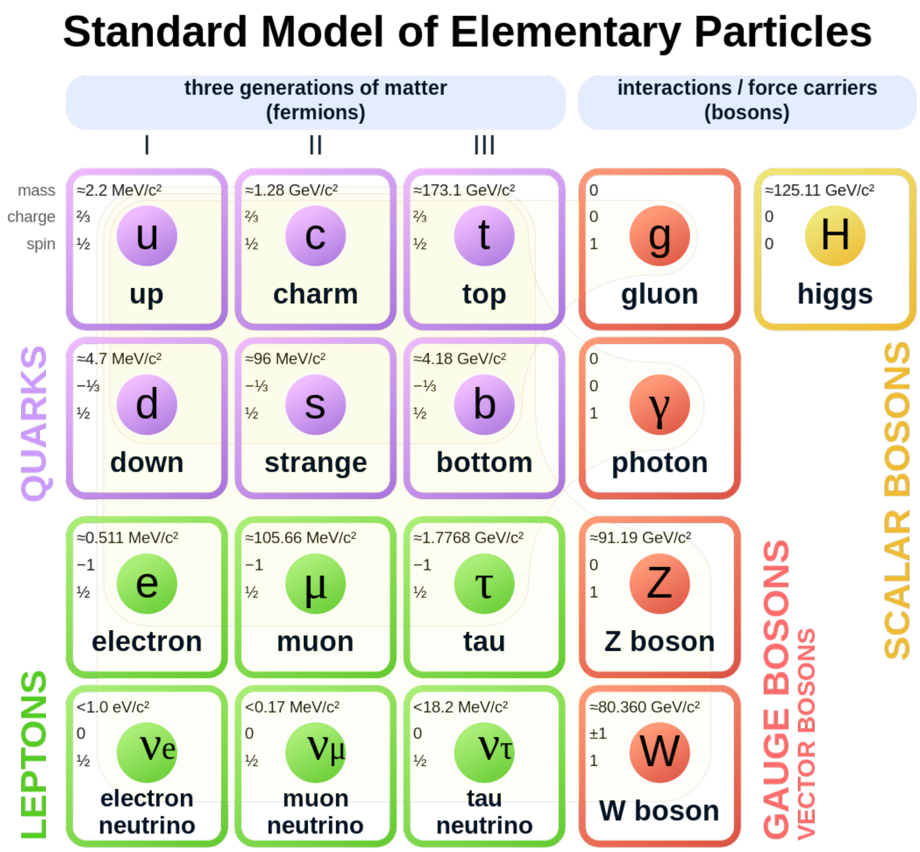

Figure 2.1: The Standard Model of particle physics. Particles are sorted according to their quantum numbers.

Fermions are further divided into quarks and leptons.

Quarks: They are fundamental particles whose existence was proposed by Murray Gell-Mann [15] and George Zweig [16] in 1964. There are six different quarks: up, down, charm, strange, top and bottom, often referred as six different flavours and organized into three groups/generations (i.e isospin doublets). Additionally, they have an electric charge which is a fraction of the electrons charge and are subjected to all fundamental forces of the SM. All quarks have different masses and carry a color charge: red, green or blue, described by **Q**uantum **C**hromo**D**ynamics (QCD) theory, which studies the interactions between quarks and gluons (i.e the bosons propagating the strong force - see section 2.3).

Furthermore, they can never be isolated in nature, that is they form bound states of **hadrons**, further divided into: mesons and baryons. **Mesons** consist of a quark and an antiquark ($q\bar{q}$), have spin 0 or 1 and masses between the mass of the electron and the mass of the proton. **Baryons** consist of 3 quarks (qqq). They are heavier than mesons, with masses greater than (or equal to) proton mass and have spin $\frac{1}{2}$ or $\frac{3}{2}$. Evidence of a structure with four of five quarks (exotic particles) are reported, namely tetraquark ($qqqq$) [17] and pentaquark ($qqqqq$) [18]. The proton is the lightest hadron consisting of two up quarks and one down. Today the list of hadrons contains more than 100 particles, with 78 discovered at the LHC up to now (May 2025). The up to date list can be found in [19].

Leptons: They are named after the greek word ”leptos” (in greek "λεπτός") meaning thin, as they have smaller masses than hadrons. Additional reason for their name is they do not present any structure (like hadrons), as they are fundamental particles. There are six known leptons, all have spin $\frac{1}{2}$ and are organized into three groups, like the quarks. Each group contains one (charged) lepton and it's corresponding neutrino. The lighter lepton is the electron (e), followed by the muon (μ) and then, the tau (τ). Neutrinos were initially considered to have zero mass, making their discovery very difficult. They were first observed by Cowan and Reines in 1956 [20] in radiation β reactions. Today, it is believed that neutrinos have a very small mass and are not massless. This allows neutrino oscillations [1] to occur, which were firstly observed between ν_μ and ν_τ as reported in 1998, by the Super Kamiokande experiment in Japan [21]. Upper limits on their masses have been determined, with the latest limit announced at only 45 GeV! by [22], but the exact value still remains unmeasured. Finally, leptons engage only via the electromagnetic and weak forces.

2.3 Fundamental Forces

2.3.1 Virtual Particles

Quantum vacuum, experiences energy fluctuations according to Heisenberg's uncertainty principle [6, 7, 8]:

$$\Delta E \cdot \Delta t \geq \hbar \tag{2.1}$$

That means that particles can constantly appear and disappear within time Δt given by the uncertainty principle. Hence the total energy may not be equal to zero at all times. These particles are called virtual particles and they violate the energy and momentum conservation law. Although this may seem wrong the first time one reads it, everything remains consistent, provided that this occurs within Δt. According to quantum field theories, forces are transmitted by propagator particles, which are quanta of the force field and are named gauge bosons. When the propagator particle is emitted and absorbed by another particle within the time Δt we say that an interaction took place.

2.3.2 Range of Forces

Let us examine the elastic interaction $A + B \to A + B$, which occurs via the propagator particle X and can be depicted through the following Feynman diagram.

[1] The phenomena where neutrinos can change flavor when they travel.

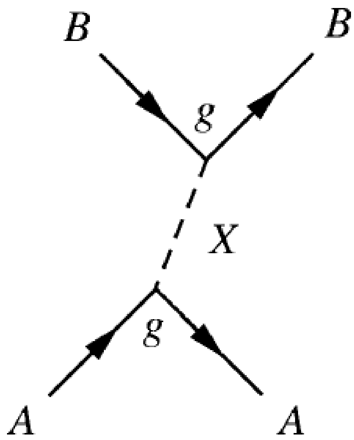

Figure 2.2: Elastic scatter of particles A and B via the particle X [7].

On the bottom vertex we have $A \to A + X$. The initial and final energy of particle A are respectively

$$E_{A,initial} = M_A c^2, \quad E_{A,final} = (p^2c^2 + M_A^2 c^4)^{1/2} \tag{2.2}$$

The energy of the emitted virtual X is:

$$E_X = (p^2c^2 + M_X^2 c^4)^{1/2} \tag{2.3}$$

The energy difference between the initial and final state is:

$$\begin{gathered} \Delta E = E_X + E_{A,final} - E_{A,initial} \Rightarrow \\ \Delta E = (p^2c^2 + M_X^2c^4)^{1/2} + (p^2c^2 + M_A^2c^4)^{1/2} - M_Ac^2 \end{gathered} \tag{2.4}$$

It is evident that:

$$\begin{gathered} p \to \infty, \quad \Delta E \to 2pc \\ p \to 0, \quad \Delta E \to M_X c^2 \end{gathered} \tag{2.5}$$

Hence, $\Delta E \geq M_x c^2$ for every possible value of the momentum p. Comparing to Heisenberg's uncertainty, written in the form $\Delta E \geq \frac{\hbar}{\Delta t}$, we calculate $\Delta t = \frac{\hbar}{M_X c^2}$. The distance throughout the force can be propagated during this time is $R = c\Delta t$, leading us to:

$$R = \frac{\hbar}{M_X c^2} \tag{2.6}$$

This is the range of the interaction (i.e the maximum distance at which the virtual X can be transmitted before it gets absorbed by particle B).

Note that for the electromagnetic force, photons are massless resulting in infinite range. On contrary, $M_W \approx 80GeV/c^2$, providing us with $R = 2 \times 10^{-3} fm$ for the range of the weak interaction (this is just a rough calculation without precision). The reasoning followed, is based on the approach presented in [7].
Typical values for the ranges of the fundamental forces can be seen in table 2.1.

2.3.3 Description of Forces

In nature, all particles are subject to (only!) four fundamental forces. These are: the strong nuclear force, the electromagnetic force the weak (nuclear) force and gravity. A brief description of each fundamental force as it can be found in [9] and [11] is the following.

Strong Nuclear Force: Responsible for the binding of protons and neutrons within the atomic nucleus. This force operates over a very short range, approximately the size of the nucleus, and is the strongest among the four fundamental interactions. It acts on quarks, is transmitted by gluons and follows the Quantum Chromodynamics theory (QCD).

Electromagnetic Force: Fundamental to the formation of atoms and molecules. It operates over long ranges via photons γ and governs the interactions between electrically charged particles, as described by Coulomb's law. In classical physics it is described by Maxwell's equations and in the quantum world it follows Quantum Electrodynamics (QED) theory.

Weak (nuclear) Force: A long-range nuclear interaction with a destabilizing effect on atomic nuclei, playing a key role in the processes of radioactive decay, energy creation in the Sun and heavy element generation inside stars. It acts on quarks, leptons and electroweak gauge bosons, is transmitted by $W^{\pm}$, Z^0 and follows the electroweak theory.

Gravity: An extremely long-range force responsible for holding planets, stars, and galaxies together. It is the weakest of the four fundamental interactions and has a negligible effect on elementary particles. It acts on all particles and theoretically is transmitted by gravitons (there is still no experimental proof). Notably, gravity is not incorporated into the Standard Model of particle physics and no satisfactory quantum field theory exists. In classical level it is described by Einstein's general theory of relativity.

Some important characteristics and usual values of parameters related to the fundamental forces, are summarized in tables 2.1, 2.2.

Interaction	Relative Strength	Range	Transmitted by
Strong	1	Short (~ 1 fm)	Eight gluons (g)
Electromagnetic	$\frac{1}{137}$	Long ($1/r^2$)	Photon (γ)
Weak	10^{-9}	Short (~ 0.001 fm)	$W^{\pm}$, Z^0
Gravitational	10^{-38}	Long ($1/r^2$)	(Graviton)

Table 2.1: Relative strengths, ranges and responsible bosons, for the four fundamental forces [10].

Interaction	Typical Lifetime (sec)	Typical σ (mb)	Example
Strong	10^{-12}	10	$\Delta \to p\pi$
Electromagnetic	$10^{-20} - 10^{-16}$	10^{-3}	$\gamma p \to p\pi^0$
Weak	10^{-12} or longer	10^{-11}	$\pi^- \to \mu^- \bar{\nu}_\mu$

Table 2.2: Typical lifetime and cross sections for particle interacting via strong, electromagnetic and weak forces. Examples of reactions are given [6].

Finally we should note that combining the fundamental constants appropriately we get the following quantity known as Planck mass.

$$M_P = \sqrt{\frac{\hbar c}{G_N}} = \sqrt{\frac{1.06 \times 10^{-34}\,\text{Js} \times 3 \times 10^8\,\text{m/s}}{6.67 \times 10^{-11}\,\text{m}^3\text{kg}^{-1}\text{s}^{-2}}} = 2.18 \times 10^{-8}\,\text{kg} = 1.22 \times 10^{19}\,\text{GeV} \tag{2.7}$$

At this energy scale, all fundamental forces were unified in the beginning of the universe. Unfortunately it is a very high energy that we will never be able to achieve in our experiments.

In combination with the Planck mass, we have the Planck length and Planck time respectively:

$$\ell_P = \sqrt{\frac{\hbar G}{c^3}} = 1.616 \times 10^{-35}\ \text{m} \tag{2.8}$$

$$t_P = \frac{\ell_P}{c} = \sqrt{\frac{\hbar G}{c^5}} = 0.539 \times 10^{-43}\ \text{s} \tag{2.9}$$

During the first $10^{-43}\ s$ which is exactly one Planck time as seen in equation 2.9 all fundamental forces (strong, electroweak and gravity) had the same strength and were unified. This era is known as the Planck epoch and no proven theory exists until today. At the end of this epoch, the temperature was $T \approx 10^{32}\ K$, the universe spanned one Planck length (equation 2.8) and the average energy per particle was $E = 10^{19}\ GeV$. At $t = 10^{-12}\ s$ the electroweak force is divided into the electromagnetic and the weak force. Since then, the four fundamental forces, exist as we know them today. It is evident that particle physics, which investigates extremely small subatomic and sub-nuclear particles, is deeply connected to cosmology, which deals with the largest structures in the universe and the evolution of the universe itself. Although a detailed study of the history of our universe lies beyond the scope of this thesis, interested readers are encouraged to consult [9, 10, 14, 23] for further information.

2.4 Invariant Mass, Frames of Reference

Suppose we have n particles each with energy E_i and momentum p_i, that do not interact with each other. Then the invariant mass of the system is given by the expression [8]:

$$M = \sqrt{E^2 - P^2} = \sqrt{\left(\sum_{i=1}^{n} E_i\right)^2 - \left|\sum_{i=1}^{n} \vec{p}_i\right|^2} \tag{2.10}$$

The invariant mass is independent of the reference frame and is widely used in experimental particle physics, in order to identify particles. The majority of the plots presented in our analysis depict the distribution of the number of events as a function of the invariant mass. The final decay products we detect with our equipment help us reconstruct this invariant mass.
The square of the invariant mass is also invariant and very useful, especially to characterize the energy scale of a collider.

$$s = M^2 = \left(\sum_{i=1}^{n} E_i\right)^2 - \left|\sum_{i=1}^{n} \vec{p}_i\right|^2 \tag{2.11}$$

We are interested in two reference frames: The Center of Mass (CM) frame and the Laboratory (L) frame. The former is defined as the system where the total momentum of the system equals to zero, while the latter is the system where one of the particles called target is in rest as the other particle moves towards it. We will examine the simple case of two particles a and b colliding, into the aforementioned systems.

In the L frame the s is given by:

$$s = (E_a + m_b)^2 - p_a^2 = m_a^2 + m_b^2 + 2E_a m_b \tag{2.12}$$

Usually the energy of the particle a is much higher than the mass of particle a and b, resulting in the simplified expression:

$$s \approx 2E_a m_b \quad \text{for} \quad E_a \gg m_a, m_b \tag{2.13}$$

In the CM frame, because $E_a^* \gg m_a$ and $E_b^* \gg m_b$ we get $E_a^* \approx p_a^*$ and $E_b^* \approx p_b^*$. Hence the s is given by:

$$s = (E_a^* + E_b^*)^2 \approx (2E^*)^2 \tag{2.14}$$

We can clearly conclude from equations 2.13 and 2.14 that at the CM frame all the energy is available for new particles production, while in the L frame only a portion of the total energy is available [8].

Figure 2.3: Comparison of two frames: Lab frame (left) and CM frame (right).

2.5 Cross-section, Branching Ration and Decay Width

Assume a target with N particles able to interact with a beam. The flux of the beam, moving towards the target is expressed by:

$$J = n_b v_i \tag{2.15}$$

where n_b in the particle density in the beam and v_i is the velocity of the particles measured at the rest reference frame of the target. The rate at which the interaction occurs, is:

$$W_r = JN\sigma_r \tag{2.16}$$

where σ_r is named cross section of this interaction and expresses the probability this interaction takes place. For each initial state, we have a number of possible final states, i.e many possible interactions r. Hence the total cross section for a process is given by the sum,

$$\sigma = \sum_r \sigma_r \tag{2.17}$$

Cross section has surface dimensions and it is measured in barns (b) with $1b = 10^{-28} m^2$. As $1b$ is usually a very big unit for subnuclear physics, mostly the subdivisions mb, μb, nb and pb are used. Additionally, in equation 2.16 the product JN constitutes another quantity, known as luminosity (L) with dimensions $[length]^{-2}[time]^{-1}$. Luminosity, expresses the flux of particles, i.e. the number of particles crossing through some space per unit time. We will present more about luminosity, at section 3.2.3, after the LHC is introduced.

The differential cross section can be defined as,

$$\frac{d\sigma}{d\Omega} = \frac{1}{JN}\frac{dn}{d\Omega} \tag{2.18}$$

where dn are the number of particles arriving at the detector. Integrating over $d\Omega$, gives us the total cross section,

$$\sigma = \int \frac{d\sigma}{d\Omega} d\Omega \tag{2.19}$$

In the general case, differential cross section depends on energy, scattering angles and spin of the particles involved [7]. When is it independent of the spin, it is called unpolarized cross section and is a function of θ only.

The analytic expression of the cross section, for different interactions is not trivial and requires many calculations. Formulas of Rutherford cross section, Mott or other processes are widely available in many textbooks [6, 7, 8] and will not be given here. In our experimental analysis, cross section is a quantity we rely heavily on.

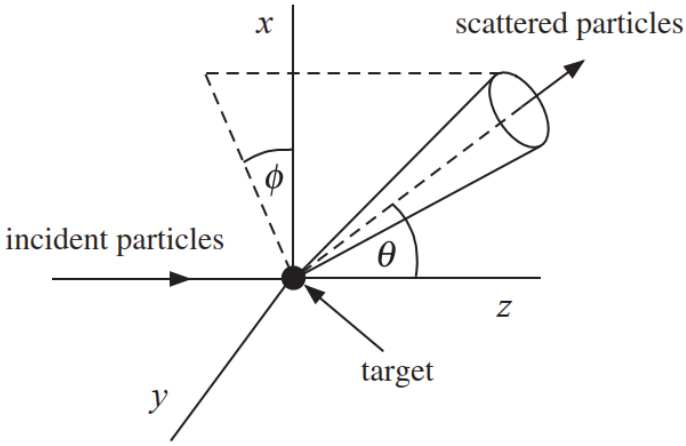

Figure 2.4: Beam interacting with a target and particles being scattered at an angle θ.

An unstable particle decays after a given time τ. This time τ, describes the initial particle and is called lifetime at rest. Through Heisenberg's uncertainty principle (equation 2.1) and using natural units ($c = \hbar = 1$), we define the natural decay width, as:

$$\Gamma = \frac{1}{\tau} \tag{2.20}$$

The particle might decay to a number of different channels f. Let us assume for the Higgs boson for example the decay channels $H \to X_i Y_i$. Each channel will have the corresponding natural decay width Γ_f. Summing over all channels, we obtain the total decay width:

$$\Gamma = \sum_f \Gamma_f \tag{2.21}$$

For each channel we can compute the Branching Ratio (BR), which is the fraction of parent particles which decay via this channel, to the total number of channels. Mathematically this is expresses as:

$$BR_f = \frac{\Gamma_f}{\Gamma} \tag{2.22}$$

Using our notation for the Higgs decay channels the above equation can be written equivalently as:

$$BR(H \to X_i Y_i) = \frac{\Gamma(H \to X_i Y_i)}{\sum_f \Gamma(H \to X_f Y_f)} \tag{2.23}$$

Combining cross section and BR, most of the analyses (and our analysis) on the Higgs boson, provide results on the signal strength. It is defined as the the fraction of the cross section times the branching ratio for a specific process, over the corresponding value expected from the SM theoretical calculations.

$$\mu = \frac{(\sigma\, BR)_{\text{exp}}}{(\sigma\, BR)_{\text{SM}}} \tag{2.24}$$

Good agreement with the SM, means μ values close to 1.0 with small errors.

Finally, we will mention the Breit-Wigner formula, which is very useful to calculate the resonance masses and widths. A complete presentation for the derivation of the formula can be found in [7]. For any reference frame, we have:

$$N(W) = \frac{K}{(W-M)^2 + \Gamma^2/4} \tag{2.25}$$

where K, is a constant depending on the number of different decay modes. This distribution is used to fit experimental data, in order to determine the resonance mass and width. A graphical representation of the formula is given below.

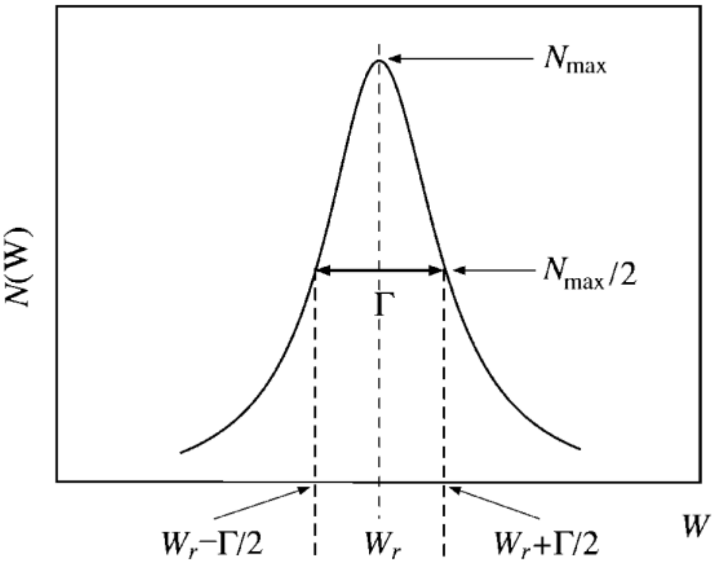

Figure 2.5: Plot of the Breit-Wigner distribution. A maxima is presented at $W = W_r$ and the width is Γ.

2.6 Lagrangian and Noether's Theorem

A central component of the mathematical structure of the Standard Model (SM) is the Lagrangian, which is defined as the difference between the kinetic energy and the potential energy,

$$L = T - V \tag{2.26}$$

where $T = T(q, \dot{q})$ and $V = V(q)$ are functions of a general position coordinate q and $\dot{q}$ is the time derivative [6, 13]. Given a Lagrangian, the action is defined as the integral over time:

$$S = \int_{t_i}^{t_f} dt\, L(q, \dot{q}, t) \tag{2.27}$$

The action is closely related to Hamilton's principle which states that nature will always choose a path in $p, \dot{q}$, that minimizes S. Because S is a functional and relies on the path taken (not only the initial and final point), finding the extremum requires a Taylor expansion. Following the process described in [13], using the action S and Hamilton's principle we can derive the Euler - Lagrange equation of the particle,

$$\frac{d}{dt}\frac{\partial L}{\partial \dot{q}} - \frac{\partial L}{\partial q} = 0 \tag{2.28}$$

Generalizing to multiple coordinates q_i $(i = 1, \dots, n)$, we obtain:

$$\frac{d}{dt}\frac{\partial L}{\partial \dot{q}_i} - \frac{\partial L}{\partial q_i} = 0 \tag{2.29}$$

In case our system is continuous the Lagrangian transforms as:

$$L(q_i, \dot{q}_i, t) \rightarrow \mathscr{L}\left(\phi, \frac{\partial \phi}{\partial x^\mu}, x^\mu\right) \tag{2.30}$$

providing us with the corresponding Euler-Lagrange Equation for fields $\phi = \phi(x, t)$

$$\frac{\partial}{\partial x^\mu}\left(\frac{\partial \mathscr{L}}{\partial(\partial_\mu \phi)}\right) - \frac{\partial \mathscr{L}}{\partial \phi} = 0 \tag{2.31}$$

The $\mathscr{L}$ is the Lagrangian density (often referred as Lagrangian) and connected to L, through the integral:

$$L = \int d^n x\, \mathscr{L} \tag{2.32}$$

where $d^n x = dx^1\, dx^2\, dx^3 \cdots dx^n$ is at the n-dimension coordinate system. It is important to point out that $\mathscr{L}$ will not depend on **x** and t, but on the fields $\phi = \phi(x, t) = \phi(x^\mu)$.

Beside the Lagrangian, also useful is the Hamiltonian, representing the total energy of the system and defined as:

$$H = T + V \tag{2.33}$$

The connection between the Lagrangian and Hamiltonian is established via the Legendre transformation,

$$p\dot{q} - L = H \tag{2.34}$$

In physics, symmetries play a major role as they are strongly connected to conservation laws. Emmy Noether published a theorem in 1918, known today as **Noether's theorem**, proving that the existence of a continuous symmetry in the action of a physical object results to the conservation of a corresponding quantity [13, 24]. Some of the most well known conservation laws and the symmetries from which arise, are summarized in table 2.3.

Symmetry	$\leftrightarrow$	Conserved Charge
rotational invariance	$\leftrightarrow$	angular momentum
translational invariance	$\leftrightarrow$	(linear) momentum
time translation invariance	$\leftrightarrow$	energy

Table 2.3: Examples of symmetries and their associated conserved quantities (via Noether's theorem).

As we explore further symmetries which arise in the QFT of the Standard Model, we obtain many more conservation laws than those listed above. Energy, momentum, electric charge (Q) and spin (S) are conserved in every interaction.
Additionally, the following quantum numbers [7, 9, 11], are conserved:

- **Lepton Number (L):** It is defined for leptons and is generally conserved in all reactions, with possible exception on cases of neutrino oscillations. For each lepton flavor there is a different lepton number, namely $L_e = 1$ for e, ν_e, $L_\mu = 1$ for μ, ν_{mu} and $L_\tau = 1$ for τ, ν_τ. Antiparticles have the opposite values and all other particles posses leptonic numbers equal to zero.

- **Baryon Number (B):** Baryons have $B = +1$, while anti-baryons $B = -1$, yielding for quarks (anti-quarks) $B = +1/3(-1/3)$. For all other particles B is equal to zero. Generally the baryon number is conserved, otherwise proton would decay to a positron and a pion ($p \rightarrow e^+ + \pi^0$), a reaction which has never been observed. We must note that in some Grand Unified Theories (GUT), the baryon number may not be conserved [9].

- **Parity (P):** Parity operator refers to the transformation of a right-handed coordinate system into a left-handed and vice-versa. The eigenvalues of this operator, constitutes the intrinsic parity of particles. It is conserved in electromagnetic and strong reactions, but not always in weak interactions (as C.S. Wu demonstrated for beta decays in [25]). Quarks, photons, electrons, muons, taus, have intrinsic $P = +1$, neutrinos have $P = -1$.

- **Helicity:** Refers to the projection of the spin in the direction of motion. If the spin is aligned with the momentum vector of the particle we have positive helicity (right-handed particles), otherwise we have negative helicity (left-handed particles). The distinction of particles into right and left handed is done since, when viewed along the momentum direction, spin corresponds to right or left handed rotational motion. It is interesting to note that only left-handed neutrinos (and right-handed anti-neutrinos) have been observed in nature.

- **Strangeness (S):** It was introduced after observing reactions of particles K, Λ, Σ which produced strange results. Only strange quarks have a non zero strangeness; with $s = -1(+1)$ for $s(\bar{s})$. In strong and electromagnetic reactions is conserved, while in weak $\Delta S = 0, \pm 1$ is permitted.

- **Isospin (I):** It is a quantum number introduced to describe a group of particles which have very similar masses. Based on this number, particles are grouped into multiplets. The simplest example is proton and neutron, forming a doublet with isospin $1/2$ and third component of isospin $I_3 = +1/2, -1/2$ for proton, neutron respectively.

- **Charm (C), Bottomness ($\tilde{B}$), Topness (T)**: Three quantum numbers defined for charm, bottom and top quarks respectively. They are conserved in strong and electromagnetic interactions, yet not always via the weak force.

- **Hypercharge (Y):** Based on the above quantum numbers it is defined as:

$$Y = B + S - \frac{C - \tilde{B} + T}{3} \tag{2.35}$$

As mentioned above and in Section 2.2, particles—both fundamental and composite—are classified into isospin multiplets. Members of a given isospin multiplet share the same spin, parity, and quantum numbers $B, S, \tilde{B}, C, T, Y$ while differing in mass and electric charge.

Suppose we have a system and we apply three operators: parity ($\hat{P}$), charge conjugation ($\hat{C}$) and time reversal ($\hat{T}$). The initial system will remain unchanged under these actions and we call this CPT invariance.

Finally, from all the above quantities, the ones related to space-time symmetries are spin, parity and charge conjugation (if the particle is eigenvalue of the C-parity operator). Hence a widely used notation, involving these is: J^{PC} [7].

2.7 Basic Equations

2.7.1 Schrodinger Equation

It creates no surprise that we will start this section, recalling the Schrodinger equation. Assume a free non relativistic particle of mass m. Then, it's energy given by classical physics is,

$$E = \frac{p^2}{2m} \tag{2.36}$$

where p is the momentum of the particle. In quantum mechanics E, p are replaced with the operators,

$$E \to -i\hbar\frac{\partial}{\partial t}, \quad \mathbf{p} \to -i\hbar\nabla \tag{2.37}$$

Substituting 2.37 into 2.36 and using the natural units, we obtain:

$$i\frac{\partial\psi}{\partial t} + \frac{1}{2m}\nabla^2\psi = 0 \Rightarrow i\frac{\partial\psi}{\partial t} = H\psi \tag{2.38}$$

which is Schrodinger's equation [6] and where

$$H = \frac{\mathbf{p}^2}{2m} = -\frac{1}{2m}\nabla^2 \tag{2.39}$$

is the Hamiltonian operator (expressing the total energy of the particle) [6, 7, 13]. A free particle solution of the Schrodinger equation is $\psi = Ne^{ipx-iEt}$. Additionally we define as probability density the quantity,

$$\rho = |\psi|^2 \tag{2.40}$$

and j as the density flux of a beam of particles. These two quantities are connected through the continuity equation:

$$\frac{\partial\rho}{\partial t} + \nabla\cdot\mathbf{j} = 0 \tag{2.41}$$

2.7.2 Special Relativity and Four Vectors

The energy of a particle at rest, is given by the famous Einstein equation:

$$E_0 = mc^2 \tag{2.42}$$

where m is the rest mass of the particle. For a particle moving with speed v and having kinetic energy T the relativistic energy is given by:

$$E = E_0 + T = mc^2 + \gamma mc^2 - mc^2 = \gamma mc^2 \tag{2.43}$$

where,

$$\gamma = \frac{1}{\sqrt{1-\frac{v^2}{c^2}}} \tag{2.44}$$

and,

$$\beta = \frac{v}{c} \tag{2.45}$$

Now taking into consideration that $p = \frac{E}{c}$ and substituting into equation 2.43 we obtain:

$$E^2 = m^2c^4 + p^2c^2 \tag{2.46}$$

and in natural units:

$$E^2 = p^2 + m^2 \tag{2.47}$$

We know that fundamental equations in physics, are Lorentz invariant. A Lorentz transformation, relates the coordinates between two inertial frames that move with a constant speed v one from the other and is given by:

$$t' = \gamma\left(t - \frac{vx}{c^2}\right) \tag{2.48}$$

$$x' = \gamma(x - vt) \tag{2.49}$$

$$y' = y \tag{2.50}$$

$$z' = z \tag{2.51}$$

The basic Lorentz invariant is $c^2t^2 - x^2$. We define four-vector as any set of four quantities transforming like (ct, x) under Lorentz transformations. Depending on how they transform, we have two types of four vectors: the contravariant and the covariant defined respectively as:

$$x^\mu = (x^0, x^1, x^2, x^3) = (x^0, \mathbf{x}) \tag{2.52}$$

$$x^\mu = (x^0, -x^1, -x^2, -x^3) = (x^0, -\mathbf{x}) \tag{2.53}$$

where $\mathbf{x}$ is the space-like three vector. A very useful example is the (contravariant) four vector of position $x^\mu = (ct, x, y, z)$ with the invariant $c^2t^2 - x^2$. Another example is the (covariant) four vector of momentum $p_\mu = (\frac{E}{c}, p_x, p_y, p_z)$, with the invariant $\frac{E^2}{c^2} - p^2$.
The contravariant and covariant vectors transform respectively as:

$$x'^\mu = \Lambda^\mu{}_\nu x^\nu \tag{2.54}$$

$$x'_\mu = \Lambda^\nu{}_\mu x_\nu \tag{2.55}$$

where the $\Lambda^\mu{}_\nu$ is related to the Lorentz transformations and defined as:

$$\Lambda^\mu{}_\nu = \begin{bmatrix} \gamma & -\gamma\beta & 0 & 0 \\ -\gamma\beta & \gamma & 0 & 0 \\ 0 & 0 & 1 & 0 \\ 0 & 0 & 0 & 1 \end{bmatrix} \tag{2.56}$$

Furthermore, we introduce the metrics $g_{\mu\nu}$ defined as:

$$g_{\mu\nu} = \begin{bmatrix} 1 & 0 & 0 & 0 \\ 0 & -1 & 0 & 0 \\ 0 & 0 & -1 & 0 \\ 0 & 0 & 0 & -1 \end{bmatrix} \tag{2.57}$$

This metrics helps us with the inner product $x^\mu x_\mu$. We the help of $g_{\mu\nu}$ we can write:

$$x^\mu x_\mu = x^0x^0 - x^1x^1 - x^2x^2 - x^3x^3 = g_{\mu\nu}x^\mu x^\nu \tag{2.58}$$

Additionally, the above metrics helps us to lower or raise the indices.

$$x_\mu = g_{\mu\nu}x^\nu, \quad x^\mu = g^{\mu\nu}x_\nu \tag{2.59}$$

Finally, before we are done with the notation of special relativity is it important to define the contravariant and covariant derivatives as well as the D'Alembertian.

$$\partial^{\mu} = \left(\frac{\partial}{\partial t}, -\nabla\right) \tag{2.60}$$

$$\partial_{\mu} = \left(\frac{\partial}{\partial t}, \nabla\right) \tag{2.61}$$

$$\Box^2 \equiv \partial^{\mu}\partial_{\mu} \tag{2.62}$$

2.7.3 Klein-Gordon Equation

Substituting the operators of equation 2.37 into the relativistic energy equation 2.47, we get the relativistic Schrodinger equation, known as Klein-Gordon equation [6] (in natural units).

$$-\frac{\partial^2\phi}{\partial t^2} + \nabla^2\phi = m^2\phi \tag{2.63}$$

Using the D'Alembertian operator (eq. 2.62), we can rewrite the Klein-Gordon equation as,

$$(\Box^2 + m^2)\phi = 0 \tag{2.64}$$

For a free particle of energy E, whose solution is $\phi = Ne^{ipx-iEt}$ we can find:

$$\rho = 2E|N|^2 \quad j = 2\mathbf{p}|N|^2 \tag{2.65}$$

We now want to calculate the eigenvalues of the Klein-Gordon equation. For this we substitute $\phi = Ne^{-ipx}$ into equation 2.63 and after calculations we obtain:

$$E = \pm\sqrt{\mathbf{p}^2 + m^2} \tag{2.66}$$

In addition to the acceptable solutions with $E > 0$ we get solutions with $E < 0$ for which it is (from eq. 2.65) $\rho < 0$. This is physically impossible and it was a really important problem to be solved at that time.

2.7.4 Dirac Equation and Antimatter

In 1927, Dirac in order to avoid this problem of $E < 0$ solutions, interpreted these negative energy states as an infinite sea of $E < 0$ electrons. Due to the exclusion principle, electrons with $E > 0$, cannot collapse into the occupied states with $E < 0$. The excitation of an electron from the energy $-E$ to $+E$, leaves a "hole" and is regarded as the presence of an anti-electron; the positron. This model works only for fermions; bosons do not follow an exclusion principle. Following this interpretation, Dirac proposed an equation that was linear both in $\frac{\partial}{\partial t}$ and in ∇ (unlike the Klein-Gordon equation).

$$H\psi = (\alpha P + \beta m)\psi \tag{2.67}$$

where β, α_i, $i = 1, 2, 3$, must satisfy for a free particle:

$$H^2\psi = (P^2 + m^2)\psi \tag{2.68}$$

With simple calculations, we can prove that (α_i, β) are matrices, whose choice is not unique. Two usual representations are [2] the Pauli-Dirac representation,

[2] The σ_i matrices are the Pauli matrices: $\sigma_1 = \begin{pmatrix} 0 & 1 \\ 1 & 0 \end{pmatrix}$, $\sigma_2 = \begin{pmatrix} 0 & -i \\ i & 0 \end{pmatrix}$, $\sigma_3 = \begin{pmatrix} 1 & 0 \\ 0 & -1 \end{pmatrix}$.

$$\alpha_i = \begin{pmatrix} 0 & \sigma_i \\ \sigma_i & 0 \end{pmatrix}, \quad \beta = \begin{pmatrix} I & 0 \\ 0 & -I \end{pmatrix} \tag{2.69}$$

and the Weyl representation,

$$\alpha_i = \begin{pmatrix} -\sigma_i & 0 \\ 0 & \sigma_i \end{pmatrix}, \quad \beta = \begin{pmatrix} 0 & I \\ I & 0 \end{pmatrix} \tag{2.70}$$

Now multiplying equation 2.67 from left with β, we obtain:

$$i\beta \frac{\partial \psi}{\partial t} = -i\beta\alpha\nabla\psi + m\psi \tag{2.71}$$

We define the Dirac-γ matrices as:

$$\gamma^\mu \equiv (\beta, \beta\alpha) \tag{2.72}$$

Now equation 2.71, can be written as:

$$(i\gamma^\mu \partial_\mu - m)\psi = 0 \tag{2.73}$$

which represents the covariant form of the Dirac equation, with ψ denoting a four component column vector satisfying the equation, named Dirac spinor [6].

Substituting $\psi = u(p)e^{-ipx}$, where u(p) is four component spinor independent of x, into 2.73 and using the notation $\not{p} = \gamma^\mu p_\mu$ we arrive at the result:

$$(\not{p} - m)u(p) = 0 \tag{2.74}$$

There are four independent solutions: two with positive energy $u^{(1,2)}$ and two with negative energy $u^{(3,4)}$ corresponding to the positron with spinors $v^{(2,1)}$. For the positron we have $u^{(3,4)}(-p)e^{-i(-p)x} \equiv v^{(2,1)}(p)e^{ipx}$. Setting E equal to -E and p equal to -p into 2.74 and using the fact that $u(-p) = v(p)$, we extract the expression of the Dirac equation for positrons [6]:

$$(\not{p} + m)v(p) = 0 \tag{2.75}$$

2.8 The Standard Model Lagrangian

Although the derivation of the full SM Lagrangian is interesting, it is complex, requires a lot of time and is beyond the purpose of this thesis. Hence, the equation will be presented without deriving it and a simple explanation of each term will be given. For a detailed analysis, many textbooks are suitable [6, 12, 13]. The full Lagrangian, is:

$$\begin{aligned} \mathscr{L}_{SM} = & -\frac{1}{4}W_{\mu\nu} \cdot W^{\mu\nu} - \frac{1}{4}B_{\mu\nu}B^{\mu\nu} - \frac{1}{4}G^a_{\mu\nu}G^{a\mu\nu} \\ & + \bar{L}i\gamma^\mu L + \bar{R}i\gamma^\mu R \\ & + \left| \left(i\partial_\mu - g_1 \frac{Y}{2} B_\mu - g_2 \frac{1}{2} \tau \cdot \mathbf{W}_\mu \right) \phi \right|^2 - V(\phi) \\ & - \left(G_1 \bar{L}\phi R + G_2 \bar{L}\phi_c R + \text{h.c.} \right) \end{aligned} \tag{2.76}$$

The D_μ is the covariant derivative, given by:

$$D_\mu = \partial_\mu - ig_1 \frac{Y}{2} B_\mu - ig_2 \frac{\tau}{2} \cdot \mathbf{W}_\mu - ig_3 \frac{\lambda}{2} \cdot G_\mu \tag{2.77}$$

where, g_1, g_2 are the electroweak coupling constants and g_3 is the strong coupling constant. In correlation with the electroweak mixing angle (θ_W), g_1, g_2 are expressed as:

$$g_1 = \frac{e}{\cos\theta_W}, \quad g_2 = \frac{e}{\sin\theta_W}, \quad \sin^2\theta_W \approx 0.23, \tag{2.78}$$

where,

$$\cos\theta_W = \frac{M_W}{M_Z} \tag{2.79}$$

In all occurrences, L refers to a left-handed fermion doublet, and R to a right-handed fermion singlet. $\bar{L}, \bar{R}$ denotes the transposed and complex conjugated vector of L,R respectively. Additionally, ϕ is a column vector, and $\phi_c = -i\tau_2\phi$. Finally, Y is the hypercharge and τ are Pauli matrices related to SU(2) generators with $\tau/2$ and λ are eight 3×3 Gell-Mann matrices which are generators of SU(3). Expanding all the above terms demands both patience and time. A general breakdown to the components is:

- First line: Kinetic energies of $W^{\pm}, Z, \gamma$ bosons ($W_{\mu\nu}, B_{\mu\nu}$) as well as gluons ($G_{\mu\nu}$) and self-interaction terms.
- Second line: Kinetic energies of quarks and leptons and their interactions with $W^{\pm}, Z, \gamma$ and gluons.
- Third line: Masses of Higgs and $W^{\pm}, Z, \gamma$. Additionally couplings of the latter to the Higgs as well as self interaction terms of the Higgs boson. This part of the Lagrangian will be studied in section 2.9.2 (some calculations necessary to link the $W^{1,2,3}$ bosons with the $W^{\pm}, Z, \gamma$ will be omitted). The $V(\phi)$ is the Higgs potential.
- Last line: Masses of quarks and leptons and their couplings to Higgs. G_1, G_2 denotes Yuakawa coupling constants. The h.c stands for hermitian conjugate and describes the the interaction of Higgs with anti-quarks and anti-leptons. Adding the h.c we ensure the Lagrangian remains a real value function.

2.9 Electroweak Symmetry Breaking

We will dive in one of the most amazing ideas, which sculpted particle physics as we know it today. This is the ElectroWeak Symmetry Breaking (EWSB). We will demonstrate it throughout two simple examples, as a pure mathematical proof will consume much space from our experimental analysis presentation below. Firstly we will study the symmetry breaking for a global symmetry resulting to Goldstone bosons. Then we will continue our exploration for the case of local symmetry breaking, which led to the Higgs Boson.

2.9.1 Spontaneous (Global) Symmetry Breaking

Let us assume a simple world, where only one complex scalar boson exists with field:

$$\phi = \frac{1}{\sqrt{2}}(\phi_1 + i\phi_2) \tag{2.80}$$

This boson is described by the Lagrangian:

$$\mathscr{L} = (\partial_\mu\phi)^*(\partial^\mu\phi) - V(\phi) \tag{2.81}$$

where the potential is expressed as:

$$V(\phi) = \mu^2\phi^*\phi + \lambda(\phi^*\phi)^2 \tag{2.82}$$

with $\lambda > 0$ (in order for the potential to present a minimum value). The minimum of the potential depends now on the sign of μ^2. There are two possibilities for the μ^2: $\mu^2 > 0$ and $\mu^2 < 0$ and we can plot the potential in the ϕ_1, ϕ_2 plane for both of them (see figure 2.6).

We must note that the Lagrangian presents a U(1) global symmetry, which means it is invariant under the transformations $\phi(x) \to \phi'(x) = e^{i\theta}\phi(x)$ [12].

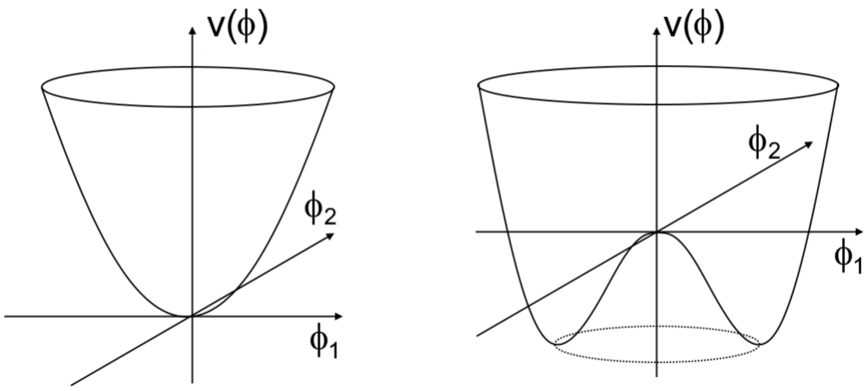

Figure 2.6: The potential $V(\phi)$ for $\mu^2 > 0$ on the left and for $\mu^2 < 0$ on the right [26].

As it can be seen from figure 2.6 for $\mu^2 > 0$ the potential presents a minimum at $\phi = 0$ whereas for $\mu^2 < 0$, it presents a circle of minima. This is the case we are interested to study in this section. The ground state (with the lowest potential) correspond to the vacuum of the system. In the case which the vacuum does not have the same symmetry as the Lagrangian of our system, then the symmetry is broken [27]. We rewrite the Lagrangian as follows:

$$\mathscr{L} = \frac{1}{2}(\partial_\mu\phi_1)^2 + \frac{1}{2}(\partial_\mu\phi_2)^2 - \frac{\mu^2}{2}(\phi_1^2 + \phi_2^2) - \frac{\lambda}{4}(\phi_1^2 + \phi_2^2)^2 \tag{2.83}$$

As we mentioned the potential presents a minima (also called vacuum expectation value -vev- [27]) located at a circle with radius,

$$v^2 = \frac{\mu^2}{\lambda} \tag{2.84}$$

Thus, in terms of ϕ_1, ϕ_2 this minima is expressed as:

$$|\phi|^2 = v^2 \Rightarrow \phi_1^2 + \phi_2^2 = v^2 \tag{2.85}$$

Without the loss of generality we can choose $\phi_1 = v^2$ and $\phi_2 = 0$. Then with the use of two new fields η, ξ we express the initial field as

$$\phi(x) = \frac{1}{\sqrt{2}}[v + \eta(x) + i\xi(x)] \tag{2.86}$$

Substituting 2.86 into equation 2.83, doing some simple calculations (they are omitted for the sake of brevity) and keeping the low order terms in which we are interested here, we obtain:

$$\mathscr{L} = \frac{1}{2}(\partial_\mu\xi)^2 + \frac{1}{2}(\partial_\mu\eta)^2 + \mu^2\eta^2 + \text{const.} + \text{cubic and quartic terms in } \eta, \xi \tag{2.87}$$

We have accomplished to expand the Lagrangian around the vacuum and now the U(1) symmetry cannot be seen in that form. It is highly important to stress out that the symmetry still exists, it is just hidden in the way we expressed our Lagrangian [13].

The first term represents the kinetic energy of a ξ field, the second one the kinetic energy of an η field and the third, the mass for the η field. We calculate $m_\eta = \sqrt{-2\mu^2}$. It is evident that there is no mass term for the ξ field. Consequently, we are left with a massless boson, called **Goldstone boson**.

In 1962 Jeffrey Goldstone, Abdus Salaam and Steven Weinberg published a paper named "Broken Symmetries" which contained their work on the existence of massless scalars as a result of a global symmetry break [28]. Today this is known as Goldstone theorem and it states that for every spontaneously broken continuous symmetry, the theory contains massless scalar particles, called Goldstone bosons. The number of Goldstone particles is equal to the number of broken generators. For a O(N) continuous symmetry there are $\frac{1}{2}N(N-1)$ generators. The unbroken symmetry (which is O(N-1)) has $\frac{1}{2}(N-1)(N-2)$ generators and $N-1$ Goldstone bosons [29]. In our example above U(1) group is isomorphic to SO(2) [30] which has the same number of generators with O(2) (O(N) has N generators). Consequently, for N = 2 we have N - 1 = 1 Goldstone bosons.

2.9.2 Englert-Brout-Higgs Mechanism

Let us now examine the case of a local symmetry breaking [6, 11, 12, 13, 29]. Consider a field ϕ which is an SU(2) doublet of complex scalar fields:

$$\phi = \begin{pmatrix} \phi^+ \\ \phi^0 \end{pmatrix} = \frac{1}{\sqrt{2}} \begin{pmatrix} \phi_1 + i\phi_2 \\ \phi_3 + i\phi_4 \end{pmatrix} \tag{2.88}$$

We want the Lagrangian we will work on, to be invariant under global SU(2) phase transformations, i.e

$$\phi \to \phi' = e^{i\alpha^a \tau^a/2}\phi \tag{2.89}$$

In order to achieve that, we choose,

$$\mathscr{L} = (\partial_\mu \phi)^\dagger (\partial^\mu \phi) - V(\phi) \tag{2.90}$$

with the potential being,

$$V(\phi) = \mu^2 \phi^\dagger \phi + \lambda(\phi^\dagger \phi)^2 \tag{2.91}$$

Given the fact we aim for a local symmetry, we have to change: (a) the α_α of the above expression to $\alpha_\alpha(x)$ and (b) replace the ∂_μ with the covariant derivative,

$$D_\mu = \partial_\mu + i\frac{g}{2}\tau^a W_\mu^a \tag{2.92}$$

where $W_\mu^a, a = 1, 2, 3$ are three gauge fields. We apply the (gauge) transformation,

$$\phi(x) \to \phi'(x) = \left(1 + i\frac{\alpha(x) \cdot \tau}{2}\right)\phi(x) \tag{2.93}$$

Under 2.93, the gauge fields become

$$W_\mu \to W'_\mu = W_\mu - \frac{1}{g}\partial_\mu \alpha - \alpha \times W_\mu \tag{2.94}$$

Substituting now equations 2.93 and 2.94 into the Lagrangian 2.90, we get

$$\mathscr{L} = (D^\mu \phi)^\dagger (D_\mu \phi) - V(\phi) - \frac{1}{4} W_{\mu\nu} \cdot W^{\mu\nu} \tag{2.95}$$

where,

$$W_{\mu\nu} = \partial_\mu W_\nu - \partial_\nu W_\mu - g W_\mu \times W_\nu \tag{2.96}$$

is the kinetic energy term for the gauge fields. We are again (like in section 2.9.1) interested in the case where $\lambda > 0$ and $\mu_2 < 0$ where the potential $V(\phi)$ has the form of the famous "Mexican hat", presented in the figure below.

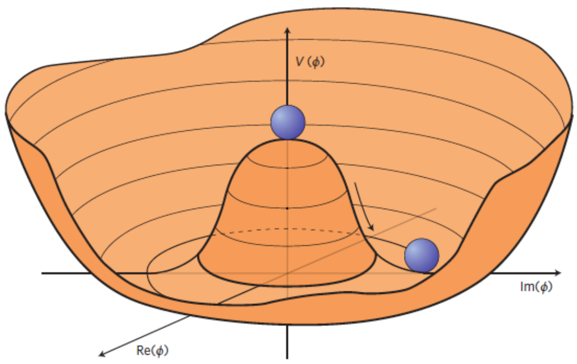

Figure 2.7: Higgs boson potential ("Mexican Hat") that leads to spontaneous symmetry breaking. The vacuum, i.e., the lowest-energy state, is described by a randomly-chosen point around the bottom of the brim of the hat [31].

Following equation 2.85, we have

$$|\phi|^2 = -\frac{\mu^2}{2\lambda} \Rightarrow \phi^\dagger \phi \equiv \frac{1}{2}\left(\phi_1^2 + \phi_2^2 + \phi_3^2 + \phi_4^2\right) = -\frac{\mu^2}{2\lambda} \tag{2.97}$$

Without the loss of generality we choose "by hand" the vacuum. Selecting:

$$\phi_1 = \phi_2 = \phi_4 = 0, \quad \phi_3 = -\frac{\mu^2}{\lambda} \equiv v^2 \tag{2.98}$$

the vacuum becomes,

$$\phi_0 = \sqrt{\frac{1}{2}} \begin{pmatrix} 0 \\ v \end{pmatrix} \tag{2.99}$$

The vacuum expectation value (vev) is equal to:

$$v = \frac{1}{(\sqrt{2} G_F)^{1/2}} \approx 246\, GeV \tag{2.100}$$

where $G_F = 1.663788(6) \times 10^{-5}\, GeV^{-2}$ [32] is the Fermi coupling constant, measured through the muon decay lifetime.
Then, with the use of a new field $h(x)$ we expand the initial field ϕ around this vacuum

$$\begin{aligned} \phi(x) = \phi + \phi_0 &= \sqrt{\frac{1}{2}} \left[\begin{pmatrix} \phi_1(x) + i\phi_2(x) \\ \phi_3(x) + i\phi_4(x) \end{pmatrix} + \begin{pmatrix} 0 \\ v \end{pmatrix} \right] \\ \Rightarrow \phi(x) &= \begin{pmatrix} \phi_1(x) + i\phi_2(x) \\ \dfrac{\phi_3(x) + i\phi_4(x) + v}{\sqrt{2}} \end{pmatrix} \end{aligned} \tag{2.101}$$

It is trivial to prove that the form of $\phi(x)$ in equation 2.101 is equivalent to

$$\phi(x) = \frac{1}{\sqrt{2}} e^{i\frac{\theta_\alpha(x)}{2}\sigma^\alpha} \begin{pmatrix} 0 \\ v + h(x) \end{pmatrix} \tag{2.102}$$

Consequently, applying the gauge transformation

$$\phi' = e^{-i\frac{\lambda_\alpha(x)}{2}\sigma^\alpha} \phi \tag{2.103}$$

and selecting $\lambda_\alpha(x) = \theta_\alpha(x)$, we are able to express the field in the (helpful) form of

$$\phi'(x) = \frac{1}{\sqrt{2}} \begin{pmatrix} 0 \\ v + h(x) \end{pmatrix} \tag{2.104}$$

We substitute this final expression we derived for the field into the Lagrangian 2.95 and we start calculating term by term.
The first term, expresses the kinetic energy of the field h(x) and is:

$$\begin{aligned} \mathscr{L}_{\text{kin1}} &= (\partial_\mu \phi)^\dagger (\partial^\mu \phi) \\ \Rightarrow \mathscr{L}_{\text{kin1}} &= \frac{1}{2}\, \partial_\mu h(x)\, \partial^\mu h(x) \end{aligned} \tag{2.105}$$

The second term is:

$$\begin{aligned} \mathscr{L}_{\text{kin2}} &= \left(ig\frac{1}{2}\tau \cdot W_\mu\, \phi \right)^\dagger \left(ig\frac{1}{2}\tau \cdot W^\mu\, \phi \right) = \left| \frac{ig}{2}\, \tau \cdot \mathbf{W}_\mu \begin{pmatrix} 0 \\ v + h(x) \end{pmatrix} \right|^2 \\ \Rightarrow \mathscr{L}_{\text{kin2}} &= \left| \frac{ig}{2} \begin{pmatrix} W^3_\mu & W^1_\mu - iW^2_\mu \\ W^1_\mu + iW^2_\mu & W^3_\mu \end{pmatrix} \begin{pmatrix} 0 \\ v + h(x) \end{pmatrix} \right|^2 \\ \Rightarrow \mathscr{L}_{\text{kin2}} &= \frac{g^2 (v + h(x))^2}{8} \left[(W^1_\mu)^2 + (W^2_\mu)^2 + (W^3_\mu)^2 \right] \end{aligned} \tag{2.106}$$

$$\begin{aligned} \mathscr{L}_{\text{kin2}} = \frac{g^2 v^2}{8} \left[(W^1_\mu)^2 + (W^2_\mu)^2 + (W^3_\mu)^2 \right] + \frac{g^2 v h(x)}{4} \left[(W^1_\mu)^2 + (W^2_\mu)^2 + (W^3_\mu)^2 \right] \\ + \frac{g^2 h^2(x)}{8} \left[(W^1_\mu)^2 + (W^2_\mu)^2 + (W^3_\mu)^2 \right] \end{aligned} \tag{2.107}$$

Comparing to the typical mass term of a boson $-\frac{1}{2}M^2 B^2_\mu$, we calculate from the first bracket of the above equation 2.107, that three massive bosons with masses $M_{1,2,3} = \frac{1}{2}gv$ are created. The remaining two bracket terms above describe the interaction of these massive gauge bosons with the h field.

Finally the third term, regarding the potential is:

$$\begin{aligned} \mathscr{L}_{H_V} &= -\frac{\mu^2}{2}(V + h(x))^2 - \frac{\lambda}{4}(V + h(x))^4 \Rightarrow \\ \mathscr{L}_{H_V} &= -\frac{\mu^2}{2}\left(V^2 + 2Vh(x) + h^2(x) \right) - \frac{\lambda}{4}(V^4 + 2V^3 h(x) + V^2 h^2(x) + 2V^3 h(x) \\ &\quad + 4V^2 h^2(x) + 2Vh^3(x) + V^2 h^2(x) + 2Vh^3(x) + h^4(x)) \end{aligned} \tag{2.108}$$

From this term we have the ability to determine the mass of the boson corresponding to the field h. We rearrange the last line in terms of the exponents of h.

$$\mathscr{L}_{H_V} = -\frac{1}{2}\Big[\left(\mu^2 V^2 + \frac{\lambda V^4}{2}\right) + (2\mu^2 V + 2\lambda V^3)h(x) + (\mu^2 + 3\lambda V^2)h^2(x) + 2\lambda V h^3(x) + \frac{\lambda}{2}h^4(x)\Big] \tag{2.109}$$

From equation 2.98 we calculate $2\mu^2 v + 2\lambda v^3 = 0$ which correspond to the coefficient of the h^1 term. Also the first term which is constant can be omitted, providing us with

$$\mathscr{L}_{H_V} = -\frac{1}{2}\left[2\lambda v^2 h^2(x) + 2\lambda v h^3(x) + \frac{\lambda}{2}h^4(x)\right] \tag{2.110}$$

This describes a massive boson and some self interactions. This boson is the **Higgs boson**, with ϕ, h being two expressions of the Higgs field and $V(\phi)$ being, the Higgs potential! Comparing with the typical mass term of a boson $-\frac{1}{2}M^2h^2$, we determine the Higgs mass:

$$-\frac{1}{2}{M_H}^2 h^2 = -\frac{1}{2}2\lambda v^2 h^2(x) \Rightarrow \tag{2.111}$$

$$M_H = \sqrt{2\lambda}v \tag{2.112}$$

It is important to stress out that the Higgs mass is free parameter in this model and scientists had no a priori knowledge of it.
The remaining two terms of $\mathscr{L}_{H_V}$ describe the (self) interaction of three and four bosons respectively, as shown in the following Feynman diagrams.

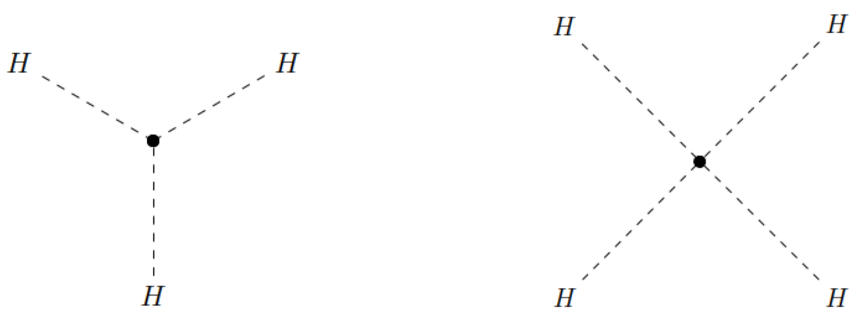

Figure 2.8: Feynman diagram demonstrating three (left) and four (right) Higgs bosons interacting. These interactions are predicted by the terms of h^3 and h^4 in the $\mathscr{L}_{H_V}$ derived above.

The coupling constants for these self interaction modes are:

$$g_{HHH} = \frac{3M_H^2}{v} \tag{2.113}$$

$$g_{HHHH} = \frac{3M_H^2}{v^2} \tag{2.114}$$

Measuring the coupling constants for the triple Higgs production for example, can apply a constrain on the Higgs mass.
Combining all the above calculations from 2.105, 2.107 and 2.110, the full Lagrangian of the Higgs boson is given by:

$$\mathscr{L}_{Higgs} = \mathscr{L}_{kin1} + \mathscr{L}_{kin2} + \mathscr{L}_V \tag{2.115}$$

where the three terms are calculated above.
We should now examine the above steps. By expressing the (Higgs) field around the vacuum of the system and substituting into the Lagrangian, the initial symmetry ($SU(2) \times U(1)$), is no longer apparent. Hence, we have the symmetry breaking $SU(2) \times U(1) \to U(1)$. Although normally, we would expect to have three Goldstone bosons, they are absorbed by the three massive gauge bosons $W^1_\mu, W^2_\mu, W^3_\mu$ in order to form their longitudinal polarization and acquire mass. Consequently, we have no Goldstone bosons, three massive gauge bosons and one massive scalar boson, the Higgs boson.

This mechanism, is known as the Englert-Brout-Higgs (EBH) mechanism and predicts the existence of a massive scalar boson, the Higgs boson, which provides mass to three massive gauge bosons. It was presented by Peter Higgs, back in 1964 [33] and 1966 [34] and separately by Francois Englert and Robert Brout [35] in 1964.

2.10 Higgs boson at the LHC

From the inception of the Higgs boson back in 1964, this particle managed to hide from physicists for nearly half a century, as the maximum energy of colliders was not sufficient for it's production. Despite the enormous efforts by many experiments like the TEVATRON [36] and LEP [37] only limits on the Higgs mass were determined. With the commission of LHC [3], it was finally discovered at 4 July 2012 [38] by both ATLAS [39] and CMS [40]. For this breakthrough Peter Higgs and Francois Englert were awarded the Nobel Prize in 2013 [41]. The mass is about M_H **= 125 GeV** and precise up to date and past results can be found in [32].

2.10.1 Production Modes

It is highly important to know the production modes of the Higgs boson as well as the theoretical cross section for each, calculated with accuracy in higher order corrections. Higher order corrections refer to Feynman diagrams of processes with loops which contribute in the total cross section. They are obtained by pertubative expansion [6]. The first order correction is Next to Leading Order (NLO). Then, it is followed by Next-to-Next to Leading Order (NNLO), Next-to-Next-to-Next to Leading Order (N3LO) e.t.c. In the LHC, there are four main production modes (for a detailed approach consult [42, 43, 44, 45] and for an up to date summary [32]), presented below.

Gluon-Gluon Fusion (ggF)

Gluon-Gluon Fusion ($gg \to H$) is the dominant production mode at the LHC, where two gluons interact forming a loop of virtual heavy quarks which then produce the Higgs boson. Higgs boson presents a much stronger coupling to heavy particles than to light ones. Hence the loop consists mostly of t quarks and rarely of b quarks, while contribution from lighter quarks is suppressed proportional to m_q^2. The structure of ggF, allows indirect measurement of the Higgs coupling to top quarks. The latest theoretical calculation of the ggF cross section is given at N3LO (QCD) + NLO (EW).

Vector Boson Fusion (VBF)

Vector Boson Fusion ($qq \to qqH$) is the subdominant production mode. Two quarks (or antiquarks) scatter, exchanging a vector boson V ($W^\pm, Z$), which radiates the Higgs boson. The scattered quarks are recognized as two hard jets in the forward region of the detector, separated with a large

[3]Large Hadron Collider (LHC) at CERN, will be introduced in section 3.2

rapidity gap. This mode is providing a relatively clean experimental signature, enabling the measurement of the strength of the direct coupling between the Higgs boson and vector bosons.

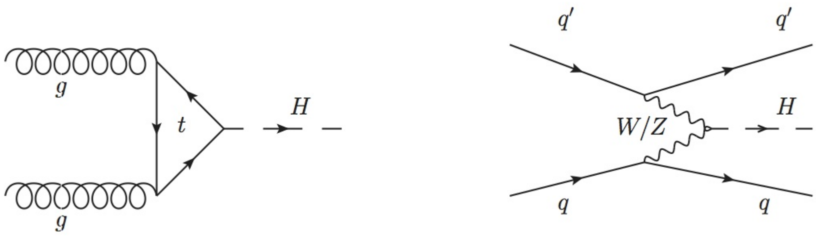

Figure 2.9: Leading Order (LO) Feynman diagrams of ggF (left) and VBF (right).

Higgs-strahlung (VH)

Higgs-Strahlung (or associated production of the Higgs boson with vector bosons), is symbolized as: $pp \to VH$, with $V = W^{\pm}, Z$. Two quarks or anti-quarks collide, producing a virtual vector boson, which then radiates a Higgs boson and the corresponding vector boson. The leptonic decay of the latter, reduces the contamination of the QCD background, yielding a clean signature. Especially in the boosted regime, the VH production mode, is suitable to study the $H \to b\bar{b}$ decay channel.

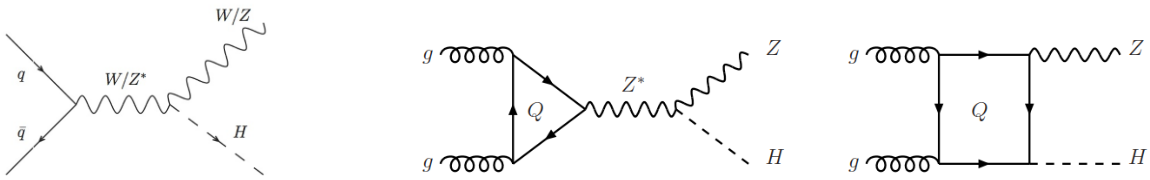

(a) (b)

Figure 2.10: LO Feynman diagrams of the VH process. The loop induced processes in (b), interfere destructively in the cross section.

Associated Top-Quark Production (ttH/tH)

Associated Top-Quark production can occur with two top quarks ($pp \to t\bar{t}H$), or with one ($pp \to tH + X$). The former, provides direct measurement of the Higgs to top Yukawa coupling, while the latter helps determining the sign of this coupling. ttH can also proceed with bottom quarks instead of top, and some Feynman diagrams at LO are:

(a) (b)

Figure 2.11: LO Feynman diagrams of the ttH process.

On the other hand, tH has a much smaller rate than ttH and at LO is represented as:

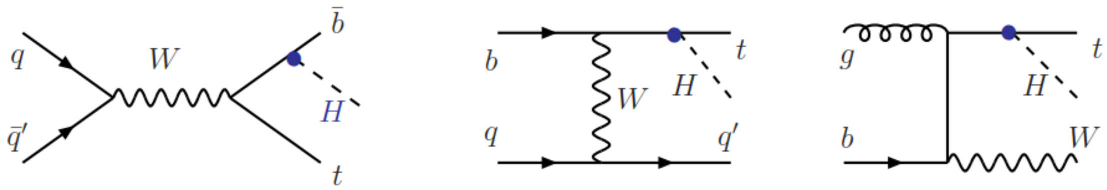

Figure 2.12: LO Feynman diagrams of the tH production mode.

Secondary production modes also exist; however they are of less importance, as they have very small cross sections [32]. The results of the up to date, most accurate calculations regarding the cross section of the main Higgs production modes presented above, are summarized in table 2.4 for the center mass energy corresponding to Run 2 and Run 3. Similar results for $\sqrt{s} = 13\,TeV$, for a boosted Higgs boson are given in 2.5. The exact formulas for the cross sections derived from higher order corrections are complex, thus they are omitted. An interesting insight can be found in [29].

$\sqrt{s}$ (TeV)	ggF	VBF	WH	ZH	ttH	total
13	$48.6^{+5.6\%}_{-7.4\%}$	$3.78^{+2.1\%}_{-2.1\%}$	$1.37^{+2.0\%}_{-2.0\%}$	$0.88^{+4.1\%}_{-3.6\%}$	$0.50^{+6.8\%}_{-9.9\%}$	$55.1^{+5\%}_{-7\%}$
13.6	$52.2^{+5.6\%}_{-7.4\%}$	$4.1^{+2.1\%}_{-1.5\%}$	$1.46^{+1.8\%}_{-1.9\%}$	$0.95^{+4.0\%}_{-3.6\%}$	$0.57^{+6.9\%}_{-9.9\%}$	$59.2^{+5\%}_{-7\%}$

Table 2.4: Cross sections (in pb) for $m_H = 125$ GeV at $\sqrt{s} = 13$ and 13.6 TeV for the Higgs boson main production modes at the LHC. The results are presented in [42, 43, 44, 45] and summarized in [32].

p_T^{cut} [GeV]	$\sum_{\text{ggF}}^{\text{NNLO approx}}$ [fb]	$\sum_{\text{VBF}}^{\text{NNLO}}$ [fb]	$\sum_{\text{VH}}^{\text{NLO}}$ [fb]	$\sum_{\text{ttH}}^{\text{NLO}}$ [fb]
450	$16.70^{+9.53\%}_{-11.76\%}$	$8.06^{+0.24\%}_{-0.23\%}$	$6.87^{+4.6\%}_{-3.49\%}$	$4.24^{+12.84\%}_{-13.15\%}$

Table 2.5: Cross sections (in fb) for the boosted Higgs boson with $p_T^{\text{cut}} = 450$ GeV at $\sqrt{s} = 13\,TeV$. The four main production modes are considered. Cross sections for ggF and VBF are given at NNLO and for VH and ttH at NLO. EW corrections are not included [46].

As we observe the he cross sections are different between the two runs. Generally the cross section of each production mode, varies as the center of mass energy changes. This can be seen in the following plot.

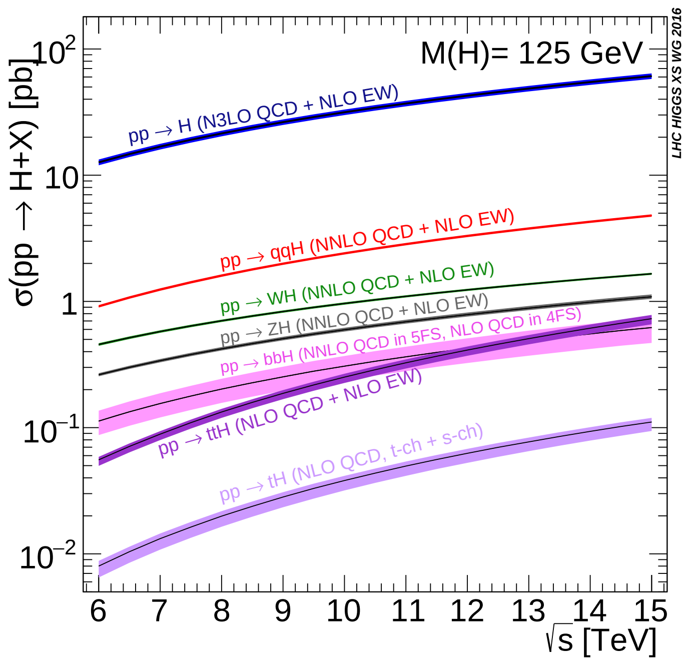

Figure 2.13: Cross section of the different Higgs production modes (given at a certain level of correction) as a function of the center of mass energy $\sqrt{s}$ for the different production modes. The bands indicate theoretical uncertainties [47].

2.10.2 Decay Modes

There are many decay modes accessible in the LHC, with the decay channel of our analysis $H \to b\bar{b}$ having the largest branching ratio of approximately 58%, known at N4LO (QCD) + NLO (EW) [32]. For the experimentally determined Higgs mass ($M_H \approx 125\,GeV$) the branching ratios of the most important decay channels are summarized in table 2.6.

Decay channel	Branching ratio	Rel. uncertainty
$H \to b\bar{b}$	5.82×10^{-1}	$^{+1.2\%}_{-1.3\%}$
$H \to W^+W^-$	2.14×10^{-1}	$\pm 1.5\%$
$H \to \tau^+\tau^-$	6.27×10^{-2}	$\pm 1.6\%$
$H \to c\bar{c}$	2.89×10^{-2}	$^{+5.5\%}_{-2.0\%}$
$H \to ZZ$	2.62×10^{-2}	$\pm 1.5\%$
$H \to Z\gamma$	1.53×10^{-3}	$\pm 5.8\%$
$H \to \gamma\gamma$	2.27×10^{-3}	2.1%
$H \to \mu^+\mu^-$	2.18×10^{-4}	$\pm 1.7\%$

Table 2.6: Branching ratios and relative uncertainties for various Higgs boson decay channels [32].

Although the decay channels $H \to \gamma\gamma$ and $H \to ZZ^* \to 4l$ have a small BR, they are included due to their fundamental role in the Higgs discovery back in 2012 [39, 40]. Both channels present a narrow peak over the background, providing very clean signature and accurate calculations of the

Higgs mass. On the other hand, although the decay channel of interest exhibits the highest branching ratio, its discrimination from the QCD background remains difficult.

The widths of the Higgs decaying to gauge bosons (fermions) is directly (almost) proportional to the HVV (Hff) coupling, given by,

$$g_{HVV} = \frac{2M_V^2}{v} = 2\left(\sqrt{2G_F}\right)^{1/2} M_V^2 \tag{2.116}$$

$$g_{Hff} = \frac{m_f}{v} = \left(\sqrt{2G_F}\right)^{1/2} m_f \tag{2.117}$$

For a Higgs decaying into quarks and leptons (where $H \to b\bar{b}$ lies) the born approximation, in order to determine the width of this decay mode is [29]:

$$\Gamma_{\text{Born}}(H \to f\bar{f}) = \frac{G_F N_c}{4\sqrt{2}\pi} M_H\, m_f^2\, \beta_f^3 \tag{2.118}$$

with $\beta = \left(1 - \frac{4m_f^2}{M_H^2}\right)^{1/2}$ representing the velocity of the fermions and $N_c = 3$ (quarks), 1 (leptons) being the color factor. The NLO approximation of Higgs decaying to a pair of quarks becomes [29]:

$$\Gamma_{\text{NLO}}(H \to q\bar{q}) \simeq \frac{3G_F}{4\sqrt{2}\pi} M_H\, m_q^2 \left[1 + \frac{4}{3}\frac{\alpha_s}{\pi}\left(\frac{9}{4} + \frac{3}{2}\log\frac{m_q^2}{M_H^2}\right)\right] \tag{2.119}$$

Finally, the total width of the Higgs boson is determined $\Gamma_H = 4.07 \times 10^{-3}\,{}^{+4.0\%}_{-3.9\%}$ GeV [32].

2.11 Beyond the Standard Model

The Standard Model is a remarkably successful theory, offering comprehensive explanations and exhibiting excellent agreement with experimental observations. However, many unanswered questions still exist. The incorporation of gravity into the SM and the discovery of graviton, the formalization of dark matter/energy (which are not predicted by the SM) and the explanation of matter/antimatter asymmetry are only some of the major open questions is modern physics. As a result many Beyond the Standard Model (BSM) theories have been developed. We will mention three such theories and a technique which parameterize possible deviations from the SM.

One of the most promising theories is **SU**per **SY**mmetry (SUSY), predicting a symmetry over bosons and fermions [48]. Every known fundamental particle of the SM has a supersymmetric partner (called ”superpartner”), with the same properties (same quantum numbers except from spin). The simplest and most studied SUSY model is the Minimal Supersymmetric Standard Model (MSSM) [49]. In this model three neutral and two charged Higgs bosons of the SM with spin equal to zero are required as well as two neutral and two charged supersymmetric Higgs bosons with spin equal to 1/2, called Higgsinos. An important quantum number conserved is the R-parity [7], defined as:

$$R = (-1)^{3(B-L)+2S} \tag{2.120}$$

Another BSM theory is the **G**rand **U**nified **T**heory (GUT), which predicts the unification of the strong with the electromagnetic and weak forces [50, 51]. The three interactions have the same strength in the theory, which is g_U. An important aspect of GUT, is that baryon number is not conserved; rather the quantity $B - L$ is conserved. Hence, protons can decay and their life time is predicted by the expression:

$$\tau \approx \frac{M_X^4}{g_U^2 M_p^5} \tag{2.121}$$

where M_X is the mass of a new vector boson of the theory. Although the proton might decay, estimations of the decay time are $\tau = 10^{32} - 10^{33}$ yr which is a lot larger than our universes life (10^{10} yr).

Finally, we mention String Theories. They are class of theories formulated in a higher-dimensional spacetime (for example ten spatial dimensions and one time dimension) where point-like particles are replaced by one-dimensional, vibrating quantum strings. [7].

An interesting question now, is how BSM physics is linked to our analysis. As we described in section 2.10.1, the ggF mode is loop induced. At low energies, the mass of the fermions of the loop are much larger than the Higgs mass. Consequently, fermions can be integrated out and the process can be regarded as a point like interaction between the gluons and the Higgs. On contrary, for higher energies the top-quark loop starts being resolved and the top Yukawa (y_t) coupling can be measured. Additionally, we are able to study possible new effects presented in the loop induced processes. With the study of boosted Higgs bosons (i.e with high transverse momentum p_T), we can measure the differential cross sections. The detection of possible deviations from the SM predicted values, could imply the existence of new Physics. It is important to stress out, that new Physics is characterized by a scale Λ which is much larger than the electroweak scale (1 TeV). A model providing information on the couplings constants is **E**ffective **F**ield **T**heory (EFT) [52]. Assuming B,L are conserved the EFT Lagrangian is written as:

$$\mathscr{L}_{\text{EFT}} = \mathscr{L}_{\text{SM}} + \sum_i \frac{c_i}{\Lambda^2}\mathscr{O}_i + h.o. \tag{2.122}$$

where c_i are named Wilson coefficients and $\mathscr{O}$ are dimension-6 operators. Concluding, studying a large number of events with loop induced processes of high Higgs p_T, we can obtain constrains on the EFT coefficients.

Now that the theory is presented sufficiently, we are ready to explore our experimental setup (i.e our collider and detector) in the next chapter.

Chapter 3

CERN, LHC and ATLAS

Detectors and colliders are among the most essential tools used by physicists in order to study fundamental particles. In this chapter we will have an interesting view at CERN, it's accelerator complex, the LHC and ATLAS, the experiment from which the data of the present analysis are obtained. Understanding how our accelerator and detector work is crucial in order to handle correctly all physical objects and be able to interpret our results. It is a necessary knowledge for every experimental physicist at CERN and a pleasant insight for every individual.

3.1 CERN

CERN, stands for European Council for Nuclear Research or in French **C**onseil **E**uropéen pour la **R**echerche **N**ucléaire). It was founded after the end of the Second World War, in 1954 (although the first meeting concerning CERN was made in late 1951 at a UNESCO meeting in Paris) [53]. Since then, CERN's mission has been to expand our knowledge in particle physics, studying elementary particles and their properties, making countless significant breakthroughs. Apart from this, CERN, has provided many useful technologies, like the World Wide Web (www), used by almost everyone today [53] as well as many other technologies with application in medical fields. A brief history of CERN's accelerators starts with the **S**ynchro**C**yclotron (SC) (with energy 600MeV), which started operating in May 1957 [54]. Later, on 24 November 1959 the **P**roton **S**ynchrotron (PS) began to work with a beam energy of 24 GeV and on 3 May 1976 the **S**uper **P**roton **S**ynchrotron (SPS) was introduced, reaching later an energy of 450 GeV. About 13 years later on 14 July 1989, the first beam of electrons circulated in the **L**arge **E**lectron–**P**ositron (LEP) collider where the beams reached an energy of 209 GeV in 2000. Finally, using the LEP's tunnel, on 10 September 2008, the **L**arge **H**adron **C**ollider (LHC) was launched and the four main experiments that exist today at CERN were built (see section 3.2), signaling the beginning of a new era in High Energy Physics [54]. When the CERN convention was signed, there were 12 member states. Today, the number has doubled, containing 24 member states [55, 56]. It also employs (according to the 2023 annual report [56]) approximately 12,500 users (scientists, staff members and students) from all over the world (member and non member states), being one of the largest and most established centers for scientific research. CERN's laboratory is located near the France-Swiss borders, with the headquarters being in Meyrin village, close to Geneva. Today's largest (active) accelerator at CERN and worldwide is the Large Hadron Collider (LHC), which will be the subject of the next section.

3.2 Large Hadron Collider (LHC)

In order to observe the Higgs boson, larger center of mass energies than those reached in previous experiments were required. To this end, the Large Hadron Collider was constructed, which is a superconducting particle (protons (p) and lead (Pb) ions) accelerator and collider. It uses the same tunnel in which LEP was located, approximately 100m below ground surface at a slight gradient of 1.4%. Its depth varies between 175 m (under the Jura mountain) and 50 m (towards lake Geneva). It measures approximately 27 km (26658.883 m precisely) circumference [57, 58]. Two opposite rotating beams are accelerated up to 6.8 TeV for Run 3 (6.5 TeV for Run 2), so that the center of mass energy reaches the world record value of $\sqrt{s}$ = 13.6 TeV for Run 3 [59] and $\sqrt{s}$ = 13 TeV for Run 2. The beams collide (interact) in four Interaction Points (IP), where the following four main experiments of CERN are located, in order to encapsulate the results of the collisions.

1. **A** **T**oroidal **L**HC **A**pparatu**S** (ATLAS) located at IP1 [60, 61].
2. **C**ompact **M**uon **S**olenoid (CMS) located at IP5 [62, 63].
3. **A** **L**arge **I**on **C**ollider **E**xperiment (ALICE) located at IP2 [64] and finally
4. **L**arge **H**adron **C**ollider **b**eauty (LHCb) located at IP8 [65].

Currently as this thesis is being written, the LHC is in Run 3 (2022-2026). It is obvious some features have changed from the previous Runs: Run 2 (2015-2018) and Run 1 (2010-2012). All technical features below, refer to Run 3 as well as Run 2, given that our analysis is based on data from both runs. More information about the initial configurations can be found in [57] and regarding the upgrades in preparation for Run 3 in [59].

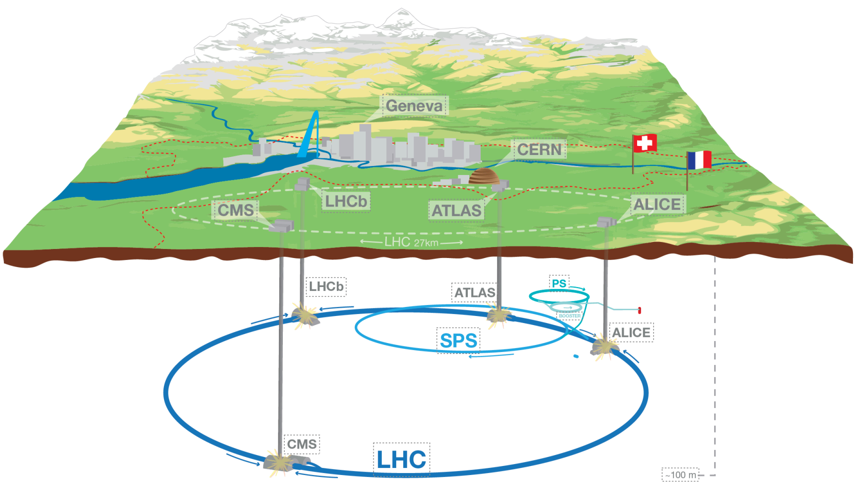

Figure 3.1: Three dimensional map of the LHC accelerator complex with the four main experiments (ATLAS, CMS, ALICE and LHCb). Note that the LHC ring is slightly curved, even though this is not clear in the figure.

3.2.1 Accelerator Complex

To achieve the remarkably high energy of 13 − 13.6 TeV, all previous CERN accelerators are used before particles enter the LHC ring, where the final acceleration takes place. Regarding proton-proton collisions, the journey of particles begin with hydrogen atoms being stripped down from their electrons. Then, H^- ions enter the **LI**near **AC**celerator 4 (LINAC4) and reach an energy of 160 MeV. During Run 2, LINAC2 was used, accelerating protons to an energy of 50 MeV. With the commission of LINAC4 in 2020, double brightness was achieved [59]. After protons exit the LINAC4, they enter the PSB which has 157 meters circumference and are accelerated to 2 GeV [59] (1.4 GeV for Run 2). Changing the main energy supply and upgrading of the RF system, was the reason the extraction energy from the PSB, increased between the two runs [59]. The next step, is the PS measuring 628m and extracting the protons at energy of 25 GeV (some of the changes from Run 2 focused on the impedance of the 10MHz system) [59]. Arriving to the fourth station, the SPS (with 7 km length), protons are accelerated from 25 GeV to 450 GeV and then, they are extracted to the LHC. Upgrading the 200MHz system, the injection protection and the beam dump devices were the most important changes on the SPS [59]. The acceleration from the point protons enter the LINAC4 up to the moments they enter the LHC takes about 4 minutes and 20 seconds. After the beam enters the LHC ring, approximately 20 additional minutes are required to reach the energy of 13.6 TeV (13 TeV for Run 2) [66]. The acceleration of the Pb ions differs, as it begins from LINAC3 and then Low Energy Ion Ring (LEIR). After they are extracted from LEIR to the PS and follow the same path [66] (with different parameters [67]). The detailed process is beyond the subject of this thesis, as only proton collisions are of interest.

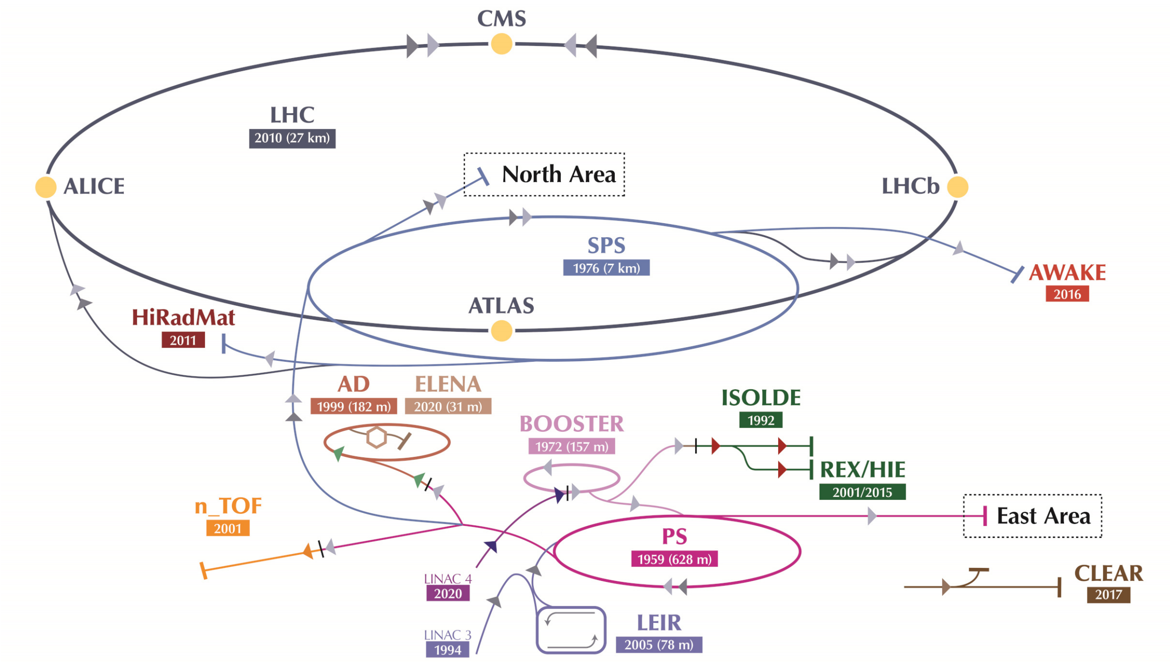

Figure 3.2: Diagram of the LHC accelerator complex used during Run 3. The same accelerator complex was used for Run 2, with LINAC2 in place of LINAC4.

3.2.2 LHC Layout and Features

LHC is actually not circular; rather, it is arranged in an octagon with eight arcs and eight Long Straight Sections (LSS) [57], as it can be seen in figure 3.3a. The main components inside the LHC ring are: superconducting magnets (magnets with extremely low electrical resistance when cooled to very low temperatures [68]), as well as Radio Frequency (RF) cavities. The superconducting magnets are made of Niobium-Titanium (NbTi) cables, producing a nominal magnetic field of $8.33\,T$, under $11080\,A$ nominal current and are cooled to $2\,K$ with helium (He). A total of 1232 dipole magnets, each with a length of 15 m, are located in the arcs and are used to bend protons. On the other hand 392 quadrupole magnets, are located in the LSS and are responsible for focusing and de-focusing the beam at the IP, as well as for the beam injection and dump [57]. Finally, the RF cavities are located inside the LSS and accelerate the protons, using a frequency of 400 MHz [57, 59].

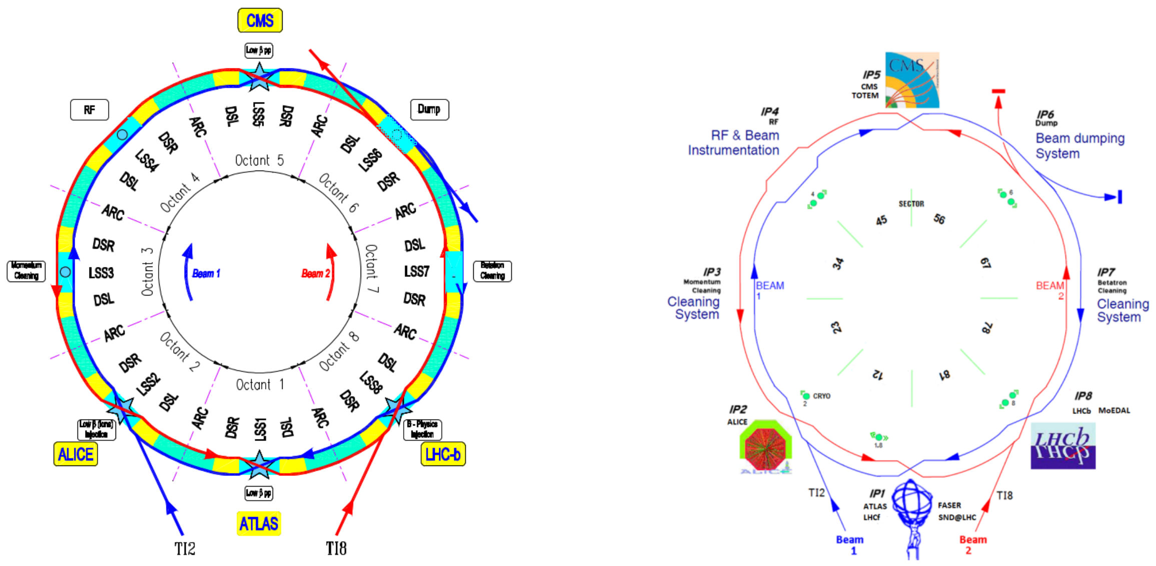

(a) (b)

Figure 3.3: LHC ring topology with the Long Straight Sections and the Interaction Points marked. On the left the diagram obtained from the initial technical design report [57] and on the right the diagram used in the report on the upgrades in preparation for Run 3 [59].

3.2.3 Basic Quantities

One of the most important quantities describing an accelerator, apart from the center mass energy, is the luminosity (defined initially, in section 2.5). For the LHC machine, where two Gaussian beams collide head-on, it can be expressed using the beam parameters, as:

$$L = \frac{N_b^2 n_b f_{\text{rev}} \gamma_r F}{4\pi \epsilon_{\text{n}} \beta^*} \tag{3.1}$$

where N_b is the number of particles per bunch, n_b the number of bunches per beam, f_{rev} the revolution frequency, γ_r the relativistic gamma factor, ϵ_n the normalized transverse beam emittance, β^* the beta function at the collision point and F a luminosity reduction factor. The beta function, describes the transverse width of the beam. Consequently, smaller β^*, translates to a more squeezed beam and higher luminosity. For this reason, the β^* value is minimized at the interaction points corresponding to ATLAS and CMS, as seen in figure 3.3. The parameter values from the initial technical design report of LHC [57], are: $N_b = 1.15 \times 10^{11}$ ppb, $n_b = 2808$ bunches, $\gamma_r = 7461$, $F = 0.835$, $f_r = 11.246 kHz$, $\epsilon_n = 3.75 \mu m$ and $\beta^*_{max} = 0.55$. Substituting into equation 3.1, we obtain $L = 10^{34} cm^{-2} s^{-1}$, which is the nominal reported value in the same report.

While the instantaneous luminosity fluctuates over time, the quantity of interest is the integrated luminosity, defined as the integral of the instantaneous luminosity over time:

$$L_{\text{int}} = \int \mathscr{L}(t)\, dt \tag{3.2}$$

Integrated luminosity represent the volume of data collected. Instantaneous and integrated luminosity are both measured in b^{-1}, although fb^{-1} is mostly used, as b^{-1} is a very big unit; $1 fb^{-1}$ corresponds approximately to 100 million million collisions. In the figure below, we can observe the total delivered luminosity as well as the recorded and the good for physics luminosity for the full period of our analysis (Run 2 and partial Run 3).

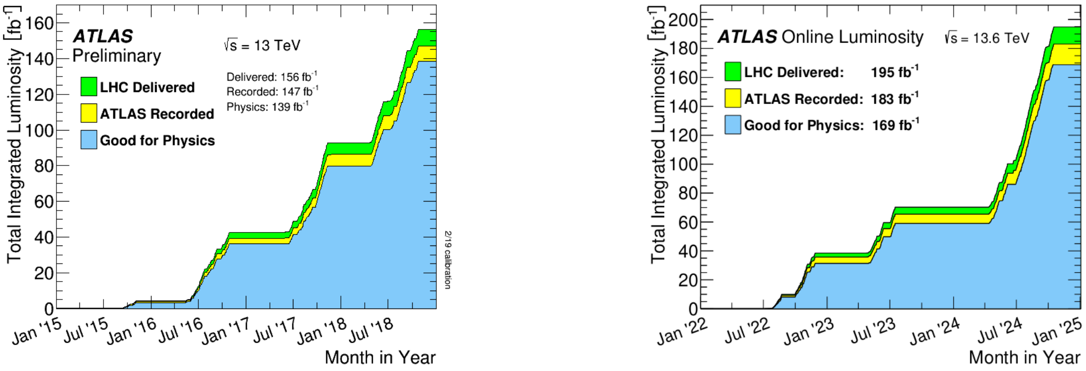

(a) (b)

Figure 3.4: Integrated luminosity for the Run 2 period (2015–2018) (left, [69]) and partial Run 3 (2022–2024) (right, [71]). The delivered luminosity (green) represents the luminosity from the start of stable beams until the ATLAS detector is put in safe mode. The recorded luminosity (yellow) represents the luminosity the Data Acquisition Systems (DAQ) record. Finally, the good for physics luminosity (blue) refers to events that pass predefined selection criteria and can be used in physics analysis.

The LHC delivered a total integrated luminosity of $156fb^{-1}$ and $195fb^{-1}$ during Run 2 and partial Run 3 respectively (with recorded and good for physics -see section 4.5- luminosities being slightly less). The peak instantaneous luminosity achieved in Run 2, was $2.1 \times 10^{34}\ cm^{-2}s^{-1}$. For Run 3, the goal is set to exceed this value, with increasing the bunch population to $N_b = 1.8 \times 10^{11}$ ppb for the 25ns beam spacing [72]. No official reports on the performance of LHC for Run 3 are published yet. Furthermore, if the cross section of a process is known, the expected rate (i.e number of events produced per second) at the LHC is determined by:

$$R_{\text{event}} = L\sigma_{\text{event}} \tag{3.3}$$

Considering the LHC design instantaneous luminosity of $L = 1 \times 10^{34} cm^{-2}s^{-1}$ and using the cross section of inelastic interactions $\sigma_{inel} = 80mb$ for both $\sqrt{s} = 13\,\text{TeV}$ and $\sqrt{s} = 13.6\,\text{TeV}$ [73], we obtain a rate of 8×10^8 events/s. Using now the integrated luminosity of one year of operation of LHC, for example 2017 with $L_{int} = 50.2fb^{-1}$ [69], we get 4×10^{15} inelastic events. With the total cross section of the Higgs boson being 50.2 pb at 13 TeV, 2.7 million Higgs are produced in comparison to the enormous volume of uninteresting events [70]. Of those 2.7 million Higgs bosons, only a small amount is eventually observed (see chapter 7 for the total expected number of Higgs in our analysis).

Finally, another important parameter is the pile-up, characterized with the number of interactions μ, which follows a Poisson distribution. Pile-up refers to bunch crossings producing many separate inelastic interactions as well as to data from preceding and subsequent bunch crossings. The second type of pile-up occurs as many sub detectors have a readout time larger than 25ns, hence potentially collecting data from different bunch crossings. We are mainly interested in the mean number of interactions per bunch crossing ($\langle\mu\rangle$), given by:

$$\mu = \frac{L_{\text{bunch}} \cdot \sigma_{\text{inel}}}{f_r} \tag{3.4}$$

where, L_{bunch} is the instantaneous luminosity of the bunch, σ_{inel} is the cross section of inelastic interactions and f_r is the revolution frequency [74].

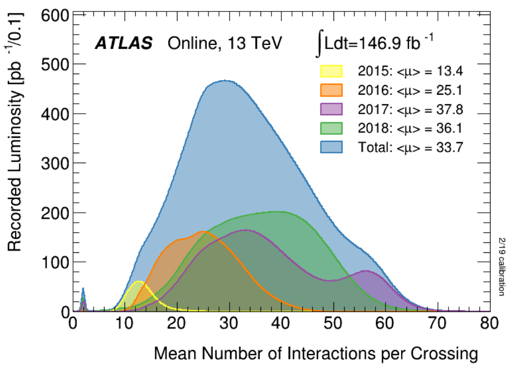

(a)

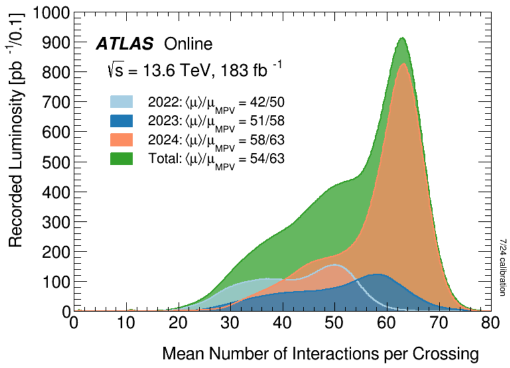

(b)

Figure 3.5: Mean number of interactions per crossing for the Run 2 period (2015–2018) (left, [69]) and partial Run 3 (2022–2024) (right, [73]). A clear shift to higher values is observed for partial Run 3. For the left figure, the mean μ value for each year appears on the plot, while for the right figure both the mean value and the Most Probable Value (MPV) appear for each year. The total integrated luminosity in each plot refers to the ATLAS recorded luminosity during this period.

3.3 ATLAS Detector

The ATLAS detector is one of the two general purpose detectors of LHC. It is located in the IP1 which is a high luminosity interaction point and measures 25m height and 44m length. It has a cylindrical shape, aligned along the beam line, covers an almost 4π solid angle with forward - backward symmetry from the IP. The total weight of the detector is 7000 tons and the design offers robust pattern recognition and high energy and momentum resolution [60]. Given that the LHC will produce roughly 8×10^8 $events/s$ and that every candidate event for new physics will be accompanied by 23 (on average) inelastic events, we understand the great challenge while designing the detector [61].

The detector was designed, taking into consideration the following basic requirements [60, 61]:

1. High granularity in order to handle the large particle flow and pileup. To achieve this, the use of fast and radiation hard electronics and sensors is required.
2. Electron and photon identification and measurement via an electromagnetic calorimeter accompanied with a hadronic calorimeter responsible to measure jets and missing transverse energy (E_T^{miss}).
3. High precision muon momentum measurements.
4. Large pseudorapidity coverage and almost full azimuthal (ϕ) coverage. The definition of these quantities is given in 3.3.1.
5. High efficiencies for physics processes of interest. This requires measurement and triggering of particles at low transerve momentum (p_T).
6. Full event reconstruction at low luminosity and efficient tracking at high luminosity.
7. Particle identification.

In order to achieve these goals, the ATLAS detector consists of the following sub detectors:

1. Inner Detector (ID)

2. Calorimeter Systems (ECal and HCal)

3. Muon Spectrometer (MS)

In addition to the aforementioned, there is a magnetic system interacting with all sub detectors, four forward detectors and a Trigger and Data Acquisition system (TDAQ). The overall detector layout is shown in figure 3.6.

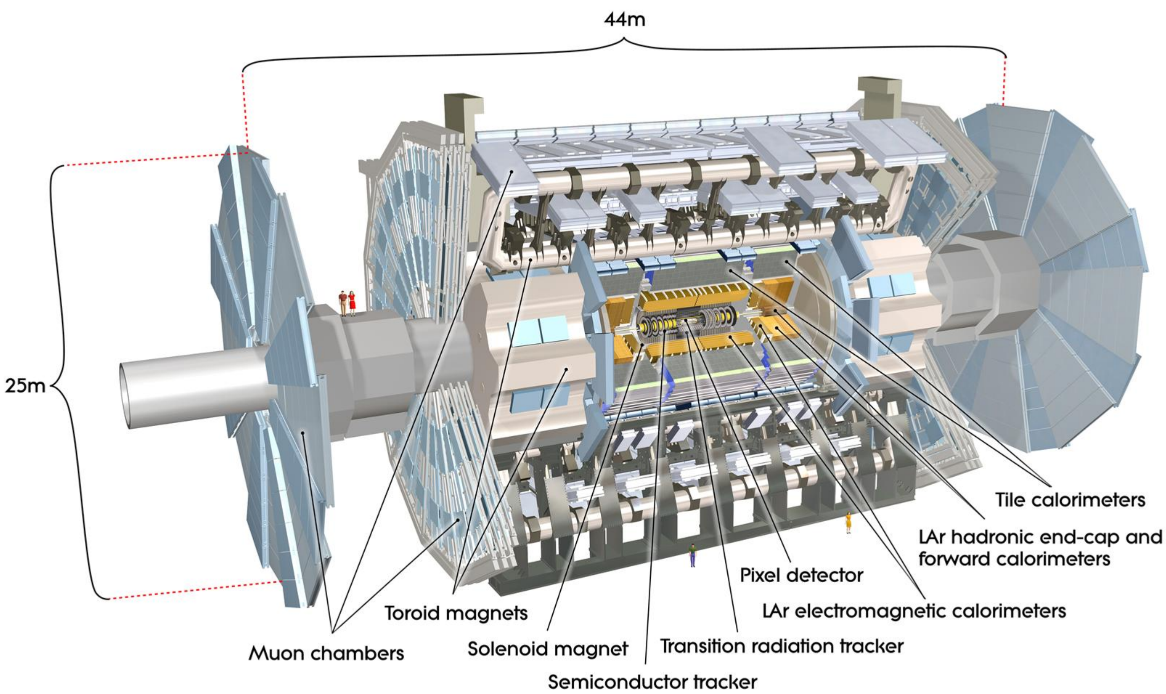

Figure 3.6: Overall layout of the ATLAS detector with the major subsystems noted. For comparison, two people are presented on the diagram, illustrating the scale of the detector.

Each of the above systems are composed of several subsystems, which is the subject of the following sections. For a more detailed approach please consult [60, 61] and [72]. As particles are produced from the collision taking place at the IP, they interact with different parts of the detector, leaving different signatures and eventually being tracked, as it can be seen in the figure below.

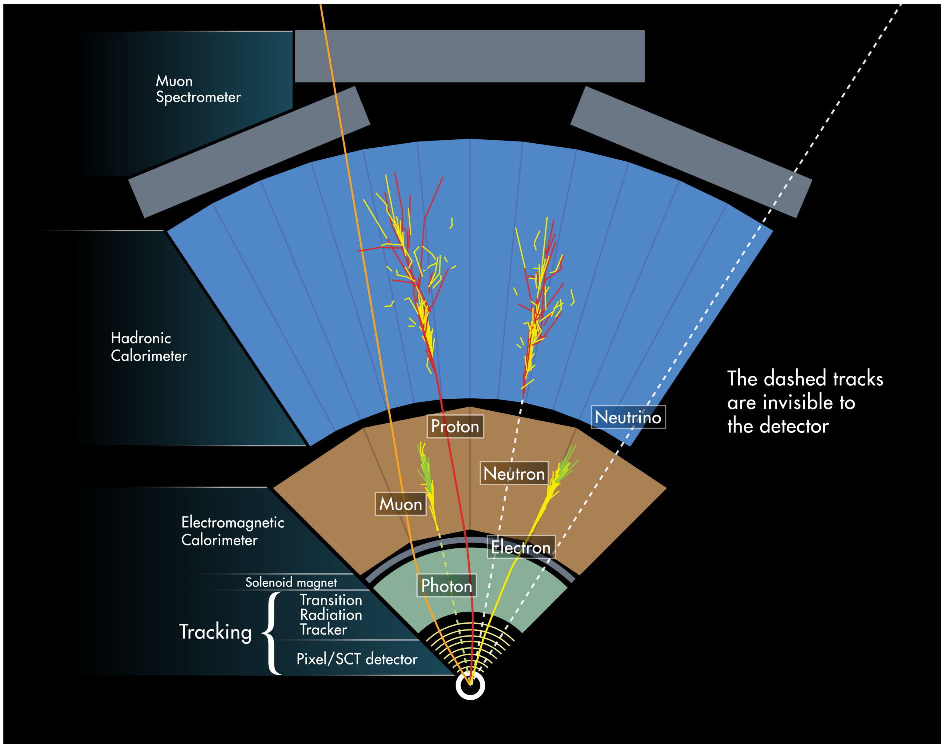

Figure 3.7: Cross sectional view of the ATLAS detector with the sub detectors. Various particles and their interaction with the detector systems are overlaid.

As requirements increased, during Long Shutdown 2 (LS2) - Phase I upgrade (2019 - 2022), the ATLAS detector underwent changes, in preparation of the Run 3 [72]. All upgrades on hardware and software aimed to:

1. Maintain and improve of the low p_T electrons and muons trigger thresholds. This provides us with rich datasets of electroweak bosons.

2. Preserve sensitivity to electroweak-scale particles yielding hadronically decaying tau leptons, jets, and missing transverse momentum.

3. Enhance the charged particles track measurements and improve the primary and secondary vertex reconstruction.

We will begin describing the coordinate system used by ATLAS. Then we will present the magnet system. Finally, we will study each of the sub detectors, as thorough as possible, mentioning the major upgrades implemented during LS2 and highlighting the differences between the runs of interest (Run 2 and Run 3). Before we end this section, it is considered important to mention that all the remarkable work related to the ATLAS experiment, is carried out by the ATLAS collaboration, which consists of more than 3000 scientists from 42 countries and 182 institutions. It constitutes one of the largest international scientific collaborations, dedicated to the advancement of scientific knowledge [75].

3.3.1 Coordinate System

The coordinate system used by ATLAS is right-handed, with the center located at nominal interaction point which is the center of the detector. The z axis lies across the beam direction and the xy plane is transverse to the beam axis. Specifically, $+x$ axis points towards the center of LHC and $+y$

points upwards. Additionally $+z$ which points towards the direction of the beam defines the side A of the detector, while $-z$ defines side C. The cylindrical shape of the detector, makes it useful to use a cylindrical coordinate system. The azimuthal angle ϕ is measured around the z axis (i.e from the $+x$ axis) and the polar angle θ is measured from the $+z$ axis. The momentum is divided into two components: the longitudinal component p_z and the transverse component p_T. Momentum and energy at the transverse plane are defined respectively as:

$$p_T = \sqrt{p_x^2 + p_y^2}, \tag{3.5}$$

$$E_T = E \sin\theta \tag{3.6}$$

The reason why transverse momentum is so important lies in the fact that p_T is Lorenz invariant for boosts along the beam axis. This allows as to relate p_T directly to observables like the invariant mass.

Another important quantity is the rapidity y which represents the velocity of a particle along the z axis and is defined as:

$$y = \frac{1}{2}\ln\left(\frac{E+p_z}{E-p_z}\right) \tag{3.7}$$

It is useful to use the rapidity instead of θ, because differences in rapidity are Lorenz invariant, whereas differences in θ are not. For high relativistic particles ($E \gg m$), the pseudorapidity is used which has the following expression:

$$\eta = -\ln\left(\tan\frac{\theta}{2}\right) \tag{3.8}$$

Note that we use the pseudorapidity (instead of rapidity) as measurements of the angle θ are easier. Additionally, $\eta = 0$ corresponds to the beam axis and $\eta = \rightarrow \pm\infty$ at $\theta \rightarrow 0, \pi$. Finally, in the $\eta - \phi$ plane the angular distance (which is also Lorentz invariant for boosts across the z direction [1]) is defined as:

$$\Delta R = \sqrt{(\Delta\eta)^2 + (\Delta\phi)^2} \tag{3.9}$$

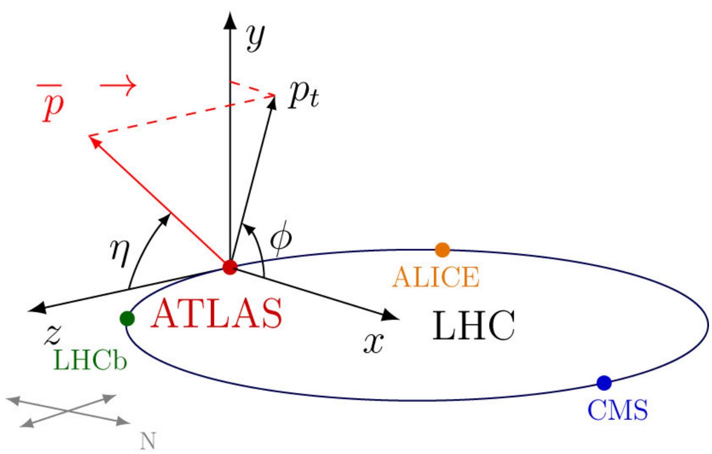

Figure 3.8: The coordinate system used by ATLAS [76].

[1]For massless particles ΔR is Lorentz invariant for longitudinal boosts. For massive particle with high p_T, as $y \approx \eta$, the ΔR is approximately invariant [27].

3.3.2 Magnet System

ATLAS uses a system of superconducting magnets, in order to bend charged particles and measure their momentum. The overall system measures 26m in length and 20m in diameter [60], weights 1315 tonnes [77] and stores 1.6GJ of energy [61]. The main parts of the system are: the Central Solenoid (CS), the Barrel Toroid (BT) and two End-Cap Toroids (ECT). An overview of the magnet system is presented in the following figure and a brief analysis of each magnet follows.

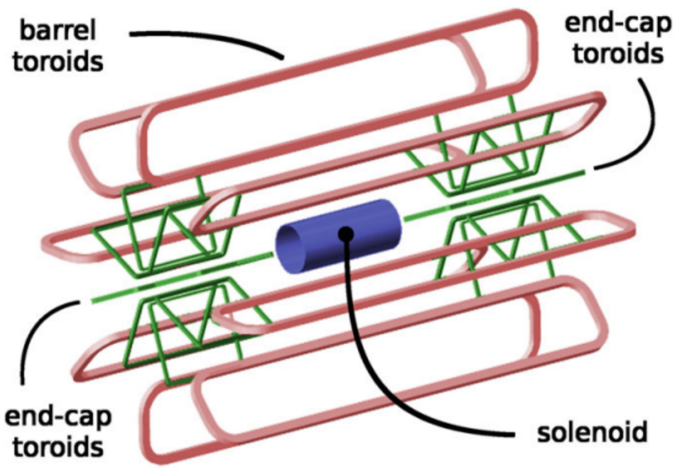

Figure 3.9: The ATLAS magnet system [78].

Central Solenoid

The CS surrounds the Inner Detector (see section 3.3.3), providing it with a 2T axial magnetic field [60]. It measures 5.8m in length, weights 5.4 tones, stores 40MJ of energy and operates at a nominal current of 7.73kA .Additionally, the CS can be charged and discharged in 30 minutes [61]. Finally, it is just 4.5cm thick and consists of 9km of superconducting niobium titanium wires [77].

Barrel Toroid

The BT has a cylindrical shape surrounding both the calorimeters and the End-Cap Toroids providing them with $3.5-4T$ field. It consists of 8 coils connected in series, operating at 20.5kA nominal current. The length of this magnet is 25.3m and it's diameter 20.1m making it the biggest magnet ever constructed! [77]. It weights 830$tonnes$, consists of 56km Al/NbTi/Cu conducting and 100km superconducting wires. The installation, started in 2004 and was completed 11 months later [61].

End-Cap Toroids

The presentation of the magnetic system is completed with two End-Cap Toroid magnets, which provide the necessary magnetic field of 3.5T for the optimization of the bending power inside the Muon Spectrometer (see section 3.3.5) [61]. They are placed at each end of the BT and line up with the CS. Each ECT is 5m long, has an outer diameter of 10.7m, weights 240tn, stores 0.25GJ of energy and operates at 20.5kA nominal current. Finally, these toroids are cooled to 4.5K using Helium (He).

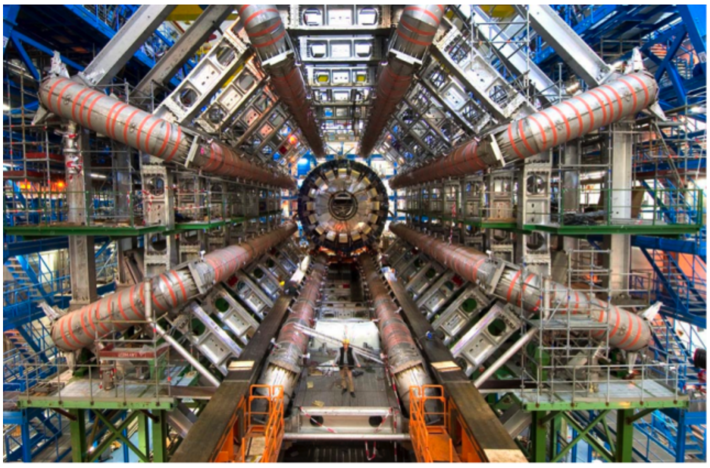

Figure 3.10: The Barrel Toroid (BT) located inside the ATLAS detector [61].

3.3.3 Inner Detector

The Inner Detector is used in order to measure the charge, momentum and paths of all charged particles. It is the closest detector layer to the beam, placed inside a $2T$ axial magnetic field generated by the CS. It forms a cylinder with a length of $5.3m$ and a radius of $1.15m$. Specifically, the ID provides: robust pattern recognition, high momentum resolution of $\frac{\sigma_{p_T}}{p_T} = 0.05\% p_T \oplus 1\%$ [2] and vertex (both primary and secondary) measurement for all charged particles within $|\eta| < 2.5$ and with $p_T > 0.5GeV$. It is composed of three main sub detectors nested co axially around the IP. From $r = 0$ being the IP, we have: the Pixel Detector with the Insertable B-Layer (IBL) $33.25mm < r < 122.5mm$, the Semiconductor Tracker (SCT) $299mm < r < 514mm$ and the Transition Radiation Tracker (TRT) $554mm < r < 1082mm$. All systems are arranged in concentric cylinders along the beam axis and in discs perpendicular to the beam in the end cap regions. Finally, the radiation background damaging the ID is dominated by charged hadron secondaries produced by inelastic $p - p$ collisions.

Pixel Detector and Insertable B-Layer

The innermost layer of the pixel detector relative to the beam is the Insertable B-Layer (IBL) which was installed during the Phase-0 Upgrade in the Long Shutdown 1 (LS1) and operates from Run 2. The insertion of the IBL, reduced the distance of the detector to the beam from $5cm$ to $3.3cm$, increasing the resolution of the track impact parameters and enhancing vertex recognition as well as flavour tagging. A new beryllium (Be) beam pipe, with inner radius $23.5mm$ (instead of the previous $29mm$) and average wall thickness $870\mu m$ accompanied the installation of the IBL. It consists of single layer silicon (Si) pixel sensors (based on two different technologies) with size $(r\phi) \times (z) = 50\mu m \times 250\mu m$ at an average radius of $r = 33.4mm$ and contains 12 million readout channels. Assembled with the readout chips they are arranged in 14 longitudinal supports (named staves), surrounding the beam pipe. A CO_2 two phase system is responsible for cooling the IBL, while the rest of the ID is cooled with the simultaneous use of a thermosiphon (using C_3F_8) and a oil-free cooling plant. As we move away from the beam, we encounter the three outer barrel layers and three discs on each side of the Pixel detector. The pixels have size $(r\phi) \times (z) = 50\mu m \times 400\mu m$ and provide intrinsic accuracies $(r\phi) \times (z) = 10\mu m \times 125\mu m$ for the barrel and $(r\phi) \times (r) = 10\mu m \times 120\mu m$ for the disc. There are approximately 80.4 million readout channels, making a total of 92.4 million readout channels for the

[2]The $\oplus$ symbol implies a quadrature addition, i.e $A \oplus B = \sqrt{A^2 + B^2}$, adding independent resolution components [79]

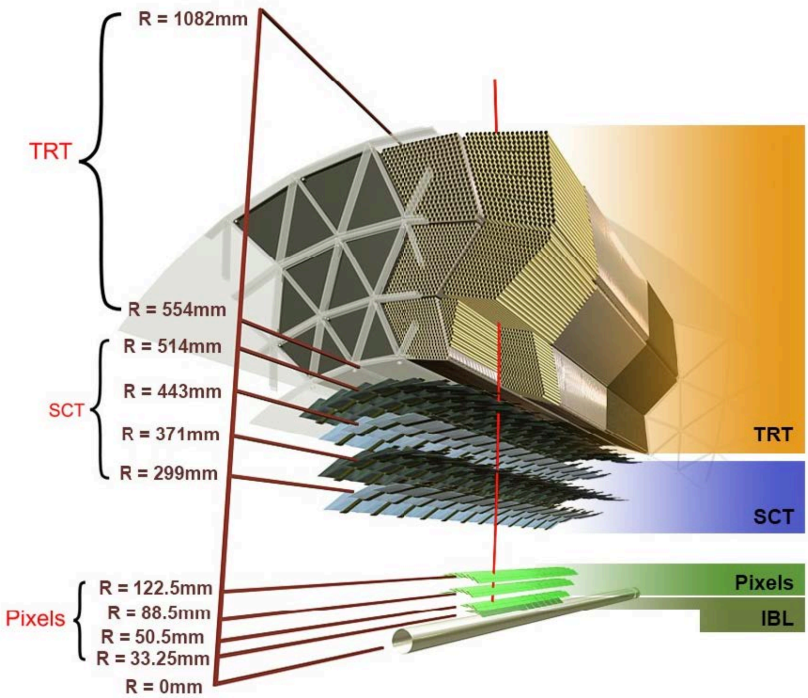

Figure 3.11: A cut-way view of the ATLAS ID, where all sub detectors are presented with their radical distance from the beam. The end cap discs for the pixels, SCT and TRT are not presented.

total sub detector. The configurated Pixel detector for Run 2 and Run 3 provides four measurements per track, with the first being in the IBL and the three next in the (three) outer most layers respectively. Finally, by the end of Run 2, pixel detector and IBL started sharing the same readout system [72].

Semiconductor Tracker

Semiconductor Tracker (SCT) is based on daisy-chained silicon sensors (strips), having a strip pitch of $80\mu m$ and measuring $12cm$ in length. It is reported to provide four to eight measurements per track (eight strip layers are crossed by each track) and consists of four barrel layers and nine end-cap disks on each side. The barrel region is constructed of silicon modules, which are created by laying two individual strips at an angle of $40mrad$, providing intrinsic accuracy $(r\phi) \times (z) = 17\mu m \times 580\mu m$. The measurement of both coordinates $r\phi$ and z is achieved using only one set of strips in each layer parallel to the beam. The end-cap discs, are arranged by a set of strips running radially and a set of stereo strips at an angle of $40mrad$, achieving intrinsic accuracy $(r\phi) \times (r) = 17\mu m \times 580\mu m$. Finally, the SCT contains 6.3 million readout channels [61, 72]. In preparation for Run 2 and Run 3, the DAQ system underwent some changes to support L1 trigger rates of 100 kHz at pileup levels up to $\langle\mu\rangle \approx 70$. Briefly mentioned, the upgrades focused on increasing the number of Read-Out Drivers (RODs) and Simple Link Interfaces (S-LINKs), remapping cables to balance data load, introducing a more efficient data compression mode ("supercondensed"), and dynamically masking noisy chips to reduce data volume at high pileup. [72].

Transition Radiation Tracker

Transition Radiation Tracker (TRT) are responsible for track identification of particles with $|\eta| < 2.0$ and $p_T > 0.5GeV$ and are build of $4mm$ gas filled straw tubes, layered with transition radiation material. The tubes have $144cm$ length in the barrel and $37cm$ in the end cap region. They are filled with two types of non flammable gas mixtures. The first (Xe based) contains: 70% Xe, 27% CO_2 and 3% O_2, while the second (Ar based) contains: 70% Ar, 27% CO_2 and 3% O_2. During Run 1, all straw modules were filled with the Xe based gas mixture. From Run 2, some modules were filled with the Ar based mixture due to gas leakage and in Run 3 the number of such modules using the Ar based mixture is even higher [72, 80]. Located at the center of the tubes are tungsten wires with $31\mu m$ diameter and a thin gold plating of $0.5 - 0.7\mu m$. Information, for the track identification with 30-36 points per track, is provided only on the $r\phi$ plane, with intrinsic accuracy $130\mu m$ per straw and a total number of readout channels is 351 thousand. Connecting the wall of the tube at a voltage of $-1.5kV$ and the wire at ground, results the wall to work as the cathode and the wire as the anode. As particles traverse the TRT, they ionize the gas and produce electrons that are collected by the anode wire. Throughout drift-time measurements, we acquire the energy of the particle. Finally, an important function of the TRT, is the capability to identify electrons and distinguish them from pions, based on their energy depositions [61, 72]. During Run 3 track occupancy [3] is reported to be 0.75, while it was 0.5 during Run 2. Taking this fact into consideration some software modifications on the TRT track reconstruction were applied. Additionally, modifications on the DAQ system were implemented to cope up with the higher frequency and pile-up situation [72].

3.3.4 Calorimeters

Calorimeters measure the energy of particles, produced during the collisions, which decay electromagnetically or via the strong force. The cover the full azimuthal angle and the region with $|\eta| < 4.9$. All ATLAS calorimeters operate as sampling calorimeters, utilizing a layered configuration of absorbing high density materials that stop incoming particles, alternating with layers of active media that measure the particle energies. The result of a particle interacting with the dense passive material of calorimeters, is cascaded decays, known as particle showers. These low energy secondary particles, deposit their energy inside the calorimeters, until they come to a stop. The active layers, absorb this energy, allowing the measurement of the energy of the initial particle [61, 72]. They are divided in five sub detectors: the LAr ElectroMagnetic Barrel calorimeter (EMB), the LAr ElectroMagnetic End-Cap calorimeter (EMEC), the Tile barrel hadronic Calorimeter (TileCal), the Hadronic End-Cap calorimeter (HEC) and the LAr Forward Calorimeter (FCal). Depending on the way particles decay, specifically electromagnetically or via the strong force, calorimeters are characterized as Electromagnetic Calorimeters (ECal) and Hadronic Calorimeters (HCal). Particles interacting via both aforementioned forces, deposit energy in both calorimeters. The importance of wide coverage in $|\eta|$, lies in the fact that is allows to detect and measure the missing transverse momentum (E_T^{miss}), useful among others in search for SUSY particles [61]. Very few changes (focusing mainly at the LAr calorimeter electronics), were required during the LS2, making the configurations for Run 2 and Run 3 mostly identical [72].

[3] Defined as the hit occupancy in straws in the path of a track of interest

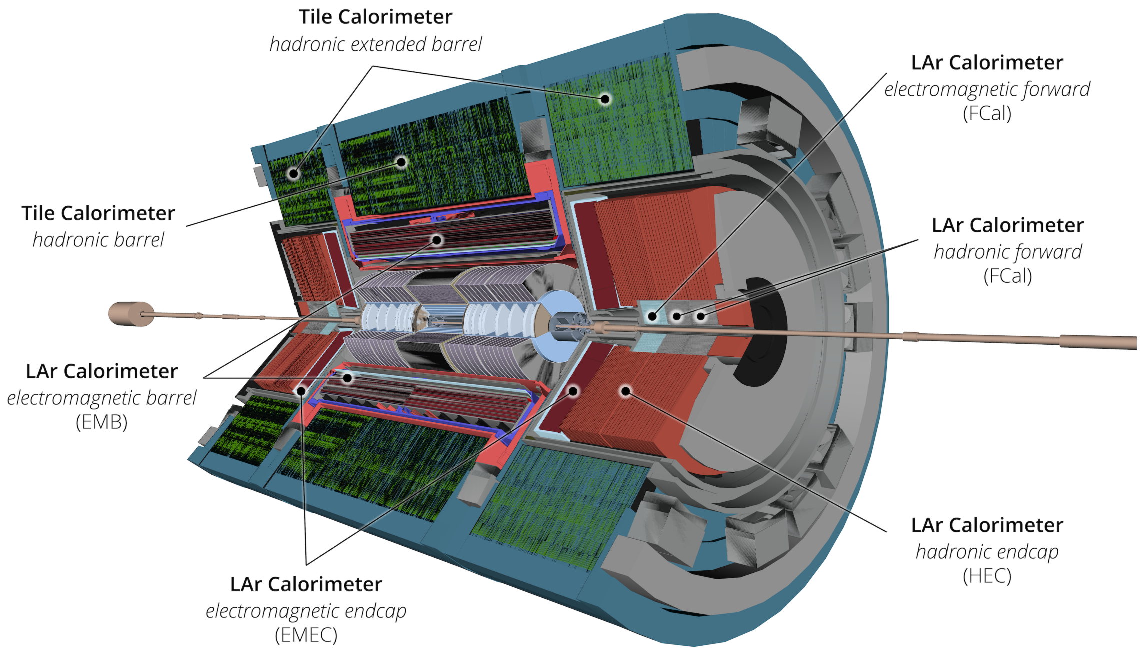

Figure 3.12: Cut-away view of the calorimeter system that measures the energies and positions of charged and neutral particles through interleaved absorber and active layers. The calorimeter covers the full azimuthal angle and regions with $|\eta| < 4.9$.

Electromagnetic Calorimeters

The electromagnetic calorimeter is made of Liquid-Argon (LAr) layers, organized in accordion shape, acting as the active material (chosen for possessing good radiation hardness) and lead absorber plates (for the first two parts), copper (for the last part) being the passive materials. The relative resolution of the ECal is:

$$\frac{\sigma_E}{E} = \frac{10\%}{\sqrt{E}} \oplus 0.7\% \tag{3.10}$$

ECal consists of three main parts: the EM Barrel Calorimeter (EMB) covering $|\eta| < 1.475$, the EM End Calorimeter (EMEC) covering $1.375 < |\eta| < 3.2$ and the first section of the Forward Calorimeter (FCal1) covering $3.1 < |\eta| < 4.9$. The EMB has $6.4\,m$ length and is formed by two half barrels. It is segmented in three layers: the first one, having resolution $\Delta\eta \times \Delta\phi = 0.0031 \times 0.0245$ allows precise position measurements. The second with resolution $\Delta\eta \times \Delta\phi = 0.025 \times 0.025$ (square cells) captures most of the shower's energy. Finally, the third one having twice the granularity in η, with resolution $\Delta\eta \times \Delta\phi = 0.05 \times 0.0245$, measures the remainder of the energy. In front of the first layer, a thin LAr layer is placed, called Pre-Sampler (PS), dedicated in energy corrections (due to losses inside the calorimeter) and covering the region $|\eta| < 1.475$.

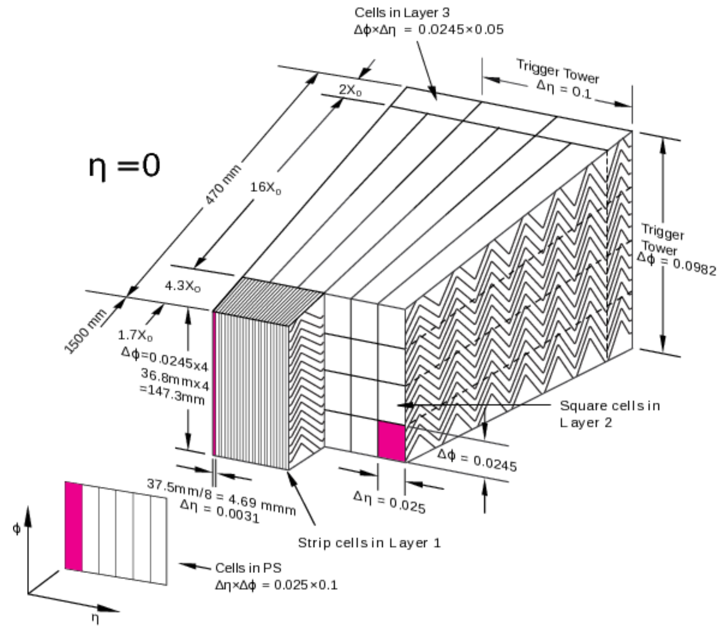

Figure 3.13: View of the different EMB layers and resolutions. The PS does not appear in the figure.

The EMEC is composed of two wheels, located on either side of the EMB, each structured into three layers and also equipped with a PS.

Hadronic Calorimeters

The HCal is divided into three regions: the TileCal covering $|\eta| < 1.7$, the LAr Hadronic Endcap Calorimeter (HEC) covering $1.5 < |\eta| < 3.2$ and the next two sections of the Forward Calorimeter (FCal2, FCal3) covering $3.1 < |\eta| < 4.9$. The TileCal uses polystyrene scintillating tiles as active material, whereas steel as passive and is further divided into the barrel region ($|\eta| < 1.0$) and the Extended Barrel ($0.8 < |\eta| < 1.7$). Both regions are divided (azimuthally) into 64 modules, each consisting of three layers. The signal generated from the scintillating tiles, is converted (after being amplified) into electrical signal by PhotoMultipliers (PMT). The HEC uses LAr as active material and copper (Cu) as passive and consists of two wheels per end cap. The energy resolution for both TileCal and HEC is given by [61]:

$$\frac{\sigma_E}{E} = \frac{50\%}{\sqrt{E}} \oplus 3\% \tag{3.11}$$

The final stages FCal2, FCal3 also use LAr as active material and copper (FCal2), tungsten (FCal3) as passive. The energy resolution for the forward calorimeters is:

$$\frac{\sigma_E}{E} = \frac{100\%}{\sqrt{E}} \oplus 10\% \tag{3.12}$$

3.3.5 Muon Spectrometer

The Muon Spectrometer is the outermost part of the ATLAS detector, primarily designed to track and precisely measure the momentum of muons traversing the entire detector volume, as well as triggering on detected particles. Most of my work on the Muon-In-Jet correction (chapter 6) is based on muons reconstructed from combined data obtained by the ID and the MS. The MS offers $|\eta| < 2.7$ coverage and is positioned within the magnetic field produced by the barrel and end-cap toroids (see section 3.3.2). This enables the bending of muons, which is essential for measuring their momentum. Specifically, the magnetic field in $|\eta| < 1.4$ is exclusively provided by the barrel toroid, while in $1.6 < |\eta| < 2.7$ by the end-cap magnets. In the region $1.4 < |\eta| < 1.6$ (known as transition region), both magnet systems contribute. The total resolution in momentum of the MS, is $\frac{\Delta p_T}{p_T} = 10\%$ for transverse momentum up to 1 TeV. During Run 2, MS was constructed based on four muon chamber types: the Monitored Drift Tube Chambers (MDT), the Cathode Strip Chambers (CSC), the Resistive Plate Chambers (RPC) and the Thin Gap Chambers (TGC). The first two are used for measuring the track coordinates in the principal bending direction (MTD's for smaller $|\eta|$, while SCS's for larger). The last two are used in the trigger system covering $|\eta| < 2.4$, with RPC's covering $|\eta| < 1.05$ and TGC's covering the rest. The detector contains barrel and end-cap regions. The barrel region consists of three concentric cylinders places at radius of $5\,m$, $7.5\,m$ and $10\,m$ around the beam axis. They contain MDT's and RPC's and cover the region $|\eta| < 1.0$. The end-cap region consists of four wheels on each side at distances (z): $7.4\,m$, $10.8\,m$, $14\,m$, $21.5\,m$ from the IP. They contain MDT's, TGC's and CSC's and cover the region $1.0 < |\eta| < 2.7$. The layout of the MS, with the Run 2 configurations can be seen in figure 3.14.

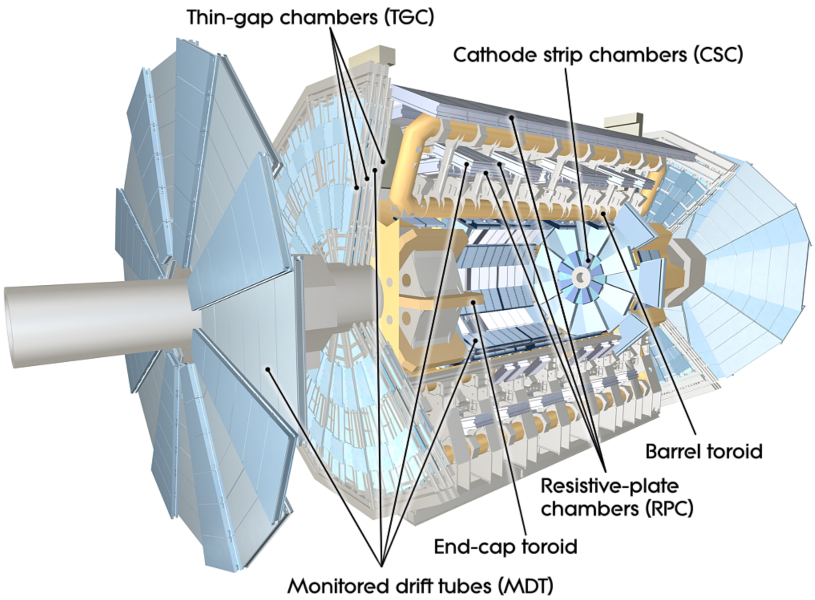

Figure 3.14: Cut-away view of the ATLAS Muon Spectrometer used for Run 2, with the different muon chambers noted.

The basic features of the four muon chamber types used, are the following:

- **MDT**: They consist of $29.97\,mm$ diameter Aluminum (Al) drift tubes, with $400\mu m$ wall thickness. The tubes are filled with a non-flammable, pressurized (at 3 bar) gas mixture $Ar-CO_2$ (93/7%) [4] which presents good aging properties. The tube acts as the cathode, while a $50\mu m$ gold-plated tungsten-rhenium wire, supplied with $3\,kV$ is the anode. While muons pass by the MDT's, they ionize the gas, producing electrons which are attracted to the wire (with a maximum drift time of $700\,ns$), whereas positive ions drift to the cathode. In the barrel region they have rectangular shape, while in the end-cap trapezoidal. Finally, they offer a single wire space resolution of $80\ \mu m$ and time resolution less than a $1\,ns$.

[4] Ar is the symbol for Argon

- **CSC**: The safe operation of MDT's (less than $150Hz/cm^2$) would be exceeded for the first layer of the end-cap region covering $|\eta| > 2.0$. Hence, MDT's are replaced with CSC's [81], safe to operate up to $1000Hz/cm^2$. They are multi-wire proportional chambers, with wires running radically. The anode wires are made of gold-plated tungsten with 3% rhenium, having $30\mu m$ diameter and are kept to $1.9\,kV$. The gas mixture, similarly to the MDT's, is $Ar-CO_2$, although not pressurized and in concentrations $80/20\%$. The space resolution is $60\mu m$ for the bending plane and $5\,mm$ for the transverse plane, while the time resolution is about $7\,ns$ (as the drift time is reduced compared to the MDT's to $40\,ns$).

- **RPC**: They consist of two parallel resistive (with volume resistivity $10^{10}\ \Omega cm$) plates made of phenolic-melaminic plastic laminate and kept at a distance of $2\,mm$, with insulating spacers. The potential difference of the gap is $9.8\,kV$ and the electric field in the gap between the plates is $4.9\,kV/mm$. The gas mixture used is: $C_2H_2F_4 - C4H10 - SF_6$ $(94.5/5/0.3\%)$, which has low flammability. With time resolution of less than $2\,ns$, RPCs are particularly suitable for triggering applications.

- **TGC**: They are multi-wire proportional chambers, focusing on muon triggering and measurement of the azimuthal coordinate of muon tracks. The wire to wire distance is $1.8\,mm$, whereas the wire to cathode distance is $1.4\,mm$. Furthermore, the TGC's are filled with a highly flammable and highly quenched gas mixture of $CO_2 - nC_5H_{12}$ $(55/45\%)$. Using a potential of $2.9\,kV$, all wires produce high electric field, which in correlation with the small wire to wire distances results in very good time resolution below $4\,ns$.

During the LS2, the major upgrade regarding the MS, was the replacement of the inner wheel at the end-cap region (known as "small wheel"), by a new detector called **N**ew **S**mall **W**heel (NSW) and covering the region $1.3 < |\eta| < 2.7$. The main objective behind this, was to sharpen the trigger thresholds turn-ons and improve discrimination against background while maintaining the trigger rate. The NSW are constructed by two new chamber types: small-strip TGC's (STGCs) and micro-mesh gaseous structure (Micromegas) detectors and must provide 50 μm spatial resolution in the transverse plane. With the commission of the NSW, triggering rates improved for lower muon p_T thresholds as well as enhanced resolution in the azimuthal coordinate. Approximately 357 thousand and 2 million channels of STGCs and Micromegas respectively were used. The MS layout used for Run 3, can be seen in figure 3.15.

The NSW retains the eight fold symmetry of the legacy and consists of sixteen sectors (eight small and eight large). The small sectors, are aligned with the barrel toroid coils, while the large sectors form a secondary plane, with the Micromegas of the different sectors overlapping. The sTGC and Micromegas detectors are each organized in quadruplet configurations, where each unit is composed of a trapezoidal module housing four gas-gap layers. Quadruplets are organized in wedges; three quadruplets form an sTGC wedge and two quadruplets a Micromegas wedge. Finally, each sector consists of two wedges, i.e sixteen active detector layers (half with sTGCs and half with Micromegas).

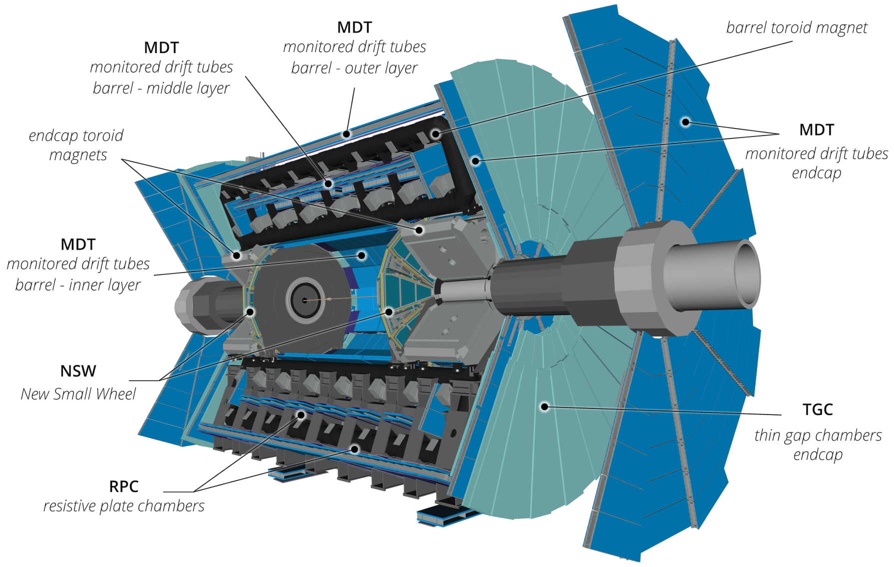

Figure 3.15: Cut-away view of the ATLAS Muon Spectrometer used for Run 3. The main change from Run 2, clearly visible on the figure, is the replacement of the inner wheels, by the New Small Wheels.

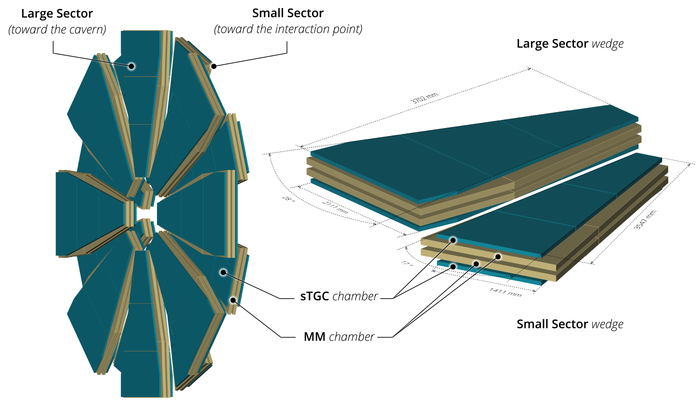

Figure 3.16: Structure of the ATLAS NSW used for Run 3. The Large and Small, large sectors and their structure appears on figure.

Before we come to an end, we will briefly present the two new technologies introduced in the NSW. Micromegas were invented in late 1990 and are gaseous particle detectors, where the traditional high voltage wires are replaced with a metallic micro mesh. They consist of a planar (drift) electrode at $-240\,V$, a gap gas of few millimeters and a micro mesh at $120-130\,\mu m$ from the readout electrode, set at $500\,V$. The baseline gas mixture is $Ar-CO_2-iC_4H_{10}$ $(93/5/2\%)$ and the backup is $Ar-CO_2$ $(93/7\%)$, with both being non flammable. As charged particles traverse the Micromegas, they ionize the gas producing electrons which then drift towards the micro mesh (see figure 3.17) and eventually the drift electrode (with a total drift time of $100\,ns$). The spatial resolution achieved in the bending plane is $100-200\mu m$ and $2.7\,mm$ in the secondary plane. Moving on, sTGC technology was developed in 1980, allows very fast on-line tracking and holds many similarities with the TGC technology. In the anode plane, the middle of the gap is connected with gold-plated tungsten wires supplied with $2.8\,kV$. The difference from the TGC's is the wire direction, which in this case is parallel to the radial axis, whereas in the TGC's wires extend azimuthally. Additionally, twenty wires form a group and share the same high voltage capacitor. The resistivity of the cathodes is significantly less than the TGC's, allowing rapid clearance of charge in the cathode plates. The readout strips are also much finer than the TGC's, being 2.7 mm wide. sTGC's provide $100 - 200$ μm spatial resolution in the bending plane and 2.6 mm in the secondary plane.

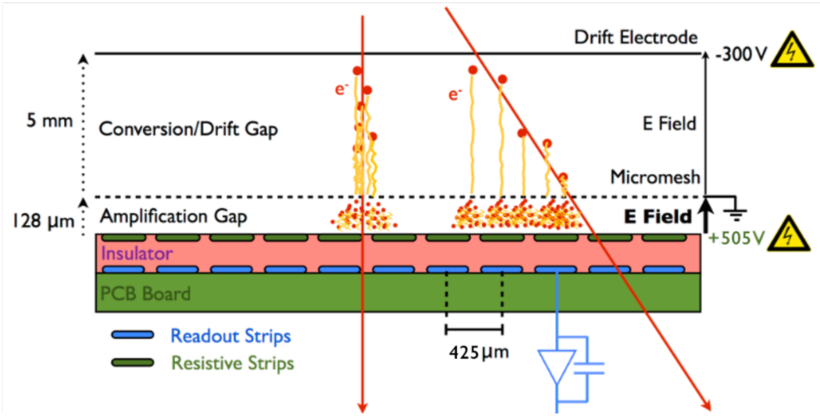

Figure 3.17: Layout and operating principle of the Micromegas detectors, used in the ATLAS NSW for Run 3.

3.3.6 Trigger and Data Acquisition System

In the LHC collisions occur every 25 ns, i.e the rate of events is 40 MHz. With the average size of a raw event reported at 1 MB for Run 2 [82] and 2.1 MB for Run 3 [72], this yields 40 TB/s and 84 TB/s to be stored for Run 2 and Run 3 respectively. The increased size of a raw event between Run 2 and Run 3, is mainly due to the increase of the pile up. This is way beyond our processing and storing abilities. Additionally, many inelastic, uninteresting events would be stored, as the cross section for inelastic processes is significantly larger than that of interesting events. Consequently, a triggering system is being used to filter the events and store only the important for physics analysis. While there were upgrades between the two runs, the trigger system consists of two levels. The Level-1 (L1) trigger, is hardware synchronous pipeline system and uses low granularity information from the calorimeters (L1Calo) and the muon detectors (L1Muon). It reduces the rate of data from 40 MHz to 100 kHz, which is allocated to different physics and has a latency of 2.5 μs to make the decision. During Run 2 trigger towers were used as input for the L1Calo while in Run 3 Super Cells (containing the sum of four to eight calorimeter cells) are used, improving the performance [72]. The High Level Trigger (HLT) is software implemented and only uses events that have been accepted by the L1 trigger. It further reduces the event rate from 100 kHz to 1 kHz (Run 2) and 3 kHz (Run 3), using offline reconstruction algorithms with information from all sub detectors. Eventually we are required to store 1 GB/s (Run 2) or 6 GB/s (Run 3). The processing time for the HLT in 2018 was 400 μs, while for Run 3 is expected to be higher. Triggers are organized into chains, known as trigger menus, reflecting the physics goals and varying from year to year. The Data Acquisition system (DAQ), transports data from sub detector electronics to offline processing, according to trigger decisions. Upgrades took place in preparation for Run 3, in order to cover the full detector. Finally, a brief discussion is dedicated to data storage. Raw files are kept in Tier-0 at CERN and then converted to Event Summary Data (ESD) containing the reconstructed objects and Analysis Object Data (AOD) containing the information of the event reconstruction in POOL/ROOT files. Then, through filtering processes, derived AOD (DAOD or xAOD) are produced meeting the needs of various physics analyses and stored at Tier-1. This is the type of files, my work is based on. Each Tier-1 facility acts as a hub for several Tier-2 and Tier-3 sites, which provide computational resources to universities and smaller laboratories.

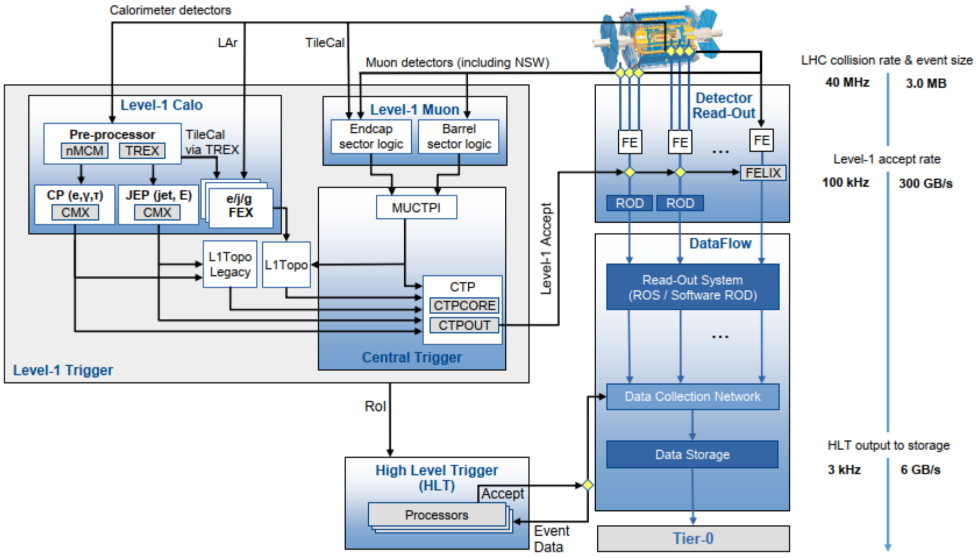

Figure 3.18: Diagram of the TDAQ system used by the ATLAS detector for Run 3.

3.4 Future at CERN

The Run 3 at the LHC is now scheduled to continue until June 2026, when the Long Shutdown 3 (LS3) is expected to begin. During the LS3, many updates will take place, in preparation for the High Luminosity LHC (HL-LHC). Run 4, is scheduled to start in June 2030 and extend CERN's leading role in science until early 2040 [83].

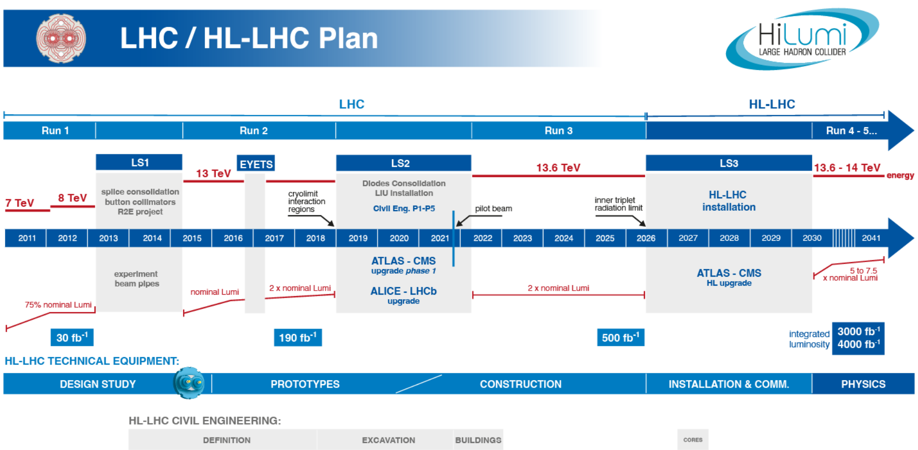

Figure 3.19: Schedule demonstrating the remaining of Run 3, the LS3 and the start of the HL-LHC.

The HL-LHC will be designed to achieve an instantaneous luminosity $L = 5 - 7 \times 10^{34}$ cm^{-2}s^{-1}, which is about 5 - 7 times higher than the luminosity delivered currently by the LHC. The ultimate beam intensity is expected to be 1.7×10^{11} protons per bunch and center of mass energy will not change (around 14 TeV) as all the effort has been focused to increase the rate of collisions. In order to achieve this, Nb_3Sn superconducting magnets with a field of 11-12T will be used. Furthermore, updates on the RF cavities and the cryogenics systems at IR1 and IR5 are necessary among many more. Pileup is anticipated to be 130-140 events per bunch crossing and HL-LHC is planned to deliver an integrated luminosity of 250 fb^{-1} per year [84]. For comparison, the total integrated luminosity, delivered by LHC for this analysis (7 years in total) is 300 fb^{-1}. Furthermore HL-LHC, is expected to produce 15 million Higgs bosons per year [70].

Finally, recently, CERN released a report on a possible Future Circular Collider (FCC), which will offer us an insight in new territories of extremely high energy [85]. In the preliminary design report FCC is proposed to be about 91 km, in a depth of approximately 200m. Firstly, it is planned to operate as an electron - positron collider (FCC-ee) and then as a hadron collider (FCC-hh) achieving a center of mass energy $\sqrt{s} = 85 - 100\,\mathrm{TeV}$. In order to achieve this high energy, magnets with a field of 14T are required [86]. Hopefully this excellent project, will eventually be implemented!

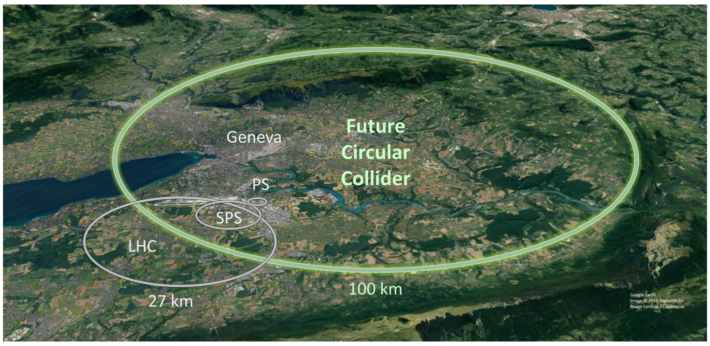

Figure 3.20: A geological map illustrating the FCC (the PS, SPS and LHC are also shown in the map).

Chapter 4

Analysis Overview

With the theoretical background now thoroughly established, it is now time we turn our attention to the analysis itself. This chapter begins with a general introduction, the motivation behind the study and the observables we expect to measure. Then, the data sets and MC samples under study are described. Moving on, event selection and the modeling of both signal and background processes are explained. Furthermore, our attention turns to event reconstruction of the most relevant to my work, physic objects. Finally, my studies on b tagging efficiencies and the muon p_T^{rel} for the evaluation of $b\bar{b}$ content, are presented.

4.1 Purpose of the Analysis

This analysis is an inclusive (all production modes are considered) search of the boosted Higgs boson in the $b\bar{b}$ decay channel, using data from the $p-p$ collisions recorded by the ATLAS detector at CERN, during the periods: Run 2 (2015-2018) and partial Run 3 (2022-2024). It is based on the previous analysis using only Run 2 data [1]. Improvement in physics objects reconstruction and analysis strategy, results in increased sensitivity by a factor of 6, with 2.2 increase in data statistics.

The boosted Higgs boson has high transverse momentum p_T. For the ggF production mode, a boosted Higgs boson can be produced with the emission of a gluon from the triangular loop (referred as Initial State Radiation (ISR)), which recoils against the Higgs. Without the ISR the p_T of Higgs would be around 20 GeV.

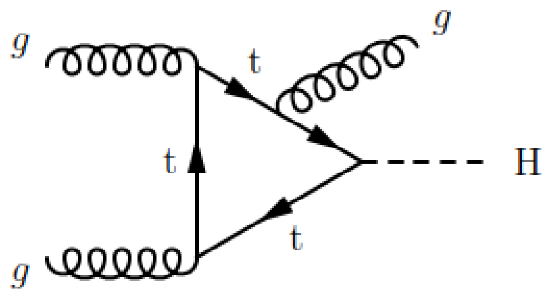

Figure 4.1: ggF production mode, with the Initial State Radiation (ISR), i.e the emission of a gluon from a triangular loop.

When the Higgs boson is produced in high p_T, the decay products have a smaller angle and become collimated in one large-R jet (figure 4.2), making the reconstruction of objects easier (see section 4.5).

On contrary, for Higgs bosons at low p_T, the detection of b quarks originating from the Higgs, is more difficult as $H \rightarrow b\bar{b}$, is imitated by many other processes as well. The angular opening of the decay products in boosted Higgs productions is:

$$\Delta R = 2\frac{m_H}{p_{T_H}} \tag{4.1}$$

In addition high p_T offers the ability to resolve loop structures, probe Higgs-gluon coupling and obtain an EFT interpretation of Higgs. As mentioned in section 2.11, new physics (NP) or else Beyond the Standard Model (BSM) physics can be parametrized through EFT, whose coefficients are suppressed by a new physics scale Λ. Studies of Higgs bosons produced with large transverse momentum probe regions of phase space where potential BSM effects may be enhanced by factors proportional to powers of p_T^H/Λ [87]. Even if the inclusive Higgs production rate is SM-like, a precise determination of the boosted Higgs p_T shape, enables the detection of BSM effects. The $b\bar{b}$ decay channel, offers the best sensitivity for this purpose.

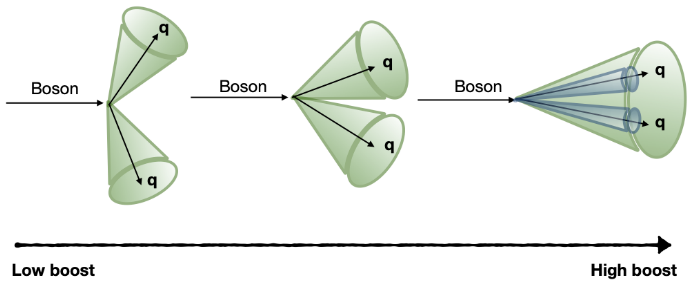

Figure 4.2: The behavior of two small jets, containing a quark (q), against the transverse momentum. For low p_T the jets are separate, while for boosted events, the decay products become collimated in one large-R jet.

While Higgs decays approximately 58% in $b\bar{b}$, this channel is considered challenging for analysis, due to it's overwhelming background from strong interactions $pp \rightarrow q\bar{q} + X$. Signal and background modeling is presented in section 4.4.

My work is mainly focused on four main tasks: the b-tagging efficiencies (section 4.5.4, a method using muon p_T^{rel} for the evaluation of $b\bar{b}$ content in the QCD background 4.7, the Jet Mass Resolution (JMR) (chapter 5) and the Muon-In-Jet correction (chapter 6). For the first subject different b-tagging algorithms are examined in order to select the optimum. In the second task the study focuses on the p_T^{rel} of the muon as an observable to access the $b\bar{b}$ content of the QCD background before and after flavour tagging. Moving on, the JMR is studied over different Working Points (WP) and over different simulation campaigns, corresponding to different data taking years. Hbb and Zbb simulation samples are used and results are accompanied by the appropriate errors. Finally, the MIJ correction is optimized, using two different methods an then integrated to the analysis. Statistical fits are performed, to measure the effect of the correction on data.

The full analysis, is expected to deliver an inclusive measurement of the Higgs signal strength μ_H (defined in 2.24) in the region $p_T > 450\,GeV$. Additionally, fiducial [1] inclusive Higgs cross section for the region $p_T > 450\,GeV$ and $|\eta^H| < 2.0$ and STXS-like [2] μ_H and Higgs cross sections for all the differential p_T bins (defined in table 4.2) will be provided. The same measurements for a ggH

[1] A well defined phase-space region of the ATLAS detector [88, 89]

[2] Simplified template cross sections (STXS) are an approach to categorize the Higgs-boson candidate events according to the properties associated with the Higgs production mode [90, 89].

enriched study are intended to be delivered. Finally, the extraction of μ_Z in the differential p_T bins is anticipated. Please note, final results, are not yet available as it is still a work in progress.

4.2 Data sets and MC samples

The full analysis uses data from full Run 2 (2015-2018) at 13 TeV and partial Run 3 (2022-2024) at 13.6 TeV. Events fulfilling some criteria (known as the Good Runs List (GRL) [91]) are suitable for physics analysis and correspond to a total integrated luminosity of 300.7 fb^{-1}. The contribution of each data taking year to the full data set is summarized in table 4.1.

Year	**Int. Lumi** (fb^{-1})
2015/16	36.6
2017	44.1
2018	58.8
Total Run 2	139.5
2022	26.1
2023	25.8
2024	109.4
Total partial Run 3	161.3
Total	300.7

Table 4.1: Integrated luminosity of the collision data set used for the analysis, year by year and total.

Monte Carlo (MC) simulations are used to model the physics processes involved (signal and background) and to compare with the data taken. The MC samples are centrally produced from ATLAS for the need of the analysis [92]. A presentation of the features the MC samples have, is considered out of scope and therefore is not included.

4.3 Event Selection

The signal selection in this analysis is based on the presence of a large-R jet recoiling against a second large-R jet, with the latter required to have $p_T > 250,$GeV. The leading jet is identified as the signal jet, while no further selection criteria are imposed on the recoil jet. In case we apply selections on the recoiling system, we can have an enriched ggH production.
A candidate jet is a large-R jet when it fulfills the following criteria:

- $p_T > 450\,GeV$
- $|\eta| < 2.0$
- $2m_J/p_T < 1$, so that the jet is considered boosted
- It contains at least two Variable-Radius (VR) jets, with $p_T > 10\,GeV$.

Moving on, the criteria our events need to fulfill are:

- Trigger at least one of the High-Level large-R jet triggers (see section 4.5.1)
- The leading large-R jet must have $p_T > 450\,GeV$, $m_J > 45GeV$

- The subleading large-R jet must have $p_T > 250\,GeV$
- At least one of the two leading jets passes the candidate jet criteria above.

A schematic representation of Higgs candidate large-R jet recoiling against a second large-R jet can be seen in figure 4.3, which is an actual event display obtained from ATLAS.

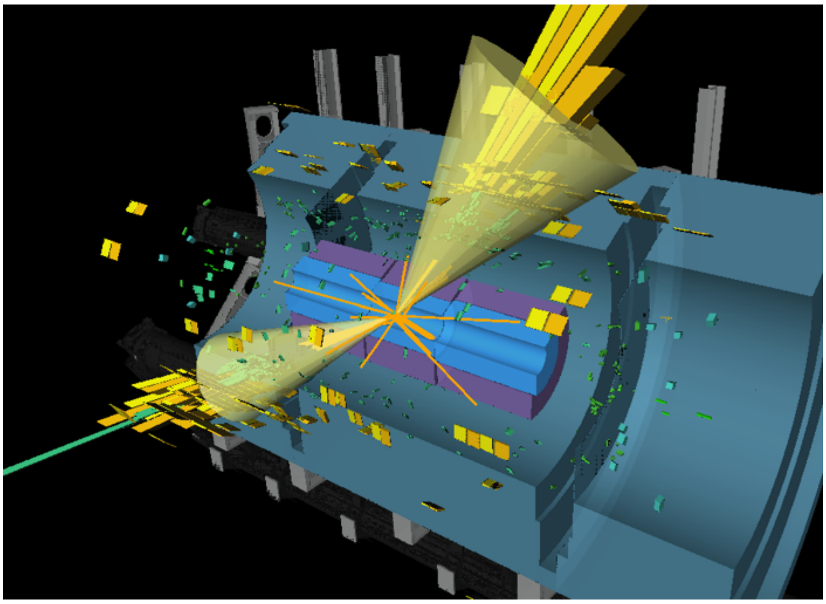

Figure 4.3: Event display of a collision inside the ATLAS detector. The jet pointing upwards is a Higgs candidate jet recoiling against a second large-R jet pointing downwards in the picture. This event has: $M = 121.3\,GeV$ and $p_T = 1029.1\,GeV$. This number of the event is: 912995192 in Run 352448.

The events are subsequently processed by the b-tagging algorithm, described in subsection 4.5.4. Events that are successfully b-tagged are classified into the Signal Region (SR), while those that fail the b-tagging requirements are assigned to the Validation Region (VR). Specifically, we have:

- **Signal Region Leading (SRL):** The leading large-R jet is tagged (no interest in the subleading jet in this case as only one candidate jet is accepted per event)
- **Signal Region Subleading (SRS):** The leading large-R jet is anti-tagged and the subleading is tagged.
- **Validation Region Leading (VRL):** The leading large-R jet is anti-tagged and no interest in the subleading jet.
- **Validation Region Subleading (VRS):** The leading and subleading large-R jet are anti-tagged.

It is important to stress out that contrary to the SR, VR accepts both leading and subleading jets in the event to avoid kinematic biases. All regions are divided in three p_T bins plus the inclusive, as shown in table 4.2.

The use of VR, is to model the QCD background and gain constraints on the data driven parametrisation when performing simultaneous fits on the SR and VR.

Finally, a last region of the analysis is the Control Region $CR_{t\bar{t}}$, containing events where an isolated muon associated with a b tagged jet is recoiling against a large-R jet. $CR_{t\bar{t}}$ is used to extract the rate of $t\bar{t}$ background.

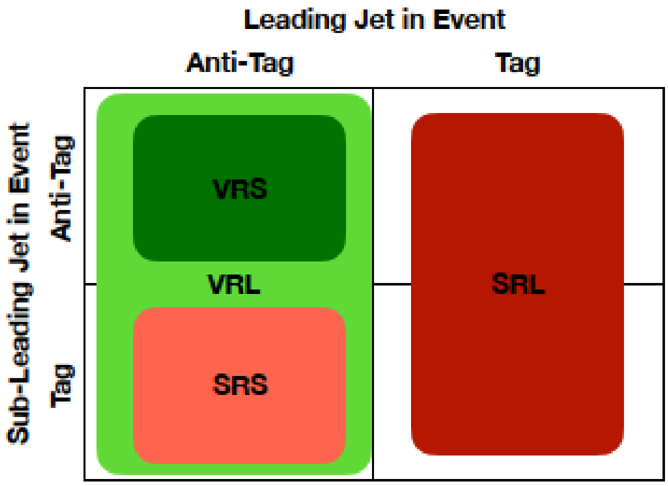

Figure 4.4: Schematic representation of Signal Region (SR) and Validation Region (VR) used for the analysis.

An analysis cut flow, for MC (histogram) and 2023 data (points), representing the fraction of accepted events, when each event selection is applied, is presented in figure 4.5.

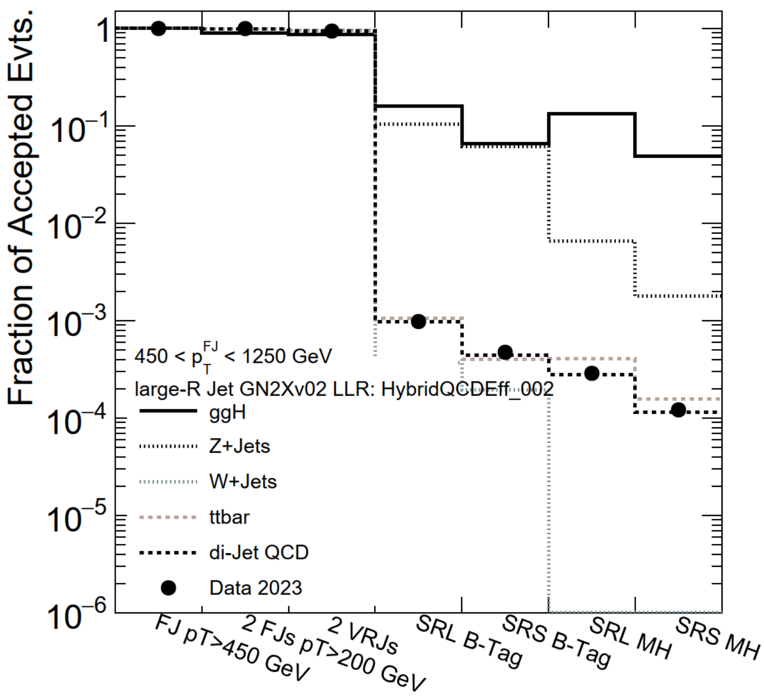

Figure 4.5: Analysis Cut Flow of the inclusive p_T region, for MC (histogram) and 2023 data (points). GN2Xv02 and a Working Point providing 0.002 QCD efficiency are used.

Name	Value
p_T^{all}	450 - 1250 GeV
p_T^{01}	450 - 650 GeV
p_T^{02}	650 - 1000 GeV
p_T^{03}	1000 - 2500 GeV

Table 4.2: Definition of p_T bins used for the analysis.

4.4 Signal and Background Modeling

Regarding the signal, only events in the mass range $105 < m_J < 140\,GeV$ are considered. All four main production modes contribute differently according to the jet p_T, as it can be seen in figure 4.6

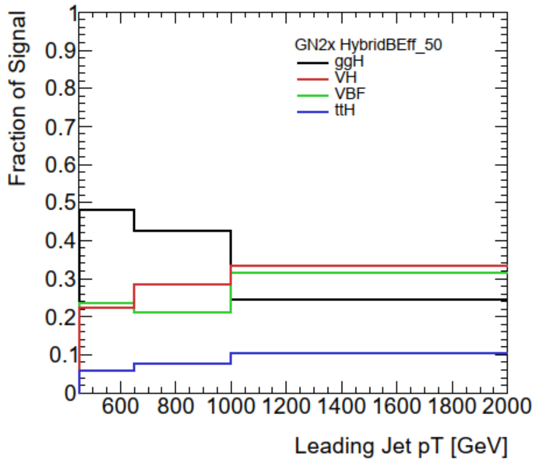

(a)

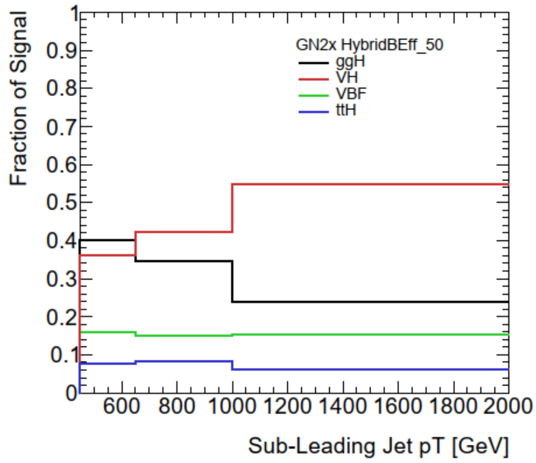

(b)

Figure 4.6: The fractional contribution of each production mode as a function of the signal candidate jet p_T to the inclusive leading (fig. 4.6a) and subleading (fig. 4.6b)) signal regions.

The background is a monotonically falling non-resonant QCD spectrum with contributions from Z+jets. Contrary to the previous analysis [1, 27], W+jets and $t\bar{t}$ production is rejected by the GN2X tagger (see section 4.5.4). Although the rate of the QCD interaction $g \to b\bar{b}$ is approximately 2×10^{-2}, the rate of di-jet events which produce a pair ob b quarks is 1.1×10^3 times larger than the Higgs boson production. As a result the background is important.
QCD is modeled by:

$$f_N\left(x \mid \vec{\theta}\right) = \theta_0 \exp\left(\sum_{i=1}^{N} \theta_i x^i\right) \tag{4.2}$$

where $x = (m_J - 140)\mathrm{GeV}/70\mathrm{GeV}$, θ_i are the parameters of the fit and N is the number of parameters.

The high statistics VR mass spectrum is used as an estimator of the QCD mass spectrum in the SR. When a simultaneous fit is performed on the SR and VR, the above function is multiplied by a transfer function t_M, in order to account for differences in the QCD spectrum of the two regions. The transfer function is defined as:

$$t_M\left(x \mid \vec{\theta}\right) = \left(1 + \sum_{i=1}^{M} \theta_i x^i\right) \tag{4.3}$$

where x and θ_i, are the same as before. A simultaneous fits on SR and VR can be found in section 6.9.

4.5 Event Reconstruction

4.5.1 Triggers

The analysis uses unprescaled HLT single large-R jet triggers, using p_T and mass offline thresholds (with exception to 2015 and 2016 where only p_T cut was applied). With introducing the mass threshold and increasing the p_T cut, triggers account successfully the detector changes over the data taking years. The additional mass cut offers the ability to use a lower p_T jet cut. The trigger chains we consider with and without mass cut (at 45 GeV) have a p_T cut of 420 and 460 GeV respectively. The trigger chain performance was studied as a function of large-R jet mass and p_T separately for each data taking years. As an example, the performance plot of the 2018 HLT trigger is provided in figure 4.7.

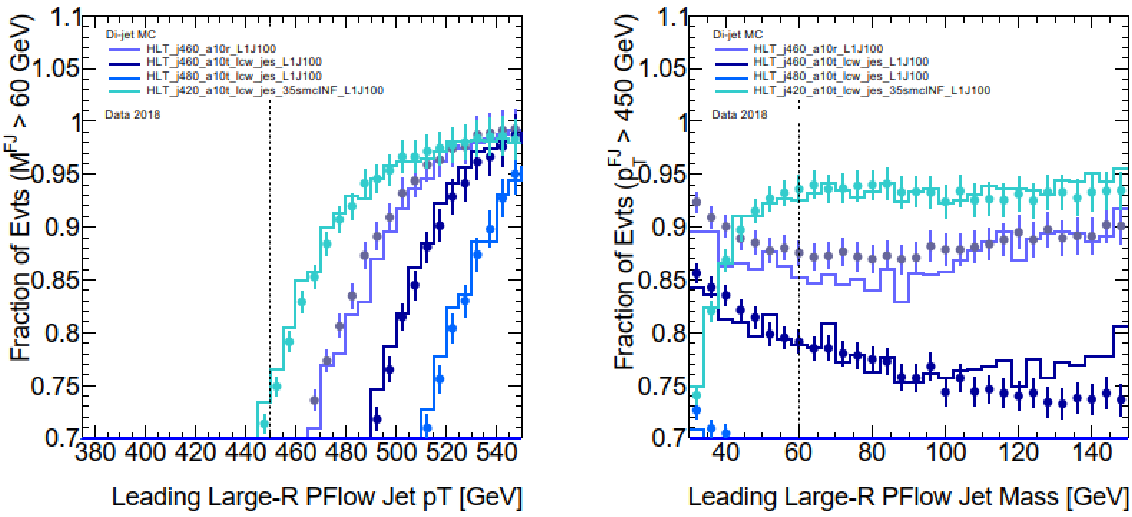

(a) (b)

Figure 4.7: Efficiency of the High Level Trigger, for Run 2 2018 data (points with error bars) and simulation (histograms) as a function of large-R jet p_T (4.7a) and PFlow mass (4.7b).

4.5.2 Hadronic Jets

The reconstruction of the candidate Higgs boson, is performed using hadronic jets, which are Unified Flow Objects (UFOs) [93]. These are based on a combination of particle-flow objects and calorimeter clusters [94], encompassing both charged and neutral components to ensure optimal performance across the broad kinematic range relevant to the analysis. Jet clustering is carried out using the anti-kT algorithm [95], with a radius parameter $R = 1.0$, as implemented in the FastJet framework [96]. In the context of this study, such jets are referred to as “large-R” jets and provide effective containment of the di-quark system originating from the decays of Z and H bosons within the transverse momentum range of interest, i.e. $p_T > 450\,GeV$ Contributions from pile-up and underlying event activity are mitigated using a grooming procedure based on the Soft-Drop algorithm.

4.5.3 Muon reconstruction

Muons have an average life time of $2.2\mu s$, corresponding to an average distance before decaying of $\langle c\tau \rangle = 658m$ [32]. As a result they can travel outside our detector and they do not stop at the calorimeters (through the production of EM or hadronic showers). Hence they leave signatures in the ID and the MS. We use Combined muons (CB), which are reconstructed by matching ID tracks to MS tracks and performing a combined track fit. Energy losses in the calorimeters are also taken into account. More information on the CB process as well as other reconstruction methods can be found in [97].

4.5.4 Flavour Tagging

Identification of high p_T large-R jets containing b quarks is crucial for our analysis. This process is called flavour tagging and will be performed by a new algorithm named GN2X. In addition GN2X results also in suppression of QCD background and removal of W and top peaks. In order to integrate this helpful tool into our analysis, a challenging calibration year by year (or MC campaign by MC campaign) is required.

GN2X is an new algorithm, developed to identify large-R jets originating from boosted Higgs bosons and decaying into $b\bar{b}$ or $c\bar{c}$ [98]. The present study utilizes version 2 Likelihood Log Ratio of GN2X, symbolized as GN2Xv02LLR. The identification of b- or c- hadron decays is achieved through charged particle tracks located within the large-R jet. GN2X uses a transformer neural network architecture [99], presenting an improved performance over the previously used taggers [100], which were implemented on a feed-forward architecture network. The inputs of GN2X base model are large-R jets and tracks. Specifically the set of parameter provided is: three for the large-R jet (mass,η, p_T) and twenty for each track (for a complete list please consult [98]). Approximately 100 tracks are fed to the network, of which on average 20 are associated to Hbb jets.

Efficiency is of great importance in the assessment of the algorithm's performance. It is defined as the fraction of Hbb jets that are correctly identified, relative to the total number of such jets, while Hcc, top, and QCD jets are considered background processes. Another way to access the taggers performance over Hbb jets, is to study the rejection of Hcc, top and QCD jets for a constant Hbb efficiency.
The discriminant of GN2X is defined as:

$$D_{\mathrm{Hbb}}^{\mathrm{GN2X}} = \ln\left(\frac{p_{\mathrm{Hbb}}}{f_{\mathrm{Hcc}} \cdot p_{\mathrm{Hcc}} + f_{\mathrm{top}} \cdot p_{\mathrm{top}} + (1 - f_{\mathrm{Hcc}} - f_{\mathrm{top}}) \cdot p_{\mathrm{QCD}}}\right) \tag{4.4}$$

where $p_{Hbb}, p_{Hcc}, p_{top}, p_{QCD}$ are probability scores generated by the neural network, representing the likelihood a jet under study being Hbb, Hcc, top or QCD respectively. Additionally, f_{Hcc},f_{top} are set for our analysis to $f_{Hcc} = 0.02$,$f_{top} = 0.25$ and describe the relative weights of p_{Hcc}, p_{top} to p_{QCD}, respectively. A threshold value of $D_{\mathrm{Hbb}}^{\mathrm{GN2X}}$ is considered, so as to achieve a desired efficiency. For every jet under study the algorithm calculates the discriminant and in case it is larger than the threshold value the jet is considered tagged.

A Working Point (WP) is established when imposing a requirement to the Hbb discriminant to provide a constant tagging efficiency as a function of the large-R jet mass on di-jet QCD background events. This ensures the shapes of the mass distributions for SR and VR are not affected by the action of GN2X. WP are defined separately for each p_T bin and for the leading/subleading regions, resulting in six different WP definitions per MC campaign or data taking year.

Apart from identifying the b quarks in our signal, GN2X offers (as already mentioned) the advantage of reducing the overwhelming QCD background. This can be seen in figure 4.8, where after flavour tagging the background is manageable and the analysis of signal is easier.

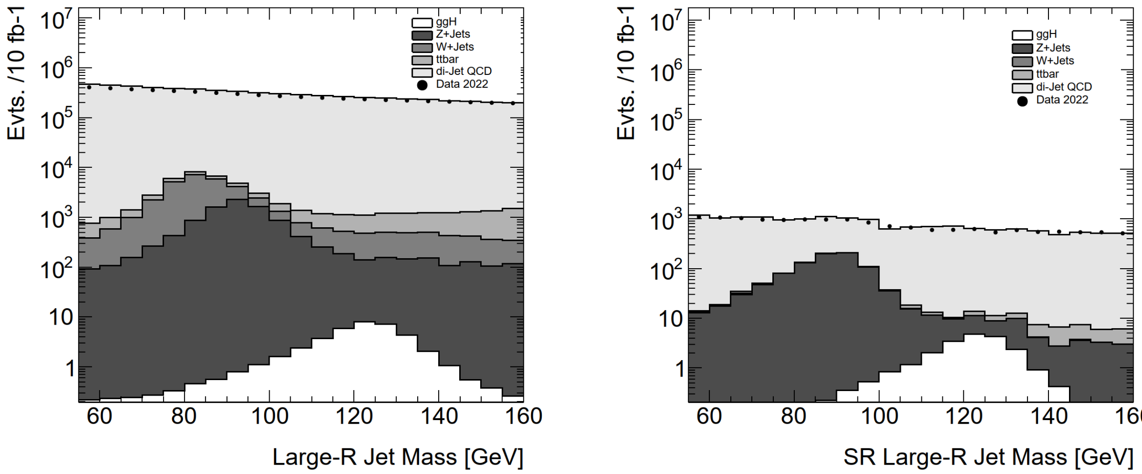

(a) (b)

Figure 4.8: Invariant mass distributions of 2022 data (points) and MC events (histograms) before (fig. 4.8a) and after (fig. 4.8b) flavour tagging is performed. The dominant QCD background (light gray), is significantly reduced after the flavour tagging.

4.6 B tagging efficiencies

We begin our study, evaluating the b tagging efficiencies of four GN2X versions; GN2Xv01, GN2Xv02, GN2Xv01LLR, GN2Xv02LLR. An MC (2022-like) simulation sample (for Hbb and Zbb) is used and the events are weighted using integrated luminosity $L_{int} = 50\,\text{fb}^{-1}$. Finally a constant WP, ”HybridQCDEff_002” is selected here. The study is performed on both Hbb and Zbb samples and the results are presented in figures 4.9, 4.10 and in tables 4.3, 4.4.

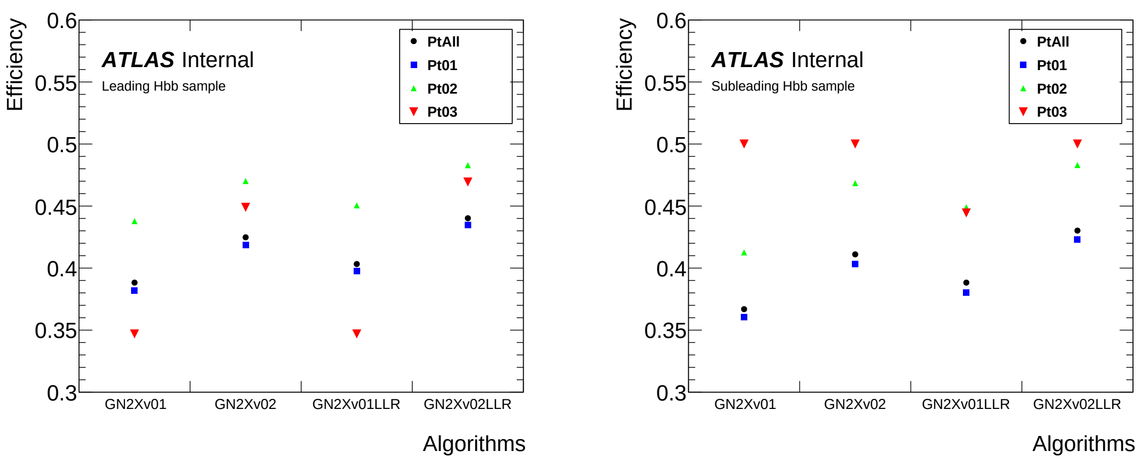

(a) (b)

Figure 4.9: B Tagging efficiencies for different GN2X versions applied on Hbb MC sample and on all p_T bins. Figure 4.9a refers to SRL and figure 4.9b refers to SRS.

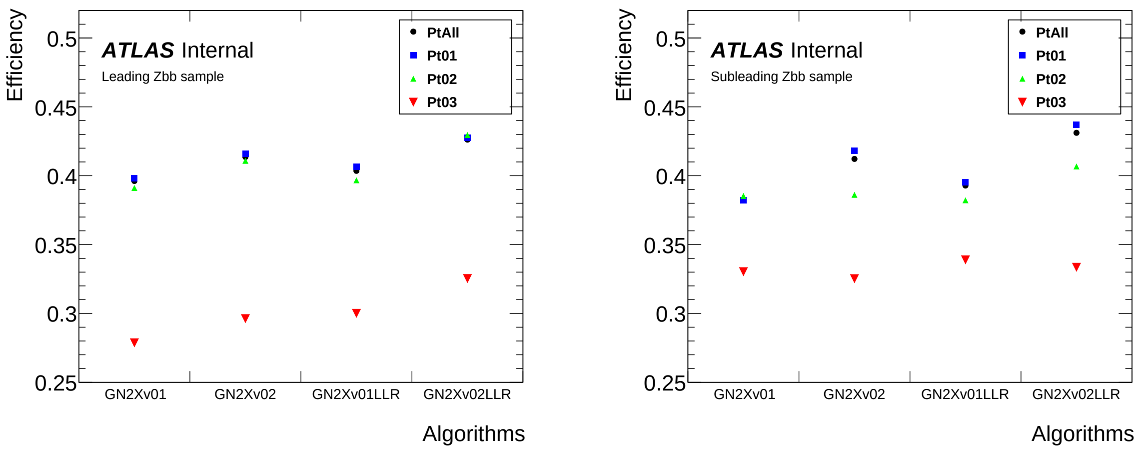

(a) (b)

Figure 4.10: B Tagging efficiencies for different GN2X versions applied on Zbb MC sample and on all p_T bins. Figure 4.10a refers to the SRL and figure 4.10b refers to the SRS.

Algorithm	p_T^{all}		p_T^{01}		p_T^{02}		p_T^{03}	
	SRL	SRS	SRL	SRS	SRL	SRS	SRL	SRS
GN2Xv01	0.388	0.367	0.382	0.361	0.438	0.413	0.347	0.500
GN2Xv02	0.425	0.411	0.419	0.403	0.470	0.468	0.449	0.500
GN2Xv01LLR	0.403	0.388	0.398	0.380	0.451	0.449	0.347	0.444
GN2Xv02LLR	0.440	0.430	0.435	0.423	0.483	0.483	0.469	0.500

Table 4.3: B tagging efficiencies for different GN2X versions applied on Hbb MC sample (SRL and SRS) across all p_T bins. The WP used is `HybridQCDEff_002`.

Algorithm	p_T^{all}		p_T^{01}		p_T^{02}		p_T^{03}	
	SRL	SRS	SRL	SRS	SRL	SRS	SRL	SRS
GN2Xv01	0.396	0.382	0.398	0.382	0.391	0.385	0.279	0.330
GN2Xv02	0.414	0.412	0.416	0.418	0.411	0.386	0.296	0.325
GN2Xv01LLR	0.404	0.393	0.406	0.395	0.397	0.382	0.300	0.339
GN2Xv02LLR	0.426	0.431	0.428	0.437	0.430	0.407	0.325	0.333

Table 4.4: B tagging efficiencies for different GN2X versions, applied on Zbb MC sample (SRL and SRS) across all p_T bins. The WP used is `HybridQCDEff_002`.

From the above tables and the corresponding plots we can observe that efficiencies at the Zbb sample are slightly higher than those at the Hbb sample, with an exception at p_T^{03} bin. Focusing on the Hbb sample, it is evident that in p_T^{all} and p_T^{01} (in which GN2X which has similar performance), slightly improved tagging is presented in the SRL than the SRS. Furthermore in all versions and for both SRL and SRS, p_T^{02} scores higher than p_T^{all}, p_T^{01}. Finally, the behavior of p_T^{03} is erratic; important increment is presented by the v02 versions in the SRL, while in the SRS a much higher efficiency from all other p_T bins is outlined. We now turn our attention to the Zbb sample. p_T^{all}, p_T^{01}, and p_T^{02} exhibit similar efficiencies, which are slightly higher in the SRL compared to the SRS. In contrast, p_T^{03} shows lower efficiency than the other p_T bins, with higher values observed in the SRS than in the SRL. Finally, as mentioned above our analysis has decided to use the GN2Xv02LLR, which has improved performance from the previous version GN2Xv01 (and GN2Xv01LLR). In the inclusive p_T bin an efficiency of approximately **0.42 - 0.44** is achieved regardless the sample.

As already mentioned, the study conducted so far, is based on MC samples which simulates Run 3, 2022 conditions. However, detector response changes over the years, creating the need to extend our study. Radiation damage is an important factor for the change of the detector response. Unfortunately this effect, despite having great importance, it was not included in MC campaign for Run 2. Hence, it is necessary to generate updated MC samples corresponding to Run 2, including this radiation damage (MCRad samples). Figure 4.11, presents the b tagging efficiency and figure 4.12 presents the tag rate across the different data taking years. Variations from year to year, can be absorbed by appropriately tuning the WP for each data taking year and MC campaign. MCRad samples are still not produced for 2017 and 2018, hence the corresponding bins are empty.

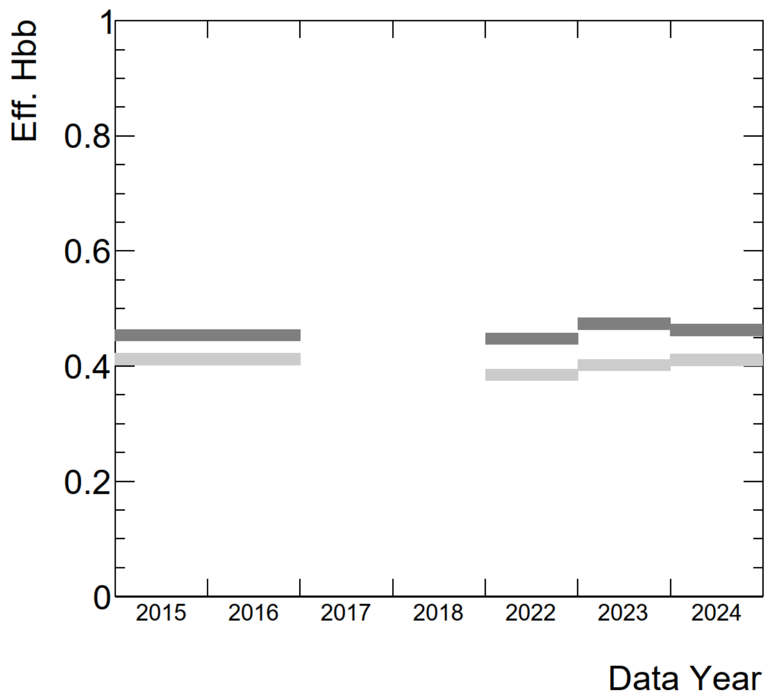

Figure 4.11: Efficiency for tagging leading (dark gray) and sub-leading (light gray) large-R jets matched to Higgs bosons decaying into $b\bar{b}$ pairs as a function of the corresponding data year of the different MC campaigns. The GN2X working point is tuned at an efficiency of 0.2% separately for each MC campaign. This plot demonstrates the stability of the performance on signal events when WPs are tuned year-by-year on the corresponding MC samples. 2017 an 2018 MCRad samples are still under production.

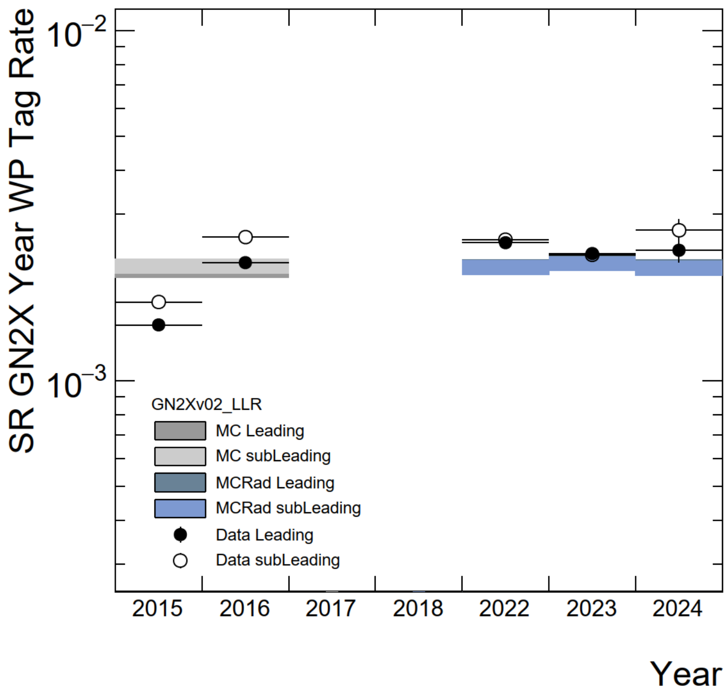

Figure 4.12: GN2X tagging rate for candidate jets as a function of the year of data taking in data (points) and simulation (colorful bands). 2017 an 2018 MCRad samples are still under production.

Finally, we should mention that new flavor tagging tools rely on low level information from hit pattern and pixel response. Hence a calibration is required focusing on the performance of tracking detectors, as well as on time granularity accounting for changes in the operational conditions. This calibration is based on two major parts: calculation of flavour tagging systematics from MC variations and calculation of flavour tagging scale factors from Zbb yields. This topic will not be explored further, as it is not central to the objectives of this thesis.

4.7 Study of the p_T^{rel}

Another part we are interested to study is the distribution of muons against their relative p_T to VR jets which are associated with (p_T^{rel}). The p_T^{rel} is defined as the p_T of the muon projected to the axis of the VR jet. A mathematical expression according to [101], is:

$$p_T^{\mathrm{rel}} = \left\|\vec{p}_\mu \times \vec{u}\right\|, \quad \text{where} \quad \vec{u} = \frac{\vec{p}_{\mathrm{jet}} + \vec{p}_\mu}{\left\|\vec{p}_{\mathrm{jet}} + \vec{p}_\mu\right\|}. \tag{4.5}$$

The shape of the p_T^{rel} distribution depends on the parent particle of the muon, giving the opportunity to further study the b tagging efficiency as in [101]. This is the reason the study will distinguish, the jets containing b hadrons and the jets not containing b hadrons, based on the truth level information of our MC samples. We believe a priori that muons associated to jets containing b hadrons will have a harder (i.e hider and more displaced from zero) p_T^{rel} distribution, in comparison to muons associated to jets containing no b hadrons. Additionally distributions, will shift to higher p_T^{rel} values as the muon p_T cut increases, will present a smaller maximum value (as less muons pass the selection criteria) and will also get wider, for both cases (jets containing/not containing b hadrons).

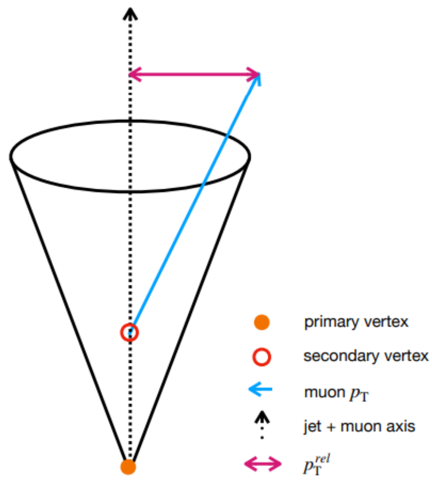

Figure 4.13: Graphical representation of a jet cone containing a b hadron decaying semileptonically at the secondary vertex. The momentum of the muon projected to the transverse to the jet axis, corresponds to p_T^{rel} of the muon [101]. The smaller the ΔR of the muon to the jet, the smaller is the p_T^{rel}.

The idea, it to study the p_T^{rel} of muons, before and after flavour tagging is applied, for jets containing/not containing b hadrons. In case these distributions are not affected by the b tagger, muon p_T^{rel} will be a good discriminant in order to perform a calculation of the b tagging efficiency (following the method of [101]). Additionally, in this case, it can also be used to evaluate the $b\bar{b}$ content of the QCD background. We begin working on the Hbb sample evaluating the muon p_T^{rel} for different muon p_T cuts, before flavour tagging. The diagrams are provided in figure 4.14, 4.15. Similar results are obtained for the Zbb sample.

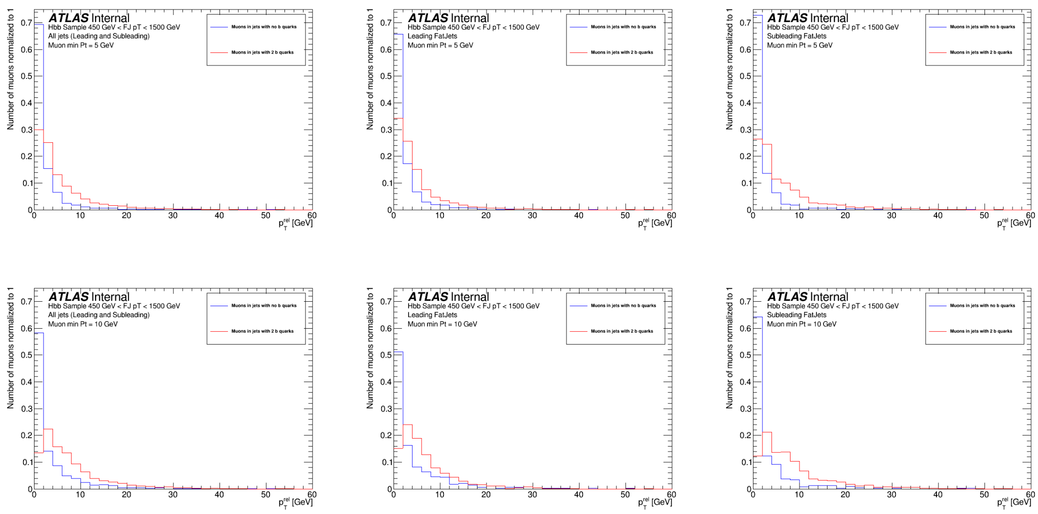

Figure 4.14: Distributions of muon p_T^{rel} for Hbb jets: All jets (left), SRL jets (middle) and SRS jets (right). Each row corresponds to a different muon p_T cut: 5, 10 GeV, from top to bottom. The blue histograms represent the jets non containing b quarks, while the red histograms the jets containing two b quarks.

Figure 4.15: Distributions of muon p_T^{rel} for Hbb jets: All jets (left), SRL jets (middle) and SRS jets (right). Each row corresponds to a different muon p_T cut: 20, 30, 40, 50, 60 GeV, from top to bottom. The blue histograms represent the jets non containing b quarks, while the red histograms the jets containing two b quarks.

The anticipated behavior discussed in section 4.7 is presented on all plots. It is evident that the width of the distributions increases and their maximum value decreases as the muon p_T cut increases. Finally the distributions shift to higher p_T^{rel} values (the MPV gets larger). There is a clear difference for a given p_T cut, between the distributions for the jets not containing b quarks and for the jets that do contain 2 b quarks. We can take advantage of this fact, to further study the efficiency of the b-tagging algorithms used in our analysis.

After examination, the muon p_T cut is selected at 10 GeV. For this cut, the distributions of all jets (leading and subleading) for the Hbb sample, before and after the flavour tagging are presented in figure 4.16.

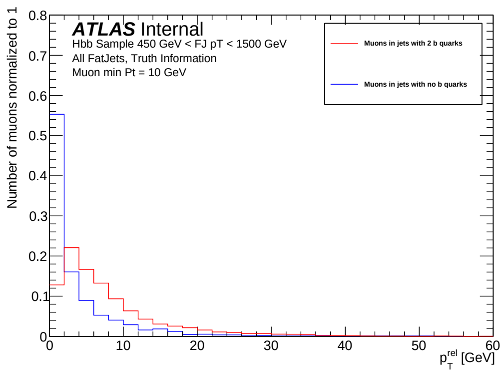

(a)

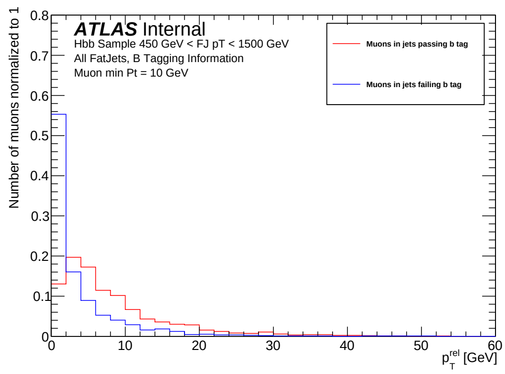

(b)

Figure 4.16: Muon p_T^{rel} distributions before (left) and after (right) flavour tagging for the Hbb sample using 10 GeV cut on the muon p_T. Blue histograms represent jets with no b quarks and red histograms jets with two b quarks.

The result is very promising as the distributions remain unchanged after the flavour tagging is applied. Muons are not affected by the GN2X tagger and this is depicted in their p_T^{rel}. Hence, this quantity is indeed appropriate in order to study the b tagging efficiency.

We expand our study for a QCD MC sample. Similarly we apply 10 GeV cut on the muon p_T^{rel} and use GN2Xv02. Please note jets will now be separated in three categories, according to the number of b quarks they contain: zero, one and two.

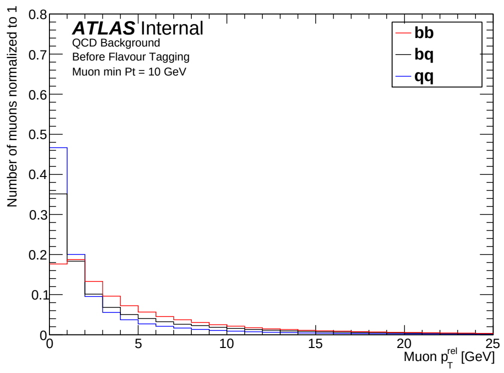

(a)

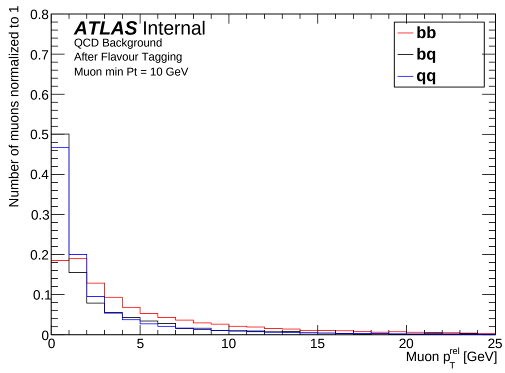

(b)

Figure 4.17: Muon p_T^{rel} distributions before (left) and after (right) flavour tagging for the QCD background using 10 GeV cut on the muon p_T. Blue histograms, represent jets with no b quarks, black with one b quark and red with two b quarks.

It is observed that bb has harder distribution from bq and qq. Distributions for all three jet categories remain the same before and after the flavour tagging. As a result muon p_T^{rel} is a good quantity also to examine the $b\bar{b}$ content in the QCD background. This is still a preliminary result and the method will be soon implemented into our analysis. Performing fits on these distributions is the final step.

Chapter 5

Study of H and Z Mass Resolution

When statistical fits are performed on data and MC, the extracted signal strengths, rely on the width of the MC invariant mass distributions, which is represented by the resolution. Therefore, studying and improving the resolution is crucial, as it directly impacts the quality of our results. We begin this chapter describing the basic quantities we use to access the resolution of mass and p_T distributions. Subsequently, we investigate the mass resolution using different Working Points of the GN2X tagger. The study is then further extended across various MC campaigns, to examine the Jet Mass Resolution (JMR) over the different data taking years, these MC simulate.

5.1 Quantity Definitions

During the analysis of MC samples, histograms corresponding to the SRL and SRS regions are initially populated. Subsequently, Gaussian fits are performed in order to extract relevant observables and derive quantitative measurements. Let us consider the Gaussian (normal) distribution, expressed by the probability density function (pdf) as:

$$f(x) = \frac{1}{\sqrt{2\pi}\,\sigma} \exp\left(-\frac{(x-\mu)^2}{2\sigma^2}\right) \tag{5.1}$$

The quantities related to this distribution [102, 103], demonstrated in figure 5.1, are the following :

- **Most Probable Value (MPV):** The average value of x, given by:

$$MPV = \langle x \rangle = \int_{-\infty}^{+\infty} x f(x)\, dx = \mu \tag{5.2}$$

- **Root-Mean-Square (RMS):** The dispersion, or standard deviation σ of the function $f(x)$, whose square is expressed as:

$$RMS^2 = \sigma^2 = \left\langle (x - \langle x \rangle)^2 \right\rangle = \int (x - \langle x \rangle)^2 f(x)\, dx \tag{5.3}$$

- **Full Width Half Maximum (FWHM):** The width of the distribution measured between the two points where the function $f(x)$ reaches half of its maximum value, providing insights into the spread or resolution of the distribution. FWHM is directly connected to RMS (σ) by the expression:

$$\text{FWHM} = \sigma\sqrt{8 \ln 2} = 2.355\,\sigma \tag{5.4}$$

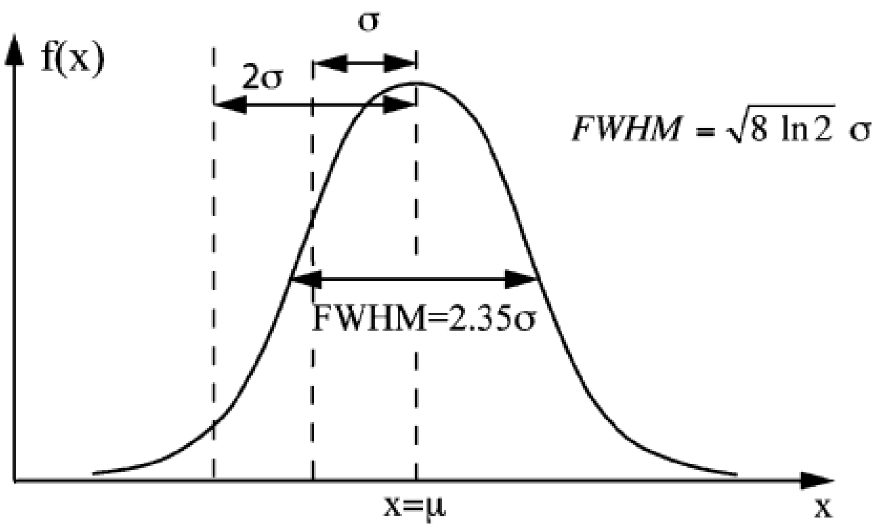

Figure 5.1: Gaussian distribution with quantities of interest marked [103].

5.2 Resolution over different Working Points of GN2X

It is crucial to understand how different WP (and efficiencies) affect our mass distributions. Once again we use the Hbb and Zbb MC samples, with integrated luminosity $L_{int} = 10\,\text{fb}^{-1}$. Utilizing PFlow masses, we obtain the following mass distributions for SRL and SRS in the inclusive p_T bin.

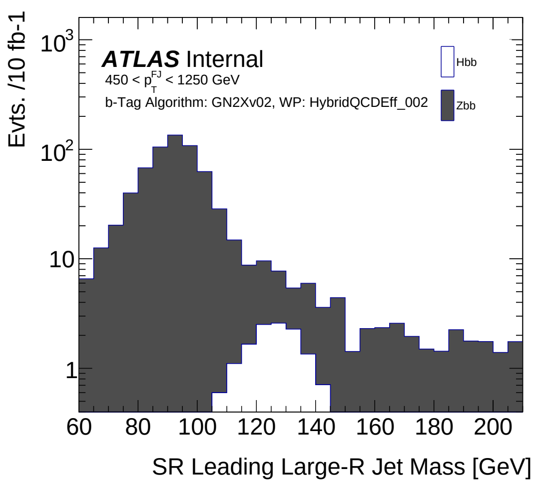

(a)

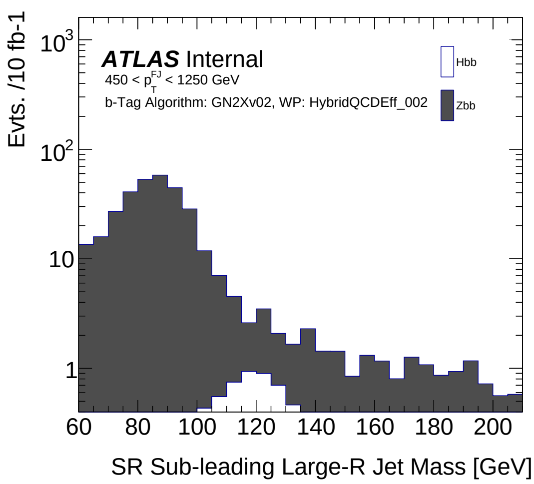

(b)

Figure 5.2: Invariant mass distributions of Hbb and Zbb jets (SRL left and SRS right) for $10\,\text{fb}^{-1}$ of MC simulation (2022-like), using PFlow masses, GN2Xv02 and Working Point HybridQCDEff_002.

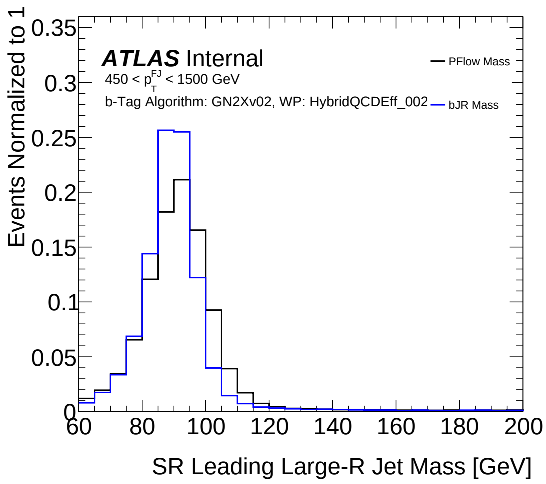

(a)

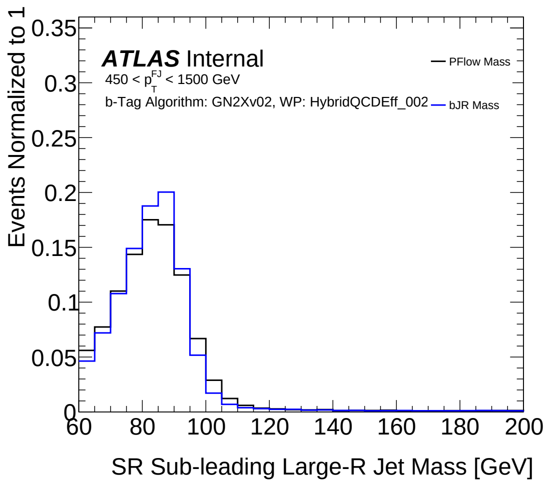

(b)

Figure 5.3: Invariant mass distributions of Zbb jets (left for SRL and right for SRS) for 10 fb^{-1} of MC simulation (2022-like), using PFlow (black) and bJR (blue) masses. The b tagging is performed with GN2Xv02 and WP HybridQCDEff_002.

The distributions of figure 5.2 present a Gaussian shape as anticipated and peaks at approximately 90 and 125 GeV which are the desired mass values for the Zbb and Hbb decay channels respectively. SRL has more events than the SRS as foreseen.

Apart from the PFlow mass (and p_T), the analysis also uses the large-R jet mass and p_T estimation given by a b jet regression (bJR) network running on top of the official large-R jet calibrated PFlow masses. The algorithm exploits the jet's kinematic features and track information, incorporating both charged and neutral constituents, in a way similar to that used by b-tagging networks. It predicts the ratio between the true and calibrated values of the transverse momentum p_T and jet mass m_J, based on training with simulated samples enriched in true b-jets. This predicted ratio is then applied as a correction to the calibrated jet to yield an improved estimate of the true jet kinematics. The model used is based on GN2X, which uses the transformer network architecture [104, 105]. Finally, we should note that the jet mass and transverse momentum p_T are regressed independently. Each regression task is handled by a different dense neural network, which takes the global jet representation as input.

For the Zbb sample, histograms for both PFlow and bJR masses, are depicted in figure 5.3. It is evident that, bJR mass distribution presents a steeper decline (as the mass increases), when compared to the PFlow mass distribution. This results in a narrower histogram, spanned around the desired MPV. The differences are greater in the SRL, than the SRS.

We wish to study the behavior of distributions, like the ones presented in figures 5.2, 5.3 under the application of different b tagging WPs. To this end, we evaluate quantities such as the FWHM, the RMS and the MPV described in section 5.1. The study focuses in the Zbb sample, however the results are similar for the Hbb channel.

In order to calculate the FWHM, RMS and MPV of a given histogram (resembling a Gaussian distribution), we develop a function. When a histogram is provided to the function, initially the half maximum value is calculated. The bins where this value is reached are located; specifically, bin1 and bin2 being the first and last bin above half maximum respectively. Then a (local) Gaussian fit around the peak value is performed in the region (center of bin1, center of bin2). The purpose of this fit is to provide a better estimation of the peak, reducing bin fluctuations of the maximum value. In case the two estimations match, the process continues; otherwise the peak value is updated and bin1, bin2 are recalculated. Moving on, with linear interpolation between $(bin1 - 1, bin1)$ and $(bin2, bin2 + 1)$ the exact values x_1, x_2, for which $f(x_1) = f(x_2) = \frac{f_{max}}{2}$, are determined. Now the FWHM is calculated straightforward as: $FWHM = x_2 - x_1$. The actual value returned by the function is the Gaussian width σ, which as mentioned in section 5.1, is given by: $\sigma = \frac{FWHM}{2.355}$. Simultaneously, a second (refined) Gaussian fit is performed at a slightly wider range than the first one. The purpose is to provide stable estimates for the RMS and MPV, which are also returned by the function.

In the plots below, all three parameters will be used. The Gaussian width extracted from FWHM refers to the sigma determined from the linear interpolation, while RMS and MPV originate from the refined Gaussian fit. For the sake of completeness we note that for an ideal Gaussian distribution, $FWHM/2.355$ and RMS returned by the above function, would have the same values. If $RMS > \frac{FWHM}{2.355}$, then the distribution has significant tales affecting the Gaussian fit (which is wider) more than the local calculation of FWHM. We choose GN2Xv02 and a working point called "HybridBEff". We define this WP for efficiencies: 10%, 20%, 30%, 40%, 50%, 60%, 69%, 77%, 85% (symbolized respectively as HybridBEff_10 etc) and we observe how the Gaussian width (σ) obtained from FWHM, the RMS and the MPV are affected, using the above WP's.

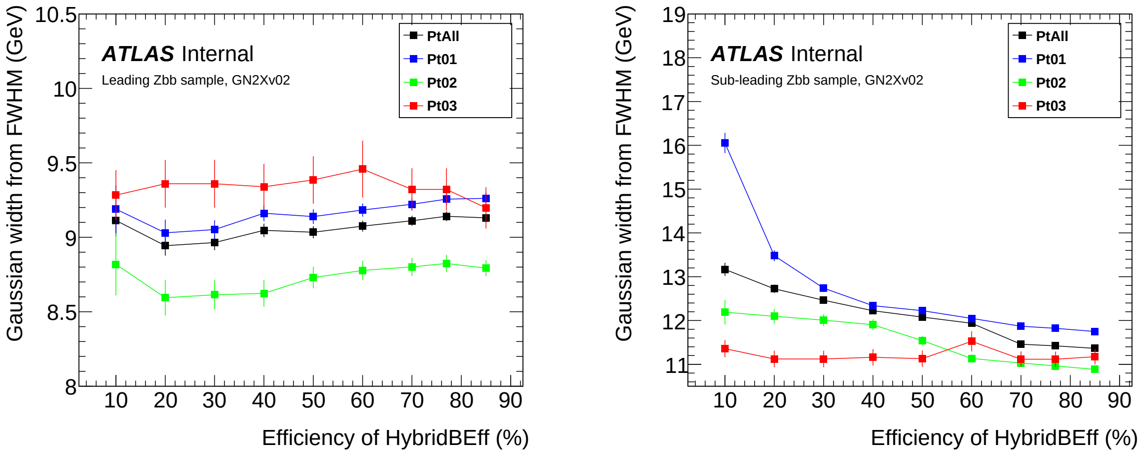

(a) (b)

Figure 5.4: Gaussian Width obtained by the FWHM for the SRL (left) and SRS (right) of the Zbb PFlow mass distributions across various efficiencies of the WP HybridBEff.

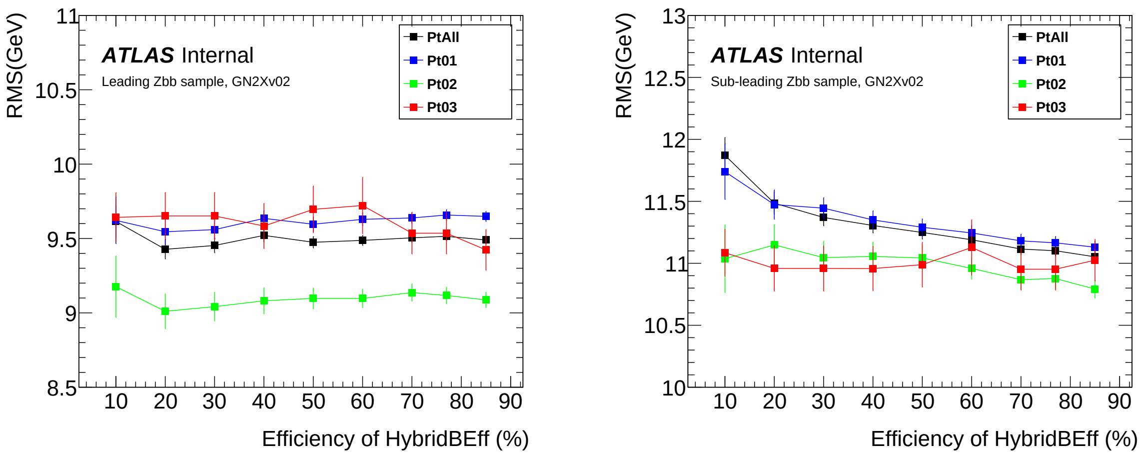

(a) (b)

Figure 5.5: RMS value obtained by the fit, for the SRL (left) and SRS (right) of the Zbb PFlow mass distributions across various efficiencies of the WP HybridBEff.

It is observed that the FWHM (fig. 5.4) and RMS (fig. 5.5) exhibit very similar values. In the SRL, the RMS is slightly higher than the FWHM, while in the SRS the opposite is true. The widths (estimated by both FWHM/2.355 and RMS) are smaller for the SRL than the SRS, as expected. Finally, for the SRL, the widths do not present fluctuations while the efficiency of the WP rises. On the other hand in the SRS, a small reduction of the widths in p_T^{all}, p_T^{01} and p_T^{02} while the WP efficiency increases is presented.

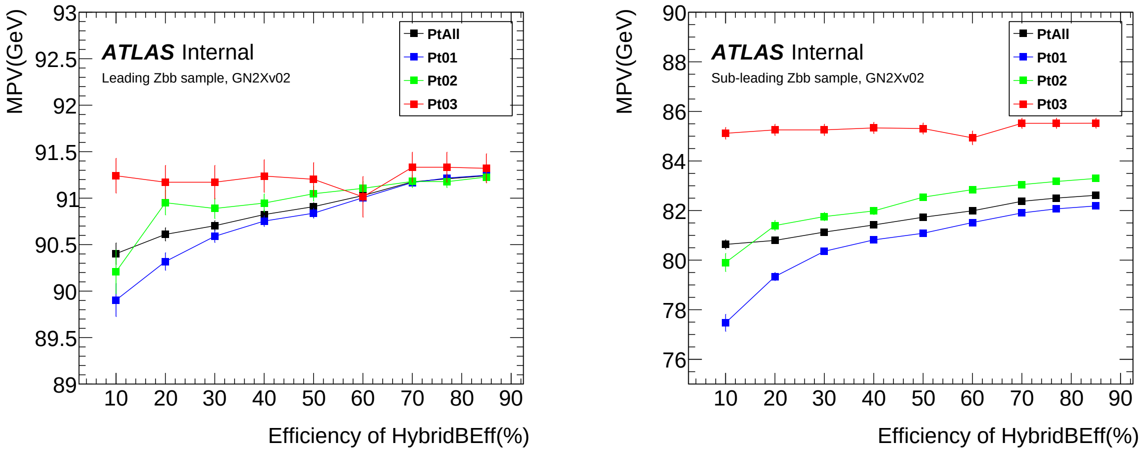

(a) (b)

Figure 5.6: MPV value obtained by the fit, for the SRL (left) and SRS (right) of the Zbb PFlow mass distributions across various efficiencies of the WP HybridBEff.

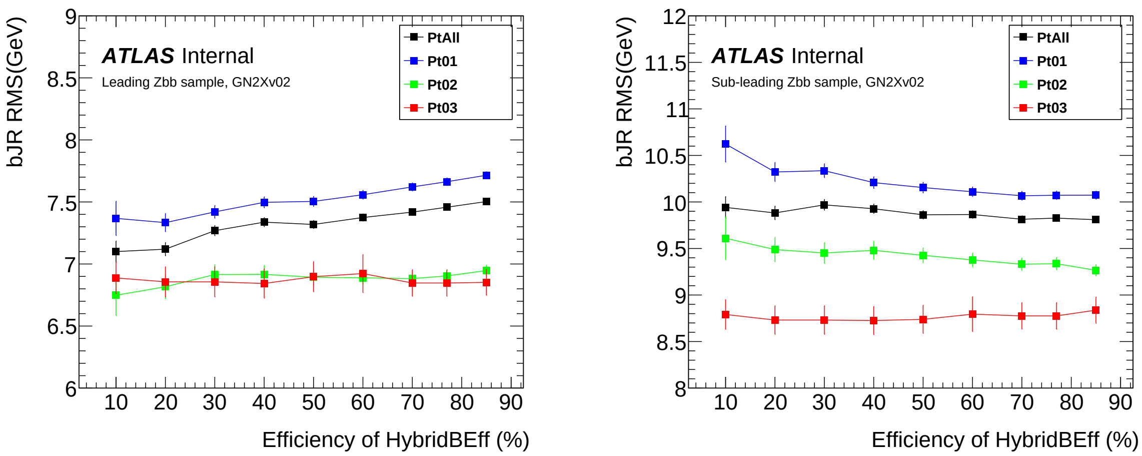

(a) (b)

Figure 5.7: RMS value obtained by the fit for the bJR mass, for the SRL (left) and SRS (right) of the Zbb mass distributions across various efficiencies of the WP HybridBEff.

It is evident we get MPV values (figure 5.6), close to 90 GeV for the SRL and 80-86 GeV for the SRS, which are appropriate for our Zbb sample. The SRL have larger MPVs than the SRS, due to semileptonic decays occurring mainly in the SRS (more in chapter 6). In both regions, the MPV increases (for all p_T bins) with WP efficiency.
Furthermore, as the relation between the FWHM/2.355 and the RMS is already pointed out, regarding the bJR mass distributions we provide only the RMS estimation. With respect to figures 5.4 and 5.5,

we observe smaller widths for the bJR masses than the PFlow masses (for both regions). Apart from p_T^{all} and p_T^{01} in the SRL which increase with the WP efficiency, stable behavior is recorded.

Beyond the aforementioned mass distributions, one can also plot the distribution of the difference between the reconstructed mass and the corresponding truth-level mass, only for the MC samples. In our ntuples this is expressed as: thisFatJet.M() - thisFatJetTruthM. The results are distributions of the large-R jets which present a mean value close to zero and are narrow (small width). This constitutes an effective way to access how accurately the jet has been reconstructed and b tagged. Ideally, we aim for distributions with MPV approximately equal to zero and with the smallest width possible. An example for the same MC Zbb sample the preceding plots refer to, is given in figure 5.8.

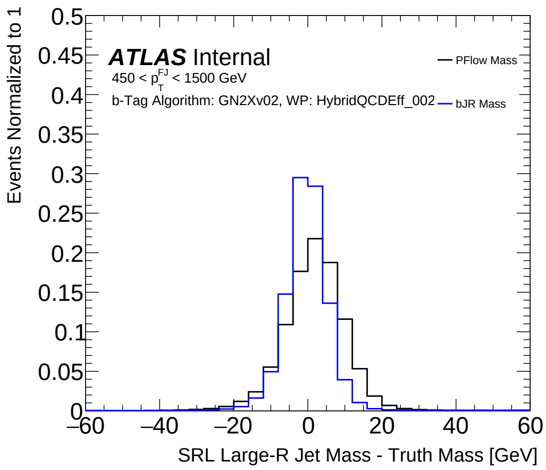

(a)

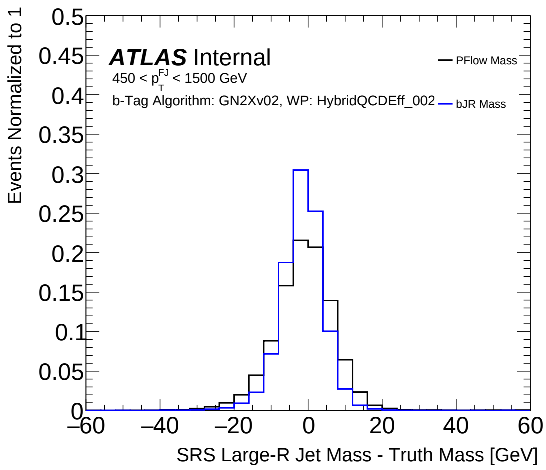

(b)

Figure 5.8: Invariant mass resolution distributions of Zbb jets (left for SRL and right for SRS) for 10 fb^{-1} of MC simulation (2022-like), using PFlow (black) and bJR (blue) masses. These distributions are obtained by subtracting the truth mass of the jet of the reconstructed jet mass. The b tagging is performed with GN2Xv02 and WP HybridQCDEff_002.

The distributions are indeed located around zero with small width (for both PFlow and bJR masses). The observations made above regarding the PFlow and bJR masses remain fully applicable here. Since the Gaussian width, RMS, and MPV exhibit the same behavior as in the initial distributions, their presentation is omitted.

Finally, three WP achieving constant QCD and Hbb efficiency and satisfactory performance (in terms of resolution and MPV) are defined in table 5.1.

WP	QCD Eff.	Hbb Eff.
QCD_001	0.001	0.330
QCD_002	0.002	0.480
QCD_005	0.005	0.675

Table 5.1: GN2X Working Points defined for the optimization of the analysis.

5.3 Resolution over the Years

Until now, our focus has been on 2022-like simulation samples. We now aim to examine how the RMS and MPV (extracted by the Gaussian fits) of our mass distributions vary across different MC campaigns corresponding to the data taking years of our analysis. The study is performed on Hbb samples, using GN2Xv02 for both PFlow and bJR masses. From each MC sample $L_{int} = 30\,\text{fb}^{-1}$ are used. In what follows, figures 5.9 to 5.12 refer to the RMS and MPV of PFlow and bJR mass distributions. Figures 5.13 to 5.16 are the corresponding for mass resolution (reco mass - truth mass) distributions. Conclusions are drawn after the plots are presented.

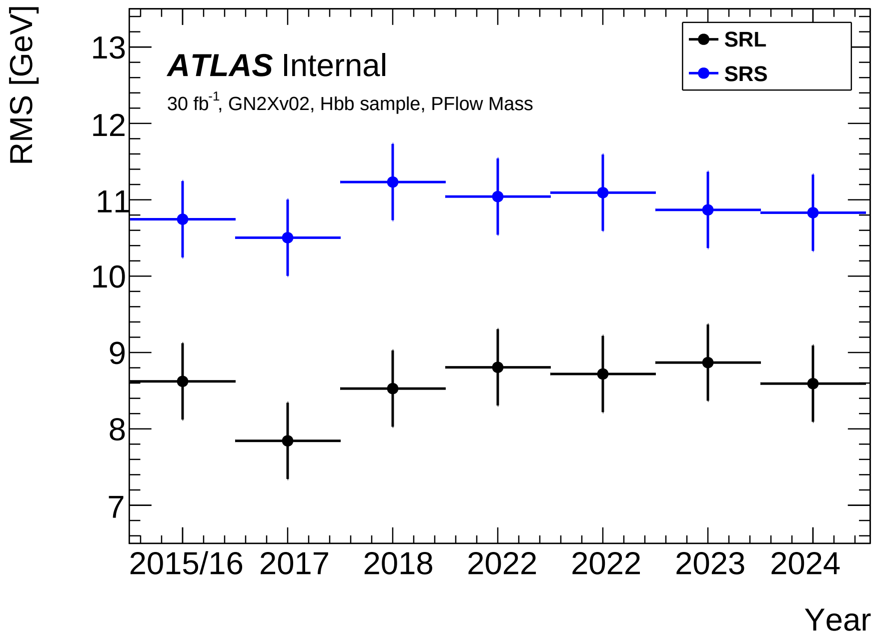

Figure 5.9: RMS of the Hbb PFlow mass (SRL and SRS) over the different MC campaigns simulating the data taking years.

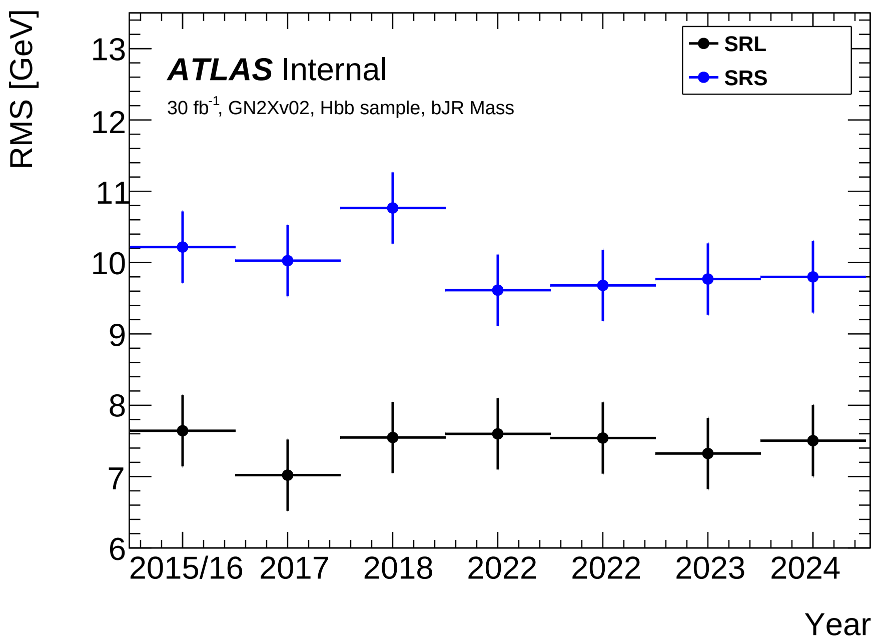

Figure 5.10: RMS of the Hbb bJR mass (SRL and SRS) over the different MC campaigns simulating the data taking years.

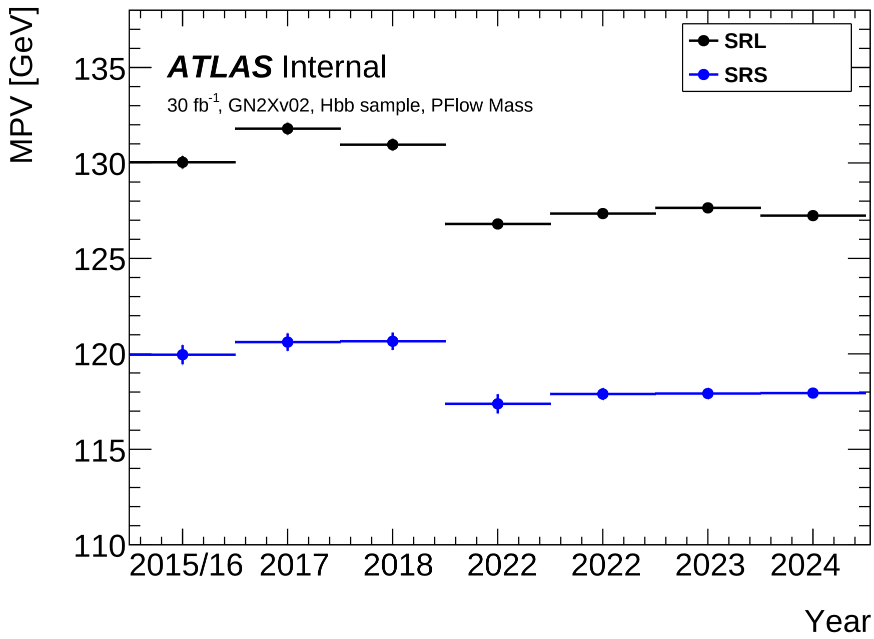

Figure 5.11: MPV of the Hbb PFlow mass (SRL and SRS) over the different MC campaigns simulating the data taking years.

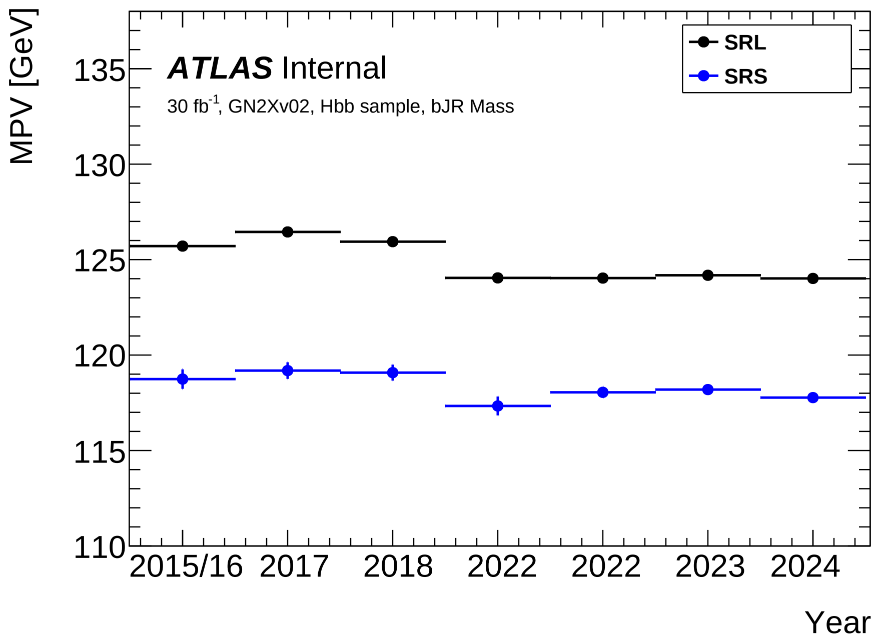

Figure 5.12: MPV of the Hbb bJR mass (SRL and SRS) over the different MC campaigns simulating the data taking years.

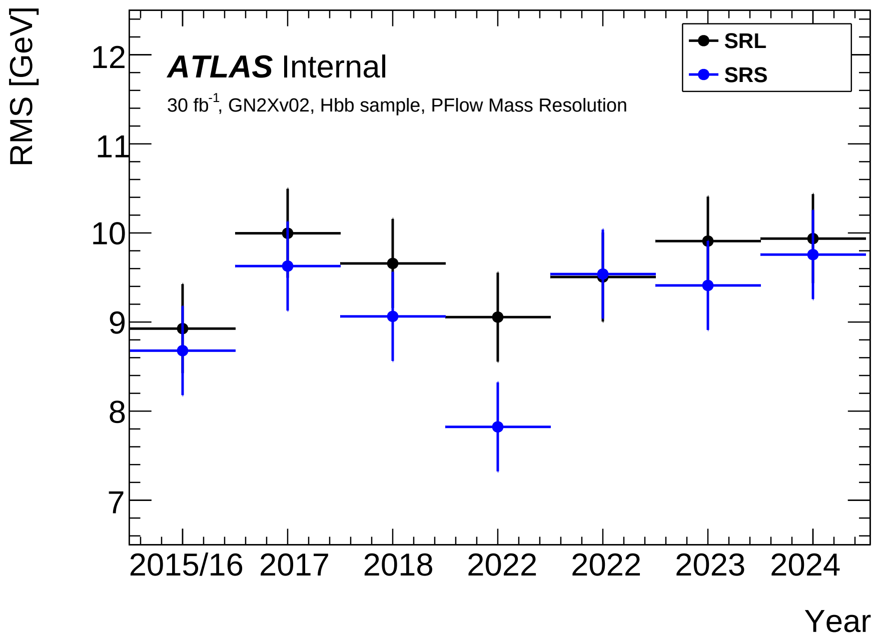

Figure 5.13: RMS of the Hbb PFlow mass resolution (SRL and SRS) over the different MC campaigns simulating the data taking years.

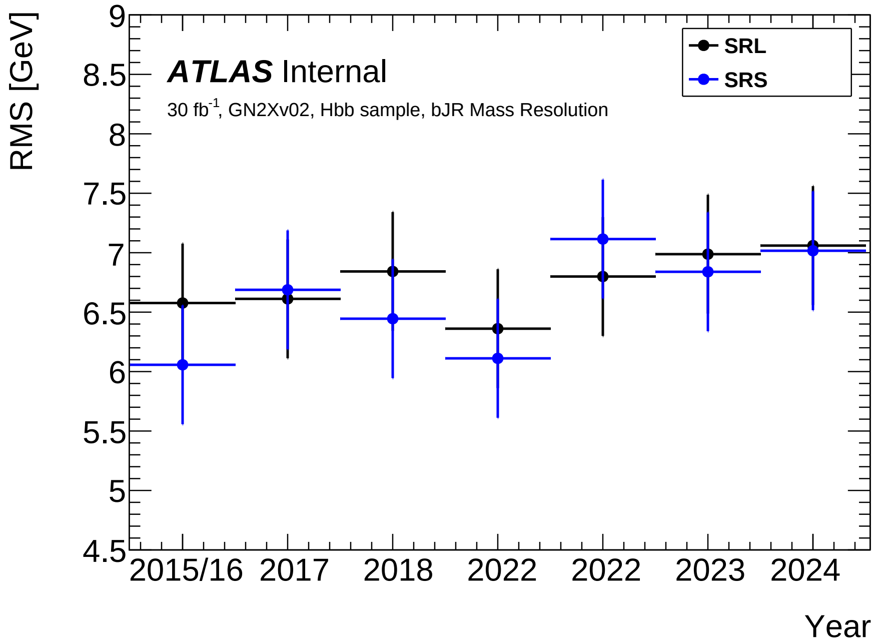

Figure 5.14: RMS of the Hbb bJR mass resolution (SRL and SRS) over the different MC campaigns simulating the data taking years.

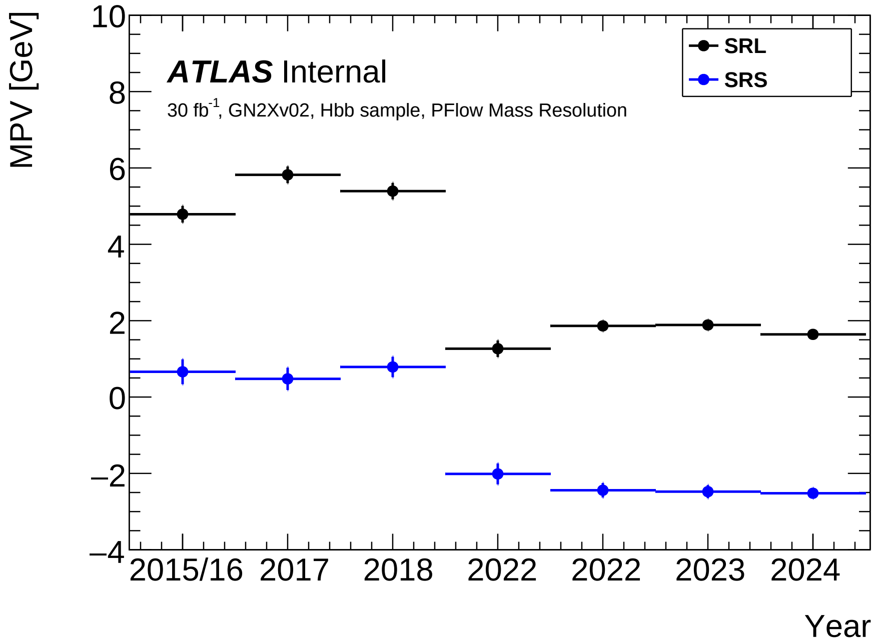

Figure 5.15: MPV of the Hbb PFlow mass resolution (SRL and SRS) over the different MC campaigns simulating the data taking years.

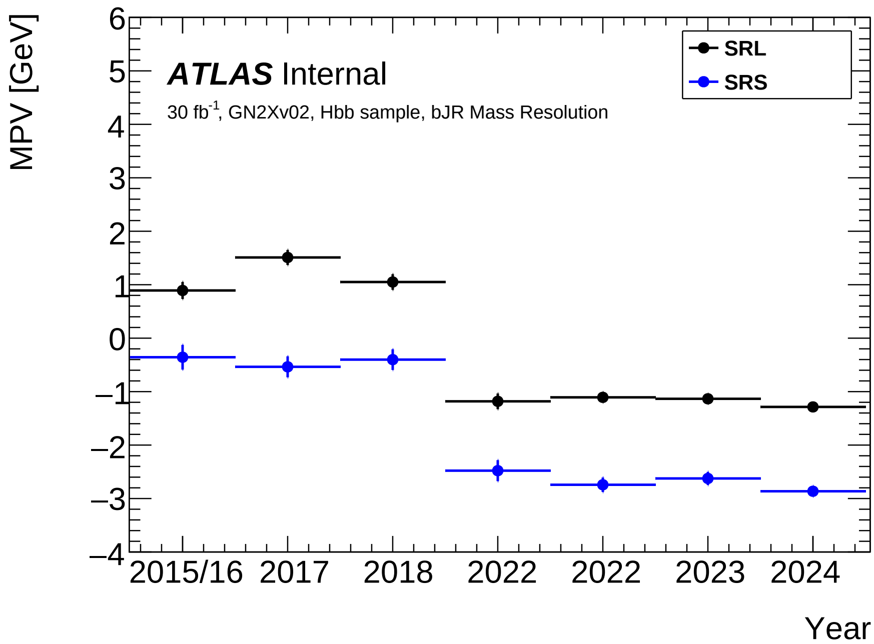

Figure 5.16: MPV of the Hbb bJR mass resolution (SRL and SRS) over the different MC campaigns simulating the data taking years.

The presented plots are of considerable interest and warrant careful examination to extract meaningful conclusions. We begin with figures 5.9 and 5.10, in which the RMS is larger for the SRS than the SRL as expected. Additionally, RMS of the mass after regression is smaller (in both regions) than the RMS of PFlow mass. Finally, the values are fairly consistent across all years. For the PFlow masses, we obtain RMS(SRL) $\approx$ 8.5GeV and RMS(SRS) $\approx$ 11GeV. On contrary for the bJR mass, it is RMS(SRL) $\approx$ 7.5GeV and RMS(SRS) $\approx$ 10GeV The same consistency is also presented by the MPV of these distributions across the different MC campaigns. As shown in figures 5.11 and 5.12 the MPV of SRL is larger (about 10 GeV) than that of SRS, for all years. This is thoroughly explained in section 6.1. After the regression the MPV of SRL decreases (from approximately 130 GeV), reaching a value of about 125 GeV which is the desired for the Higgs sample. In the SRS only slight changes occur in the MPV between PFlow and bJR masses, with values being around 120 GeV.

Generally, the same conclusions are true for the resolution (reco mass - truth mass) distributions. Stability is present in all figures 5.13, 5.14, 5.15 and 5.16. It is important to note, that RMS of SRL and SRS are very similar for both PFlow and bJR res. MPV values are correctly close to zero and have smaller differences between SRL and SRS, in bJR mass resolution (figure 5.16) than in PFlow mass resolution (figure 5.15).

Chapter 6

Muon-In-Jet Correction

Escaping muons from the calorimeters, impacts the resolution and eventually our results. In order to improve the resolution and the most probable value of our mass distributions, the Muon-in-Jet Correction (MIJ) is developed. First of all, some useful definitions are provided. Then two different methods of the MIJ correction are considered and the optimum is selected, along with the optimum muon selection criteria. The optimization is based on the Correction and Mistag Rate. Furthermore, the MIJ is tested on Hbb and Zbb MC samples (both PFlow and bJR), as well as on MC QCD multi-jet and 2022 Data, all with integrated luminosity $L_{int} = 10\,\mathrm{fb}^{-1}$. Finally, the MIJ is integrated into our analysis. A statistical fit is performed to extract the signal strength of Z (μ_Z) before and after the correction, in order to observe the improvement on the statistical uncertainty.

6.1 Need for the Correction

The dominant decay mode of the Higgs boson is $H \to b\bar{b}$, with approximately 58% branching ratio [27]. Similarly, the Z boson decay mode: $Z \to b\bar{b}$, is very important with a branching ratio of 15% [32].

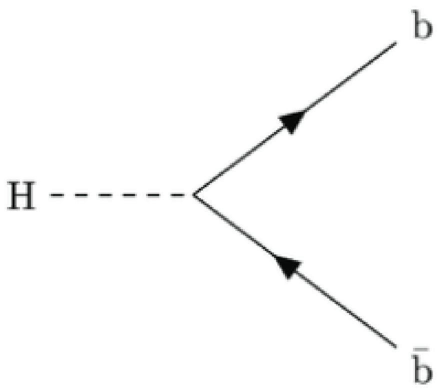

(a)

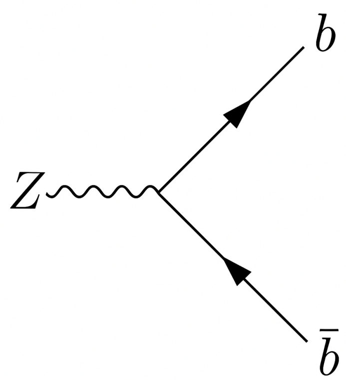

(b)

Figure 6.1: Higgs decay to $b\bar{b}$ (fig. 6.1a) and Z decay to $b\bar{b}$ (fig. 6.1b)

As a result the $b\bar{b}$ is presented in a large percentage of our samples. The b quarks can decay semileptonically with a branching ratio $BR(b \to \mu\nu X) \approx 10\%$ [106, 107], where a W boson, a charm (c) quark and neutrino are also produced [27], as shown in the following Feynman diagram:

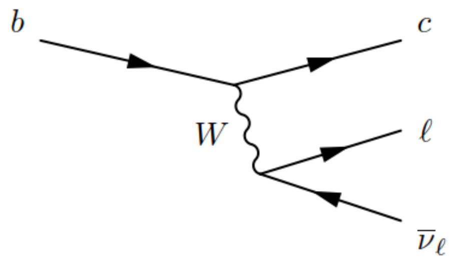

Figure 6.2: Bottom quark decaying semileptonically

Furthermore, b quarks also decay to charm quarks (one of the ways is depicted above) which also decay semileptonicaly. The branching ratio of this cascaded decay is approximately $BR(b \rightarrow c \rightarrow \mu\nu X) \approx 10\%$ [107]. In total the branching ratio of semileptonic decays from one b quark is about 20%.

The muon and the neutrino that are produced are not captured in any calorimeter and they escape (see figure 6.3).

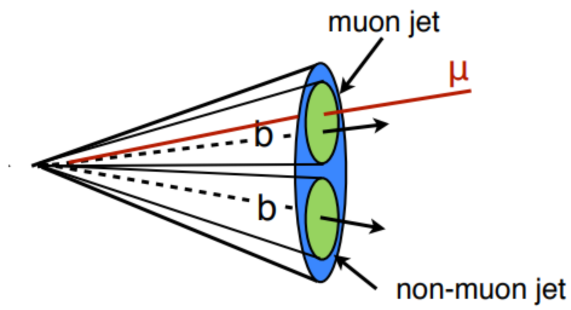

Figure 6.3: A Large-R jet with two smaller b-tagged jets and an escaping muon matching to one of the two b tagged jets. The muon needs to be matched to the jet (the large-R jet or the smaller VR jet) and the four momentum of the jet to be corrected.

As a result, the mass distribution of the jets (as well as the energy and p_T) shift to lower values and become wider. We should note that these semileptonic decays mainly occur in the SRS jets. Hence it is necessary to correct the four momenta of the jets for the escaping muons. A neutrino correction is not being considered at this time. The application of MIJ is expected to cause the mass distribution of the jet to shift to higher peaks and get narrower [1, 27]. That means a higher MPV and a smaller FWHM for the jet after the correction, compared to the values before the correction.

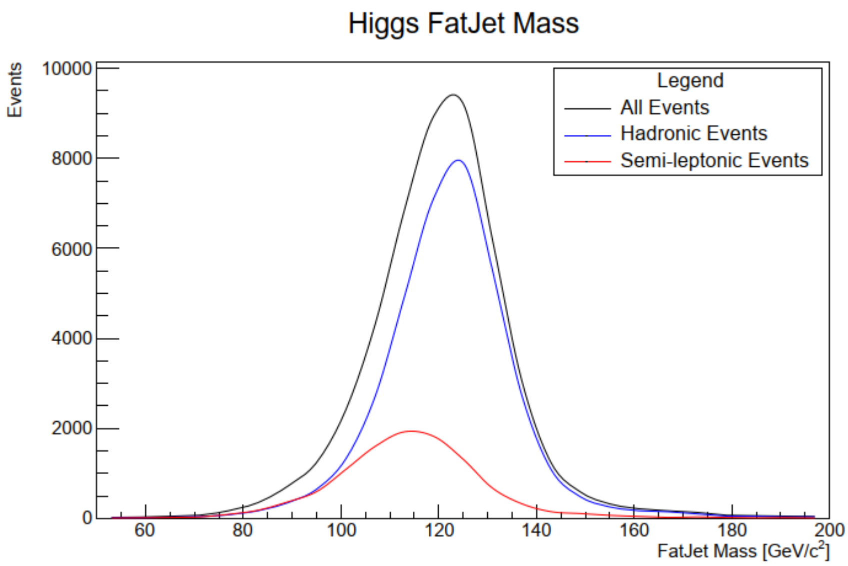

Figure 6.4: Higgs mass distribution divided in hadronic and semileptonic decays of the b quarks from the Higgs boson. Semileptonic decays present a wider distribution with a lower MPV, than the hadronic decays.

6.2 Definitions

For each jet containing muons within a Delta R (defined in equation 3.9), we apply the correction:

$$p^{\mu}_{\mathrm{J,\,corr}} = p^{\mu}_{\mathrm{J}} + p^{\mu}_{\mathrm{muon}} \tag{6.1}$$

Note: The μ here, does not represent the muon, but the indices of the four momenta vector.
Very interesting for our analysis is the Correction Rate (*CorrRate*), defined as:

$$\text{Correction Rate} = \frac{\text{Corrected large-}R\text{ Jets}}{\text{All large-}R\text{ Jets}}, \tag{6.2}$$

When a correction is applied but it should not, we are led to a mistag. The factors contributing to the mistag rate are mainly two. The first is a reconstructed muon (often refereed as reco muon) that is matched to a jet, but does not match a truth muon. The second one, is a muon that is matched to a jet but was not produced from a b (or c) quark. The reason that muons originating from a c quark are considered as a valid correction, lies in the fact that the (cascaded) decay: $b \to c \to \mu X$ is not considered a mistag. Consequently, the mistag rate is defined as:

$$\text{Mistag Rate} = \frac{\text{Corrected large-}R\text{ Jets that muon is A OR is B}}{\text{All large-}R\text{ Jets}}, \tag{6.3}$$

where A = not produced by b or c quarks and B = not truth matched. For simplicity we symbolize the mistag rate as MR which consists (as explained above) of the following two components:

$$\mathrm{MR}_1 = \frac{\text{Corrected large-}R\text{ Jets that muon is not produced by b or c quarks}}{\text{All large-}R\text{Jets}} \tag{6.4}$$

and

$$\mathrm{MR}_2 = \frac{\text{Corrected large-}R\text{ Jets that muon is not truth matched}}{\text{All large-}R\text{Jets}} \tag{6.5}$$

The errors for both the CorrRate and the MR, are calculated using the binomial formula, which is appropriate for trials with large statistics, were a cut is applied [108].

$$\sigma_f = \sqrt{\frac{f(1-f)}{N_{\text{tot}}}} \tag{6.6}$$

where f is the corresponding rate and N_{tot} the total number of large-R jets.

6.3 Method

Our analysis considers two potential methods of implementing the MIJ correction. The first relies on large-R jets and the second on Variable-Radius (VR) jets associated with the large-R jets. The second method was followed in the previous published analysis [1, 27].

6.3.1 MIJ with Large-R jets

We first read the files and store the reconstructed and the truth muons to appropriate vectors. Initially we apply a cut on the p_T of the reconstructed (reco) muons. The selection of the cut must be determined after an optimization analysis is conducted. Then we try to match the muons to a large-R jet using:

$$\Delta R < 0.8 \tag{6.7}$$

If this criteria is satisfied we apply the correction given by equation 6.1, otherwise no correction takes place. Then, (for the MC samples only), we can also match the reco muons to truth muons, using:

$$\Delta R < 0.2 \tag{6.8}$$

and

$$\left| \frac{p_{T,\text{reco}} - p_{T,\text{true}}}{p_{T,\text{true}}} \right| < 0.2 \tag{6.9}$$

If the above two criteria are not satisfied this is taken into consideration by the MR_2. Finally, taking advantage of our ntuple's structure we can study the object from which our muon originated. The branch (of our ntuple tree) that provides us this information is called ”leptonParentPdgId”. According to [32] the codes for the b and c quarks are 5 and 4 respectively. If the ”leptonParentPdgId” has another value (for example it has sometimes the code 15 which represents the tau lepton), the correction is false and that is accounted for in the MR_1. It is important to point out that even a false correction is recognized, we still apply it in the MC samples. The reason behind this is that in real data we do not have a way to recognize false corrections. We simply search for these mistags in order to have an estimation on the MR and be able to optimize the correction.

6.3.2 MIJ for the VR jets

Each large-R jet contains two or more VR jets (a jet with less than two VR jets cannot pass the jet selection criteria, see section 4.3).

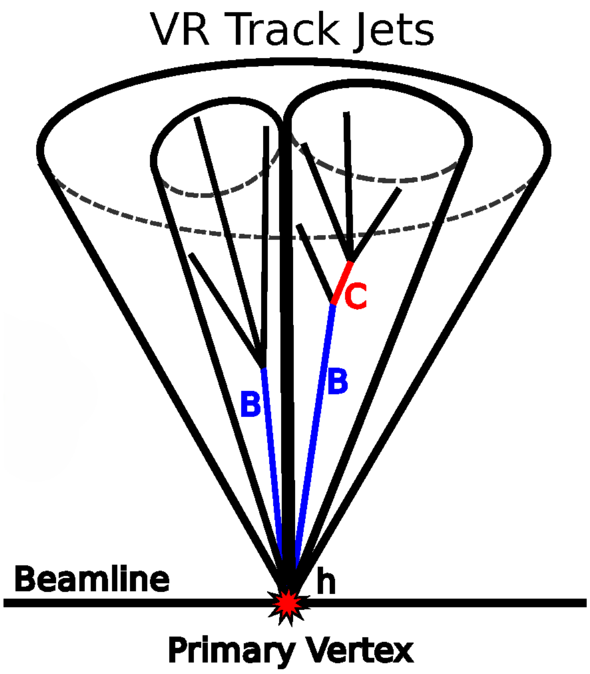

Figure 6.5: A Large-R jet containing two VR jets.

The (effective) radius of the VR jet varies with the jet p_T, as:

$$R \to R_{\mathrm{eff}}(p_{\mathrm{T}}) = \frac{\rho}{p_{\mathrm{T}}} \tag{6.10}$$

where ρ is a parameter (expressed in GeV) defining how fast a VR jets shrinks in correlation with p_T. It is evident that VR jets shrink as p_T increases [109]. The VR jet is characterized by two more parameters, R_{min}, R_{max}, which prevent the jet becoming too large at low p_T, or too small at high p_T. The values used in the previous analysis are: $\rho = 30$ GeV, $R_{min} = 0.02$ and $R_{max} = 0.4$ [27]. We must note the cone of a VR jet, reflects more accurately the size of the jet.

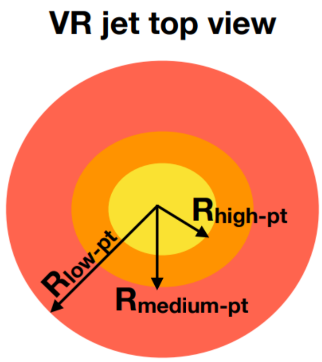

Figure 6.6: Graphical representation of a VR jet size, against the transverse momentum (p_T).

We begin the correction finding for each large-R jet, the two leading VR jets it contains. We then calculate the Delta R of the muons with these two selected jets and choose the smallest Delta R. We examine if the following inequality is satisfied:

$$\Delta R_{\mu,\mathrm{VR\ jet}} < \min\left(0.4,\ 0.04 + \frac{10\ \mathrm{GeV}}{p_T^{jet}}\right) \tag{6.11}$$

Note: The right hand side of the inequality, is an empirical formula, derived from the characteristics of the VR jet and also used in the previous analysis [27].
In case our condition is met we continue with the correction exactly as in equation 6.1. The definition for the correction and mistag rates are similar. The only difference is we replace the large-R jet with the VR jet and in equation 6.6 the N_{tot} represents the total number of the VR jets that were considered for correction.

6.3.3 Fitting Framework and Likelihood Definition

The fitting framework is based on XML Analytic Workspace Builder (xmlAnaWSBuilder) which is widely used in the ATLAS Higgs Group. XmlAnaWSBuilder creates RooFit workspaces using one-dimensional observables.

The statistical analysis of the data uses a binned likelihood function whose maximum correspond to the best description of data. It is defined as the product over all bins of the Poisson probability to observe N_b^{obs} data events given a prediction of $N_b^{exp}(\mu, k, \theta)$ events in a certain bin i:

$$L(\mu, \mathbf{k}, \theta) = \prod_{i \in \text{bins}} \frac{\left(N_i^{\text{exp}}(\mu, \mathbf{k}, \theta)\right)^{N_i^{\text{data}}}}{N_i^{\text{data}}!} \cdot e^{-N_i^{\text{exp}}(\mu, \mathbf{k}, \theta)} \tag{6.12}$$

In this likelihood formulation, the predicted number of events (given in equation 6.13) depends on three groups of parameters: the signal strength μ, the scale factors $k = k_1, \ldots, k_j$, and the nuisance parameters (NP) $\theta = \theta_1, \ldots, \theta_j$.

$$N_i^{\text{exp}}(\mu, \mathbf{k}, \theta) = \mu \cdot N_{i,\text{sig}}^{\text{exp}}(\theta) + \sum_{b \in \text{bkg}} k_b \cdot N_{i,b}^{\text{exp}}(\theta) \tag{6.13}$$

The signal strength (μ), which is the parameter of interest, scales the amount of signal linearly, without any prior constraint or penalty in the likelihood function. The nuisance parameters θ_i, encode the dependence of the prediction on systematic uncertainties into continuous parameters into the likelihood. The prior knowledge for each NP, is expressed by Gaussian penalty terms Gauss(0,θ_i,1), which are added to the likelihood. Hence, θ_i are expressed in standard deviations. This results in log normal dependence of the predicted rates, for specific parameter values. Maximizing the likelihood function (maximized log-likelihood value - MLL), with respect to all parameters, the nominal fit results (μ, σ_μ), are obtained. The profile likelihood ratio test statistic, is given by:

$$q_\mu = -2 \ln \left[\frac{\mathcal{L}(\mu, \hat{\mathbf{k}}, \hat{\theta}_\mu)}{\mathcal{L}(\hat{\mu}, \hat{\mathbf{k}}, \hat{\theta})} \right] \tag{6.14}$$

where $\hat{\mu}$ and $\hat{\theta}$ are the parameters that maximize the likelihood (with the constraint $0 < \mu < \hat{\mu}$), and $\hat{\theta}_\mu$ are the nuisance parameter values that maximize the likelihood for a given μ [110]. This test statistic is used to quantify how compatible the observed data are with a specific hypothesized signal strength μ, compared to the best fit to the data. Additionally, the extraction of local p_0 values is possible and if no signal is found in this procedure, exclusion intervals can be derived using the CLs method [111].

6.4 MIJ for the Large-R jets

6.4.1 MIJ for the Hbb Sample

Firstly, it is important to study the correction and mistag rate against muon min p_T that is applied. Following the first approach discussed in section 6.3.1, the correction and mistag rate against muon min p_T are respectively the following:

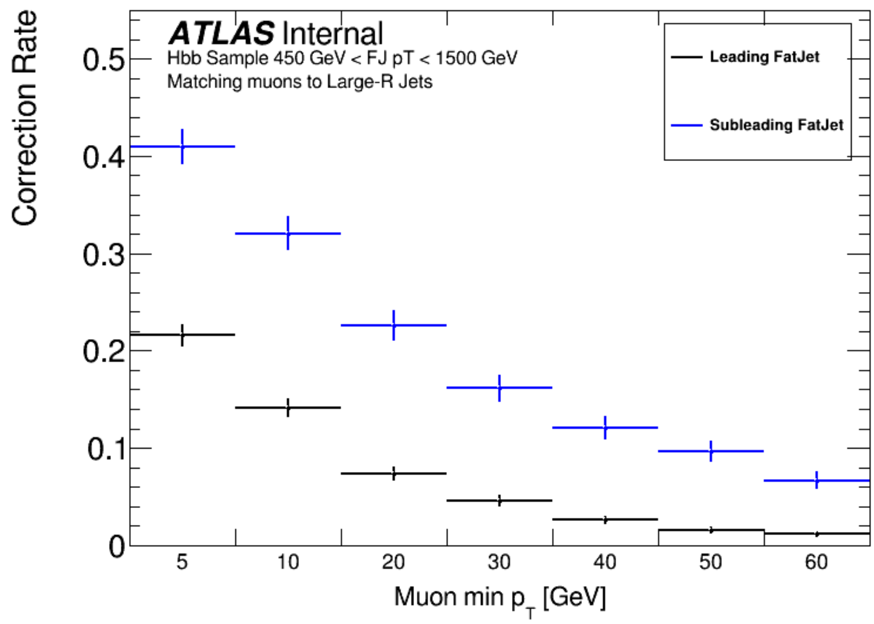

Figure 6.7: Correction Rate for the SRL and SRS of Hbb jets.

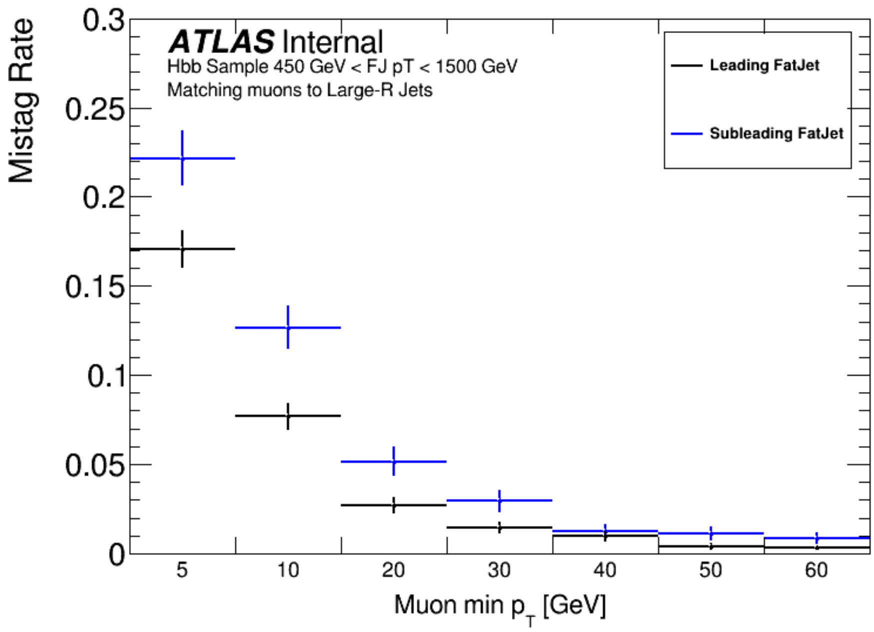

Figure 6.8: Mistag Rate for the SRL and SRS of Hbb jets.

We clearly observe that the correction rate is higher (almost double) for the SRS than the SRL. This is expected as most semileptonic decays occur in the Subleading jets. Also as the p_T cut increases, less muons pass the selection and less corrections are applied, leading to a very small correction rate.

Regarding now figure 6.8, the mistag rate for Muon min pT > 5 GeV, is unexpectedly high, compared also with the results from Run 2 analysis [27]. The mistag rate, gets half for muon min p_T = 10 GeV and drops significantly for p_T cuts above 20 GeV. Additionally the MR is higher in the SRS than the SRL.

A breakdown of the Mistag Rate for the SRS only, in it's two components is considered, in table 6.1, in order to determine the contribution of each component.

p_T Cut (GeV)	MR	MR_1	MR_2	MR_1/MR	MR_2/MR
5	0.221 ± 0.0155	0.008	0.213	0.038	0.962
10	0.126 ± 0.0124	0.007	0.119	0.055	0.945
20	0.051 ± 0.0082	0.004	0.047	0.081	0.919
30	0.029 ± 0.0063	0.003	0.026	0.095	0.905
40	0.013 ± 0.0041	0.001	0.011	0.111	0.889
50	0.011 ± 0.0039	0	0.011	0	1
60	0.008 ± 0.0034	0	0.008	0	1

Table 6.1: Table of MR for the Hbb SRS, with the values of components MR_1, MR_2, and their contribution to MR for the muon p_T cuts being under examination.

We can clearly observe that the MR_2 constitutes on average 95% of the MR. That means the MR is dominated by muons that do not match truth muons. Muons that are not originating from b or c quarks seem to play a more insignificant role.

After separating the jets to the Leading and Subleading regions, we match the reconstructed muons with $p_T > 10\,\text{GeV}$ to the jets. Then we apply the correction mentioned in section 6.2. We are interested in the mass distributions with and without the correction and begin our study with PFlow objects. For each distribution, the RMS and MPV are evaluated before and after the correction, in order to examine and optimize the effect MIJ has.

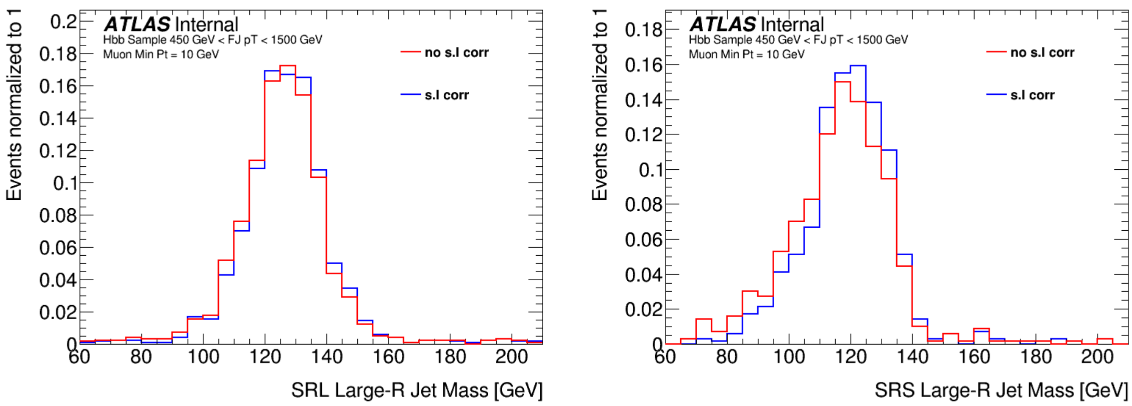

Figure 6.9: Mass distributions of the Hbb sample for all jets with and without the correction for the Leading (left) and Subleading (right) jets, in the inclusive p_T region, using PFlow objects. The muon min p_T is 10 GeV. On the y-axis events are normalized to one.

	SRL			SRS		
Quantity (GeV)	Before	After	Change (%)	Before	After	Change (%)
RMS	11.82	11.72	-0.93	12.75	11.47	-10.04
MPV	126.12	127.69	1.24	116.17	119.36	2.75

Table 6.2: RMS and MPV of all Hbb jets before and after correction, in the inclusive p_T bin using PFlow mass. The muon min p_T is 10 GeV.

Regarding figure 6.9 and the corresponding table 6.2, we get the anticipated behavior. The correction in the SRL is very rare resulting in very slight shift in the mass distribution. On the other hand in the SRS the correction shifts the mass peak higher and decreases the RMS.

Furthermore, for all the plots that will follow the muon min p_T is 10 GeV. Figure 6.10, present the mass distributions of the SRL jets, before and after the correction, in each p_T bin, and figure 6.11, presents the corresponding for the SRS. Results of the RSM and MPV before and after correction are summarized in tables 6.3, 6.4, 6.5. We study separately, all large-R jets and the muonic jets (i.e jets containing muon(s)).

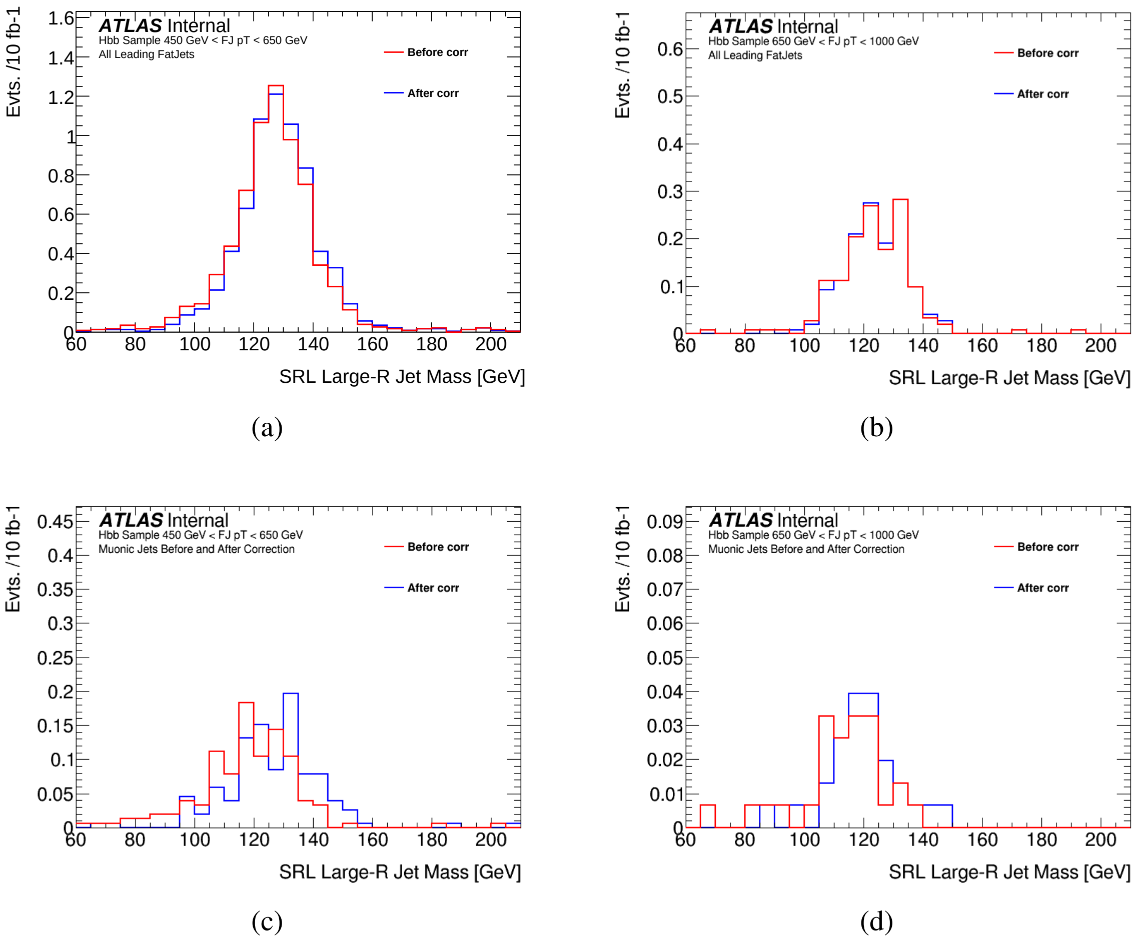

(a) (b) (c) (d)

Figure 6.10: Leading large-R jets for the Hbb sample before and after correction for All jets on top and for the muonic jets (i.e. jets containing muons) on the bottom, using PFlow objects.

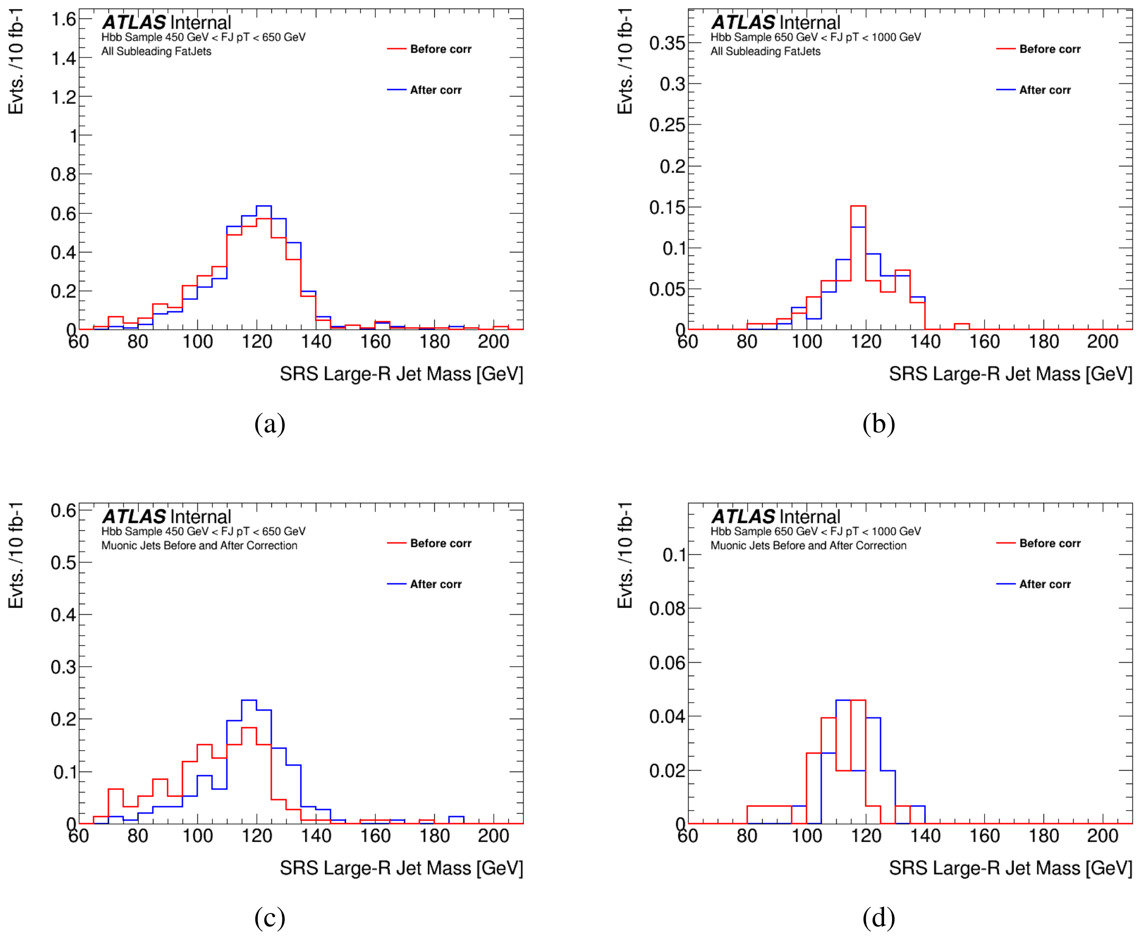

Figure 6.11: Subleading FatJets for the Hbb sample before and after correction for All jets on top and for the muonic jets (i.e. jets containing muons) on the bottom, using PFlow objects.

For both the SRL and the SRS there was a problem with the plots for the p_T^{03} (1000 - 2500 GeV), as the statistics were too small (In the SRS there were only 5 jets, creating a problem). Hence these plots are omitted. On contrary for the Zbb sample no problem occurred, as it can be seen in section 6.4.2. It is evident that even though in muonic jets the effect of the correction is clear in both SRL and SRS, when accessing all large-R jets, the MIJ mostly affects the SRS.

	SRL			SRS		
Quantity (GeV)	Before	After	Change (%)	Before	After	Change (%)
RMS	12.15	12.07	-0.66	13.09	11.77	-10.08
MPV	126.56	128.23	1.32	115.89	119.20	2.86

Table 6.3: RMS and MPV of all Hbb large-R jets before and after correction for p_T : 450 - 650 GeV

	SRL			SRL		
Quantity (GeV)	Before	After	Change (%)	Before	After	Change (%)
RMS	10.22	9.78	-4.31	13.74	11.41	-16.96
MPV	124.05	125.52	1.19	120.18	122.35	1.81

Table 6.4: RMS and MPV of all Hbb large-R jets before and after correction for p_T: 650 - 1000 GeV

	SRL			SRL		
Quantity (GeV)	Before	After	Change (%)	Before	After	Change (%)
RMS	14.27	13.81	-3.22	14.02	11.65	-16.90
MPV	117.43	131.31	11.82	106.38	118.19	11.1

Table 6.5: RMS and MPV of muonic Hbb large-R jets before and after correction for p_T: 450 - 650 GeV

We now apply the correction on the Hbb sample for the mass after regression (bJR) and plot the mass distributions of the SRL and SRS. Results for the inclusive p_T bin, are presented in figure 6.12 and table 6.6 and the conclusions are similar to the ones drawn above for PFlow objects.

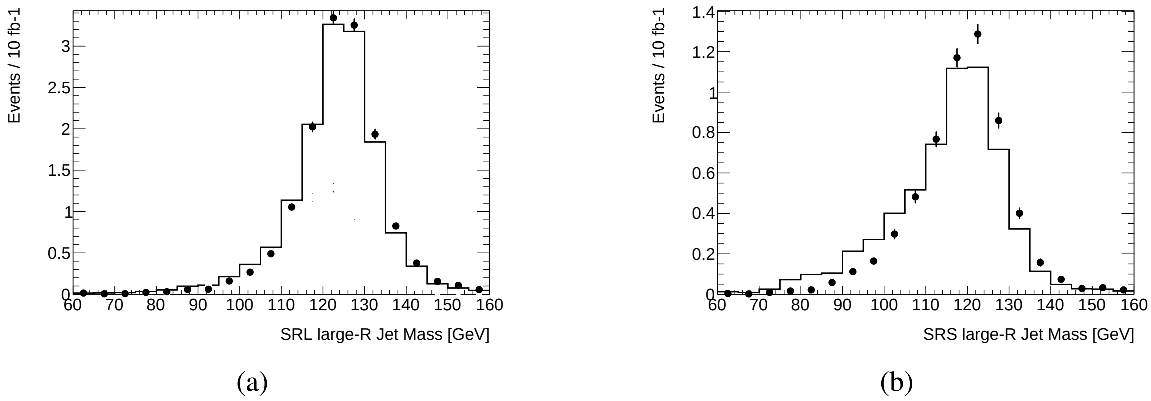

Figure 6.12: MIJ applied on the Hbb MC sample, using the mass after regression (bJR). On the left is the SRL and on the right is the SRS. Histograms present the mass before the correction and points the mass after the correction. The behavior is similar with the PFlow masses.

	SRL			SRS		
Quantity (GeV)	Before	After	Change (%)	Before	After	Change (%)
RMS	8.79	8.61	-2.05	12.21	10.37	-15.07
MPV	123.77	124.94	0.95	116.07	119.35	2.83

Table 6.6: RMS and MPV of all Hbb large-R jets before and after correction, in the inclusive p_T bin using the mass after regression (bJR).

6.4.2 MIJ for the Zbb sample

Similar with section 6.4.1, the plots of the correction and mistag rate for the Zbb sample against the muon min p_T, are the following:

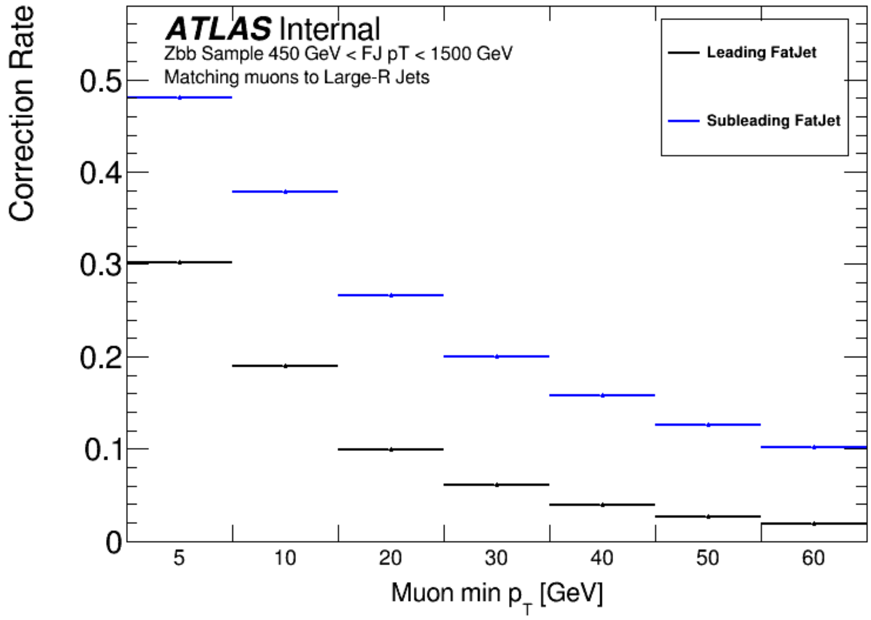

Figure 6.13: Correction Rate for the SRL and SRS for Zbb jets

We observe higher correction rates for the SRS than the SRL (exactly the same behavior as for the Hbb sample in section 6.4.1). The correction rate decreases, as the muon min p_T increases, as less muons pass the selection criteria.

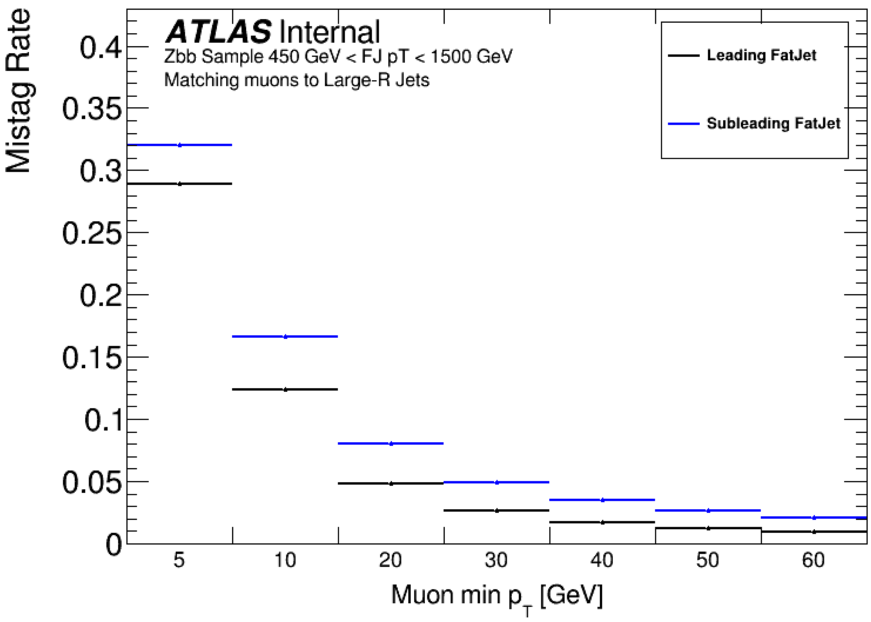

Figure 6.14: Mistag Rate for the SRL and SRS for Zbb jets

Once again (as for the Hbb sample) the Mistag Rate for the first two bins is unexpectedly high. It is evident, CorrRate and MR are higher for the Zbb sample, than the corresponding values in the Hbb

jets.
Note: For both figures 6.13, 6.14, we have very small error bars (they are difficult to distinguish) in comparison with the corresponding plots for the Hbb sample. This happens mainly, due to the larger number of available samples for the Z boson compared to those for the Higgs boson. Larger statistics leads to smaller errors.

As in section 6.4.1 the breakdown of MR, for the Zbb sample in it's components is given in table 6.7.

Muon p_T Cut (GeV)	MR	MR_1	MR_2	MR_1/MR	MR_2/MR
5	0.326 ± 0.0021	0.009	0.316	0.028	0.972
10	0.170 ± 0.0017	0.008	0.163	0.046	0.954
20	0.082 ± 0.0012	0.006	0.077	0.069	0.931
30	0.051 ± 0.0010	0.004	0.047	0.081	0.919
40	0.036 ± 0.0008	0.003	0.033	0.082	0.918
50	0.028 ± 0.0007	0.002	0.026	0.071	0.929
60	0.021 ± 0.0007	0.002	0.020	0.072	0.928

Table 6.7: MR for the SRS Zbb, with the values of components MR_1, MR_2, and their contribution to MR for the muon p_T cuts under examination.

Once again (like for the Hbb sample), MR mostly consists of the component MR_2 (on average 94%). We begin the study with PFlow objects, in the inclusive p_T bin, using all large-R jets. Results are presented in 6.15 and in table 6.8.

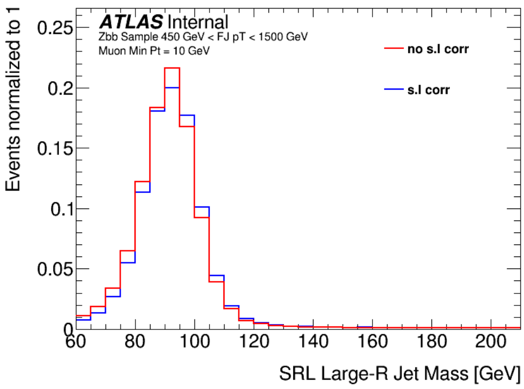

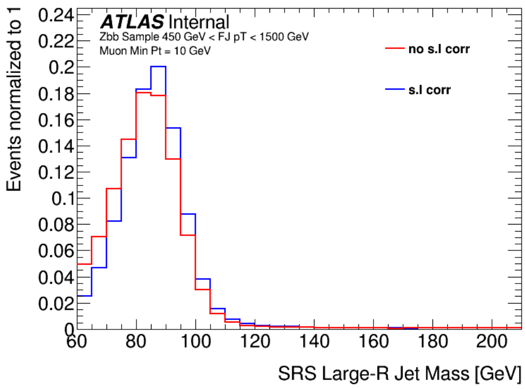

Figure 6.15: Mass distributions for the Zbb sample for all jets with and without the correction for the Leading (left) and Subleading (right) jets, using PFlow objects.

	SRL			SRS		
Quantity (GeV)	Before	After	Change (%)	Before	After	Change (%)
RMS	9.78	9.62	-1.64	11.16	10.12	-9.32
MPV	91.01	92.44	1.57	82.52	85.25	3.31

Table 6.8: RMS and MPV of all Zbb large-R jets, in the inclusive p_T bin, before and after correction using PFlow mass.

We now focus, on each p_T bin for all large-R jets and muonic jets using PFlow objects. Results are presented in figures 6.16 (SRL), 6.17 (SRS) and in tables 6.9, 6.10, 6.11 (all jets) and 6.12, 6.13, 6.14.

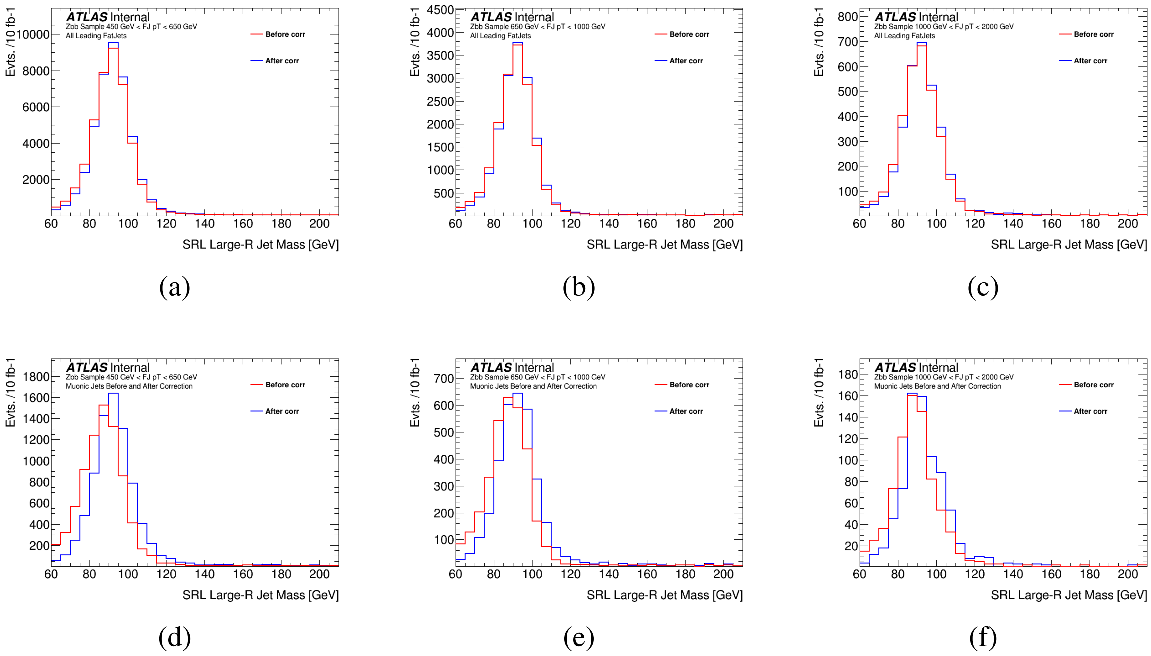

Figure 6.16: Leading large-R jets for the Zbb sample before and after correction for All jets on top and muonic jets (i.e. jets containing muons) on the bottom, using PFlow objects. The columns correspond to p_T^{01}, p_T^{02}, p_T^{03}, ordered from left to right.

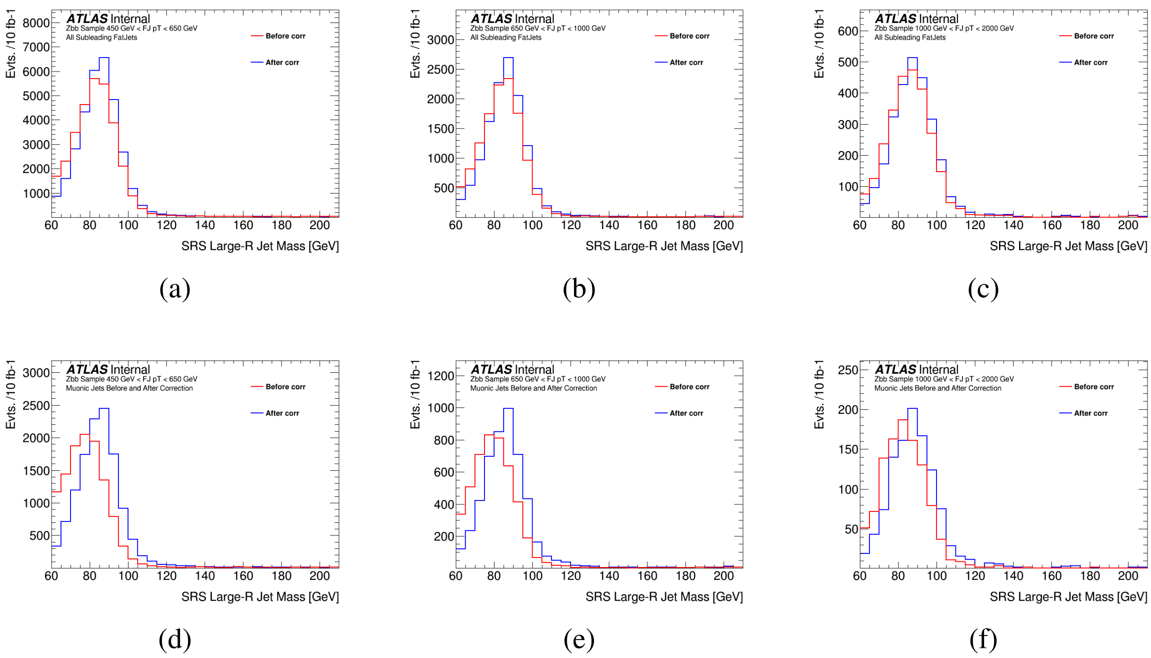

Figure 6.17: Subleading large-R jets for the Zbb sample before and after correction for All jets on top and muonic jets (i.e. jets containing muons) on the bottom, using PFlow objects. The columns correspond to p_T^{01}, p_T^{02}, p_T^{03}, ordered from left to right.

	SRL			SRS		
Quantity (GeV)	Before	After	Change (%)	Before	After	Change (%)
RMS	9.94	9.74	-2.01	10.69	10.15	-5.05
MPV	91.00	91.94	1.03	82.07	84.70	3.20

Table 6.9: RMS and MPV of all Zbb large-R jets before and after correction for p_T: 450 - 650 GeV

	SRL			SRS		
Quantity (GeV)	Before	After	Change (%)	Before	After	Change (%)
RMS	9.36	9.27	-0.96	11.26	9.93	-11.81
MPV	91.03	91.85	0.90	83.29	85.51	2.67

Table 6.10: RMS and MPV of all Zbb large-R jets before and after correction for p_T: 650 - 1000 GeV

	SRL			SRS		
Quantity (GeV)	Before	After	Change (%)	Before	After	Change (%)
RMS	9.94	9.82	-1.21	11.56	11.00	-4.84
MPV	91.27	92.17	0.99	85.40	87.33	2.26

Table 6.11: RMS and MPV of all Zbb large-R jets before and after correction for p_T: 1000 - 2500 GeV

	SRL			SRS		
Quantity (GeV)	Before	After	Change (%)	Before	After	Change (%)
RMS	10.91	10.48	-3.94	11.28	10.17	-9.84
MPV	86.41	92.03	6.50	76.25	84.05	10.23

Table 6.12: RMS and MPV of muonic Zbb large-R jets before and after correction for p_T: 450 - 650 GeV

	SRL			SRS		
Quantity (GeV)	Before	After	Change (%)	Before	After	Change (%)
RMS	10.30	10.24	-0.58	10.87	9.94	-8.56
MPV	87.17	91.73	5.23	78.47	84.71	7.95

Table 6.13: RMS and MPV of muonic Zbb large-R jets before and after correction for p_T: 650 - 1000 GeV

	SRL			SRS		
Quantity (GeV)	Before	After	Change (%)	Before	After	Change (%)
RMS	10.94	10.53	-3.75	11.18	10.72	-4.11
MPV	88.59	92.66	4.59	82.09	87.10	6.10

Table 6.14: RMS and MPV of muonic Zbb large-R jets before and after correction for p_T: 1000 - 2500 GeV

Once again the MIJ mostly affects the SRS, as seen in the above plots and in the tables, where generally the % change (of RMS and MPV) is much higher in the SRS than the SRL. After the correction the MPV of the mass of all large-R jets, gets closer to the desired value of 90 GeV, for the SRS, but does not reach this value as the lost energy is not fully compensated (remember the energy of the escaping muons).
Now, the study is extended to the bJR mass, presented in figure 6.18 and table 6.15. The behavior before and after the correction (% change) is the same of for PFlow objects.

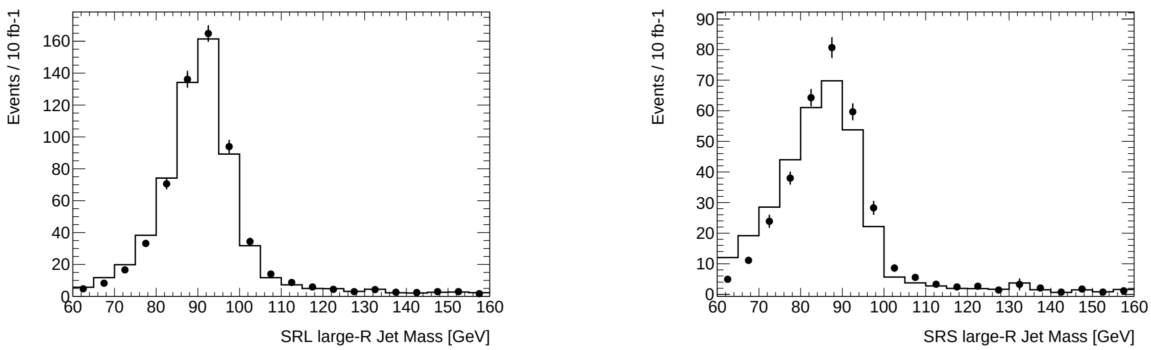

(a) (b)

Figure 6.18: MIJ applied for on the Zbb MC sample, using the mass after regression (bJR), in the inclusive p_T bin. On the left is the SRL and on the right is the SRS. Histograms show the mass before the correction and points the mass after the correction. The behavior is similar with the PFlow masses.

	SRL			SRS		
Quantity (GeV)	Before	After	Change (%)	Before	After	Change (%)
RMS	7.51	7.37	-1.86	9.78	8.57	-12.37
MPV	89.1	90.32	1.37	82.61	85.00	2.85

Table 6.15: RMS and MPV of all Zbb large-R jets before and after correction using the mass after regression (bJR).

6.4.3 MC QCD and Data 2022

We implement MIJ into our analysis flow for 10 fb^{-1} of the same samples as for the 2022 data and present results in figure 6.19.

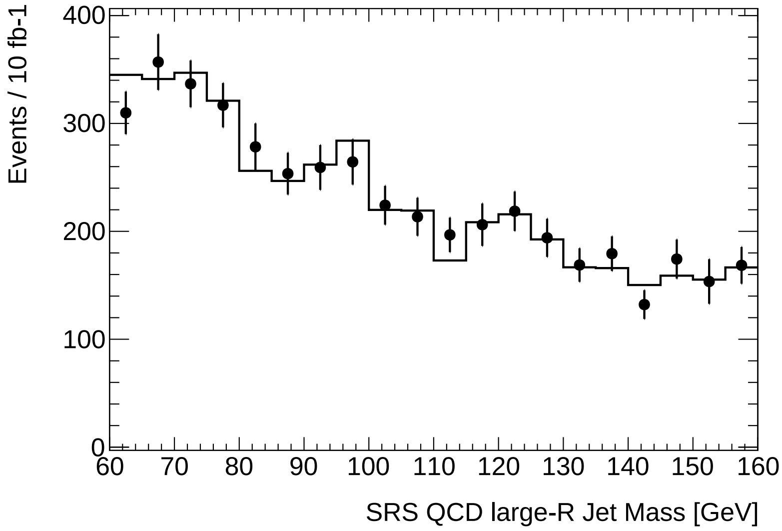

(a)

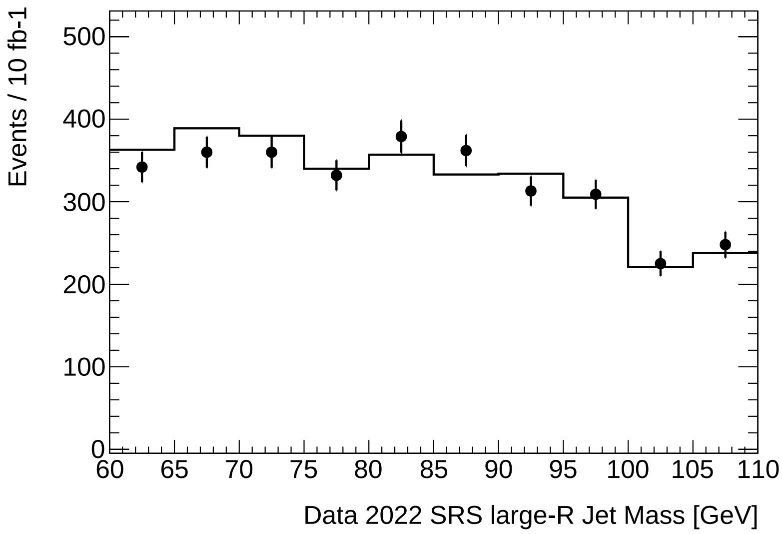

(b)

Figure 6.19: MIJ applied for QCD MC sample (top) and 10 fb^{-1} of Data 2022 (bottom), using the mass after regression (bJR), in the SRS region. Histograms show the mass before correction and points the mass after correction.

We can observe from figures 6.19 and 6.31, that MIJ correction causes many events to migrate from the first bin of 60 GeV to higher masses, leaving this bin underpopulated (turn-on effect). As a result, it was necessary to lower the minimum mass of the large-R jet, from 60 GeV (which was originally) to 45 GeV. This decision, is consistent with the trigger response, as for a mass cut of 45 GeV we are still on the trigger plateau, as it can be seen in figure 6.20, for the HLT of 2022. Lowering the mass below 45 GeV may lead to problems.

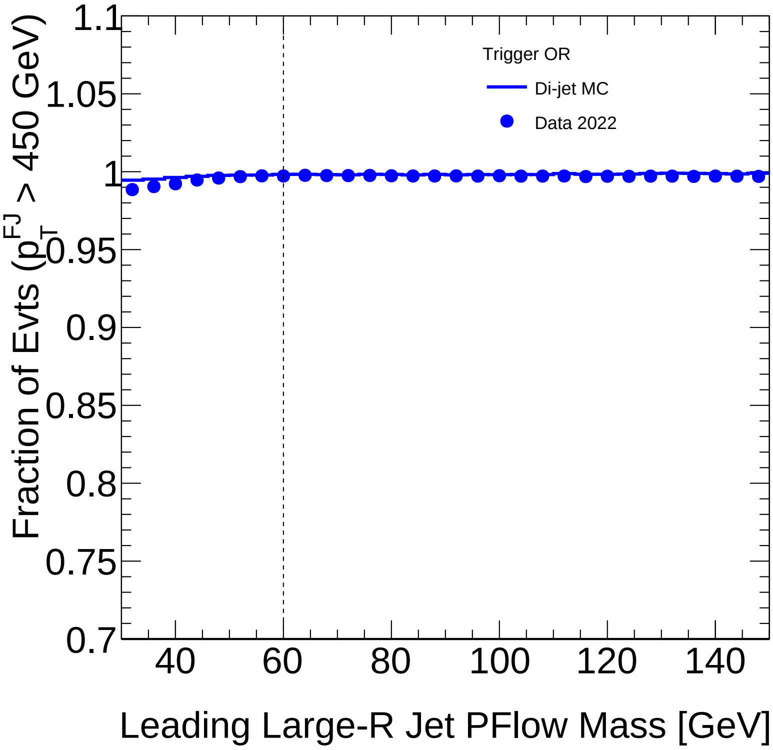

Figure 6.20: Trigger response for MC (line) and 2022 data (points) against the large-R jet Mass. Above 45 GeV the trigger presents a plateau and we must operate in this region.

Using a 10 GeV cut on the muon p_T, the Correction Rates for the SRL and SRS across the different samples and $10 fb^{-1}$ of 2022, are summarized in table 6.16.

Sample	**ggH**	**Zbb**	**QCD**	**Data 2022** (10 fb^{-1})
CorrRate SRL	0.179	0.189	0.178	0.153
CorrRate SRS	0.331	0.345	0.312	0.305

Table 6.16: Correction rates for different samples in SRL and SRS regions using 2022 data.

A generally good agreement is presented between data and MC, with slightly smaller values in data. CorrRates of the SRL appear to be half the CorrRates of the SRS, on all samples and in data.

6.5 MIJ for the VR jets

In correlation, with section 6.4, the present section contains the results for the MIJ implemented using VR jets.

6.5.1 MIJ for the Hbb sample

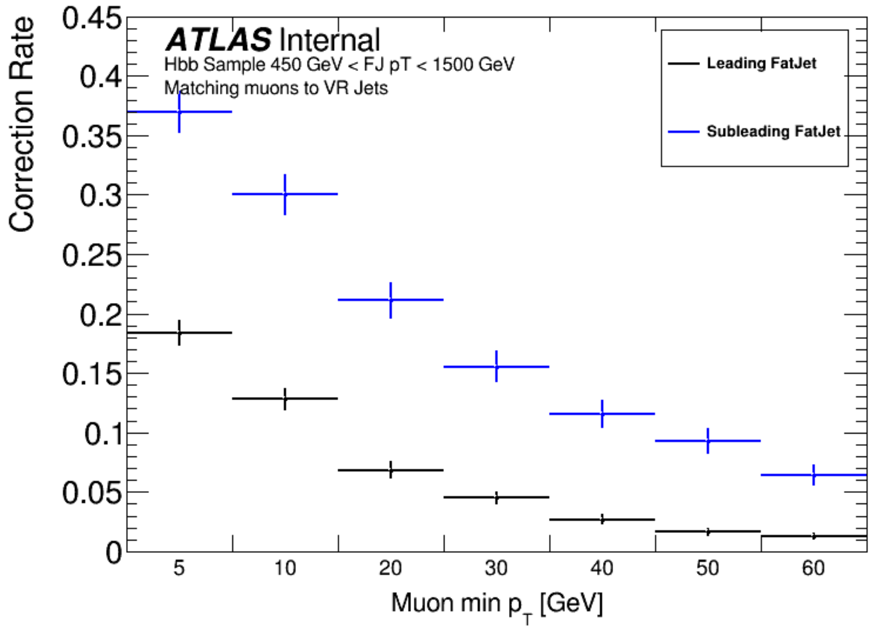

Figure 6.21: Correction Rate for the Hbb sample when the MIJ is applied to the VR jets.

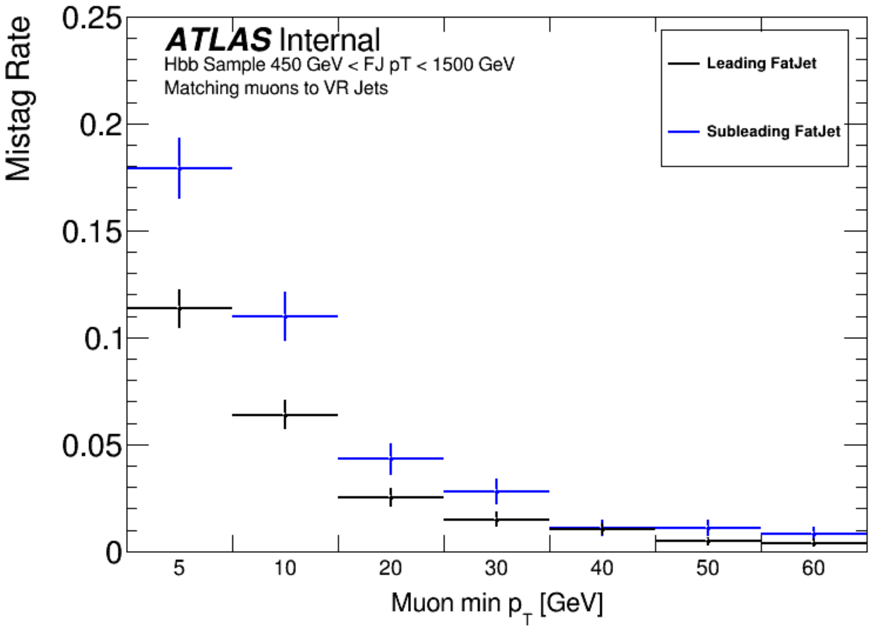

Figure 6.22: Mistag Rate for the Hbb sample when the MIJ is applied to the VR jets.

	Correction Rate		Mistag Rate	
	PRD	This Analysis	PRD	This analysis
SRL	0.140	0.130	0.014	0.006
SRS	0.330	0.300	0.022	0.110

Table 6.17: Correction and mistag rates for SRL and SRS regions in previous analysis [27] and the present analysis.

The conclusions reached with the first method based on large-R jets remain valid here as well. Choosing the muon min p_T at 10 GeV, we can compare our results with the Run 2 analysis [27], in table 6.17. We now have similar correction rates, but a much higher (about 5 times) mistag rate, compared to previous (Run 2 only) analysis.

6.5.2 MIJ for the Zbb sample

For the sake of completeness, the same plots for the Zbb sample, are presented in figures 6.23, 6.24.

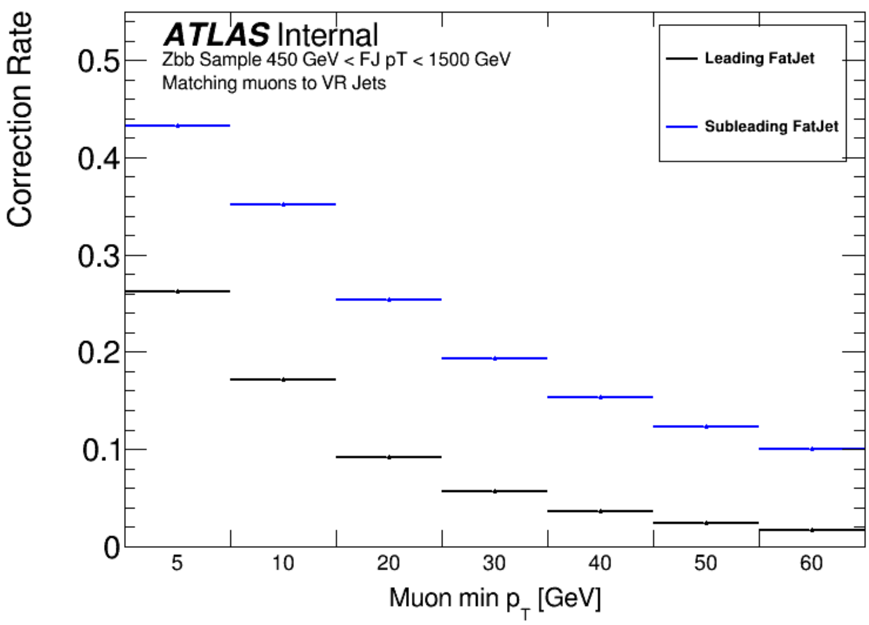

Figure 6.23: Correction Rate for the Zbb sample when the MIJ is applied to the VR jets.

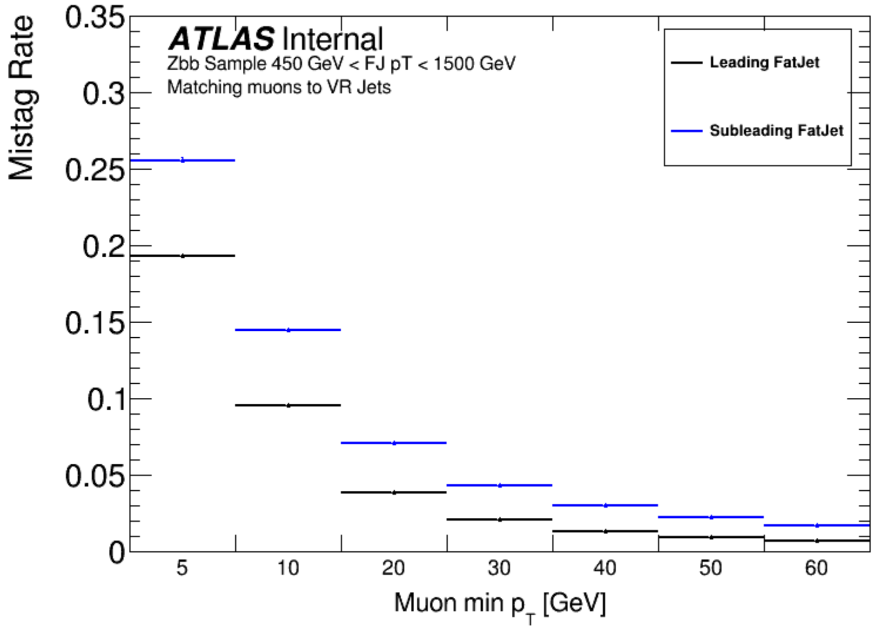

Figure 6.24: Mistag Rate for the Zbb sample when the MIJ is applied to the VR jets.

Both the correction and mistag rates are slightly higher for the Zbb sample, compared to the ones for the Hbb sample. Finally, we observe, both for the Hbb and Zbb samples smaller Correction Rates and Mistag Rates, using the method for VR jets. A thorough comparison of the two methods is conducted in the following section.

6.6 Comparison of the two approaches

We will collect our data into tables 6.18, 6.19 for the Hbb sample (and 6.20, 6.21 for the Zbb sample), in order to determine the change of the Correction and Mistag Rate between the two approaches (correction using large-R jets and correction using VR jets).

Muon p_T Cut (GeV)	$CorrRate_{LR}$	$CorrRate_{VR}$	Decrease (%)
5	0.411 ± 0.0183	0.369 ± 0.0180	10.14
10	0.322 ± 0.0174	0.300 ± 0.0171	6.90
20	0.228 ± 0.0156	0.211 ± 0.0152	7.32
30	0.164 ± 0.0138	0.156 ± 0.0135	5.08
40	0.124 ± 0.0123	0.115 ± 0.0119	6.74
50	0.097 ± 0.0110	0.093 ± 0.0108	4.28
60	0.067 ± 0.0093	0.064 ± 0.0091	4.17

Table 6.18: Correction Rate comparison on the Hbb SRS sample, for the two different methods and for the potential muon p_T cuts.

Muon p_T Cut (GeV)	MR_{LR}	MR_{VR}	Improvement (%)
5	0.221 ± 0.0155	0.179 ± 0.0143	38.86
10	0.126 ± 0.0124	0.110 ± 0.0117	13.19
20	0.051 ± 0.0082	0.043 ± 0.0076	16.21
30	0.029 ± 0.0063	0.028 ± 0.0061	4.77
40	0.013 ± 0.0041	0.011 ± 0.0039	11.12
50	0.011 ± 0.0039	0.011 ± 0.0039	0.0
60	0.008 ± 0.0034	0.008 ± 0.0034	0.0

Table 6.19: Mistag Rate comparison on the Hbb SRS sample, for the two different methods and for the potential muon p_T cuts.

Muon p_T Cut (GeV)	$CorrRate_{LR}$	$CorrRate_{VR}$	Decrease (%)
5	0.490 ± 0.0022	0.431 ± 0.0022	11.79
10	0.388 ± 0.0022	0.352 ± 0.0021	9.33
20	0.277 ± 0.0020	0.254 ± 0.0020	8.18
30	0.210 ± 0.0018	0.193 ± 0.0018	7.77
40	0.166 ± 0.0017	0.153 ± 0.0016	7.61
50	0.134 ± 0.0015	0.123 ± 0.0015	7.72
60	0.109 ± 0.0014	0.101 ± 0.0014	7.76

Table 6.20: Correction Rate comparison on the Zbb SRS sample, for the two different methods and for the potential muon p_T cuts.

Muon p_T Cut (GeV)	MR_{LR}	MR_{VR}	Improvement (%)
5	0.326 ± 0.0021	0.255 ± 0.0020	21.57
10	0.170 ± 0.0017	0.145 ± 0.0016	15.12
20	0.083 ± 0.0012	0.071 ± 0.0012	14.17
30	0.051 ± 0.0010	0.043 ± 0.0009	15.58
40	0.036 ± 0.0008	0.030 ± 0.0008	17.25
50	0.028 ± 0.0007	0.022 ± 0.0007	19.34
60	0.022 ± 0.0007	0.017 ± 0.0006	21.52

Table 6.21: Mistag Rate comparison on the Zbb SRS sample, for the two different methods and for the potential muon p_T cuts.

The MIJ correction performed on VR jets provides us generally with better MR rates accompanied by a reduction (expected and small) on the correction rates. We are in front of a dilemma and a trade-off is necessary. Tables 6.18 through 6.21 demonstrate clearly, that the (desired) reduction of the MR is more significant than the (unwanted) smaller correction rates. **Consequently, we decide to apply the MIJ using the VR jets. We also choose the muon p_T cut to be 10 GeV.** For this cut the correction and mistag rates for the SRS are: $(30 \pm 1.71)\%$, $(10.97 \pm 1.17)\%$ respectively for the Hbb ($(35.16 \pm 0.21)\%$ and $(14.47 \pm 0.16)\%$ for the Zbb sample).

About the notations on the above tables, $CorrRate_{LR}$ refers to the correction rate of the large-R jets and $CorrRate_{VR}$ is the correction rate on the VR jets. Similarly for the MR. The Decrease(%) and Improvement (%) are calculated as:

$$\text{Decrease (\%)} = \frac{CorrRate_{LR} - CorrRate_{VR}}{CorrRate_{LR}} \times 100 \tag{6.15}$$

$$\text{Improvement (\%)} = \frac{MR_{LR} - MR_{VR}}{MR_{LR}} \times 100 \tag{6.16}$$

Note: In the above percentages, the $CorrRate$ and MR are substituted with their corresponding values without the errors.

Both rates ($CorrRate$ and MR) decrease, so the raw percentage of change is negative. We choose to include in the tables above, the absolute value and have only positive change rates. In that way for the $CorrRate$ were the decrease is considered as unwanted we name it ”Decrease” to show the negative effect. With respect to that, the change of the MR which is desired, is marked as ”Improvement”.

6.7 Correction and Mistag Rates Over the Years

Using different Hbb MC samples, simulating the data taking years of our analysis, we extend the study of correction and mistag rates.

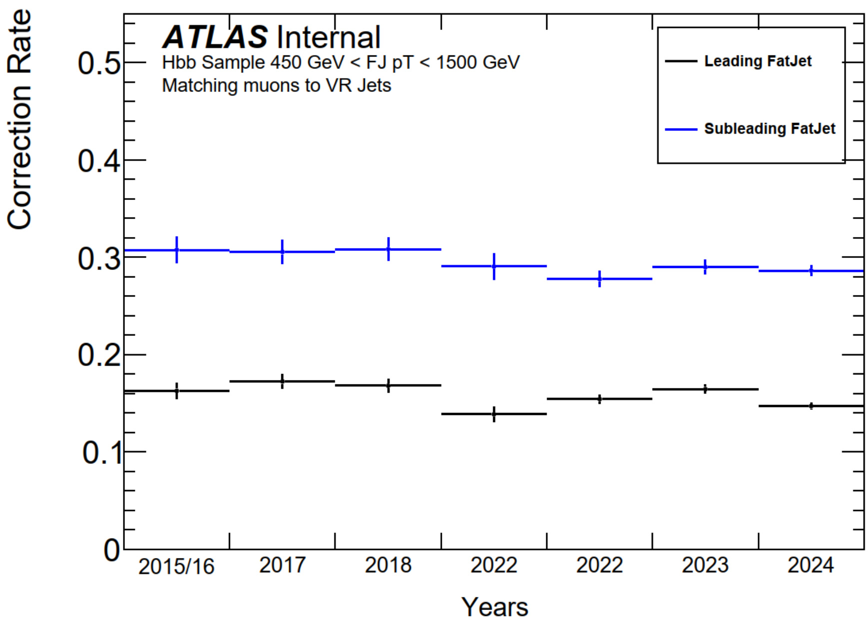

Figure 6.25: Correction Rates for the Hbb sample across different MC campaigns, simulating the data taking years.

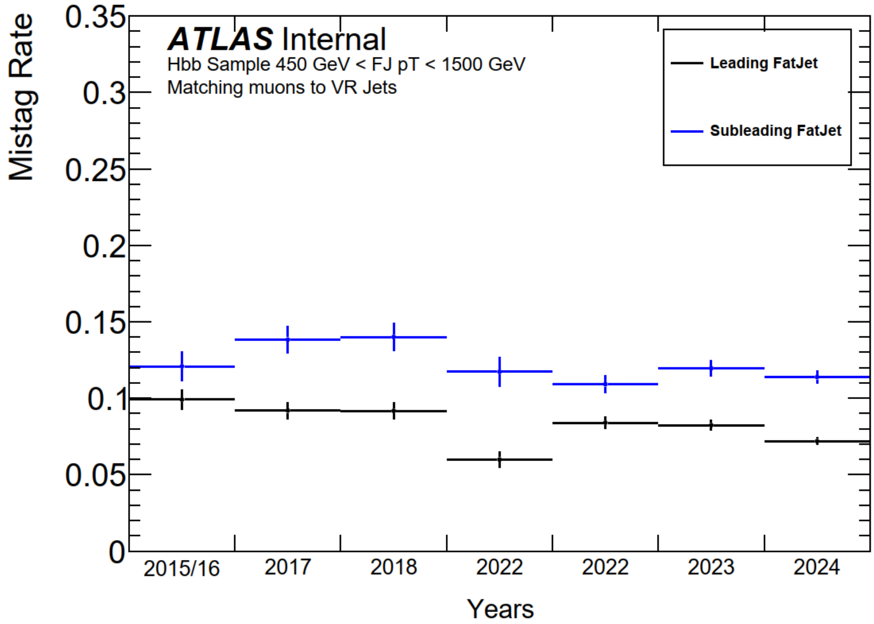

Figure 6.26: Mistag Rates for the Hbb sample across different MC campaigns, simulating the data taking years.

The Correction Rate (fig. 6.25), presents a very stable behavior across the all years with CorrRate(SRL) = 0.18 and CorrRate(SRS) = 0.3 approximately. Furthermore, the Mistag Rate (fig. 6.26), presents also a fairly stable behavior (slightly less stable though than the correction rate). Approximately, we can observe MR(SRL) = 0.06 - 0.1 and MR(SRS) = 0.11 - 0.14.

6.8 Resolution Before and After MIJ Over the Years

Following the study conducted in section 5.3, we wish to examine the resolution of the SRS mass distributions before and after the application of MIJ, using Hbb MC samples corresponding to the data taking years of our analysis.

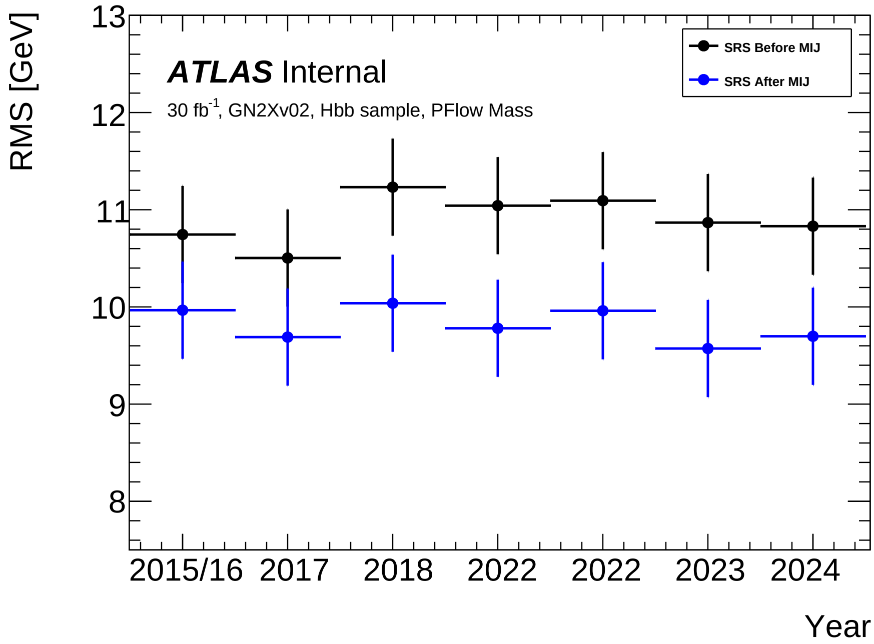

Figure 6.27: RMS of the Hbb SRS, PFlow mass before and after MIJ over the different MC campaigns simulating the data taking years.

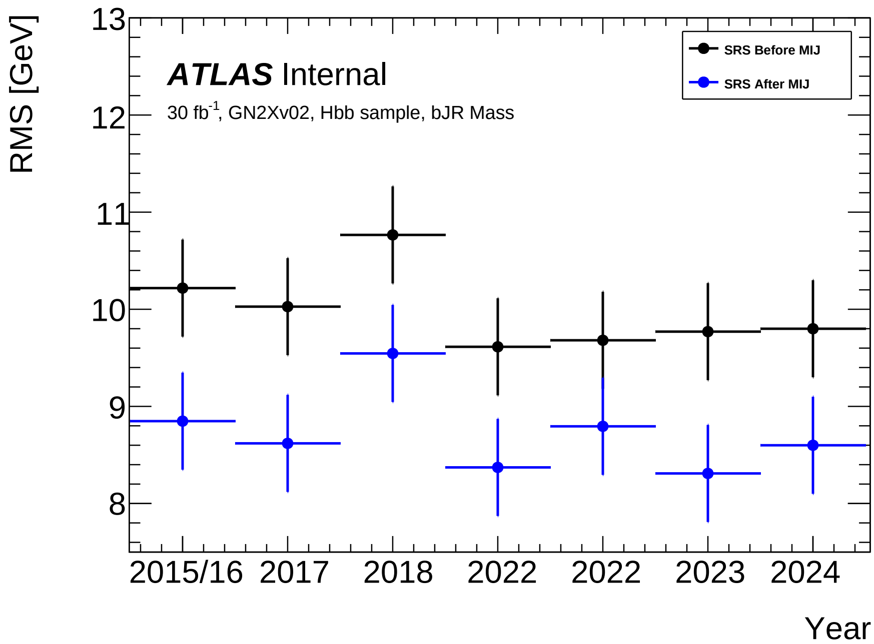

Figure 6.28: RMS of the Hbb SRS, bJR mass before and after MIJ over the different MC campaigns simulating the data taking years.

Smaller values of RMS, about 10%, are observed after the correction is applied through all years. The same decrease, about 10%, is apparent in the bJR RMS (figure 6.28) after the MIJ, with the initial and final values being 1 GeV lower than the corresponding values for PFlow mass.

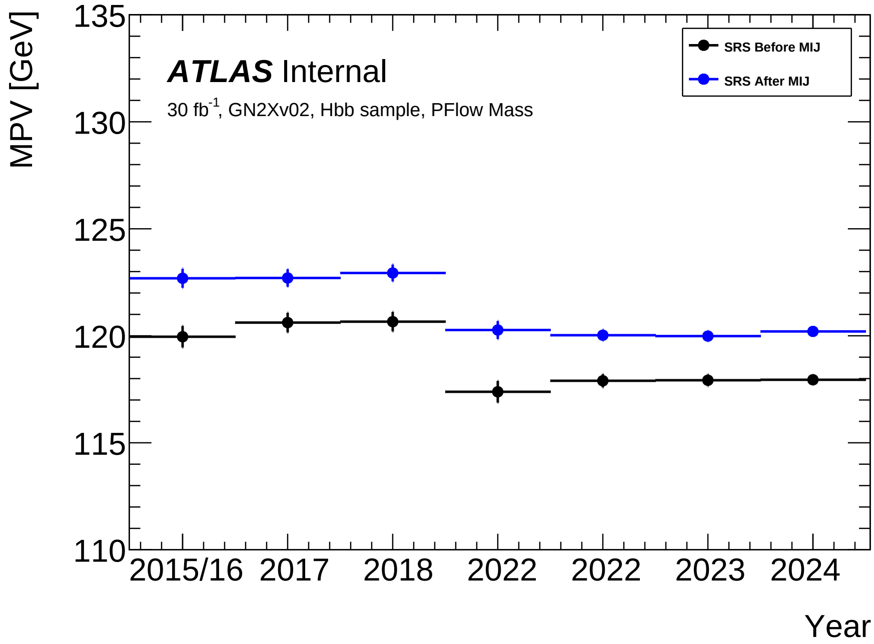

Figure 6.29: MPV of the Hbb SRS, PFlow mass before and after MIJ over the different MC campaigns simulating the data taking years.

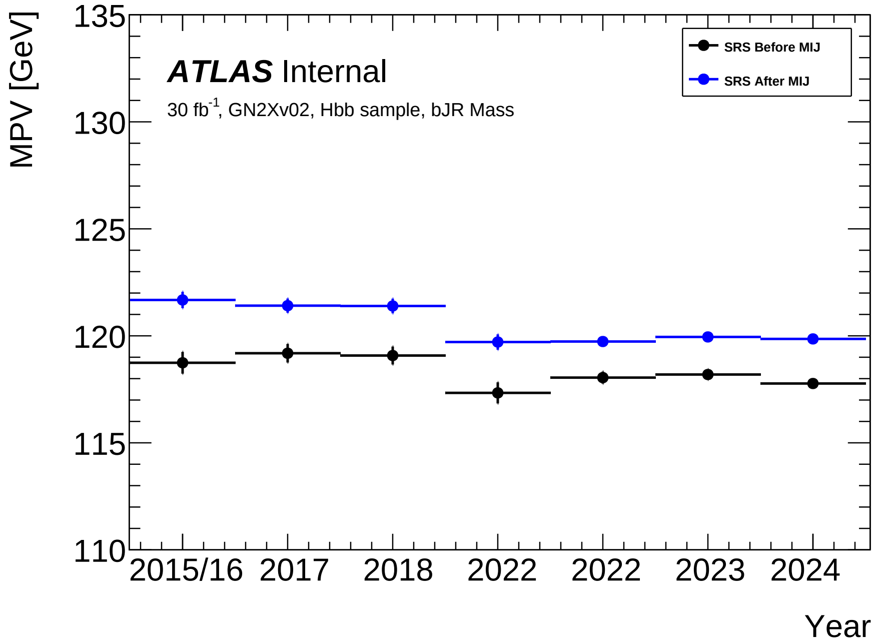

Figure 6.30: MPV of the Hbb SRS, bJR mass before and after MIJ over the different MC campaigns simulating the data taking years.

Larger values of MPV, about 1.6 - 2.5%, are detected after the correction in comparison with the corresponding ones before MIJ, for both PFlow and bJR. The behavior of MPV between PFlow and bJR masses is almost identical, with the measurements for the bJR being about 1 GeV smaller. After the correction is applied the distributions have an MPV closer to the desired 125 GeV for the Hbb sample, but not exactly 125 GeV as the correction does not fully compensate for the lost energy.

6.9 Statistical Fit

After reviewing the application of the MIJ on the MC samples, it is decided to be applied only in the SRS. For the leading region as shown in the sections above, the MIJ has a small effect. The problems created (related to the trigger response) when the MIJ is applied in this region as well, outweigh the benefits for our analysis.

Hence, we integrated the MIJ in our analysis cutflow and tested the effect in the extraction of μ_Z with 10 fb^{-1} of 2022 Data. After performing a statistical fit only (in the Signal Region only), we obtained the following plots before and after the correction.

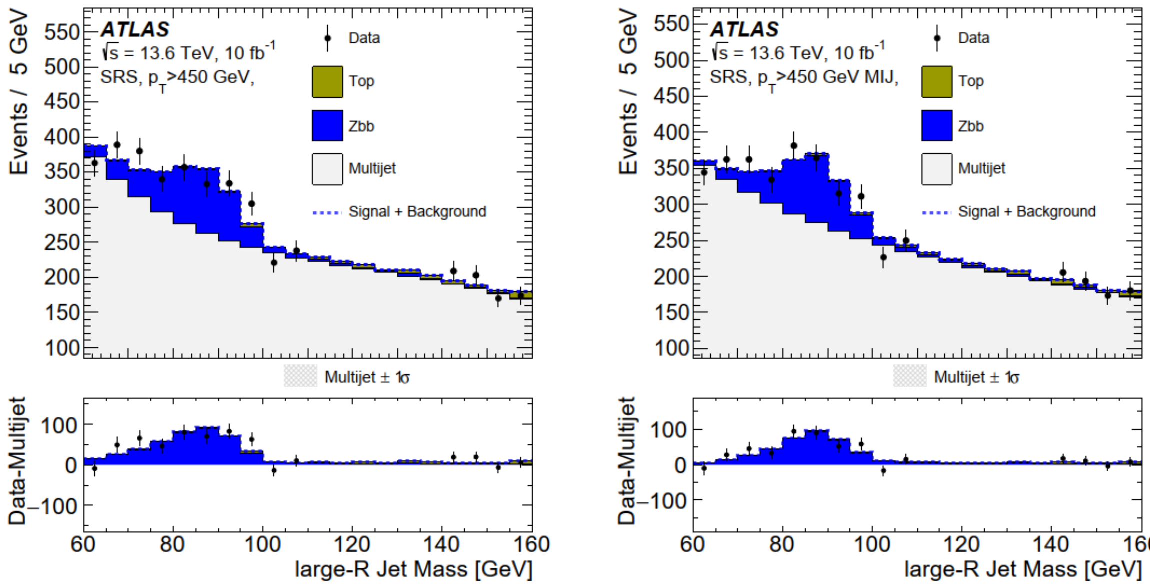

(a) (b)

Figure 6.31: Fitted histograms before (left) and after the application of MIJ (right) for different MC samples and for 10 fb^{-1} data of 2022. The fit is performed only on the SRS. The presence of the Z boson at 90 GeV is clear in the data points. The Higgs boson cannot be seen yet due to the ATLAS blinding policy. On top the full spectrum with the QCD background and on bottom without QCD.

A similar fit performed simultaneously on SR and VR on the same amount of 2022 data, is presented in figure 6.32, where both leading (left) and subleading (right) regions are included.

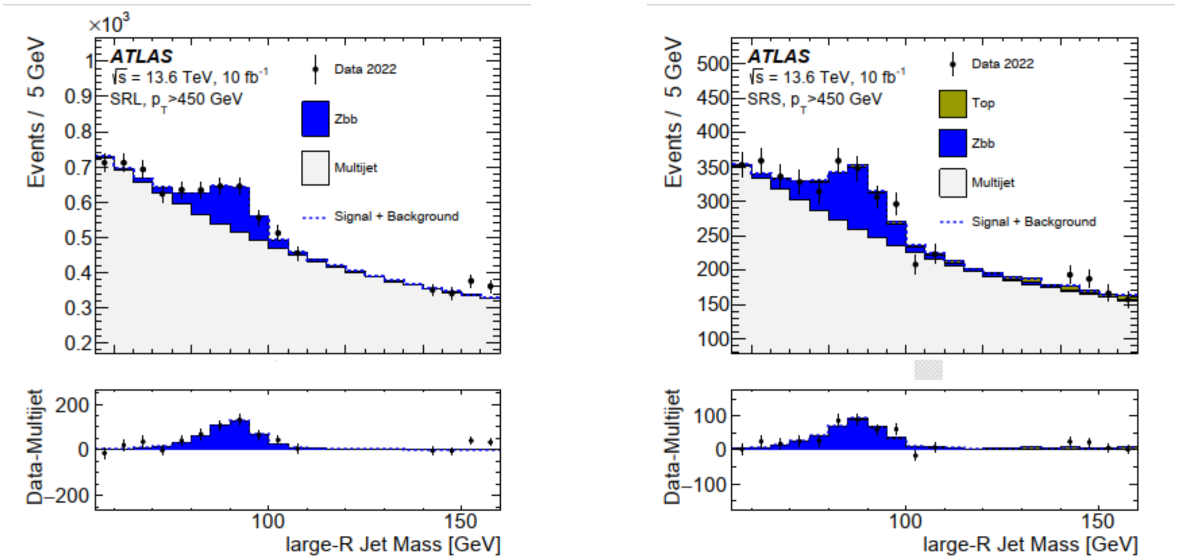

(a) (b)

Figure 6.32: Combined fit on SR and VR for SRL (left) and SRS (right) using different MC samples and $10fb^{-1}$ data of 2022. This fit is after the MIJ correction is applied only in the SRS. The presence of the Z boson at 90 GeV is clear from the fata points. The Higgs boson cannot be seen yet due to the ATLAS blinding policy. On top the full spectrum with the QCD background and on bottom without QCD.

As seen from figure 6.31 the application of the MIJ causes the mass distributions to shift to higher masses and become narrower as mentioned many times above. On the region of 90 GeV we have the presence of the Z boson (note this is only 10 fb^{-1}, very small statistics). The data on the mass region of the Higgs boson are blinded according to ATLAS policies.

The signal strengths of Z, before and after the MIJ are respectively:

$$\mu_{Z,before} = 1.374 \pm 0.3483$$
$$\mu_{Z,after} = 1.160 \pm 0.2958$$

A **15%** reduction in statistical uncertainty is observed following the application of the Muon-In-Jet correction in the Subleading region, representing a notable improvement.

The correction successfully fulfilled its objectives—enhancing the resolution and increasing the Most Probable Value—thereby improving the overall results. Consequently, it will be applied to all samples and datasets used in the analysis.

Chapter 7

Conclusion

I have presented the inclusive, boosted $H \to b\bar{b}$ analysis, using Run 2 ($\sqrt{s}$ = 13 TeV) and partial Run 3 ($\sqrt{s}$ = 13.6 TeV) data of p-p collisions recorded by the ATLAS detector at CERN. This data set corresponds to an integrated luminosity of 300 fb^{-1}. Data statistics have increased from the previous published analysis [1], by a factor of 2.2 and result sensitivity by a factor of 6. My contributions to the analysis, were focused on the four main tasks, I successfully completed and presented in the chapters above. A summary of the main results and conclusions follows.

Firstly, I studied the b tagging efficiency of different versions of the GN2X flavour tagging algorithm. The optimum was GN2Xv02LLR, providing an efficiency 42-44% in both SRL and SRS, for all MC samples and across all p_T bins. Slightly higher efficiencies were presented in the SRL. The study was extended (see figure 4.11) across the different MC campaigns, resulting in stable efficiency across the different data taking years, when the Working Points are tuned year by year. The same holds true for the GN2X Tag Rate, presented in 4.12.

Furthermore, I studied the muon p_T^{rel} distributions and developed a preliminary method for evaluating the b tagging efficiency or the $b\bar{b}$ content of the QCD background. The muon min p_T is selected at 10 GeV and the validity of the method is established by figures 4.16 and 4.17. The first plot depicts the muon p_T^{rel} distribution before and after flavour tagging for the SR. On contrary the second plot presents the same distribution, but for the QCD background. Distributions of jets (classified into categories according to the containment of zero, one or two quarks), before and after flavour tagging remain unchanged, proving that muon p_T^{rel} is a good discriminant for our needs.

Subsequently, I focused on the study of H and Z Jet Mass Resolution (JMR). With a custom function, I calculated the σ from the FWHM, the RMS and the MPV of various jet mass distributions (for both PFlow and bJR masses) using Working Points, corresponding to different Hbb efficiencies. An important finding, is the RMS (and σ) of the SRS is larger that that of the SRL, while for the MPV the opposite is true. With the use of bJR masses, smaller widths (about 20%) are presented and hence better resolution is achieved. In most cases, the behavior is almost flat as function of the Hbb efficiency and the different p_T bins have almost the same values. The study was further extended in different MC campaign samples, demonstrating a fairly steady performance.

My last and biggest task, was the Muon-In-Jet correction, which I developed, optimized and applied into the analysis. Most of the results, are generally in good agreement with the corresponding ones, from the previous published analysis (PRD). After the implementation of the method was tested through two different methods, a comparison was performed (see 6.6) and the best one using VR jets was selected (the same method was used in the PRD). The examination of the correction and mistag rate from plots 6.21, 6.22 respectively, led to the selection of the muon min p_T to be 10 GeV. For this cut the correction and mistag rates for the Hbb SRS sample, are: 0.3 (0.33 in PRD) and 0.11 (0.022 in PRD). Therefore, similar correction rate is achieved, with five times larger mistag rate. We must also note, that the main reason of mistags are fake muons (muons that do not match truth muons).

The implementation of the MIJ correction on the Hbb and Zbb MC samples (for both PFlow and bJR objects) motivated the decision to apply the correction exclusively in the SRS, lowering the large-R jet minimum mass to 45 GeV. A statistical fit only, was performed on 10 fb^{-1} of 2022 data, before and after the correction (only in the SRS) and demonstrated a 15% reduction in the statistical uncertainty of μ_Z when the correction was applied. This great result confirms the effectiveness of the correction. and soon MIJ, will be implemented into all MC samples and data sets of the analysis.

Apart from the results of my work, final results will become available once the analysis is completed, and readers are encouraged to look out for the corresponding publication by the end of 2025. Performing calculations on MC samples, the total number of expected events for each category in the SR and VR, are given in table 7.1.

Process	SR (Events / 300 fb^{-1})	VR (Events / 300 fb^{-1})
Higgs	1.2k	1.3k
Z+jets	28.5k	344k
W+jets	0.4k	940k
ttbar	1.4k	532k
QCD jj	457k	215M

Table 7.1: Number of expected events for various processes in the signal (SR) and validation (VR) regions for $450 < p_T < 1250$ GeV with 300 fb^{-1}.

Finally, the total expected uncertainties (systematic and statistical) of the signal strengths (μ_H and μ_Z), the analysis aims to measure are presented in table 7.2. For comparison the uncertainties of the previous published analysis are also given in the second column. Regarding the first three blocks of the table, 2σ accuracy is expected, while the previous analysis offered $\frac{1}{3}\sigma$. For the last block, referring to the highest p_T bin, one σ accuracy is expected, in comparison to Run 2 analysis which had $\frac{1}{6}\sigma$.

I would like to conclude with a brief personal reflection on my future prospects. I plan to remain actively involved in the analysis team until the end of 2025, by which time the project is expected to conclude. Beyond that point, I intend to apply for a Ph.D in Physics. My background as an electrical engineer will support me in pursuing my dream of a career in Physics.

Combined	PRD Analysis (136 fb^{-1})	This Analysis (300 fb^{-1})
$450 < p_T < 1250$ GeV		
μ_H	± 3.2	± 0.49
μ_Z	± 0.17	± 0.03
$450 < p_T < 650$ GeV		
μ_H	± 3.3	± 0.50
μ_Z	± 0.17	± 0.03
$650 < p_T < 1000$ GeV		
μ_H	± 6.0	± 0.95
μ_Z	± 0.33	± 0.06
$p_T > 1$ TeV		
μ_H	± 30	± 6.5
μ_Z	± 1.6	± 0.30

Table 7.2: Expected accuracies on signal strengths μ_H and μ_Z for different p_T bins, comparing the PRD analysis (136 fb^{-1}) with this analysis (300 fb^{-1}).

Περίληψη (Summary in Greek)

Η παρούσα διπλωματική εργασία, αφορά τη μελέτη ενός μποζονίου Higgs όταν αυτό παράγεται με όλους τους δυνατούς τρόπους στον επιταχυντή LHC, έχοντας υψηλή εγκάρσια ορμή (p_T). Χρησιμοποιούνται δεδομένα από το πείραμα ATLAS του CERN, κατά τη διάρκεια των περιόδων: Run 2 (2015-2018) και Run 3 (2022-2024), με συνολική ολοκληρωμένη φωτεινότητα $L_{int} = 300 fb^{-1}$ (βλ. πίνακα 4.1). Στη συγκεκριμένη ενότητα θα δοθεί μια εκτενής περίληψη στα ελληνικά, όσων έχουν προηγηθεί, με κατάλληλες αναφορές στο κείμενο.

Θεωρητικό Υπόβαθρο

Η πληρέστερη θεωρία στην σωματιδιακή φυσική είναι το Καθιερωμένο Πρότυπο (ΚΠ) (βλ. 2.2). Το ΚΠ περιλαμβάνει όλα τα στοιχειώδη σωματίδια και τις αλληλεπιδράσεις τους με τρεις από τις τέσσερεις θεμελιώδεις δυνάμεις 2.3 (ήτοι, την ισχυρή, την ασθενή και την ηλεκτρομαγνητική). Η βαρύτητα δεν συμπεριλαμβάνεται και η εισαγωγή της στη θεωρία αυτή, αποτελεί ένα από τους μεγαλύτερους στόχους της σύγχρονης φυσικής. Τα στοιχειώδη σωματίδια χωρίζονται σε φερμιόνια (ημι-ακέραιο σπιν) και μποζόνια (ακέραιο σπιν). Τα πρώτα, χωρίζονται περαιτέρω σε κουάρκ (quarks) και λεπτόνια. Υπάρχουν συγκεκριμένα έξι διαφορετικά κουάρκ (διαφορετικές γεύσεις όπως συνηθίζεται να λέγεται), οργανωμένα σε τρεις γενιές. Ακόμη υπάρχουν τρεις γενιές λεπτονίων, όπου κάθε μια περιέχει το ηλεκτρόνιο ή το μιόνιο ή το ταυ και το αντίστοιχο νετρίνο του. Τα νετρίνο έχουν θεωρητικά μηδενική μάζα, πρακτικά όμως έχουν μια πολύ μικρή (μη μηδενική μάζα) και μερικά άνω όρια έχουν βρεθεί από διάφορα πειράματα. Αξίζει να σημειωθεί ότι μόνο τα up, down κουάρκ και το ηλεκτρόνιο συμμετέχουν στον σχηματισμό της καθημερινής ύλης. Αναφορικά με τα μποζόνια, τα διανυσματικά μποζόνια είναι υπεύθυνα για τη μετάδοση των δυνάμεων, ενώ το μόνο γνωστό βαθμωτό μποζόνιο, το μποζόνιο Higgs, είναι υπεύθυνο για τη μάζα των σωματιδίων. Στη συνέχεια, μερικά μεγέθη, τα οποία είναι χρήσιμα στην πειραματικές αναλύσεις, είναι η αναλλοίωτη μάζα και το τετράγωνο της (s), που ορίζονται στις σχέσεις 2.10,2.11. Σημαντική ακόμη είναι και η ενεργός διατομή (σ), η οποία χαρακτηρίζει την πιθανότητα να πραγματοποιηθεί μια διαδικασία και μετριέται σε barn, με $1b = 10^{-28}m^2$ (βλ. 2.5). Ακολούθως, ο λόγος διακλάδωσης (BR) εκφράζει την πιθανότητα να διασπαστεί ένα σωματίδιο μέσω ενός συγκεκριμένου καναλιού (βλ. σχ. 2.22, 2.23), ενώ το πλάτος Γ χαρακτηρίζει το πλάτος της κατανομής της αναλλοίωτης μάζας ενός σωματιδίου και συνδέεται με τον μέσο χρόνο ζωής του (βλ. σχ. 2.20). Στην παράγραφο 2.6, ορίζεται η λαγκρατζιανή (L), ως η διαφορά μεταξύ κινητικής και δυναμικής ενέργειας, η οποία χρησιμοποιείται ευρέως στην φυσική στοιχειωδών σωματιδίων. Διατυπώνεται επίσης, το θεώρημα της Noether, σύμφωνα με το οποίο, για κάθε συνεχή συμμετρία ενός συστήματος, υπάρχει μια ποσότητα που διατηρείται. Δίνονται μερικά παραδείγματα συμμετριών και οι αντίστοιχες διατηρούμενες ποσότητες (βλ. πίνακα 2.3) καθώς και διάφοροι κβαντικοί αριθμοί των σωματιδίων που διατηρούνται. Φυσικά δεν μπορούν να παραλειφθούν μερικές από τις βασικότερες εξισώσεις, όπως η εξίσωση του Schrodinger 2.38, η εξίσωση Klein-Gordon 2.63 και η εξίσωση Dirac 2.73. Ορίζονται επίσης τα απαραίτητα μαθηματικά της ειδικής σχετικότητας και τα τετρανύσματα και η πλήρης λαγκρατζιανή του ΚΠ αναλύεται στην παράγραφο 2.8. Ιδιαίτερη έμφαση δίνεται στο κομμάτι της λαγκρατζιανής που περιγράφει το μποζόνιο Higgs. Ετσι, αναπτύσσεται το θεώρημα Γκολτνστοουν (Goldstone), σύμφωνα με το οποίο αν η συνεχής συμμετρία μιας λαγκρατζιανής σπάσει αυθόρμητα, εμφανίζονται τόσα άμαζα μποζόνια Goldstone όσα η διαφορά των γεννητόρων της συμμετρίας της λαγκρατζιανής με τον αριθμό των γεννητόρων της κατάστασης κενού (βλ. 2.9.1). Ακολούθως, παρουσιάζεται διεξοδικά ο μηχανισμός Englert-Brout-Higgs (βλ. 2.9.2), ο οποίος οδήγησε στην θεωρητική ανακάλυψη του μποζονίου Higgs το 1964. Εκτός από την θεωρητική παρουσίαση του μποζονίου Higgs, είναι αναγκαία και η γνώση της πειραματικής πλευράς του, ήτοι πως αυτό μπορεί να παραχθεί από τις διαθέσιμες διατάξεις και μέσω ποιων καναλιών διάσπασης μπορεί να μελετηθεί. Παρουσιάζονται, συνεπώς οι τέσσερεις βασικές μέθοδοι παραγωγής του Higgs στον Μεγάλο Επιταχυντή Αδρονίων (LHC): gluon-gluon Fusion (ggF), Vector Boson Fusion (VBF), Higgs Strahlung (VH) και associated top production (ttH/tH). Τα αντίστοιχα διαγράμματα Feynman, δίνονται στα σχήματα: 2.9, 2.10, 2.11, 2.12. Στους πίνακες 2.4, 2.5, δίνονται οι θεωρητικά εκτιμώμενες ενεργές διατομές κάθε μεθόδου παραγωγής, για την περίπτωση ενός "απλού" Higgs και ενός με υψηλή p_T αντίστοιχα. Είναι φανερό οτι και στις δύο περιπτώσεις, η ggF είναι ο κυρίαρχος τρόπος παραγωγής. Επιπροσθέτως, στον πίνακα 2.6 δίνονται τα διάφορα κανάλια διάσπασης του Higgs, συνοδευόμενα από τον αντίστοιχο λόγο διακλάδωσης. Το κανάλι της ανάλυσης μας, το $b\bar{b}$, είναι το κυρίαρχο με $BR = 58.2\%$. Η παρουσίαση της θεωρίας κλείνει με συνοπτική εισαγωγή σε θεωρίες πέρα από το ΚΠ (βλ. 2.11. Η σημαντικότερη που αξίζει να αναφερθεί είναι η θεωρία της Υπερσυμμετρίας (SUSY), η οποία υπαγορεύει μια συμμετρία μεταξύ φερμιονίων και μποζονίων, προβλέποντας ότι κάθε σωματίδιο έχει έναν υπερσυμμετρικό σύντροφο με σπιν που διαφέρει κατά $\frac{1}{2}$.

CERN, LHC και ανιχνευτής ATLAS

Για να καταφέρουμε να παράξουμε και να μελετήσουμε μποζόνια Higgs, είναι απαραίτητο να έχουμε πολύ υψηλές ενέργειες. Προς το σκοπό τούτο κατασκευάστηκε και ο Μεγάλος Επιταχυντής Αδρονίων (Large Hadron Collider - LHC), ικανός να επιταχύνει πρωτόνια και βαριά ιόντα, σε ένα από τα μεγαλύτερα ερευνητικά κέντρα στον κόσμο, το CERN το οποίο βρίσκεται στα σύνορα Γαλλίας και Ελβετίας. Πρόκειται για ένα εξαιρετικό κατασκεύασμα, που τοποθετήθηκε στο τούνελ στο οποίο βρισκόταν ο Επιταχυντής Ηλεκτρονίων - Ποζιτρονίων (LEP), έχει περιφέρεια 27 km και βρίσκεται κατά μέσο όρο 100m κάτω από τη Γη. Χρησιμοποιεί όλους τους προηγούμενους ανιχνευτές, οργανωμένους σε μια αλυσίδα, οι οποίοι αυξάνουν σταδιακά την ενέργεια των σωματιδίων πριν την εισαγωγή τους στον LHC (βλ. 3.2.1). Μέσα στον LHC, με χρήση διπολικών υπεραγώγιμων μαγνητών, η δέσμη των πρωτονίων καμπυλώνεται κατά μήκος των τροχιών τους, ενώ με χρήση τετραπολικών μαγνητών εστιάζεται και από-εστιάζεται η εν λόγω δέσμη. Τέλος με χρήση συστήματος ραδιοσυχνοτήτων (RF) τα σωματίδια επιταχύνονται (βλ. 3.2.1). Οι συγκρούσεις των δύο αντίθετα κινούμενων δεσμών, πραγματοποιούνται σε τέσσερα σημεία κατά μήκος της περιφέρειας του LHC. Στα σημεία αυτά βρίσκονται υψηλής ακρίβειας ανιχνευτές, ένας από τους οποίους είναι ο ATLAS, τα δεδομένα του οποίου χρησιμοποιήθηκαν στην παρούσα διπλωματική εργασία (βλ. 3.3). Ο ATLAS είναι γενικού σκοπού ανιχνευτής, με μήκος 44m και ύψος 25m. Ζυγίζει επίσης 7000 τόνους και καλύπτει μια στερεά γωνία σχεδόν 4π. Αποτελείται από τρία υποσυστήματα. Το πρώτο είναι, ο εσωτερικός ανιχνευτής (ID), ο οποίος μετράει την ορμή, το φορτίο και τη διαδρομή όλων των φορτισμένων σωματιδίων (βλ. 3.3.3). Στη συνέχεια βρίσκονται τα θερμιδόμετρα (ηλεκτρομαγνητικό και αδρονικό) για την μέτρηση της ενέργειας σωματιδίων που αλληλεπιδρούν μέσω της ηλεκτρομαγνητικής ή της ισχυρής δύναμης, παράγοντας καταιονισμούς (βλ. 3.3.4). Τέλος στο εξωτερικό τμήμα του ανιχνευτή βρίσκεται το μιονικό φασματόμετρο, με στόχο τον εντοπισμό και την μέτρηση της ορμής των μιονίων (βλ. 3.3.5). Μεγάλο μέρος της εργασίας μου αφορά τα μιόνια, καθιστώντας τον υπό-ανιχνευτή αυτό ιδιαίτερα σχετικό με την εργασία. Επιπροσθέτως, υπάρχει και ένα σύστημα μαγνητών, το οποίο χρησιμοποιείται για να κάμψει τα σωματίδια, έτσι ώστε να μετρηθεί η ορμή τους (βλ. 3.3.2). Ενα άλλο σημαντικό συναφές ζήτημα, είναι ότι ο όγκος των δεδομένων που παράγεται από τις συγκρούσεις είναι τεράστιος (40 TB/s και 84 TB/s για το Run 2 και Run 3 αντιστοίχως). Χρησιμοποιείται επομένως ένα σύστημα σκανδαλισμού (trigger system) για να επιλεχθούν τα χρήσιμα για ανάλυση γεγονότα, με αποτέλεσμα να αποθηκεύονται τελικά μόνο 1 GB/s και 6 GB/s για τα δύο Run αντιστοίχως (βλ. 3.3.6). Τα γεγονότα αυτά αποθηκεύονται από σύστημα απόκτησης δεδομένων (Data Acquisition System - DAQ). Κλείνοντας την παράγραφο αυτή, δίνονται μερικοί ορισμοί σημαντικών μεγεθών. Η φωτεινότητα (L) εκφράζει τον ρυθμό των σωματιδίων που διέρχονται διαμέσου μιας επιφάνειας ανά μονάδα του χρόνου (βλ. εξ. 3.1) και μετριέται σε $cm^{-2}s^{-1}$. Ολοκληρώνοντας την φωτεινότητα ως προς το χρόνο, λαμβάνουμε την ολοκληρωμένη φωτεινότητα (L_{int}), η οποία εκφράζει τη συνολική ποσότητα των δεδομένων που έχουν ληφθεί (βλ. εξ. 3.2) και μετριέται συνήθως σε fb^{-1}. Δεδομένης της ολοκληρωμένης ή στιγμιαίας φωτεινότητας του πειράματός μας και την ενεργό διατομή μιας υπό μελέτης διεργασίας (για παράδειγμα μποζόνια Z), ο ρυθμός εμφάνισης τέτοιων διεργασιών, δίνεται από 3.3. Τέλος, τρία σημαντικά μεγέθη σχετιζόμενα με το σύστημα συντεταγμένων του ATLAS (βλ. 3.3.1, είναι η εγκάρσια ορμή (p_T - βλ. εξ. 3.5), η ψευδοωκύτητα (pseudorapidity - βλ. εξ. 3.8) και η γωνιακή απόσταση (ΔR - Βλ. εξ. 3.9).

Σύνοψη της Ανάλυσης

Η ανακάλυψη του μποζονίου Higgs το 2012 δεν αποτέλεσε το τέλος, αλλά την απαρχή μιας νέας εποχής, στην οποία το Higgs μπορεί να αξιοποιηθεί ως εργαλείο για την αναζήτηση νέας φυσικής πέρα από το Καθιερωμένο Πρότυπο. Στο πνεύμα αυτό, η ανάλυση μελετάει ένα μποζόνιο Higgs, με υψηλή εγκάρσια ορμή (boosted). Προκειμένου να παραχθεί κατά αυτόν τον τρόπο είναι απαραίτητη η ύπαρξη Ακτινοβολίας Αρχικής Κατάστασης (Initial State Radiation - ISR). Η ακτινοβολία αυτή, στην περίπτωση παραγωγής μέσω ggF, αναφέρεται στην εκπομπή ενός γκλουνίου από τον τριγωνικό βρόχο των top κουάρκ (βλ. σχ. 4.1). Χωρίς την εκπομπή αυτή του γκλουνίου, το παραγόμενο Higgs θα είχε εγκάρσια ορμή της τάξης των 20 GeV μόνο. Ο λόγος που θέλουμε υψηλή p_T, είναι διότι μπορούμε να αναλύσουμε τον τριγωνικό βρόχο στην μέθοδο παραγωγής ggF (διαφορετικά η αλληλεπίδραση σε μικρές p_T θεωρείται σημειακή) και να λάβουμε μετρήσεις για τη σύζευξη του Higgs με τα top κουάρκ. Απώτερος στόχος μας είναι να μετρήσουμε την ισχύ σήματος (μ), που ορίζεται στην εξίσωση 2.24 και να εξετάσουμε αν εμφανίζονται αποκλίσεις από το ΚΠ, οι οποίες μπορεί να υποδηλώνουν την ύπαρξη Νέας Φυσικής (ή Φυσικής Πέρα από το Καθιερωμένο Πρότυπο). Τέτοιες πιθανές αποκλίσεις δεν εμφανίζονται σε χαμηλές τιμές p_T. Τα παραγόμενα σωματίδια από μια σύγκρουση εμφανίζονται σε μορφή ενός κώνου, τον οποίο ονομάζουμε "jet". Το πλεονέκτημα όταν αυξάνεται η εγκάρσια ορμή είναι ότι τα σωματίδια αποκτούν μικρότερη γωνιακή απόκλιση και τα επιμέρους jet, μπορούν να ανακατασκευαστούν σε ένα μεγάλο jet (βλ. σχ. 4.2). Οταν ένα τέτοιο jet, έχει $p_T > 450$ GeV, $|\eta| < 2.0$, $2m_J/p_T < 1$ και περιέχει τουλάχιστον δύο jet μεταβλητής ακτίνας (Variable Radius - VR) με $p_T > 10$ GeV, τότε το ονομάζουμε "large-R jet". Προκειμένου να ληφθεί υπόψη ένα γεγονός για την ανάλυσή μας, θα πρέπει: να γίνεται αποδεκτό από τουλάχιστον έναν σκανδαλιστή υψηλού επιπέδου (High Level Trigger - HLT), το κυρίαρχο (βάσει p_T) large-R jet να έχει $p_T > 450$ GeV και $m_J > 45$ GeV, το δευτερεύον (subleading) jet να έχει $p_T > 250$ GeV και τουλάχιστον ένα από τα δύο κυρίαρχα jet να είναι large-R jet. Στην περίπτωση λοιπόν, που ένα γεγονός γίνεται αποδεκτό, κατηγοριοποιείται σε τρεις περιοχές: την Περιοχή Σήματος (Signal Region - SR), την Περιοχή Επιβεβαίωσης (Validation Region - VR) και την Περιοχή Ελέγχου (Control Region - CR). Η πρώτη περιοχή αφορά jet, τα οποία περιέχουν b quarks (η ανίχνευση ενός b quark αναλύεται στην επόμενη παράγραφο). Ενα τέτοιο jet για ευκολία το ονομάζουμε b-jet. Η περιοχή σήματος χωρίζεται περαιτέρω σε κυρίαρχη (Signal Region Leading - SRL) αν το κυρίαρχο large-R jet είναι b-jet και δευτερεύουσα (Signal Region Subleading - SRS) αν το κυρίαρχο jet δεν είναι b-jet, ενώ το δευτερεύον είναι. Η VR, αφορά jet τα οποία δεν είναι b-jet και χρησιμοποιείται για να παραμετροποιήσει το υπόβαθρο QCD. Χωρίζεται, επίσης, σε κυρίαρχη περιοχή (VRL), όταν το κυρίαρχο jet δεν είναι b-jet και δευτερεύουσα (VRS) όταν τόσο το κυρίαρχο όσο και το δευτερεύον δεν είναι b-jet. Ενα βοηθητικό σχήμα είναι το 4.4. Τέλος, η περιοχή επιβεβαίωσης χρησιμοποιείται για να υπολογιστεί ο λόγος του $t\bar{t}$ υποβάθρου. Αποτελείται από γεγονότα, όπου ένα απομονωμένο μιόνιο συσχετισμένο με ένα b-jet, ανακρούσει σε ένα large-R jet. Επιπροσθέτως, η περιοχή της εγκάρσιας ορμής χωρίζεται σε τρεις υπο-περιοχές και τη συνολική η οποία καλύπτει $450 < p_T < 1250$ GeV (βλ. πίνακα 4.2). Προκειμένου να μελετήσουμε τις διάφορες διεργασίες, βασιζόμαστε σε προσομοιώσεις Monte Carlo (MC), οι οποίες αποτελούν ένα ισχυρότατο εργαλείο που χρησιμοποιείται στο CERN. Οι μελέτες πρώτα πραγματοποιούνται σε δείγματα MC, τα οποία προσομοιάζουν κάθε χρονιά λειτουργίας του ανιχνευτή μας και έπειτα επεκτείνονται σε πραγματικά δεδομένα. Στο τέλος δίνονται οι κατανομές αναλλοίωτης μάζας των δειγμάτων MC και πάνω τους εναποτίθενται τα δεδομένα για να εξεταστεί αν υπάρχει συμφωνία ή όχι με ο,τι αναμένεται από την θεωρία. Η παραγωγή των δειγμάτων MC, ξεφεύγει από τον σκοπό της παρούσας διπλωματικής. Ενα ακόμα σημαντικό ζήτημα είναι η συμμετοχή κάθε τρόπου παραγωγής του Higgs στο σήμα μας. Δύο σχετικά διαγράμματα παρουσιάζονται στο σχ. 4.6, δείχνοντας το κλάσμα συμμετοχής κάθε μεθόδου παραγωγής του Higgs, στις SRL και SRS, ως συνάρτηση της εγκάρσιας ορμής του jet. Το υπόβαθρο της ανάλυσης μας είναι κυρίως ένα φθίνον, QCD φάσμα με συνεισφορές από τα jet του μποζονίου Z. Αξίζει να σημειωθεί, ότι τα W+jets και $t\bar{t}$ υπόβαθρα τα οποία υπήρχαν στην προηγούμενη δημοσιευμένη ανάλυση, αφαιρούνται από τον αλγόριθμο που πραγματοποιεί την ανίχνευση γεύσης. Σχετικά με το QCD υπόβαθρο, αυτό μοντελοποιείται με βάση την εξίσωση 4.2 και την περιοχή VR, όπως ήδη αναφέρθηκε. Καθώς, στη συνέχεια πραγματοποιούνται στατιστικές προσαρμογές συνδυαστικά στην περιοχή σήματος και επιβεβαίωσης, προκειμένου να ληφθούν υπόψιν οι διαφορές μεταξύ των δύο αυτών περιοχών, ορίζεται επίσης μια συνάρτηση μεταφοράς (βλ. εξ. 4.3). Πριν ολοκληρώσουμε την παρούσα παράγραφο, θα αναφερθούμε τέλος, στην ανακατασκευή των αντικειμένων. Χρησιμοποιούμε αρχικά σκανδαλιστές υψηλού επιπέδου (HLT) διαφορετικούς για κάθε χρονιά, με κατώφλι στη μάζα και την εγκάρσια ορμή (εκτός από το 2015 και 2016 όπου υπήρχε μόνο περιορισμός στην εγκάρσια ορμή). Θέτουμε κατώφλι μάζας τα 45 GeV και κατώφλι p_T τα 460 GeV (χωρίς περιορισμό στη μάζα, το κατώφλι p_T είναι 420 GeV). Τα αδρονικά jet, που χρησιμοποιούνται για την αναγνώριση των προϊόντων μια σύγκρουσης, είναι Ενοποιημένα Αντικείμενα (σωματιδιακής) Ροής (Unified Flow Objects - UFOs). Βασίζονται σε πληροφορίες από τη ροή των σωματιδίων και τα θερμιδόμετρα. Η ομαδοποίηση των jet (jet clustering), πραγματοποιείται από τον αλγόριθμο anti-kT με ακτίνα R = 1.0, υλοποιημένο στο λογισμικό FastJet. Η ανακατασκευή μιονίων, βασίζεται σε συνδυαστική πληροφορία από τον εσωτερικό ανιχνευτή και το μιονικό φασματόμετρο. Ο συγκεκριμένος τρόπος ανακατασκευής ονομάζεται συνδυαστικός (combined). Όλα τα μιόνια, που χρησιμοποιήθηκαν είναι συνδυαστικά. Τέλος, στην ανακατασκευή αντικειμένων ανήκει και η ανίχνευση γεύσης, στην οποία αφιερώνεται η επόμενη παράγραφος.

Απόδοση ανίχνευσης b quark

Ο εντοπισμός των b quark στο σήμα μας, είναι εξαιρετικά σημαντικός και πραγματοποιείται από έναν αλγόριθμο (με όνομα GN2X) βασισμένο σε νευρωνικά δίκτυα τύπου transformer, μια αρχιτεκτονική που χρησιμοποιείται από αρκετά εργαλεία τεχνητής νοημοσύνης. Υπάρχουν τέσσερεις εκδόσεις του αλγορίθμου. Εκτελέστηκε συνεπώς μελέτη της απόδοσης όλων των διαφορετικών εκδόσεων του αλγορίθμου, πάνω σε δείγματα MC, συγκεκριμένα Hbb και Zbb. Η μελέτη έγινε ξεχωριστά για SRL και SRS και ξεχωριστά για κάθε περιοχή p_T. Τα αποτελέσματα συνοψίζονται στους πίνακες 4.3, 4.4 και στα αντίστοιχα διαγράμματα 4.9, 4.10. Βρέθηκε λοιπόν, ότι επιτυγχάνεται απόδοση 40-44% όταν επιλέγεται η έκδοση "GN2Xv02LLR" ανεξαρτήτως δείγματος, περιοχής p_T, ή περιοχής σήματος (SRL ή SRS). Η μελέτη επεκτάθηκε και σε διαφορετικά δείγματα MC που προσομοιάζουν τα διαφορετικά χρόνια από τα οποία η ανάλυση αντλεί δεδομένα (βλ. σχ. 4.11). Σταθερή απόδοση 40-44% εμφανίζεται κατά τα διαφορετικά έτη, με την απόδοση στην SRL να είναι ελαφρώς μεγαλύτερη. Στη συνέχεια, μελετήθηκε επίσης και η ανίχνευση b quark, στο QCD υπόβαθρο, στο οποίο αναφερόμαστε ως TagRate και παρουσιάζεται στο διάγραμμα 4.12. Αξίζει τέλος, να σημειωθεί ότι ο αλγόριθμος GN2X, εκτός από αναγνώριση των b quark, μειώνει και το κυρίαρχο υπόβαθρο της QCD, παρέχοντας μας την ευκολία να προχωρήσουμε σε ανάλυση του σήματός μας (βλ. σχ. 4.8).

Μέθοδος ανίχνευσης περιεχομένου $b\bar{b}$ στο QCD υπόβαθρο

Δεδομένου ότι ο αλγόριθμος GN2X αγνοεί την ύπαρξη των μιονίων, εξετάστηκε η ιδέα να χρησιμοποιηθεί ένα μέγεθος σχετικό με τα μιόνια, με σκοπό να υπολογιστεί (για επαλήθευση) η απόδοση του GN2X και στη συνέχεια, το περιεχόμενο $b\bar{b}$ του QCD υποβάθρου. Ως υποψήφιο μέγεθος επιλέχθηκε η εγκάρσια ορμή των μιονίων σε σχέση με τον άξονα ενός VR jet, με το οποίο έχουν συσχετιστεί. Το μέγεθος αυτό συμβολίζεται p_T^{rel} (βλ. σχ. 4.13). Βασιζόμενοι σε δείγματα MC μελετάμε την κατανομή της p_T^{rel} των μιονίων πριν την ανίχνευση γεύσης για πολλά διαφορετικά κατώφλια στην p_T των μιονίων (βλ. σχ. 4.14, 4.15). Διαχωρίζουμε τα jet σε δύο κατηγορίες ανάλογα αν περιέχουν δύο ή κανένα b quark. Επιλέγουμε ως κατάλληλο κατώφλι τα 10 GeV και προχωράμε στον σχεδιασμό των κατανομών πριν και μετά την ανίχνευση γεύσης (βλ. σχ. 4.16). Παρατηρούμε ότι οι κατανομές παραμένουν ίδιες, γεγονός που υποδεικνύει ότι το εν λόγω μέγεθος παραμένει αναλλοίωτο, κατά την ανίχνευση γεύσης και άρα είναι πράγματι κατάλληλο για τον υπολογισμό της απόδοσης του GN2X. Οι κατανομές έχουν επίσης την αναμενόμενη μορφή, τα jet χωρίς b quark έχουν κατανομή πιο στενή και συγκεντρωμένη πιο κοντά στο μηδέν, ενώ τα jet με δύο b quark παρουσιάζουν κατανομές με μεγαλύτερο πλάτος και μέση τιμή πιο απομακρυσμένη από το μηδέν. Στη συνέχεια επεκτείνουμε την μελέτη και σε MC δείγματα QCD. Χρησιμοποιούμε και πάλι 10 GeV ως κατώφλι για την p_T των μιονίων, ωστόσο αυτή τη φορά χωρίζουμε τα jet σε τρεις κατηγορίες, ανάλογα αν περιέχουν μηδέν, ένα ή δύο b quark αντίστοιχα. Σχεδιάζουμε τις κατανομές πριν και μετά την ενέργεια του GN2X (βλ. σχ. 4.17). Παρατηρούμε και στην περίπτωση αυτή, ότι οι κατανομές δεν επηρεάζονται από τη δράση του GN2X, με αποτέλεσμα η p_T^{rel} των μιονίων να αποτελεί κατάλληλο μέγεθος για να εξεταστεί το περιεχόμενο $b\bar{b}$ στο υπόβαθρο QCD. Πρόκειται για μια υποσχόμενη μέθοδο, η οποία βρίσκεται ακόμα σε εξέλιξη.

Μελέτη της Διακριτικής Ικανότητας Μάζας

Η διακριτική ικανότητα (resolution) στις κατανομές αναλλοίωτης μάζας στα δείγματα MC, είναι πρωταρχικής σημασίας για την ποιότητα του αποτελέσματός μας. Αυτό διότι, οι στατιστικές προσαρμογές που πραγματοποιούνται για την εξαγωγή του τελικού μας αποτελέσματος, βασίζονται στα δείγματα MC. Η διακριτική ικανότητα εκφράζεται μέσω του πλάτους των κατανομών αναλλοίωτης μάζας, δηλαδή όσο πιο μικρό το πλάτος τόσο καλύτερη η διακριτική ικανότητα. Η θέση της κορυφής της κατανομής αποτελεί ένδειξη της μάζας του αρχικού σωματιδίου και κατέχει εξίσου σημαντική θέση στην ανάλυση. Οι κατανομές αναλλοίωτης μάζας (βλ. σχ. 5.2), έχουν Γκαουσιανό σχήμα (βλ. σχ. 5.1). Επομένως για τη μελέτη της διακριτικής ικανότητας, βασιζόμαστε στα μεγέθη: Μέση τιμή (Most Probable Value - MPV) που ορίζεται από τη σχέση 5.2, διασπορά ή τυπική απόκλιση (Root Mean Square

- RMS), της οποίας το τετράγωνο ορίζεται από την σχέση 5.3 και πλάτος στο μισό του μέγιστου ύψους της κατανομής (Full Width Half Maximum - FWHM), το οποίο σχετίζεται με την RMS, μέσω της έκφρασης 5.4. Σκοπός είναι, λοιπόν να μελετήσουμε τα μεγέθη αυτά για MC δείγματα Zbb, συναρτήσει διαφορετικών σημείων εργασίας της ανίχνευσης b κουάρκ. Συγκεκριμένα χρησιμοποιείται το WP: HybridBEff, για αποδόσεις: 10%, 20%, 30%, 40%, 50% , 60%, 69%, 77%, 85%. Η μελέτη επίσης πραγματοποιείται ξεχωριστά σε κάθε περιοχή σήματος και p_T. Προς τούτου, αναπτύσσεται μια συνάρτηση, η οποία με είσοδο μια κατανομή, υπολογίζει αρχικά την μέγιστη τιμή της. Στη συνέχεια εντοπίζονται οι δύο κλάσεις (bin 1 και bin 2), οι οποίες είναι η πρώτη και η τελευταία κλάση, όπου η κατανομή έχει τιμή πάνω από το μισό του μεγίστου. Πραγματοποιείται ακολούθως μια τοπική Γκαουσιανή προσαρμογή στην περιοχή της κορυφής (κέντρο bin 1, κέντρο bin 2), με στόχο μια καλύτερη εκτίμηση της μέγιστης τιμής. Σε περίπτωση σημαντικής διαφοράς των δύο εκτιμήσεων, η τιμή της κορυφής της κατανομής ανανεώνεται και οι κλάσεις bin1, bin2 υπολογίζονται εκ νέου. Στη συνέχεια, εφαρμόζεται γραμμική παρεμβολή στα διαστήματα (bin1 - 1, bin1) και (bin2, bin2 + 1), όπου εξάγονται οι τιμές x_1, x_2 για τις οποίες ισχύει: $f(x_1) = f(x_2) = \frac{f_{max}}{2}$. Το FWHM, υπολογίζεται απευθείας ως: $FWHM = x_2 - x_1$, ενώ τα RMS και MPV λαμβάνονται από μια δεύτερη Γκαουσιανή προσαρμογή, σε μια πιο ευρεία περιοχή από την αρχική. Τελικά, η συνάρτηση επιστρέφει το σ μέσω του FWHM και τιμές RMS και MPV. Πριν την παρουσίαση των αποτελεσμάτων σημειώνεται, ότι η μάζα των jets μπορεί να ανακατασκευαστεί με δύο τρόπους: είτε με χρήση της πληροφορίας ροής σωματιδίων (PFlow mass), που αποτελεί τη συμβατική μέθοδο, είτε με ένα νέο μοντέλο παλινδρόμησης (bJR mass). Αναφορικά με το bJR μοντέλο, αυτό βασίζεται στον ίδιο αλγόριθμο που πραγματοποιεί την ανίχνευση γεύσης (τον GN2X), ο οποίος εκτελείται έπειτα από την ανακατασκευή με την συμβατική μέθοδο (PFlow). Ο αλγόριθμος αξιοποιεί τα κινηματικά χαρακτηριστικά του jet και πληροφορίες από ίχνη, ενσωματώνοντας τόσο φορτισμένα όσο και ουδέτερα συστατικά. Προβλέπει τον λόγο μεταξύ των πραγματικών και βαθμονομημένων τιμών της εγκάρσια; ορμής (p_T) και της μάζας m_J, και εφαρμόζει τη διόρθωση αυτή για να βελτιώσει την εκτίμηση της πραγματικής κινηματικής του jet. Μια σύγκριση δύο κατανομών (για SRL και SRS) με χρήση τόσο των PFlow μαζών όσο και των bJR μαζών, παρατίθεται στο σχήμα 5.3. Είναι φανερό, ότι οι μάζες bJR παρουσιάζουν μια πιο στενή κατανομή (με καλύτερη επομένως διακριτική ικανότητα) και με πιο κοντινή στην επιθυμητή μέση τιμή. Τα αποτελέσματά αναφορικά με τη διασπορά σ μέσω του FWHM και της RMS, παρουσιάζονται στα διαγράμματα 5.4, 5.5. Υπάρχει αρκετά καλή ταύτιση μεταξύ των δύο εκτιμήσεων (σ και RMS) και για τις δύο περιοχές. Ακόμη, όλες οι περιοχές p_T έχουν παραπλήσιες τιμές σ και RMS. Τέλος, οι τιμές στην SRS, είναι μεγαλύτερες (κατά περίπου 20%) από αυτές της SRL. Στη συνέχεια, στο σχήμα 5.6, παρουσιάζεται μια ελαφρά αύξηση του MPV συναρτήσει της απόδοσης του σημείου εργασίας. Όλες οι περιοχές p_T, έχουν παραπλήσιες τιμές. Για την SRS, οι MPV είναι περίπου 80 - 86 GeV και είναι χαμηλότερες από τις τιμές για την SRL, που είναι περίπου 90 GeV, το οποίο είναι και το επιθυμητό. Ο λόγος που τα SRS jet έχουν χαμηλότερη MPV θα γίνει κατανοητός στην επόμενη παράγραφο. Τέλος, στο σχήμα 5.7, παρουσιάζονται οι τιμές RMS των bJR μαζών, οι οποίες ακολουθούν την ίδια συμπεριφορά με τις PFlow μάζες, ωστόσο είναι περίπου 20% μικρότερες από τις αντίστοιχες RMS των PFlow μαζών. Στο σημείο αυτό, επεκτείνουμε τη μελέτη μας και σε άλλες εκστρατείες MC, οι οποίες προσομοιάζουν διαφορετικές χρονιές λήψης δεδομένων. Στο σχήμα 5.9 απεικονίζεται η σταθερή συμπεριφορά της RMS, συναρτήσει των διαφορετικών χρονιών τις οποίες προσομοιάζουν τα MC δείγματα μας. Οι τιμές στην SRS, είναι κατά 20% περίπου υψηλότερες από αυτές της SRL. Όπως επίσης φαίνεται στο σχήμα 5.11, η τιμή MPV διατηρείται σε σταθερά επίπεδα μεταξύ των διαφορετικών ετών. Στα σχήματα 5.10 και 5.12 δίνονται τα αντίστοιχα διαγράμματα για τις bJR μάζες. Τέλος, στα σχήματα 5.13 έως 5.16, απεικονίζονται τα αντίστοιχα μεγέθη για κατανομές reco mass - truth mass. Στις κατανομές αυτές δηλαδή (βλ. σχ. 5.8), υπολογίζεται η διαφορά μεταξύ πραγματικής και ανακατασκευασμένης μάζας, με σκοπό να αξιολογηθεί η απόδοση της ανακατασκευής.

Διόρθωση Muon-In-Jet

Τα μιόνια έχοντας μέσο χρόνο ζωής $2.2\mu s$, διανύουν μια μέση απόσταση 658m προτού διασπαστούν. Συνεπώς, αρκετά μιόνια "δραπετεύουν" από τα πρώτα στάδια του ανιχνευτή και μετριούνται τελικά από το μιονικό φασματόμετρο (το οποίο βρίσκεται εξωτερικά των θερμιδόμετρων). Συνεπώς, καθώς τα jet ανακατασκευάζονται με πληροφορίες από τα θερμιδόμετρα, δημιουργείται ένα έλλειμμα ενέργειας σε jet τα οποία περιέχουν μιόνια, καθώς αυτά δεν λαμβάνονται υπόψη στην ανακατασκευή του jet. Τα b-jet στην ανάλυση μας, είναι αρκετά δεδομένου ότι ο λόγος διακλάδωσης του Higgs σε $b\bar{b}$ είναι 58% και αντιστοίχως $BR(Z \to b\bar{b}) = 15\%$ (βλ. σχ. 6.1). Ακόμα, ισχύουν $BR(b \to \mu\nu X) \approx 10\%$ και $BR(b \to c \to \mu\nu X) \approx 10\%$. Δηλαδή, 20% περίπου των b quark διασπώνται ημι-λεπτονικά παράγοντας ένα μιόνιο, ένα αντινετρίνο μιονίου και ένα c quark, όπως φαίνεται στο διάγραμμα Feynman 6.2. Το φαινόμενο αυτό είναι κυρίαρχο στην δευτερεύουσα περιοχή σήματος (SRS). Επομένως, σε αρκετές περιπτώσεις υπάρχει απώλεια ενέργειας κατά την ανακατασκευή των jet, γεγονός που χειροτερεύει την διακριτική ικανότητα μάζας. Συγκεκριμένα, εξαιτίας αυτού του φαινομένου, οι κατανομές αναλλοίωτης μάζας αποκτούν μεγαλύτερο πλάτος (χειρότερη διακριτική ικανότητα) και μετατοπίζονται προς χαμηλότερες μέσες τιμές μάζας από τις επιθυμητές (βλ. σχ. 6.4). Αναπτύσσουμε συνεπώς, μια διόρθωση Muon-In-Jet με στόχο να λάβουμε υπόψη την ενέργεια των μιονίων που σχετίζονται με τα jet και να βελτιώσουμε την ποιότητα του αποτελέσματός μας. Είναι σημαντικό να τονιστεί, ότι δεν αναπληρώνουμε πλήρως τη "χαμένη" ενέργεια, καθώς μέρος αυτής μεταφέρεται από το νετρίνο, για το οποίο δεν θα πραγματοποιηθεί καμία διόρθωση. Αρχικά ορίζουμε το ποσοστό διόρθωσης (Correction Rate, εξίσωση 6.2) και ποσοστό ψευδών διορθώσεων (Mistag Rate, εξίσωση 6.3), τα οποία θα μας βοηθήσουν να βελτιστοποιήσουμε τη διόρθωση, η οποία δίνεται από τη σχέση 6.1. Εξετάζουμε δύο διαφορετικές μεθόδους, η πρώτη βασισμένη σε large-R jet και η δεύτερη βασισμένη σε VR jet (η οποία εφαρμόστηκε και στην προηγούμενη ανάλυση του Run 2). Τα μιόνια πρέπει να ικανοποιούν τις συνθήκες 6.7 ή 6.11, αντίστοιχα για τις δύο μεθόδους. Και στις δύο περιπτώσεις κατά την μελέτη MC δειγμάτων, όταν τα μιόνια δεν ταυτίζονται με τα truth μιόνια (δηλαδή, δεν ικανοποιούν τις συνθήκες 6.8 και 6.9) ή δεν προέρχονται από b ή c κούαρκ, η διόρθωση θεωρείται ότι δεν θα έπρεπε να πραγματοποιηθεί και αυτό λαμβάνεται υπόψη από το ποσοστό ψευδών διορθώσεων. Μελετάμε και για τις δύο μεθόδους, τα ποσοστά διόρθωσης και ψευδών διορθώσεων συναρτήσει διαφορετικών κατωφλιών στην εγκάρσια ορμή των μιονίων. Για την πρώτη μέθοδο τα διαγράμματα είναι: 6.7, 6.8 για το Hbb δείγμα και 6.13, 6.14 για το Zbb δείγμα. Τα ποσοστά διόρθωσης είναι διπλάσια στην SRS από την SRL και μειώνονται καθώς αυξάνεται η ελάχιστη p_T των μιονίων. Αντίστοιχα, τα ποσοστά ψευδούς διόρθωσης είναι μεγαλύτερα στην SRS από την SRL (λιγότερο όμως από διπλάσια) και μειώνονται συναρτήσει της ελάχιστης p_T των μιονίων. Στο δείγμα Zbb επιτυγχάνονται ελαφρώς μεγαλύτερα ποσοστά από το Hbb. Για τη δεύτερη μέθοδο που βασίζεται σε VR jet, τα αντίστοιχα διαγράμματα είναι: 6.21, 6.22 για το Hbb δείγμα και 6.23, 6.24 για το Zbb. Μια λεπτομερής σύγκριση των δύο μεθόδων (βλ. 6.6) υποδεικνύει ότι η δεύτερη είναι βέλτιστη. Επιλέγεται ελάχιστη τιμή $p_T = 10$ GeV για την εγκάρσια ορμή των μιονίων και αποφασίζεται η διόρθωση να εφαρμόζεται μόνο στην δευτερεύουσα (SRS) περιοχή. Τα ποσοστά διόρθωσης και ψευδούς διόρθωσης, για το Hbb δείγμα, είναι λοιπόν 0.3 και 0.11, αντιστοίχως. Προς σύγκριση (βλ. και πίνακα 6.17), τα αντίστοιχα ποσοστά για την προηγούμενη δημοσιευμένη ανάλυση ήταν: 0.33 και 0.022. Παρατηρούμε λοιπόν, ότι έχουμε ελαφρώς μικρότερο ποσοστό διόρθωσης με πέντε φορές, όμως, μεγαλύτερο ποσοστό ψευδών διορθώσεων. Η μελέτη της διόρθωσης επεκτείνεται και σε δείγμα MC QCD καθώς και σε $10 fb^{-1}$ από δεδομένα του 2022. Μια σύγκριση των ποσοστών διόρθωσης για SRL και SRS, ανάμεσα στα διαφορετικά MC δείγματα και τα $10\,\mathrm{fb}^{-1}$ από τα δεδομένα του 2022 παρουσιάζεται στον πίνακα 6.16. Εμφανίζεται αρκετά καλή συμφωνία μεταξύ MC και δεδομένων, με διπλάσια περίπου ποσοστά στην SRS από την SRL. Στη συνέχεια η μελέτη ποσοστού διορθώσεων και λανθασμένων διορθώσεων επεκτείνεται και σε MC Hbb δείγματα, τα οποία προσομοιάζουν τα διαφορετικά χρόνια από τα οποία λαμβάνει δεδομένα η ανάλυση (βλ. 6.7). Σταθερή συμπεριφορά παρουσιάζουν και τα δύο ποσοστά συναρτήσει των διαφορετικών MC εκστρατειών, με CorrRate(SRS) = 0.3 και MR(SRS) = 0.11-0.14. Ομοίως μελετάται ανά τα χρόνια και η διακριτική ικανότητα μάζας (μέσω της RMS) καθώς και η μέση τιμή (MPV) των κατανομών αναλλοίωτης μάζας για PFlow και bJR jet, πριν και μετά τη διόρθωση στην SRS (βλ. 6.8). Συγκεκριμένα, παρατηρείται 10% μείωση στις τιμές RMS και 1.6-2.5% αύξηση στις τιμές MPV μετά την διόρθωση. Ενα σημαντικό πρόβλημα, με το οποία ήρθαμε αντιμέτωποι, ήταν ότι μετά την εφαρμογή της διόρθωσης στα δεδομένα (ή στο MC QCD δείγμα), αρκετά γεγονότα από την πρώτη κλάση (για τον σχεδιασμό των ιστογραμμάτων το διάστημα μάζας 60-160 GeV, χωρίζεται σε κλάσεις των 5 GeV), μετατοπίζονται προς υψηλότερες τιμές μάζας (βλ. 6.19). Ως αποτέλεσμα, η πρώτη κλάση εμφανίζεται με λιγότερα γεγονότα, από ο,τι θα περιμέναμε. Επομένως, μπορούμε να μειώσουμε την ελάχιστη μάζα, την οποία τα large-R jet πρέπει να έχουν για να επιλεχθούν από τον σκανδαλιστή υψηλού επιπέδου (HLT) από 60 GeV που ήταν αρχικά σε 45 GeV. Ετσι, η πρώτη κλάση (60-65 GeV) θα καλύπτεται από γεγονότα των χαμηλότερων κλάσεων (45 - 60 GeV), οι οποίες, όμως, δεν απεικονίζονται στα διαγράμματα μας, καθώς δεν είναι στην περιοχή ενδιαφέροντός μας. Αυτή η επιλογή ελάχιστη μάζας είναι συνεπής με την απόκριση των σκανδαλιστών, καθώς για 45 GeV βρισκόμαστε στο σταθερό τμήμα της γραφικής παράστασης (βλ. 6.20), γεγονός απαραίτητο για ομαλή λειτουργία. Μετά την ολοκλήρωση της μελέτης βελτιστοποίησης της διόρθωσης MIJ, αυτή εντάσσεται στην ανάλυσή μας. Πραγματοποιείται στατιστική προσαρμογή (statistical fit), σε $10\,\mathrm{fb}^{-1}$ από δεδομένα του 2022 [1], με σκοπό να εξαχθεί η στατιστική αβεβαιότητα του σήματος ισχύος του μποζονίου Z (μ_Z), πριν και μετά τη διόρθωση (βλ. σχ. 6.31). Το αποτέλεσμα είναι 15% μείωση της εν λόγω αβεβαιότητας με την εφαρμογή της διόρθωσης, γεγονός που επισφραγίζει την επιτυχία της. Η διόρθωση, λοιπόν, πράγματι επιτυγχάνει τους στόχους της και θα ενσωματωθεί σε όλα τα δείγματα MC και σύνολα δεδομένων.

[1] Να σημειωθεί ότι τα δεδομένα του μποζονίου Higgs (δηλαδή δεδομένα στο εύρος μάζας 105 - 140 GeV) καλύπτονται και δεν είναι φανερά, λόγω σχετικής πολιτικής του ATLAS, για αναλύσεις που βρίσκονται ακόμα σε εξέλιξη.

Bibliography

[1] ATLAS Collaboration, "Constraints on Higgs boson production with large transverse momentum using $H \to b\bar{b}$ decays in the ATLAS detector," *Phys. Rev. D*, vol. 105, no. 9, p. 092003, May 2022, doi: 10.1103/PhysRevD.105.092003. (cit. on pp. 21, 71, 76, 98, 100, and 125)

[2] J. Chadwick, "The existence of a neutron," *Proc. R. Soc. Lond. A*, vol. 136, no. 830, pp. 692–708, Jun. 1932, doi: 10.1098/rspa.1932.0112. (cit. on p. 23)

[3] C. D. Anderson, "The apparent existence of easily deflectable positives," *Science*, vol. 76, no. 1967, pp. 238–239, Sep. 1932, doi: 10.1126/science.76.1967.238. (cit. on p. 23)

[4] P. A. M. Dirac, "The quantum theory of the electron," *Proc. R. Soc. Lond. A*, vol. 117, no. 778, pp. 610–624, Feb. 1928, doi: 10.1098/rspa.1928.0023. (cit. on p. 23)

[5] "Worldwide particle physics discoveries," Fermi National Accelerator Laboratory, [Online]. Available: `https://www.fnal.gov/pub/science/particle-physics-101/worldwide-discoveries.html` (Accessed: Apr. 29, 2025). (cit. on p. 23)

[6] F. Halzen and A. D. Martin, *Quarks and Leptons*. John Wiley & Sons, 1984. (cit. on pp. 18, 23, 25, 27, 30, 31, 34, 36, 37, 40, and 44)

[7] B. R. Martin, *Particle Physics*. John Wiley & Sons Canada, Ltd., 2017. (cit. on pp. 13, 23, 25, 26, 29, 30, 31, 32, 33, 34, 48, and 49)

[8] A. Bettini, *Introduction to Elementary Particle Physics*. Cambridge University Press, 2014. (cit. on pp. 23, 25, 28, 29, and 30)

[9] R. A. Serway, C. J. Moses, and C. A. Moyer, *Modern Physics*. Beijing: Tsinghua University Press, 2008. (cit. on pp. 23, 26, 28, 32, and 33)

[10] H. D. Young and R. A. Freedman, *University Physics with Modern Physics*. Addison Wesley Longman, 2003. (cit. on pp. 18, 23, 27, and 28)

[11] G. Kane, *Modern Elementary Particle Physics*, 2nd ed. Cambridge, UK: Cambridge University Press, 2017. (cit. on pp. 23, 26, 32, and 40)

[12] J. Iliopoulos and T. N. Tomaras, *Elementary Particle Physics: The Standard Theory*. Oxford Academic, 2021, doi:10.1093/oso/9780192844200.001.0001. (cit. on pp. 23, 37, 39, and 40)

[13] M. Robinson, *Symmetry and the Standard Model*. Springer, New York, NY, 2011, doi:10.1007/978-1-4419-8267-4. (cit. on pp. 23, 31, 32, 34, 37, and 40)

[14] J. D. Vergados, *The Standard Model and Beyond*. New Jersey: World Scientific, 2018. (cit. on pp. 23 and 28)

[15] M. Gell-Mann, "A schematic model of baryons and mesons," *Physics Letters*, vol. 8, no. 3, pp. 214–215, 1964, doi: 10.1016/S0031-9163(64)92001-3. (cit. on p. 24)

[16] G. Zweig, "An SU(3) model for strong interaction symmetry and its breaking. Version 2," in *Developments in the Quark Theory of Hadrons, Vol. 1: 1964–1978*, D. B. Lichtenberg and S. P. Rosen, Eds. CERN, 1964, pp. 22–101, CERN-TH-412, doi: 10.17181/CERN-TH-412. (cit. on p. 24)

[17] LHCb Collaboration, "Observation of structure in the J/ψ-pair mass spectrum," *Science Bulletin*, vol. 65, no. 23, pp. 1983–1993, Dec. 2020, doi: 10.1016/j.scib.2020.08.032. (cit. on p. 25)

[18] R. Aaij *et al.*, "Observation of $J/\psi p$ resonances consistent with pentaquark states in $\Lambda_b^0 \to J/\psi K^- p$ decays," *Phys. Rev. Lett.*, vol. 115, no. 7, Aug. 2015, doi: 10.1103/PhysRevLett.115.072001. (cit. on p. 25)

[19] P. Koppenburg, "New particles discovered at the LHC," *Koppenburg.ch*, 2015. [Online]. Available: `https://www.koppenburg.ch/particles.html`. (cit. on p. 25)

[20] C. L. Cowan, F. Reines, F. B. Harrison, H. W. Kruse, and A. D. McGuire, "Detection of the free neutrino: A confirmation," *Science*, vol. 124, pp. 103–104, 1956, doi:10.1126/science.124.3212.103. (cit. on p. 25)

[21] Y. Fukuda *et al.*, "Evidence for oscillation of atmospheric neutrinos," *Phys. Rev. Lett.*, vol. 81, no. 8, pp. 1562–1567, Aug. 1998, doi:10.1103/physrevlett.81.1562. (cit. on p. 25)

[22] M. Aker *et al.*, "Direct neutrino-mass measurement based on 259 days of KATRIN data," *arXiv preprint* arXiv: 2406.13516, 2024. [Online]. Available: `https://arxiv.org/abs/2406.13516`. (cit. on p. 25)

[23] NASA, "Overview – NASA Science," *science.nasa.gov*, 2024. [Online]. Available: `https://science.nasa.gov/universe/overview/#big-bang`. (Accessed: May 04, 2025). (cit. on p. 28)

[24] E. Noether, "Invariant variation problems," *Transport Theory and Statistical Physics*, vol. 1, no. 3, pp. 186–207, Jan. 1971, doi:10.1080/00411457108231446. (cit. on p. 32)

[25] C. S. Wu, E. Ambler, R. W. Hayward, D. D. Hoppes, and R. P. Hudson, "Experimental test of parity conservation in beta decay," *Phys. Rev.*, vol. 105, no. 4, pp. 1413 (cit. on p. 33)

[26] A. Basalaev, "Evidence for Higgs boson decays to a low mass lepton pair and a photon with the ATLAS detector at the LHC," thesis, Hamburg University, 2021. [Online]. Available: `https://cds.cern.ch/record/2798268`. (cit. on pp. 13 and 39)

[27] C. M. Helling, "Search for the decay of Higgs bosons at high transverse momentum in the $\mathrm{H} \to b\bar{b}$ channel with the ATLAS detector," Ph.D. thesis, UC Santa Cruz, 2021. [Online]. Available: `https://escholarship.org/uc/item/3w69g61b`. (cit. on pp. 19, 39, 58, 76, 97, 98, 100, 101, 102, 104, and 116)

[28] J. Goldstone, A. Salam, and S. Weinberg, "Broken symmetries," *Phys. Rev.*, vol. 127, no. 3, pp. 965–970, Aug. 1962, doi:10.1103/PhysRev.127.965. (cit. on p. 40)

[29] A. Djouadi, "The anatomy of electroweak symmetry breaking," *Physics Reports*, vol. 457, no. 1–4, Feb. 2008, doi:10.1016/j.physrep.2007.10.004. (cit. on pp. 40, 46, and 48)

[30] P. Woit, *Quantum Theory, Groups and Representations*. Springer Cham, 2017, doi:10.1007/978-3-319-64612-1. (cit. on p. 40)

[31] J. Ellis, M. K. Gaillard, and D. V. Nanopoulos, "A historical profile of the Higgs boson," in *The Standard Theory of Particle Physics*, L. Maiani and G. Rolandi, Eds. World Scientific, 2016, pp. 255–274, doi:10.1142/9789814733519_0014. (cit. on pp. 13 and 41)

[32] S. Navas *et al.*, "Review of particle physics," *Phys. Rev. D*, vol. 110, no. 3, p. 030001, 2024, doi:10.1103/PhysRevD.110.030001. (cit. on pp. 18, 41, 44, 46, 47, 48, 78, 97, and 100)

[33] P. W. Higgs, "Broken symmetries and the masses of gauge bosons," *Phys. Rev. Lett.*, vol. 13, no. 16, pp. 508–509, Oct. 1964, doi:10.1103/PhysRevLett.13.508. (cit. on p. 44)

[34] P. W. Higgs, "Spontaneous symmetry breakdown without massless bosons," *Phys. Rev.*, vol. 145, no. 4, pp. 1156–1163, May 1966, doi:10.1103/PhysRev.145.1156. (cit. on p. 44)

[35] F. Englert and R. Brout, "Broken symmetry and the mass of gauge vector mesons," *Phys. Rev. Lett.*, vol. 13, no. 9, pp. 321–323, Aug. 1964, doi:10.1103/PhysRevLett.13.321. (cit. on p. 44)

[36] TEVNPH Working Group, "Combined CDF and D0 Search for Standard Model Higgs Boson Production with up to 10.0 fb^{-1} of Data," arXiv:1203.3774 [hep-ex], 2012. Available: `https://arxiv.org/abs/1203.3774`. (cit. on p. 44)

[37] "Physics Letters B," vol. 565, pp. 61–75, Jul. 2003. doi: 10.1016/S0370-2693(03)00614-2. (cit. on p. 44)

[38] "CERN experiments observe particle consistent with long-sought Higgs boson," *CERN*, Jul. 2012. [Online]. Available: `https://home.cern/news/press-release/cern/cern-experiments-observe-particle-consistent-long-sought-higgs-boson`. (cit. on p. 44)

[39] G. Aad *et al.* [ATLAS Collaboration], "Observation of a new particle in the search for the Standard Model Higgs boson with the ATLAS detector at the LHC," *Phys. Lett. B*, vol. 716, no. 1, pp. 1–29, Sep. 2012. doi: 10.1016/j.physletb.2012.08.020. (cit. on pp. 44 and 47)

[40] S. Chatrchyan *et al.*, "Observation of a new boson at a mass of 125 GeV with the CMS experiment at the LHC," *Phys. Lett. B*, vol. 716, no. 1, pp. 30–61, Sep. 2012, doi: 10.1016/j.physletb.2012.08.021. (cit. on pp. 44 and 47)

[41] The Nobel Prize in Physics 2013, *NobelPrize.org*, 2013. [Online]. Available: `https://www.nobelprize.org/prizes/physics/2013/press-release/` (Accessed: Apr. 12, 2025). (cit. on p. 44)

[42] S. Dawson *et al.*, "Handbook of LHC Higgs Cross Sections: 1. Inclusive Observables," *CERN, Geneva, Switzerland*, 2011. doi: 10.5170/CERN-2011-002. (cit. on pp. 18, 44, and 46)

[43] B. Mellado *et al.*, "Handbook of LHC Higgs Cross Sections: 2. Differential Distributions", *CERN, Geneva, Switzerland*, 2012. [Online]. doi: 10.5170/CERN-2012-002. (cit. on pp. 18, 44, and 46)

[44] C. T. Potter *et al.*, "Handbook of LHC Higgs Cross Sections: 3. Higgs Properties: Report of the LHC Higgs Cross Section Working Group", *CERN, Geneva, Switzerland*, 2013. doi: 10.5170/CERN-2013-004. (cit. on pp. 18, 44, and 46)

[45] CERN, "Handbook of LHC Higgs Cross Sections: 4. Deciphering the Nature of the Higgs Sector", CERN Yellow Reports: Monographs, vol. 2, *CERN, Geneva, Switzerland*, 2017. doi: 10.23731/CYRM-2017-002. (cit. on pp. 18, 44, and 46)

[46] K. Becker *et al.*, "Precise predictions for boosted Higgs production," *SciPost Phys. Core*, vol. 7, no. 1, 2024, doi: 10.21468/scipostphyscore.7.1.001. (cit. on pp. 18 and 46)

[47] "LHC Higgs Working Group", *CERN*, 2025. [Online]. Available: https://twiki.cern.ch/twiki/bin/view/LHCPhysics/HiggsXSBR (Accessed: Apr. 29, 2025). (cit. on pp. 13 and 47)

[48] J. Ellis, "Supersymmetry and Grand Unification," arXiv:hep-ph/9512335, 1995. Available: https://arxiv.org/abs/hep-ph/9512335 (cit. on p. 48)

[49] C. Csáki, "The minimal supersymmetric standard model," *Mod. Phys. Lett. A*, vol. 11, no. 08, pp. 599–613, Mar. 1996, doi: 10.1142/S021773239600062X. (cit. on p. 48)

[50] K. Kang, "Introduction to grand unification theories," in *Proc. 15th Rencontres de Moriond: II: Electroweak and Unified Theory Predictions*, 1980, pp. 413–426, report no. BROWN-HET-423, C80-03-09-7. (cit. on p. 48)

[51] D. V. Nanopoulos, "Grand unified theories: A fresh look," *Phys. Scripta*, vol. 24, p. 873, 1981, doi: 10.1088/0031-8949/24/5/011. (cit. on p. 48)

[52] R. Penco, "An introduction to effective field theories," arXiv:2006.16285 [hep-th], 2020. Available: https://arxiv.org/abs/2006.16285. (cit. on p. 49)

[53] "Our History | CERN," *Home.cern*, Oct. 11, 2019. [Online]. Available: https://home.cern/about/who-we-are/our-history (Accessed: Mar. 06, 2025). (cit. on p. 50)

[54] "CERN's first accelerator - the Synchrocyclotron - starts up | timeline.web.cern.ch," *timeline.web.cern.ch*. [Online]. Available: https://timeline.web.cern.ch/cerns-first-accelerator-synchrocyclotron-starts (Accessed: Mar. 10, 2025). (cit. on p. 50)

[55] CERN, "Member States | CERN," *Home.cern*, Sep. 23, 2019. [Online]. Available: https://home.cern/about/who-we-are/our-governance/member-states (Accessed: Mar. 22, 2025). (cit. on p. 50)

[56] CERN, *CERN Annual Report 2023*. Geneva: CERN, 2024. doi: 10.17181/AnnualReport2023. (cit. on p. 50)

[57] O. S. Brüning, P. Collier, P. Lebrun, S. Myers, R. Ostojic, J. Poole, and P. Proudlock, *LHC Design Report*. Geneva: CERN, 2004. CERN Yellow Reports: Monographs. doi: 10.5170/CERN-2004-003-V-1 (cit. on pp. 13, 51, 52, and 53)

[58] CERN, "Facts and figures about the LHC," *Home.cern*. [Online]. Available: https://home.cern/resources/faqs/facts-and-figures-about-lhc (Accessed: Mar. 10, 2025). (cit. on p. 51)

[59] G. Arduini *et al.*, "LHC Upgrades in preparation of Run 3," *J. Instrum.*, vol. 19, no. 05, p. P05061, 2024. doi: 10.1088/1748-0221/19/05/P05061. (cit. on pp. 13, 51, 52, and 53)

[60] ATLAS Collaboration, *ATLAS Detector and Physics Performance: Technical Design Report, Volume 1*, CERN, Geneva, Tech. Des. Rep. ATLAS, 1999. [Online]. Available: https://cds.cern.ch/record/391176. (cit. on pp. 51, 55, 56, and 59)

[61] ATLAS Collaboration, "The ATLAS experiment at the CERN Large Hadron Collider," *JINST*, vol. 3, p. S08003, 2008, doi:10.1088/1748-0221/3/08/S08003. (cit. on pp. 14, 51, 55, 56, 59, 60, 61, 62, and 64)

[62] CMS Collaboration, "CMS Physics: Technical Design Report Volume 1: Detector Performance and Software," CERN-LHCC-2006-001 / CMS-TDR-8-1, 2006, doi:10.2172/2510878. (cit. on p. 51)

[63] CMS Collaboration, "CMS Technical Design Report, Volume II: Physics performance," *J. Phys. G*, vol. 34, no. 6, pp. 995–1579, 2007, doi:10.1088/0954-3899/34/6/S01. (cit. on p. 51)

[64] ALICE Collaboration, "The ALICE experiment at the CERN LHC," *J. Instrum.*, vol. 3, no. 08, p. S08002, Aug. 2008, doi:10.1088/1748-0221/3/08/S08002. (cit. on p. 51)

[65] LHCb Collaboration, "The LHCb detector at the LHC," *JINST*, vol. 3, p. S08005, 2008, doi:10.1088/1748-0221/3/08/S08005. (cit. on p. 51)

[66] *The Accelerator complex*, CERN, [Online]. Available: `https://home.cern/science/accelerators/accelerator-complex` (Accessed: Mar. 16, 2025). (cit. on p. 52)

[67] C. Zannini *et al.*, "Beam performance with the LHC injectors upgrade," *JACoW HB*, vol. 2023, pp. 1–8, 2024. [Online]. Available: `https://cds.cern.ch/record/2900871`. (cit. on p. 52)

[68] *Superconductivity*, Encyclopædia Britannica, Encyclopædia Britannica, Inc. [Online]. Available: `https://www.britannica.com/science/superconductivity`. (Accessed: Apr. 1, 2025). (cit. on p. 52)

[69] ATLAS Collaboration, "ATLAS Luminosity Public Results Run 2," *CERN TWiki*. [Online]. Available: `https://twiki.cern.ch/twiki/bin/view/AtlasPublic/LuminosityPublicResultsRun2`. (Accessed: Apr. 7, 2025). (cit. on pp. 13, 14, 54, and 55)

[70] CERN, "High-Luminosity LHC," *CERN*, [Online]. Available: `https://home.cern/science/accelerators/high-luminosity-lhc` (Accessed: Jun. 9, 2025). (cit. on pp. 54 and 70)

[71] ATLAS Collaboration, "ATLAS Public Data Quality Results," *CERN TWiki*. [Online]. Available: `https://twiki.cern.ch/twiki/bin/view/AtlasPublic/DataQualityResults`. (Accessed: Apr. 7, 2025). (cit. on pp. 13 and 54)

[72] The ATLAS Collaboration, "The ATLAS experiment at the CERN Large Hadron Collider: a description of the detector configuration for Run 3," *Journal of Instrumentation*, vol. 19, no. 05, p. P05063, May 2024. [Online]. doi: 10.1088/1748-0221/19/05/P05063. (cit. on pp. 54, 56, 57, 61, 62, and 68)

[73] ATLAS Collaboration, "ATLAS Luminosity Public Results Run 3," *CERN TWiki*. [Online]. Available: `https://twiki.cern.ch/twiki/bin/view/AtlasPublic/LuminosityPublicResultsRun3`. (Accessed: Apr. 7, 2025). (cit. on pp. 14, 54, and 55)

[74] G. Aad *et al.*, "Luminosity determination in pp collisions at $\sqrt{s} = 13$ TeV using the ATLAS detector at the LHC," *The European Physical Journal C*, vol. 83, no. 10, Oct. 2023. doi: 10.1140/epjc/s10052-023-11747-w. (cit. on p. 54)

[75] ATLAS Collaboration, "Introduction to the ATLAS Experiment," *ATLAS Open Data*, 2025. [Online]. Available: https://opendata.atlas.cern/docs/documentation/introduction/introduction_ATLAS#the-collaboration. (Accessed: May 04, 2025). (cit. on p. 57)

[76] G. Strong, "On the impact of selected modern deep-learning techniques to the performance and celerity of classification models in an experimental high-energy physics use case," *Machine Learning: Science and Technology*, vol. 1, Sep. 2020. doi: 10.1088/2632-2153/ab983a. (cit. on pp. 14 and 58)

[77] ATLAS Collaboration, "Magnet System," *ATLAS Experiment at CERN*. [Online]. Available: https://atlas.cern/Discover/Detector/Magnet-System. (Accessed: May 04, 2025). (cit. on p. 59)

[78] L. K. Bryngemark, "The ATLAS Experiment," in *Search for New Phenomena in Dijet Angular Distributions at* $\sqrt{s} = 8$ *and 13 TeV*, Cham: Springer International Publishing, 2017, pp. 39–49. [Online]. doi: 10.1007/978-3-319-67346-2_4. (cit. on pp. 14 and 59)

[79] F. Cavallari, "Performance of calorimeters at the LHC," *J. Phys.: Conf. Ser.*, vol. 293, no. 1, p. 012001, Apr. 2011, doi: 10.1088/1742-6596/293/1/012001. (cit. on p. 60)

[80] M. Aaboud *et al.*, "Performance of the ATLAS Transition Radiation Tracker in Run 1 of the LHC: tracker properties," *J. Instrum.*, vol. 12, no. 05, p. P05002, May 2017, doi: 10.1088/1748-0221/12/05/P05002. (cit. on p. 62)

[81] T. Argyropoulos *et al.*, "Cathode Strip Chambers in ATLAS: Installation, Commissioning and in Situ Performance," *IEEE Trans. Nucl. Sci.*, vol. 56, no. 3, pp. 1568–1574, 2009, doi: 10.1109/TNS.2009.2020861. (cit. on p. 66)

[82] The ATLAS Collaboration, "Operation of the ATLAS trigger system in Run 2," *J. Instrum.*, vol. 15, no. 10, p. P10004, Oct. 2020, doi: 10.1088/1748-0221/15/10/P10004. (cit. on p. 68)

[83] CERN, "Updated schedule for CERN's accelerators," *CERN*, 2025. [Online]. Available: https://home.web.cern.ch/news/opinion/accelerators/updated-schedule-cerns-accelerators. (Accessed: Apr. 3, 2025). (cit. on p. 69)

[84] O. S. Brüning *et al.*, *High-Luminosity Large Hadron Collider (HL-LHC): Technical Design Report*. Geneva: CERN, 2020. CERN Yellow Reports: Monographs. doi: 10.23731/CYRM-2020-0010. (cit. on p. 70)

[85] CERN, "CERN releases report on the feasibility of a possible Future Circular Collider," *CERN*, Mar. 31, 2025. [Online]. Available: https://home.cern/news/news/accelerators/cern-releases-report-feasibility-possible-future-circular-collider. (Accessed: Apr. 21, 2025). (cit. on p. 70)

[86] M. Benedikt, W. Bartmann, J.-P. Burnet, C. Carli, A. Chance, P. Craievich, M. Giovannozzi, C. Grojean, J. Gutleber, K. Hanke, A. Henriques, P. Janot, C. Lourenco, M. Mangano, T. Otto, J.H. Poole, S. Rajagopalan, T. Raubenheimer, E. Todesco, L. Ulrici, T.P. Watson, G. Wilkinson, F. Zimmermann, and B. Auchmann, *Future Circular Collider Feasibility Study Report Volume 2: Accelerators, technical infrastructure and safety*, CERN, Geneva, CERN-FCC-ACC-2025-0004, 2025. doi: 10.17181/CERN.EBAY.7W4X. (cit. on p. 70)

[87] M. Grazzini, A. Ilnicka, M. Spira, and M. Wiesemann, "Modeling BSM effects on the Higgs transverse-momentum spectrum in an EFT approach," *J. High Energy Phys.*, vol. 2017, no. 3, p. 115, Mar. 2017, doi: 10.1007/JHEP03(2017)115. (cit. on p. 72)

[88] ATLAS Collaboration, "ATLAS measures WZ production at 13.6 TeV," *ATLAS Experiment - Briefing*, Mar. 5, 2024. [Online]. Available: https://atlas.cern/Updates/Briefing/Run3-WZ-CrossSection. (Accessed: Jun. 9, 2025). (cit. on p. 72)

[89] LHC Higgs Cross Section Working Group, "Fiducial and differential cross sections, and Simplified Template Cross Sections (STXS)," *CERN Twiki*, [Online]. Available: https://twiki.cern.ch/twiki/bin/view/LHCPhysics/LHCHWGFiducialAndSTXS. (Accessed: Jun. 9, 2025). (cit. on p. 72)

[90] ATLAS Collaboration, "Simplified Template Cross Sections (STXS)," *ATLAS Experiment - Glossary*. [Online]. Available: https://atlas.cern/glossary/stxs (Accessed: Jun. 9, 2025). (cit. on p. 72)

[91] ATLAS Collaboration, "Good Runs List (GRL) definition," *ATLAS Open Data Portal*, [Online]. Available: https://opendata.atlas.cern/docs/documentation/data_collection/GRL_definition. (Accessed: Jun. 9, 2025). (cit. on p. 73)

[92] ATLAS Collaboration, "Introduction to Monte Carlo simulations," *ATLAS Open Data Portal*, [Online]. Available: https://opendata.atlas.cern/docs/documentation/monte_carlo/introduction_MC. (Accessed: Jun. 9, 2025). (cit. on p. 73)

[93] M. Aaboud *et al.* [ATLAS Collaboration], "Jet reconstruction and performance using particle flow with the ATLAS Detector," *Eur. Phys. J. C*, vol. 77, no. 7, 2017. doi: 10.1140/epjc/s10052-017-5031-2. (cit. on p. 77)

[94] ATLAS Collaboration, "Improving jet substructure performance in ATLAS using Track-CaloClusters," ATL-PHYS-PUB-2017-015, CERN, Geneva, 2017. [Online]. Available: https://cds.cern.ch/record/2275636 (cit. on p. 77)

[95] M. Cacciari, G. P. Salam, and G. Soyez, "The anti-k_t jet clustering algorithm," *J. High Energy Phys.*, vol. 2008, no. 04, p. 063, Apr. 2008, doi: 10.1088/1126-6708/2008/04/063. (cit. on p. 77)

[96] M. Cacciari, G. P. Salam, and G. Soyez, "FastJet user manual," *Eur. Phys. J. C*, vol. 72, no. 3, p. 1896, Mar. 2012, doi: 10.1140/epjc/s10052-012-1896-2. (cit. on p. 77)

[97] G. Aad *et al.*, "Muon reconstruction and identification efficiency in ATLAS using the full Run 2 pp collision data set at $\sqrt{s}$ = 13 TeV," *Eur. Phys. J. C*, vol. 81, no. 7, 2021. doi: 10.1140/epjc/s10052-021-09233-2. (cit. on p. 78)

[98] ATLAS Collaboration, "Transformer Neural Networks for Identifying Boosted Higgs Bosons decaying into $b\bar{b}$ and $c\bar{c}$ in ATLAS," CERN, Geneva, Tech. Rep. ATL-PHYS-PUB-2023-021, 2023. [Online]. Available: https://cds.cern.ch/record/2866601. (cit. on p. 78)

[99] NVIDIA, "What Is a Transformer Model?," *NVIDIA Blog*, Jun. 13, 2022. [Online]. Available: https://blogs.nvidia.com/blog/what-is-a-transformer-model/. (Accessed: Jun. 9, 2025). (cit. on p. 78)

[100] ATLAS Collaboration, "Efficiency corrections for a tagger for boosted $H \to b\bar{b}$ decays in pp collisions at $\sqrt{s} = 13$ TeV with the ATLAS detector," CERN, Geneva, Tech. Rep. ATL-PHYS-PUB-2021-035, 2021. [Online]. Available: https://cds.cern.ch/record/2777811. (cit. on p. 78)

[101] ATLAS Collaboration, "Measurement of the b-jet identification efficiency with the p_T^{rel} method in multi-jet events using pp collisions at $\sqrt{s} = 13$ TeV with the ATLAS Detector", CERN, Geneva, Tech. Rep. ATL-PHYS-PUB-2022-025, 2022. [Online]. Available: https://cds.cern.ch/record/2809692. (cit. on pp. 15, 82, and 83)

[102] R. C. Fernow, *Introduction to Experimental Particle Physics*. Oxford University Press, 1986. doi: 10.1017/9781009290098. (cit. on p. 86)

[103] S. Tavernier, *Experimental Techniques in Nuclear and Particle Physics*. Springer Science & Business Media, 2010. (cit. on pp. 15, 86, and 87)

[104] A. Vaswani, N. Shazeer, N. Parmar, J. Uszkoreit, L. Jones, A. N. Gomez, L. Kaiser, and I. Polosukhin, "Attention Is All You Need," arXiv preprint arXiv:1706.03762, 2023. [Online]. Available: https://arxiv.org/abs/1706.03762. (cit. on p. 88)

[105] S. Shleifer, J. Weston, and M. Ott, "NormFormer: Improved Transformer Pretraining with Extra Normalization," arXiv preprint, arXiv:2110.09456, 2021. [Online]. Available: https://arxiv.org/abs/2110.09456. (cit. on p. 88)

[106] M. Acciarri *et al.* [L3 Collaboration], "Measurement of the branching ratios $b \to e\nu X$, $\mu\nu X$, $\tau\nu X$ and νX," *Z. Phys. C*, vol. 71, no. 3, pp. 379–389, 1996. [Online]. Available: https://cds.cern.ch/record/302713, doi: 10.1007/s002880050184. (cit. on p. 97)

[107] P. Abreu *et al.* [DELPHI Collaboration], "Measurement of the semileptonic b branching fractions and average b mixing parameter in Z decays," *Eur. Phys. J. C*, vol. 20, pp. 455–478, 2001. [Online]. doi: 10.1007/s100520100690. (cit. on pp. 97 and 98)

[108] M. Paterno, *Calculating Efficiencies and Their Uncertainties*, FERMILAB-TM-2286-CD, Fermi National Accelerator Laboratory, Batavia, IL, USA, May 2004. (cit. on p. 100)

[109] ATLAS Collaboration, "Variable Radius, Exclusive-k_T, and Center-of-Mass Subjet Reconstruction for Higgs($\to b\bar{b}$) Tagging in ATLAS," CERN, Geneva, Tech. Rep. ATL-PHYS-PUB-2017-010, 2017. [Online]. Available: https://cds.cern.ch/record/2268678. (cit. on p. 101)

[110] G. Cowan, K. Cranmer, E. Gross, and O. Vitells, "Asymptotic formulae for likelihood-based tests of new physics," *The European Physical Journal C*, vol. 71, no. 2, Feb. 2011, doi: 10.1140/epjc/s10052-011-1554-0. (cit. on p. 102)

[111] A. L. Read, "Presentation of search results: the CLs technique," *Journal of Physics G: Nuclear and Particle Physics*, vol. 28, no. 10, pp. 2693, Sep. 2002, doi: 10.1088/0954-3899/28/10/313. (cit. on p. 102)